Dissertation

zur Erlangung des Doktorgrades (Dr. rer. nat.) am Fachbereich Geowissenschaften der Freien Universität Berlin

Sea-level and solid-Earth feedbacks on ice-sheet dynamics

vorgelegt von Hannes Konrad aus Heidelberg

im Februar 2015

Erstgutachter:	Prof. Dr. Maik Thomas
Zweitgutachter:	Prof. Dr. Giorgio Spada
Datum der Disputation:	8. Juni 2015

Abstract

Ice sheets fundamentally contribute to the climate system by exchanging freshwater with the oceans and influencing the Earth's radiative balance via their surface albedo. On the other hand, changing climatic conditions (precipitation, air and ocean temperature) as well as geothermal heat fluxes control the advance and retreat of ice sheets during glacial cycles. With the changing ice and ocean load on the Earth's surface, their evolution forces the redistribution of mantle material in the Earth's interior and causes changes of the gravity field and the displacement of the surface, both leading to sea-level change. The gravitational and deformational response depends on the viscoelastic structure of the solid Earth, which in turn has an effect on the dynamic evolution of the ice sheets.

In this thesis, a coupled model for ice and solid-Earth dynamics is realized, consistently accounting for surface loading of the Earth by redistribution of ice and ocean masses. It incorporates all primary feedbacks of viscoelastic deformation and gravitationally consistent sea level on the evolution of the modeled ice sheets. In idealized scenarios, it is found that the feedback mechanisms are most important at the boundary between grounded ice and oceans. This feedback is shown to be not adequately accounted for in an approximative representation of the solid-Earth deformation, commonly used in ice-sheet modeling. A possible future collapse of the West Antarctic Ice Sheet (WAIS) in a warming climate including rising sea levels is found to be prevented or delayed by soft viscoelastic Earth structures (i.e. featuring a thin lithosphere and a low-viscous asthenosphere), corresponding to the West Antarctic rift system. It is found that the iterative adjustment of the paleo bathymetry, necessary to match present-day observation of the bathymetry, as well as the ongoing relaxation imply shallower ambient ocean depths in Antarctica for stiffer Earth structures (i.e. featuring a thick lithosphere and a high-viscous mantle) during the last glacial cycle, leading to more stability during intermittent periods of warming preceding the Last Glacial Maximum (LGM). The findings on the future WAIS stability for softer Earth structures and the additional pre-LGM stability of the Antarctic Ice Sheet for stiffer Earth structures largely depend on the strength of the applied forcing of the ice dynamics. If, however, the ice sheet is forced to a tipping point, the solid-Earth structure may turn the balance towards stabilization or considerable ice-mass loss and associated sea-level rise. Therefore, the simultaneous consideration of ice dynamics and the Earth's deformational and gravitational response as in the presented coupled model provides a more reliable insight into ice dynamics.

Zusammenfassung

Die polaren Eisschilde tragen mit dem Austausch von Süßwasser mit den Ozeanen und dem Einfluss ihrer Oberflächenalbedo auf die Strahlungsbilanz der Erdoberfläche maßgeblich zum Klimasystem bei. Gleichzeitig verursachen Änderungen der klimatischen Randbedingungen (Niederschlag, Luft- und Ozeantemperaturen) und Geothermie Vorstöße und Rückzüge der Eisschilde während der Vereisungszyklen. Die sich dadurch ändernde Eis- und Ozeanlast auf der Erdoberfläche verursacht eine Umverteilung von Material im Erdmantel, was Veränderungen im Schwerefeld, Verschiebungen der Erdoberfläche und im Zusammenspiel dieser beiden Effekte Meeresspiegeländerungen bewirkt. Die Reaktion des Schwerefeldes und der Erddeformation auf Laständerungen hängt von der viskoelastischen Struktur der festen Erde ab, die dadurch Einfluss auf die Entwicklung der Eisschilde hat.

Im Rahmen dieser Arbeit wurde ein gekoppeltes numerisches Modell für die Dynamik von Eisschilden und der festen Erde realisiert, welches die Belastung der Erde durch die Umverteilung von Eis- und Ozeanmassen berücksichtigt. Dadurch lassen sich die vorrangigen Rückkopplungsmechanismen von Meeresspiegeländerungen und Verschiebungen der Erdoberfläche auf die Entwicklung der modellierten Eisschilde einbinden. In vereinfachten Szenarien kann der Übergang von aufsitzendem Eis zum Ozean, bzw. zum Schelfeis, als wichtigste Schnittstelle von Eis- und Erddynamik ausgemacht werden. Dieser Rückkopplungsmechanismus ist in einer näherungsweisen Beschreibung der Deformation der festen Erde, wie sie in der numerischen Modellierung von Eisschilden verwendet wird, nur unzulänglich repräsentiert. Der mögliche zukünftige Kollaps des Westantarktischen Eisschildes (West Antarctic Ice Sheet; WAIS) in einem wärmeren Klima einschließlich ansteigenden Meeresspiegels wird bei Annahme von weichen Erdstrukturen (d.h. dünne elastische Lithosphäre und niedrig-viskose Asthenosphäre), die der westantarktischen Riftzone entsprechen, verhindert oder verzögert. Die iterative Anpassung der Paleobathymetrie, die zur Reproduktion der gemessenen heutigen Bathymetrie notwendig ist, und die kontinuierliche Relaxation der festen Erde bedingen während des letzten Vereisungszyklus im Falle von steiferen Erdstrukturen (d.h. dicke elastische Lithosphäre und hoch-viskoser Mantel) zu flacheren Ozeanen in der direkten Umgebung des Antarktischen Eisschildes. Dies führt zu erhöhter Stabilität während zwischenzeitlicher Ozeanerwärmung vor dem Höhepunkt der letzten Eiszeit (Last Glacial Maximum; LGM). Die Befunde zur zukünftigen Stabilität des WAIS unter der Annahme weicher Erdstrukturen und zur zusätzlichen Stabilität des Antarktischen Eisschildes vor dem LGM im Falle steifer Erdstrukturen hängen stark vom klimatischen Antrieb der Eisdynamik ab. Wenn sich der Eisschild jedoch an einem kritischen Punkt befindet, kann die Erdstruktur den Ausschlag in Richtung einer Stabilisierung einerseits oder eines beträchtlichen Eismassenver-

lustes und des damit einhergehenden Meeresspiegelanstieges andererseits geben. Entsprechend erlaubt die gleichzeitige Berücksichtigung von Eisdynamik und Erddeformation sowie Schwerefeldänderungen, wie sie im hier vorgestellten Modell gegeben ist, verlässlichere Erkenntnisse über Eisdynamik.

Erklärung

Ich versichere, dass ich die vorliegende Dissertation selbstständig verfasst habe und keine anderen als die angegebenen Quellen und Hilfsmittel benutzt habe. Ein Promotionsverfahren wurde zu keinem früheren Zeitpunkt an einer anderen Hochschule oder bei einem anderen Fachbereich beantragt.

Hannes Konrad
Potsdam, Februar 2015

Contents

1 Introduction

During the Quaternary, the past 2.6 million years, the global mean sea level varied by over 100 m in response to the storage and discharge of ice on the continents in alternating glacial and interglacial periods (Fairbridge, 1961). In a complex interplay of atmospheric CO_2 content and orbital forcing, which is to date not fully understood (Roe and Allen, 1999; Paillard, 2001), climate conditions changed, causing ice sheets to form, vanish partially or completely, and re-advance again (Hays et al., 1976). The cold climate conditions in terms of surface air and ambient ocean temperature caused the ice sheets to build up over longer periods of time. The ice cover advanced into areas which have been unglaciated or covered by oceans during the shorter interglacial periods characterized by a warmer climate

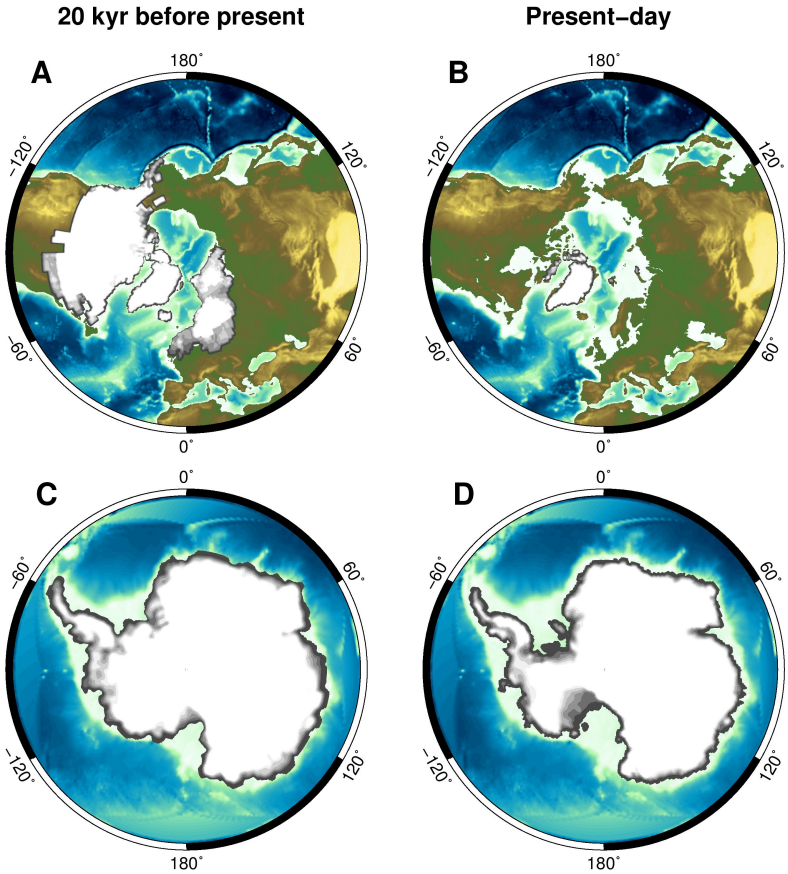

Figure 1.1
Northern hemispheric (A and B) and Antarctic (C and D) ice sheets at the Last Glacial Maximum (LGM; 20 kyr before present) and at present-day. The retreat of the ice sheets from their LGM extent towards present-day released a water volume corresponding to more than 100 m sea-level rise into the global oceans (see main text). The illustration is based on the ICE-5G glacial history (Peltier, 2004), on the BEDMAP2 data set for Antarctic ice thickness (Fretwell et al., 2013), and on the ETOPO1 global bathymetry (Amante and Eakins, 2009).

(e.g. Imbrie et al., 1992; Petit et al., 1999). Large Water masses, which had been contained in the oceans during the interglacials, were bound in the high-latitude ice sheets of Europe, North America, Greenland, and Antarctica, as well as in many glaciated mountain ranges during the cold periods (Figure 1.1A,C), leading to a drop of global mean sea level by more than 100 m w.r.t. to present-day (e.g. Rohling et al., 1998; Lambeck and Chappell, 2001). In turn, the retreat of the ice sheets in the interglacials (Figure 1.1B,D) released the stored water into the oceans, causing sea-level rise and transgression of shore lines. Signatures of this alternation are recorded for example in sedimentary deposits containing the past isotopic composition of ocean water (cf. Figure 1.2).

The periodical exchange of mass between the ice sheets and the oceans affects the load on the Earth's surface, which causes redistribution of mantle material in the Earth's interior and by that displacement of the Earth's surface (e.g. Nansen, 1928; Haskell, 1935), referred to as the glacial-isostatic adjustment (GIA). The redistribution of mass – be it ice mass, ocean mass, or mantle material – also implies changes of the gravity field of the Earth. In the absence of dynamic changes in the ocean and the atmosphere, the ocean surface coincides with an isoline of the gravitational potential (Gauß, 1828), specified as geoid. Therefore, sea-level changes are not only driven by water storage in and discharge from the ice sheets, but also by the geoid displacement caused by the evolution of the mass distribution (Farrell and Clark, 1976).

The continental ice sheets, however, do not only control the evolution of sea level and solid-Earth deformation, but they are themselves affected by rising or falling sea levels in their marine-based portions (e.g. Denton et al., 1986; Siegert and Dowdeswell, 2004; Pollard and DeConto, 2009), as well as by vertical motion of the Earth's surface (e.g. van den Berg et al., 2008). In the traditional approach to sea-level modeling, the ice-sheet evolution is retrieved from geological records (Peltier, 1994, 2004), from geomorphological evidence (Ivins and James, 2005; Ivins et al., 2013) or from numerical ice-sheet modeling (Whitehouse et al., 2012a,b) – partially constrained by geodetic observations (e.g. Peltier et al., 2014). The glacial history is then applied to a solid-Earth model in order to infer GIA and to interprete observations of paleo relative sea level (RSL), i.e. the combined effect from surface displacement and geoid evolution (e.g. Lambeck et al., 1990; Milne et al., 1998; Kaufmann and Lambeck, 2000; Peltier, 2004; Klemann and Wolf, 2005; Stocchi and Spada, 2009; Stocchi et al., 2013). In these GIA investigations, the coupling between the solid-Earth/sea-level response and the ice-sheet evolution is neglected. Ice-sheet models, on the other hand, typically employ a simple parameterization of the solid Earth (e.g. Le Meur and Huybrechts, 1996; Huybrechts,

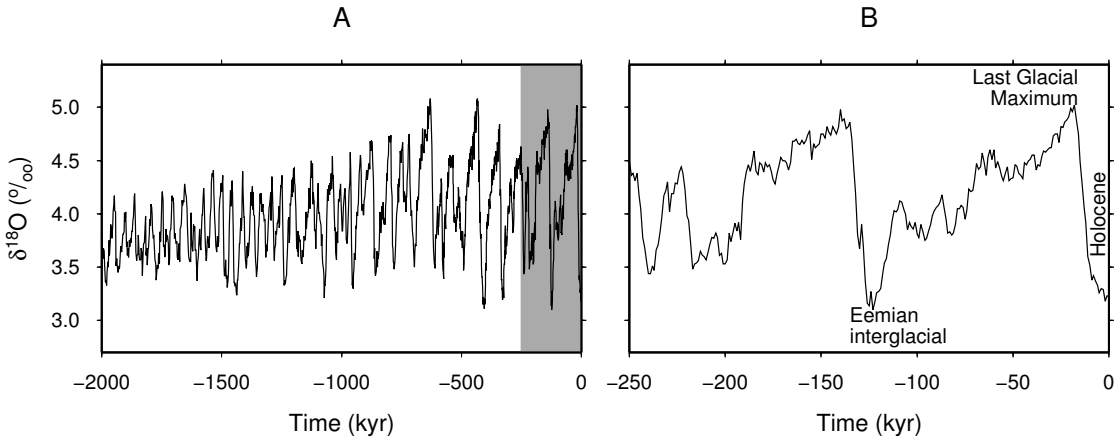

Figure 1.2
Globally stacked time series of benthic δ^{18}O (Lisiecki and Raymo, 2005). To a first-order approximation, the isotopic composition of oxygen in layered marine sediments, for which δ^{18}O is a measure, indicates the alternation of the continental ice volume during glacials and interglacials (Shackleton, 1987). A: The illustrated period covers the Quarternary from 2000 kyr before present ($\hat{=} -2000$ kyr) until today ($\hat{=} 0$ kyr). The grey shading indicates the period illustrated in B (the last two glacial cycles).

2002; Greve and Blatter, 2009; Greve et al., 2011; Pollard and DeConto, 2012b; Bindschadler et al., 2013), which does not allow for interpreting RSL data, predicting present-day GIA signals in the geodetic data sets, or inverting for physical properties of the Earth's interior.

There have been efforts to model the evolution of ice sheets and the respective viscoelastic deformational response more completely (e.g. Le Meur and Huybrechts, 1996, 1998; van den Berg et al., 2008; Olaizola et al., 2012). The conclusions on the necessity of a full viscoelastic representation of the solid Earth compared to the simpler representations differed in these studies. Newer studies including a gravitationally consistent description of sea-level (Gomez et al., 2012, 2013; de Boer et al., 2014) point at the importance of the coupling mechanisms between ice and the solid Earth, particularly for the evolution of marine-based ice sheets.

1.1 Main interaction mechanisms between ice and solid-Earth dynamics

The most straightforward interaction of ice sheets with the solid Earth concerns the loading nature of the ice sheets: While an ice sheet builds up, the underlying planetary surface is depressed by the respective weight. Likewise, the decreasing

weight of a decreasing ice column unloads the Earth at the respective site and loads the ocean where correspondingly the water column increases. These loading and unloading cycles as well as the related changes in the gravity field force the viscoelastic deformation of the solid Earth. In turn, the response of the solid Earth to this forcing affects the evolution of the ice sheets, mainly via the following three mechanisms, which are – to different extents – studied in this thesis.

1.1.1 Surface elevation and surface mass balance

The higher an ice sheet grows, the colder the air is at its upper surface. This cooling at the surface implies lower precipitation rates and therefore a lower surface mass balance (SMB) in the accumulation areas of the ice sheet (e.g. Oerlemans, 1980; Huybrechts, 1993). With less accumulation, the growth of the ice sheet is slowed down. The response of the Earth to the growing ice column is subsidence of the Earth surface by which also the ice-sheet surface subsides and is again subjected to warmer conditions, also featuring more precipitation and thus a higher SMB. Ultimately, this leads to more ice volume stored in the ice sheet than if no bedrock subsidence occured.

This feedback is of course also important during deglaciation, when the related uplift of the unloaded Earth implies lower temperatures at the ice sheet's surface and consequently less accumulation, but possibly also to a reduced melt water production in the ablation areas, e.g. for the Greenland Ice Sheet.

In the scope of this thesis, it shall briefly be studied how the characteristics of solid-Earth relaxation, i.e. the magnitudes of deformation (determined by the thickness of the lithosphere) and time scales (determined by asthenospheric and mantle viscosities) affect the growth of ice sheets via this feedback mechanism. The mechanism itself is prescribed in terms of the surface temperatures and the SMB depending on the surface elevation of the ice sheet at a given site.

1.1.2 Bedrock deformation and basal ice velocities

The bedrock gradient as a boundary condition for the velocity field affects the ice dynamics in the lower part of an ice sheet. For example, the ice velocities close to the base in the case of a static ice–rock interface (no sliding and no melting) would follow the topography gradients. The reponse of the solid Earth implies a modulation of the bedrock gradient. This is, however, of a much longer wave-length than the typical roughness of the bedrock topography as exemplarily illustrated for the Antarctic Ice Sheet in Figure 1.3. Additionally, the effects are overlaid by the changes in the ice thickness that led to the solid-Earth response in the first

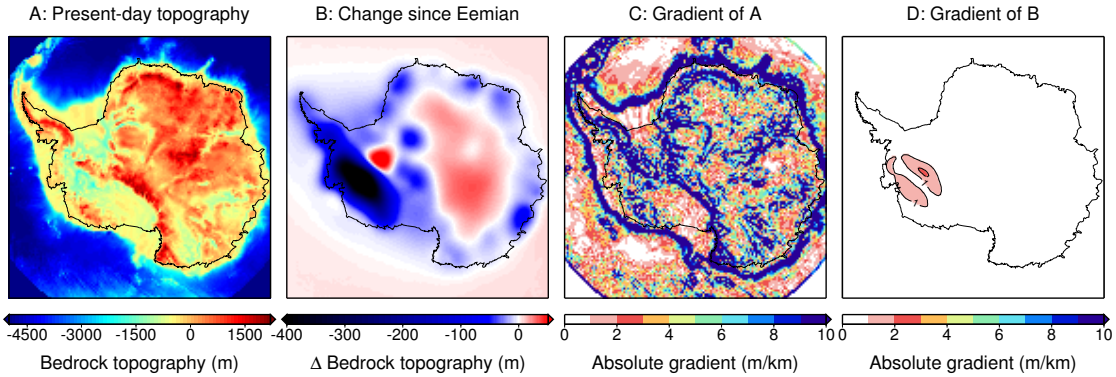

Figure 1.3
A: Present-day bedrock topography of Antarctica from the BEDMAP2 data set (Fretwell et al., 2013). B: Exemplary change in bedrock topography since the last interglacial (Eemian). The data are from the 'soft' Earth structure as discussed in Chapter 5. C: Absolute of the BEDMAP2 bedrock gradient. D: Absolute of the gradient of the field shown in B.

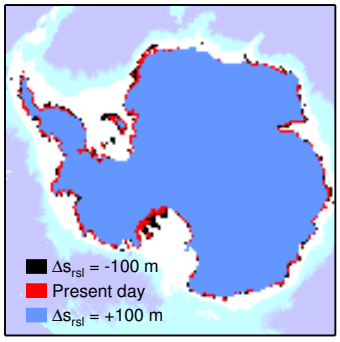

Figure 1.4
Effect of instantaneously applied RSL changes $\Delta s_{\mathrm{rsl}} = \pm 100$ m on the Antarctic grounding line: The blue areas are grounded if $\Delta s_{\mathrm{rsl}} = +100$ m (increasing sea levels); the red areas are additionally grounded under present-day conditions ($\Delta s_{\mathrm{rsl}} = 0$ m); the black areas are those which would also ground if $\Delta s_{\mathrm{rsl}} = -100$ m (falling sea levels).

place. For these two reasons, this feedback mechanism is considered less important in the scope of this thesis and therefore only treated briefly.

1.1.3 Relative sea level and grounding-line position

A rather intuitive feedback from Earth dynamics to ice dynamics can be inferred from the floating criterion for ice shelves: Here, the weight of the ice column is less than the weight of the respective ocean water column if no ice was present, so that the ice floats on the ocean according to Archimedes' principle. At the grounding line (GL; the transition from grounded ice to floating ice), the weight of the ocean water column and of the ice column are equal. When the height of the ocean water column (the relative sea level; RSL) changes due to sea-level rise or fall or due to vertical motion of the bedrock, ice might ground or ungrounded. This is, however, a relatively weak mechanism by itself as Figure 1.4 illustrates: Even a large RSL change of ± 100 m results in relatively little instantaneous float-

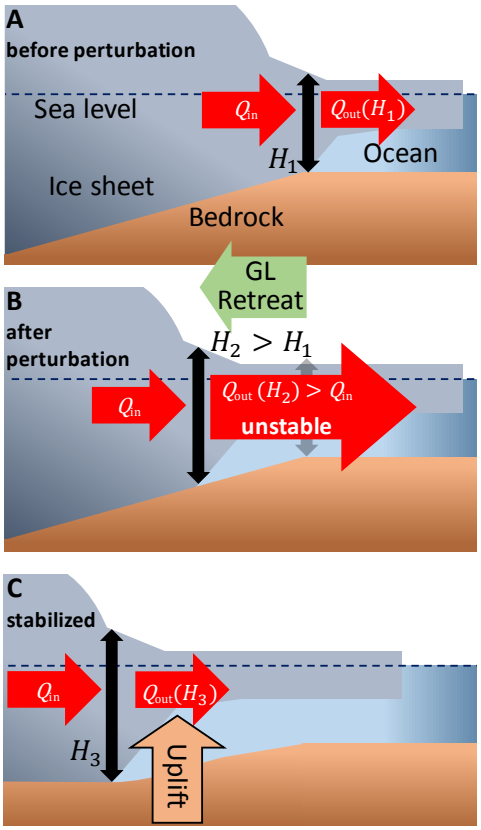

Figure 1.5
The Marine Ice Sheet Instability (MISI): The ice sheet rests on a bed that is deepening inwards from the GL. In the metastable state (A), the flux from the interior (Q_{in}) to the grounding line (GL) is in balance with the flux through the GL (Q_{out}). Once this metastable state is perturbed, i.e. the GL retreats slightly (B), the GL is situated at a location with deeper ocean and so also with thicker ice column (the weight of the ocean water column equals the weight of the ice column at the GL). The flux through the GL is larger (see main text) which leads to ongoing GL retreat – the MISI. The bedrock uplift eventually stops the GL retreat by lowering the relative sea level at the GL (C): The fluxes to and through the GL are in balance again.

ing/grounding according to the floating criterion alone. The floating or grounding, however, also has an impact on the stress regime at the specific locations and in their surroundings. With this impact of RSL changes on ice dynamics, it becomes a major driver for the evolution of the ice sheet on glacial time scales (e.g. Pollard and DeConto, 2009).

This is not only true for pure sea-level changes in terms of eustatic sea-level rise or fall, for example due to changes of the northern hemispheric ice-sheet volumes. If the surface deformation under a marine-based ice sheet is large enough, it can also affect the ice dynamics, in principle without altering global sea-levels. One example of particular interest here is the situation studied by Gomez et al. (2012). A marine-based ice sheet that is situated on an inward deepening bedrock is subject to the so-called Marine Ice Sheet Instability (MISI). The MISI has been proposed and described by Weertman (1974) and subsequently treated by e.g. Thomas and Bentley (1978) and Schoof (2007). Figure 1.5 illustrates the MISI situation before (A) and during the retreat (B). While the GL rests on the top of the slope, the mass flux from the ice sheet's interior to the GL is in balance with the flux through

the GL into the ice shelf, which defines a metastable state: A perturbation of this state that leads to GL retreat downward the slope leads to a deeper ocean at the GL, which leads to a thicker ice column at the GL according to the floating criterion ($H_1 < H_2$ in Figure 1.5 with H standing for ice thickness). The increasing ice thickness leads to a larger outflow into the ice shelf. As this is not compensated by the flux from the ice sheet's interior to the GL, the ice sheet retreats until the GL reaches a flat or reversly sloped bed. The MISI mechanism is particularly important for the West Antarctic Ice Sheet, which is in large parts marine-based and beneath which the bedrock deepens towards the interior of Marie Byrd Land (cf. Chapter 4). It should, however, be noted that the direction of the surface slope is not the only quantity controlling GL stability, as the general stress state can also lead to stable situations on a backward slope (e.g. Gudmundsson et al., 2012; Gudmundsson, 2013).

The retreat of the GL during the MISI implies loss of grounded ice, not only at formerly grounded areas which are now floating, but also in the GL's hinterland. This loss of grounded ice unloads the solid Earth, which responds with uplift, delayed with respect to the forcing. Gomez et al. (2012) found that this uplift eventually stabilizes the marine-based ice sheet because it ultimately reduces the RSL at the GL (Figure 1.5C). It does not only hold for marine-based ice sheets on retrograde slopes as illustrated in Figure 1.5, but in principal for any ice-sheet geometry with a direct ice–ocean interface. Consequently, there is also a feedback with an advancing GL: The crustal subsidence following the GL advance and the associated loading of the solid Earth locally increases the ocean depth. This, in turn, provides a negative feedback on the GL advance. In each case, the solid Earth represents a stabilizing mechanism counteracting GL retreat or advance.

1.2 Outline of the thesis

This thesis aims at investigating the above feedback mechanisms in a state of the art ice-sheet/solid-Earth modeling system including a gravitationally consistent description of sea level.

In Chapter 2, the necessary continuum mechanical theory for large-scale ice dynamics of ice sheets and ice shelves and solid-Earth relaxational dynamics, as well as the theory of the sea-level equation is outlined and the respective numerical models are introduced. The description of the coupling of the ice-sheet models and the self-gravitating viscoelastic solid-Earth model (SGVEM) and a respective evaluation conclude this chapter.

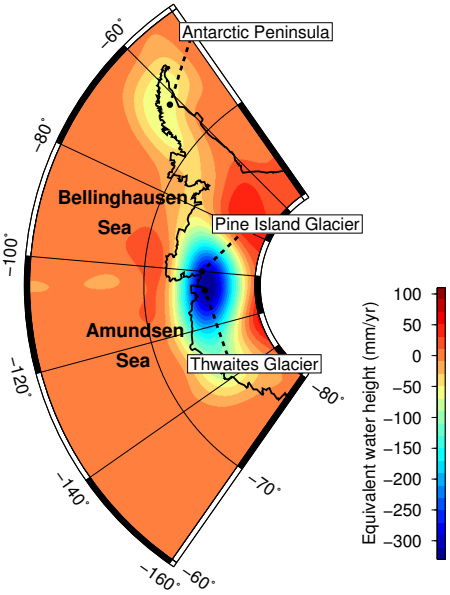

Figure 1.6
Linear trends of ice-mass variations (in equivalent water height) along the West Antarctic Amundsen Sea coast and in the Antarctic Peninsula as measured by the Gravity Recovery And Climate Experiment (GRACE) during 2002 and 2014. The data are from Release-2 by the Center for Space Research, University of Texas (Bettadpur, 2012) from Legendre degree 2 to 96, with a Wiener optimal filter applied (Sasgen et al., 2006). Note the prominent ice-mass loss of the region around Pine Island Glacier and Thwaites Glacier. Courtesy of Ingo Sasgen.

The coupled model system is first applied to idealized settings in Chapter 3, where the focus lies on the characterization of the differences between a simpler representation of solid-Earth relaxation as it is common in ice-sheet models and the continuum-mechanical SGVEM approach. In the simpler representation, the so-called 'elastic lithosphere / relaxing asthenosphere' model (ELRA), the lithosphere is considered a thin plate with infinite horizontal extent, whereas the viscous mantle flow is modeled by one *a priori* relaxation time. Systematic differences occur in the responses of the ELRA representation and the SGVEM. Their impact on ice dynamics is found to be particularly large if the sea level is considered consistently as shown in Section 3.2.

In Chapters 4 and 5, the Antarctic Ice Sheet (AIS) is studied by means of the fully coupled model system. Chapter 4 focusses on the future evolution of the West Antarctic Ice Sheet (WAIS), which is of particular interest due to its potential for rapid disintegration (e.g. Conway et al., 1999; Joughin and Alley, 2011) and due to the accelerated mass loss observed in the satellite era (Figure 1.6). The study finds that an externally forced retreat of the WAIS can be stopped or delayed by the Earth's response in the presence of low-viscous asthenospheric layers, which represent a realistic assumption for the West Antarctic rift system underlying the WAIS. The external forcing comprises an increase of the surface air temperature and the ocean temperature in the sensitive Amundsen Sea Sector of the West Antarctic coast (Figure 1.6), as well as sea-level rise from the melting of glaciers and the Greenland Ice Sheet.

Finally, Chapter 5 addresses the AIS during the last glacial cycle, i.e. the last ∼120 kyr, with a special focus on the grounded ice evolution under the assumptions of different viscoelastic structures of the solid Earth. It is shown that the reconstructed paleo bathymetry for the Eemian interglacial depends on the viscoelastic structure of the Earth, and that the viscosity distribution thereby affects the ice-dynamical evolution, particularly in today's shelf areas surrounding the AIS. Depending on the applied Earth structure, the AIS is more or less vulnerable to interim ice-mass loss prior to the Last Glacial Maximum. Neglecting the reconstruction of the paleo bathymetry introduces a bias towards a smaller ice volume through the complete glacial cycle, independent of the applied Earth structure.

Chapter 6 draws final conclusions and gives an outlook on the potential of future improvements in the framework of the coupled model system.

2 Theoretical background and numerical aspects

2.1 Basics concepts in continuum mechanics

The complex dynamics of large ice masses, such as the polar ice sheets, and of the interior of the Earth, and specifically their response to changes in their surroundings, i.e. oceans and atmosphere in the case of ice sheets and the surface load in the case of the solid Earth, can be described mathematically by continuum mechanical methods. Balance laws that quantify how physical quantities change in space and time form the basis for continuum mechanics. In this context, the following balance laws shall be considered:

1. conservation of mass,
2. balance of linear momentum,
3. balance of angular momentum, and
4. conservation of energy.

The individual characteristics of the studied materials are described by constitutive equations. They relate for instance a material's deformation to the applied stress. The constitutive equations are combined with the balance laws. Finally, boundary conditions for the continuum-mechanical fields need to be prescribed so that the quantities of interest can be solved for.

There are two frames of reference in continuum mechanics. In the Lagrangian frame, the motion of specific particles in a continuum is considered in terms of their displacement from a reference state. The Eulerian frame in contrast adresses a continuum mechanical problem by considering the evolution of the continuum in time at specific locations. The two frames differ in terms of the design of the balance laws. The continuum mechanical approach to ice dynamics is typically the Eulerian one. In contrast to that, viscoelastic solid-Earth dynamics are captured in the Lagrangian frame, as one is interested in the displacement of the Earth surface and deeper layers in the Earth, which can be considered as deviation from a reference state. Due to this difference, and due to the fact, that there are still further differences between ice and solid-Earth dynamics, such as the constitutive

equations or the solution for gravity in the case of the solid Earth, the relevant equations for modeling ice and Earth dynamics will be introduced separately in the following.

2.2 Ice dynamics

Ice dynamics are driven by gravity and mainly influenced by the mass balance at the upper and lower surfaces of the ice body and (in the case of a non-floating setting such as an ice sheet or a glacier) the bedrock topography under the ice. The quantities of interest are typically the ice thickness distribution $H(x, y, t)$ as a function of the horizontal coordinates x and y and time t, the velocity field $\vec{v}(x, y, z, t)$ (also depending on the vertical coordinate z), and the temperature field $T(x, y, z, t)$.

Ice is an almost incompressible medium. In the context of large-scale ice dynamics, the only exception from the assumption of incompressibility is the firn column at the top of an ice sheet. Its shallowness (60 – 70 m of firn vs. up to 4000 m of ice; Cuffey and Paterson, 2010) allows us to neglect lower densities and the related compactional processes in the firn column. Therefore, the density of ice is assumed to be constant in space and time ($\rho = 910$ kg/m^3; Cuffey and Paterson, 2010).

Another characteristic of ice is that it deforms viscously under applied stress in the relevant stress range (Cuffey and Paterson, 2010). A common constitutive equation for the flow of polycrystalline ice will be discussed below. What is of interest at this stage, however, is the resulting inert behaviour of ice when compared to other fluids such as water: For example the velocities in the Greenland outlet glacier Jakobshavn Isbrae, which is among the fastest moving glaciers on Earth, do not exceed 18 km/yr (Joughin et al., 2014a). The slow velocities of ice allow us to neglect accelerational and centrifugal contibutions in the linear momentum balance (Greve and Blatter, 2009). Therefore, only gravity (expressed via the gravitational acceleration $\vec{g}$) remains for driving ice dynamics.

The energy budget of ice typically accounts for internal energy density $\varepsilon(T)$, heat transport in terms of heat flux $\vec{q}_{\mathrm{h}}(T)$, dissipative energy loss and external forcing such as insolation expressed via specific radiation power r_{sol}. The dissipative energy loss is given by the trace of the product of the Cauchy stress tensor $\underline{\boldsymbol{\tau}}$ and the strain rate tensor $\underline{\dot{\boldsymbol{\epsilon}}}$, which is given by

$$\underline{\dot{\boldsymbol{\epsilon}}}(x, y, z, t) = \frac{1}{2}\left(\operatorname{grad}\vec{v} + (\operatorname{grad}\vec{v})^{\mathrm{T}}\right) \quad . \tag{2.1}$$

Here, the superscript 'T' stands for the transposed of the respective tensor. See Appendix A for the definition and notation of operations on tensors.

Given these remarks on ice-specific aspects of continuum mechanics, one can derive the following equations from the general conservation principles mentioned in Section 2.1 (see e.g. Greve and Blatter (2009) for a detailed derivation):

$$\begin{aligned} \operatorname{div} \vec{v} &= 0 && (2.2)\\ \operatorname{div} \underline{\boldsymbol{\tau}} + \rho \vec{g} &= 0 && (2.3)\\ \underline{\boldsymbol{\tau}} &= \underline{\boldsymbol{\tau}}^{\mathrm{T}} && (2.4)\\ \frac{\partial \varepsilon}{\partial t} + \vec{v} \cdot \operatorname{grad} \varepsilon &= \operatorname{tr}\left(\underline{\boldsymbol{\tau}} \cdot \underline{\dot{\boldsymbol{\epsilon}}}\right) + \operatorname{div} \vec{q}_{\mathrm{h}} + \rho r_{\mathrm{sol}} && (2.5) \end{aligned}$$

Note that the conservation of angular momentum directly implies the symmetry of the stress tensor (Eq. 2.4).

The constitutive relations for polycrystalline ice

Eqs. 2.2 – 2.5 form a system to retrieve the three components of $\vec{v}$ and the scalar quantity T (via ε and $\vec{q}_{\mathrm{h}}$). One needs, however, to relate the internal energy ε and the heat flux $\vec{q}_{\mathrm{h}}$ to the temperature T via empirical constitutive relations. Furthermore, as the six free components of the stress tensor $\underline{\boldsymbol{\tau}}$ are also unknown, a constitutive relation that relates $\underline{\boldsymbol{\tau}}$ and (in the case of a viscous medium such as ice) the strain rate tensor $\underline{\dot{\boldsymbol{\epsilon}}}$ is needed. The relation between internal energy and temperature is the caloric equation of state:

$$\varepsilon(T) = \rho \, c_{\mathrm{ice}} \, T \tag{2.6}$$

where c_{ice} is the specific heat of ice and – following the authors of the employed ice-sheet models (Thoma et al., 2014; Pollard and DeConto, 2012b, see below) – assumed constant in the experiments in this thesis. The heat flux–temperature relation follows Fourier's law of heat conduction (Greve and Blatter, 2009):

$$\vec{q}_{\mathrm{h}} = -\kappa \operatorname{grad} T \tag{2.7}$$

where κ is the heat conductivity of ice. Likewise, as in the case of c_{ice}, it is assumed to be constant here.

A constitutive relation for so-called secondary creep of polycrystalline ice in the relevant stress regime has been proposed by Glen (1955). It starts from the

description of an incompressible Newtonian fluid with viscosity η_{Ice}:

$$\underline{\boldsymbol{\tau}}^{\mathrm{D}} = 2\,\eta_{\mathrm{Ice}}\,\underline{\dot{\boldsymbol{\epsilon}}}\ . \tag{2.8}$$

The stress deviator $\underline{\boldsymbol{\tau}}^{\mathrm{D}} = \underline{\boldsymbol{\tau}} + p\underline{\mathbb{1}}$ is the stress tensor corrected for the hydrostatic pressure $p = -1/3\,\mathrm{tr}\,(\underline{\boldsymbol{\tau}})$ as the latter should not affect the deformation. Here, $\underline{\mathbb{1}}$ stands for the unity tensor. In general, η_{Ice} cannot be expected to be a constant value. Instead, it depends on the stress state of the ice body which makes the constitutive relation for ice nonlinear. (Glen, 1955) proposed the following empirical relation:

$$\eta_{\mathrm{Ice}}^{-1} = 2\,A(T,p)\,{\tau_{\mathrm{e}}}^{n-1} \ \text{with} \tag{2.9}$$

$$\tau_{\mathrm{e}} = \sqrt{\frac{1}{2}\mathrm{tr}\left(\underline{\boldsymbol{\tau}}^{\mathrm{D}\,2}\right)}\ . \tag{2.10}$$

Here, A is the so-called rate factor, n is the flow law exponent, and τ_{e}, being the second invariant of $\underline{\boldsymbol{\tau}}^{\mathrm{D}}$, is the effective stress. The exponent n is widely chosen to equal 3 (Cuffey and Paterson, 2010). Eq. 2.9 in combination with Eq. 2.8 is an empirical description of the secondary creep of polycrystalline ice known as Glen's Generalized Flow Law (Glen, 1955; Nye, 1957).

There are situations (also in this thesis), in which the rate factor A is assumed constant. This assumption leads to the situation that the mechanics affect the thermodynamics via the dissipative term $\mathrm{tr}(\underline{\boldsymbol{\tau}} \cdot \underline{\dot{\boldsymbol{\epsilon}}})$ in Eq. 2.5, but no feedbacks occur from the thermodynamics on the mechanics. A more adequate way is to consider an Arrhenius relationship for $A(T,p) = A(T')$ (Greve and Blatter, 2009) with $T' = T + 9.8 \times 10^{-8}\ \mathrm{K/Pa}^{-1} p$ being the temperature relative to the pressure melting point:

$$A(T') = A_0\,e^{-Q_{\mathrm{act}}/(R_{\mathrm{gas}}T')}\ . \tag{2.11}$$

Here, Q_{act} is the activation energy for creep and $R_{\mathrm{gas}} = 8.314\ \mathrm{J\ mol^{-1}\ K^{-1}}$ is the universal gas constant. See Table 2.1 in the framework of the numerical model description (Sections 2.2.3 and 2.2.4) for values of A_0 and Q_{act}. Another established relation for $A(T')$ is the one by Hooke (1981):

$$A(T') = A'_0\,e^{3C_{\mathrm{H}}/(T_{\mathrm{H}}-T')^{k_{\mathrm{H}}} - Q_{\mathrm{act}}/(R_{\mathrm{gas}}T')}\ , \tag{2.12}$$

in which the first term in the exponent on the right-hand side is related to the activation of self-diffusion. Again, see Table 2.1 for values of A'_0, C_{H}, k_{H}, and Q_{act}. By Eqs. 2.8 and 2.9, the relation between the stress deviator $\underline{\boldsymbol{\tau}}^{\mathrm{D}}$ and the strain

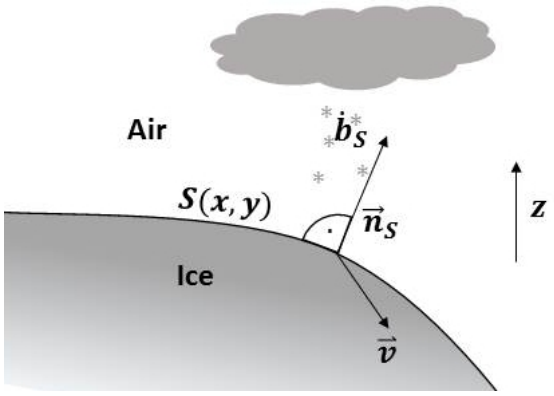

Figure 2.1
Kinematic boundary condition at the upper surface of an ice sheet.

rate tensor $\underline{\dot{\epsilon}}$ is given by

$$\underline{\dot{\epsilon}} = \frac{1}{2\,\eta_{\mathrm{Ice}}}\,\underline{\tau}^{\mathrm{D}} = A(T')\,\tau_{\mathrm{e}}^{n-1}\,\underline{\tau}^{\mathrm{D}} \quad , \tag{2.13}$$

which links the velocity field $\vec{v}$ to $\underline{\tau}^{\mathrm{D}}$ via Eq. 2.1.

The equation for ice thickness

Here, an equation for the spatio-temporal evolution of the ice thickness shall be derived from the principle of mass conservation and geometric considerations. As already implied above, let the coordinate system be chosen such that the z-axis points vertically upwards (i.e. anti-parallel to the gravitational force) and let $S(x, y, t)$ be the z-coordinate of the free upper surface of the ice sheet or shelf. Then it is

$$S(x, y, t) - z = 0 \tag{2.14}$$

on the ice body's upper surface, from which the normal vector $\vec{n}$ on this surface (Figure 2.1) can be easily derived: $\vec{n}_S = (-\partial S/\partial x, -\partial S/\partial y, 1)^{\mathrm{T}}$. The kinematic boundary condition for this free surface is (Greve and Blatter, 2009):

$$\frac{\partial S}{\partial t} - \vec{n}_S \cdot \vec{v}|_{z=S} = \frac{\partial S}{\partial t} + \left(v_x\,\frac{\partial S}{\partial x} + v_y\,\frac{\partial S}{\partial y} - v_z \right)\Bigg|_{z=S} = \dot{b}_S \tag{2.15}$$

The surface mass balance (SMB; in m/yr) $\dot{b}_S$ is the product of the ice budget (also in m/yr) perpendicular to the surface and the length of the normal vector $\vec{n}$.

The corresponding kinematic boundary condition at the ice base $B_{\mathrm{Ice}}(x, y, t)$ is:

$$\frac{\partial B_{\mathrm{Ice}}}{\partial t} + \left(v_x \frac{\partial B_{\mathrm{Ice}}}{\partial x} + v_y \frac{\partial B_{\mathrm{Ice}}}{\partial y} - v_z \right) \Bigg|_{z=B_{\mathrm{Ice}}} = \dot{b}_B \tag{2.16}$$

In the case of an ice sheet, it is $B_{\mathrm{Ice}} = B$ with bedrock elevation $B(x, y, t)$ and the time evolution of B being the subject of solid Earth deformation as described in Section 2.3.

Integrating the equation for mass continuity 2.2 over the vertical coordinate z, application of Leibniz' rule, and inserting Eqs. 2.15 and 2.16 yields an equation for ice thickness $H = S - B_{\mathrm{Ice}}$ (Greve and Blatter, 2009):

$$\frac{\partial H}{\partial t} = -\frac{\partial}{\partial x}\left(H\,\overline{v}_x\right) - \frac{\partial}{\partial y}\left(H\,\overline{v}_y\right) + \dot{b} \ \text{ with} \tag{2.17}$$

$$\overline{v}_{x,y} = \frac{1}{H}\int_{B_{\mathrm{Ice}}}^{S} v_{x,y}\,\mathrm{d}z \ \text{(mean horizontal velocities).} \tag{2.18}$$

Note that the composition of $\dot{b} = \dot{b}_S - \dot{b}_B$ is due to the convention of normal vectors pointing outwards both at the ice surface and base: $\dot{b}_S > 0$ means mass gain at the surface while $\dot{b}_B > 0$ means mass loss at the base. Eq. 2.17 is fundamental for the computation of ice dynamics. However, the transport term (divergence of the horizontal velocity field multiplied by the ice thickness) can only be quantified by computing horizontal velocities from the strongly coupled Eqs. 2.3 – 2.5 and 2.13, of which the latter also introduces nonlinearity into the mathematical system.

Temperature evolution in the ice

For thermodynamics, it can be shown that horizontal heat convection is negligible, so that, by accounting for the constitutive Eqs. 2.6, 2.7, and 2.13, the equation for energy conservation 2.5 can be formulated as (Greve and Blatter, 2009):

$$\rho\, c_{\mathrm{ice}} \left(\frac{\partial T}{\partial t} + \vec{v} \cdot \mathrm{grad}\, T \right) = \kappa \frac{\partial^2 T}{\partial z^2} + 2\, A(T')\, \tau_{\mathrm{e}}^{n+1} \ , \tag{2.19}$$

where the last term on the right-hand side stands for dissipative heating.

2.2.1 Boundary conditions for ice dynamics

Surface and basal mass balance

The SMB $\dot{b}_{\mathrm{S}}$ describes the atmospheric input of ice into the ice sheet or shelf and consists of precipitation, melting, refreezing, evaporation, and run-off and

might therefore also take negative values. It serves as a boundary condition for the velocity field $\vec{v}$ via Eq. 2.15. The same holds for the basal mass balance $\dot{b}_B$, which is made up of basal melting and freezing. Melt water that percolates from the surface into the ice body might refreeze inside the ice body or be transported through the ice which can be considered as a porous medium. This is a very important issue in glaciology (Cuffey and Paterson, 2010), but will not be treated further in this thesis, except for the consideration of basal sliding due to melt water at the base (see below).

Stress-free ice surface

Atmospheric pressure and wind stress are negligible when compared to the stress field inside the ice body. Therefore, the ice surface is considered stress-free:

$$\underline{\boldsymbol{\tau}}|_{z=S} \cdot \vec{n}_S = 0 \ , \tag{2.20}$$

with normal vector $\vec{n}_S$ as shown in Figure 2.1.

Basal sliding

For ice sheets, a similar approach for basal stresses would imply a known stress field in the solid Earth. As this is usually not available, it is substituted by an empirical law for basal sliding that links basal horizontal velocities to basal stress. Note that the coupling between ice and solid-Earth dynamics, as it is treated in this thesis and described in Section 2.4, does not include a full treatment of stresses at the ice–bedrock interface. This would not be feasible because the deformation of ocean sediments under sliding ice, for example, cannot be treated by the applied viscoelastic Earth model. Consequently, the basal sliding approach as it is shown here holds for any experiment in the scope of this thesis. Weertman (1957) proposed a power law for the relation between basal stress $\vec{\tau}_B = \underline{\boldsymbol{\tau}}|_{z=B} \cdot \vec{n}_B$ (with $\vec{n}_B$ being the basal normal vector) and basal velocity $\vec{v}_B$. It is formulated as (Cuffey and Paterson, 2010):

$$\vec{v}_B = \vec{v}|_{z=B} = C^{-1/m} \ |\vec{\tau}_B|^{1/m-1} \, \vec{\tau}_B \ . \tag{2.21}$$

Here, m is the basal friction exponent, and C is the basal friction coefficient, which depends on the material of the underlying bedrock and the amount of melt water at the base. The floating of ice shelves on the ocean implies zero friction at the ice shelf base which is simply represented by $C = 0$.

Boundary conditions for the temperature field

Boundary conditions for thermodynamics typically are

- surface temperatures T_S for the ice surface (Dirichlet), and
- geothermal/oceanic heat flux (depending on whether the ice is grounded or floating) (Neumann), or
- melting-point or colder temperatures (Dirichlet) at the ice base.

2.2.2 Common approximations in modeling of ice dynamics

The so-called Full-Stokes system as given by the full momentum balance in Eq. 2.3 can be reasonably simplified for certain regimes in ice dynamics so that the numerical solution for the velocities becomes computationally less expensive. The two most common approximations are the Shallow Ice Approximation (SIA), which is typically applied for modeling the flow of large-scale ice dynamics of ice sheets and the Shallow Shelf Approximation (SSA), which is used for modeling the dynamics of ice shelves and fast flowing ice streams supplying the ice shelves.

Shallow Ice Approximation

The SIA only accounts for vertical shear stresses $\tau_{xz} = \tau^{\mathrm{D}}_{xz}$ and $\tau_{yz} = \tau^{\mathrm{D}}_{yz}$. There are regimes in an ice sheet where this assumption does not hold. These are (Greve and Blatter, 2009):

- In the vicinity of an ice dome, the motion is generally vertical and thus the ice is dominated by vertical normal stress (τ_{zz}).
- At the ice sheet's margins, the ice surface becomes steep and so normal stress in horizontal directions becomes dominant.
- In regions with a highly variable bedrock topography, at least the lower parts of the ice are also influenced by the stress components neglected in the SIA.
- Within fast flowing ice streams, shear deformation is negligible compared to basal sliding. Therefore, these are typically treated by the SSA (see below).
- In grounding zones, just upstream of the grounding line of an ice sheet, the stress is already affected by the downstream dominance of longitudinal stresses in the ice shelf (cf. Section 2.2.4).

Neglecting $\tau^{\mathrm{D}}_{xy} = \tau_{xy}$ and the normal stresses τ^{D}_{xx}, τ^{D}_{yy}, τ^{D}_{zz} allows to integrate the momentum balance 2.3 w.r.t. the vertical coordinate z. With the likewise simplified

expression for the basal stress,

$$\tau_{B,i} = \rho\, g\, H \frac{\partial S}{\partial i} \text{ for } i \in \{x, y\} \ , \tag{2.22}$$

Glen's Flow Law (Eq. 2.13) yields the horizontal velocities,

$$\begin{aligned} v_i \ &= \ C^{-1/m} \left(\rho\, g\, H\right)^{1/m} \left|\vec{\nabla}_{\mathrm{h}} S\right|^{1/m-1} \frac{\partial S}{\partial i} \\ &\quad - 2\left(\rho g\right)^n \left|\vec{\nabla}_{\mathrm{h}} S\right|^{n-1} \frac{\partial S}{\partial i} \int_B^z A(T')(S - z')^n \mathrm{d}z' \quad \text{for } i \in \{x, y\} \end{aligned} \tag{2.23}$$

Here, it is $\vec{\nabla}_{\mathrm{h}} S = (\partial S/\partial x, \partial S/\partial y)^{\mathrm{T}}$. For a detailed derivation, see e.g. Greve and Blatter (2009). In Eq. 2.23, the horizontal velocities only depend on the local geometric setting (S, B and horizontal gradient of S). By that, the ice thickness equation 2.17 and Eq. 2.23 yield a non-linear diffusion equation for the ice sheet surface S:

$$\frac{\partial S}{\partial t} = \vec{\nabla}_{\mathrm{h}} \cdot \left[\mathcal{D}(S, B, \vec{\nabla}_{\mathrm{h}} S) \vec{\nabla}_{\mathrm{h}} S\right] + \dot{b} + \frac{\partial B}{\partial t} \tag{2.24}$$

with $\mathcal{D}(S, B, \vec{\nabla}_{\mathrm{h}} S)$ given by Eq. 2.23. Once, this diffusion equation is solved, v_x and v_y can be computed diagnostically from Eq. 2.23 and subsequently v_z from the mass continuity equation 2.2. Ice thickness 2.24 and temperature evolution 2.19 are coupled via the velocity field. Still, the simplifications of the SIA, as they manifest in Eq. 2.24, allow for a very fast solution of ice-sheet dynamics.

Shallow Shelf Approximation

In constrast to the SIA, where one assumes sticky conditions and so dominance of shear stresses at the ice sheet's base, the ocean–ice interface at the base of ice shelves does not provide any friction. Therefore, vertical shear deformation can be neglected, and consequently the vertical gradients of vertical shear stress and of horizontal velocities (Greve and Blatter, 2009):

$$\frac{\partial \tau_{iz}}{\partial z} \approx 0 \ \text{ and } \ \frac{\partial v_i}{\partial z} \approx 0 \ \text{ for } i \in \{x, y\} \ . \tag{2.25}$$

This holds also approximately for ice streams which are located above low-frictional bedrock and where melt-water at the base decreases the basal resistance for the flow (Cuffey and Paterson, 2010). This makes v_x and v_y functions of only x, y, and t ($v_x = \overline{v}_x$ and $v_y = \overline{v}_y$ in the equation for ice thickness 2.17) and allows vertical integration of the momentum balance 2.3, which eventually yields

$$\overbrace{\frac{\partial}{\partial x}\left[2\,H\,\overline{\eta}_{\mathrm{Ice}}\left(2\frac{\partial v_x}{\partial x}+\frac{\partial v_y}{\partial y}\right)\right]+\frac{\partial}{\partial y}\left[H\,\overline{\eta}_{\mathrm{Ice}}\left(\frac{\partial v_x}{\partial y}+\frac{\partial v_x}{\partial y}\right)\right]}^{=\tau_x^{\mathrm{L}}} = \rho g H\frac{\partial S}{\partial x}+\tau_{B,x} \quad , \tag{2.26}$$

$$\overbrace{\frac{\partial}{\partial y}\left[2\,H\,\overline{\eta}_{\mathrm{Ice}}\left(2\frac{\partial v_y}{\partial y}+\frac{\partial v_x}{\partial x}\right)\right]+\frac{\partial}{\partial x}\left[H\,\overline{\eta}_{\mathrm{Ice}}\left(\frac{\partial v_x}{\partial y}+\frac{\partial v_y}{\partial x}\right)\right]}^{=\tau_y^{\mathrm{L}}} = \rho g H\frac{\partial S}{\partial y}+\tau_{B,y} \quad . \tag{2.27}$$

Here, $\overline{\eta}_{\mathrm{Ice}}$ stands for the vertically integrated viscosity. In the case of ice shelves, basal shear stresses $\tau_{B,x}$ and $\tau_{B,y}$ are zero. In contrast to the SIA, the SSA Eqs. 2.26 and 2.27 yield a velocity field v_x and v_y that is not solely determined at each point by the local geometry (S, B, and $\vec{\nabla}_{\mathrm{h}}S$), which makes the solution of the non-linear equation system much more expensive due to the necessary iteration. The annotations τ_x^{L} and τ_y^{L} are introduced for later reference in Section 2.2.4.

Employment of SIA and SSA

In the two models for large-scale ice dynamics (RIMBAY and PennState3d, see below), which are employed in this thesis, the SIA approximation is used for grounded ice and SSA for floating ice in principal. RIMBAY is also capable of so-called Higher-Order (HO) and Full-Stokes (FS) modeling. These more accurate (HO) or precise (FS) approaches are, however, not feasible for large-scale dynamics due to their computational cost. As described in more detail below, PennState3d employs a combination of SSA and SIA for low-frictional grounded areas.

Grounded (inland) ice and floating (shelf) ice can be easily identified by comparing the water equivalent of the ice column with the height of the ocean water column, i.e. with the relative sea level (RSL) s_{rsl}:

$$\begin{aligned} H\,\rho/\rho_{\mathrm{oc}} < s_{\mathrm{rsl}} \quad &\Rightarrow \quad \text{floating,} \\ H\,\rho/\rho_{\mathrm{oc}} = s_{\mathrm{rsl}} \quad &\Rightarrow \quad \text{grounding line,} \\ H\,\rho/\rho_{\mathrm{oc}} > s_{\mathrm{rsl}} \quad &\Rightarrow \quad \text{grounded.} \end{aligned} \tag{2.28}$$

Note that $s_{\mathrm{rsl}} > 0$ stands for a rock surface below sea level (ocean), $s_{\mathrm{rsl}} < 0$ stands for a rock surface above sea level (land mass) and $s_{\mathrm{rsl}} = 0$ marks the coastline (see also Section 2.3.2).

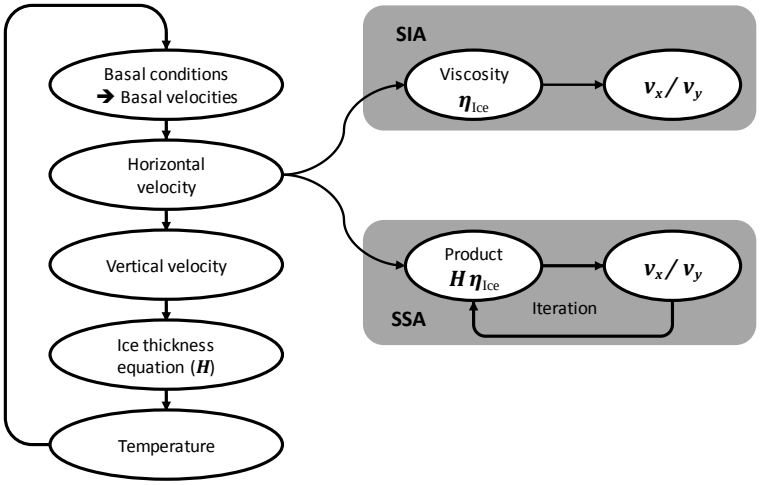

Figure 2.2
Sequence of iteratively solved variables in RIMBAY. Adapted from Figure 2 in Thoma et al. (2014). The left loop stands for the evolution in time.

2.2.3 The ice-dynamics model RIMBAY

Based on the implementation by Pattyn (2003), RIMBAY has been developed by Thoma et al. (2010, 2012, 2014). It applies the finite difference method to solve the momentum balance simplified by the SIA for grounded ice and by the SSA for floating ice on a staggered Arakawa C-grid (Arakawa and Lamb, 1977), i.e. the horizontal velocities are computed between the grid nodes for the geometric quantities (ice thickness H, surface elevation S, bedrock elevation B). The temporal structure for solving for the ice dynamical quantities (ice thickness H, velocity field $\vec{v}$ and temperature T) in RIMBAY is illustrated in Figure 2.2. Details on the numerics can be found in Thoma et al. (2014).

The vertical dependencies are not treated along a fixed geo-referenced vertical z-axis, but by the terrain-following and normalized σ_{v} coordinate:

$$\sigma_{\mathrm{v}} = \frac{S - z}{H} \quad . \tag{2.29}$$

The surface ($z = S$) is represented by $\sigma_{\mathrm{v}} = 0$ whereas the base ($z = B_{\mathrm{Ice}}$) is $\sigma_{\mathrm{v}} = 1$. The ice body is then divided into a fixed number of vertical layers which differ in thickness as the ice thickness differs in the horizontal directions.

In the RIMBAY scenarios in this thesis, either a uniform flow rate factor A, or the relation in Eq. 2.12 by Hooke (1981) is applied. The respective parameters are listed in Table 2.1. The exponent in the sliding law 2.21 is $m = 3$ where basal sliding is considered.

	Value	Unit	Temperature range	in Eq.	Used by
A_0	3.615×10^{-13}	s^{-1} Pa^{-3}	$T' \leq 263.15$ K	2.11	PennState3d
	1.7345×10^{3}	s^{-1} Pa^{-3}	$T' > 263.15$ K	2.11	PennState3d
Q_{act}	60	kJ mol^{-1}	$T' \leq 263.15$ K	2.11	PennState3d
	139	kJ mol^{-1}	$T' > 263.15$ K	2.11	PennState3d
A'_0	2.9498×10^{-9}	s^{-1} Pa^{-3}	–	2.12	RIMBAY
T_H	280	K	–	2.12	RIMBAY
C_H	0.16612	K^{k_H}	–	2.12	RIMBAY
k_H	1.17	–	–	2.12	RIMBAY
Q_{act}	78.8	kJ mol^{-1}	–	2.12	RIMBAY

Table 2.1
Parameters for the temperature and pressure dependence of the ice viscosity in the case of $n = 3$ in Eq. 2.13; values from Greve and Blatter (2009); Pollard and DeConto (2012b); Hooke (1981); Thoma et al. (2014).

2.2.4 The ice-dynamics model PennState3d

The PennState3d model has been developed by Pollard and DeConto (2005, 2009, 2012b). Just as RIMBAY, it solves for the ice-dynamical quantities based on the SIA and SSA on a staggered Arakawa C-grid and treats the vertical dependencies via the relative depth coordinate σ_v. Minor conceptual differences to RIMBAY are:

- The time stepping is different for the different components: The ice thickness and velocities are computed with a time step $\Delta t_{Ice} = O(0.1 - 1.0$ yr). The temperature field is updated every 50 years.
- The basal sliding exponent is $m = 2$. The flow rate factor A is parameterized by Eq. 2.11 – cf. Table 2.1.

An important conceptual advance from the separated SIA and SSA approaches as well as the subgrid treatments of grounding-line dynamics and pinning points are outlined below. For details, see Pollard and DeConto (2012b).

Entanglement of SIA and SSA

Although both approximations neglect certain contributions to the momentum balance 2.3, the individual SSA and SIA equations interact in three ways.

1. The respective strain-rate components from the SIA and SSA velocities are applied in the other approximation when computing τ_e for the viscosity in Eq. 2.13, which leads to a lower viscocity and thus to softer ice.

2. Vertical shear in the SIA velocity solution results in a difference between depth-averaged velocity and basal velocity, which is accounted for in the SSA equations.
3. A further coupling between SIA and SSA is established by reducing the driving stress in the SIA by the respective gradient of the longitudinal stress as solved by the SSA:

$$\tau_{iz} = -\left(\rho g(S-z)\frac{\partial S}{\partial i} - \tau_i^{\mathrm{L}}\,\sigma_{\mathrm{v}}(z)\right) \text{ for } i \in \{x, y\} \tag{2.30}$$

with τ_x^{L} and τ_y^{L} defined in Eqs. 2.26 and 2.27. The scaling by depth $\sigma_{\mathrm{v}}(z)$ is due to the fact that the SSA-quantities τ_x^{L} and τ_y^{L} are averaged over the complete ice thickness whereas only ice above the depth $S-z$ can be accounted for in the stress balance of Eq. 2.30.

This entanglement of SIA and SSA makes it necessary to iterate the solutions of SIA and SSA before a final velocity field for a given time results. For computational efficiency, it is only done in areas with basal sliding coefficients below a fixed mid-range value; for stickier beds, the SIA solution dominates and SSA would be negligible.

Improved grounding line dynamics

In both RIMBAY and PennState3d, the model domain is resolved with a resolution of 10 to 40 km. As indicated e.g. by the work of Pattyn et al. (2012, 2013), this resolution is too coarse for an accurate description of the transition from the inland ice stress regime (approximated by the SIA) to the shelf-ice stress regime (approximated by the SSA). Consequently, the migration of the grounding line (GL), i.e. the transition from grounded ice to floating ice (cf. Eq. 2.28), is also inaccurate if no further constraints on the ice flux through the GL (henceforth 'GL flux') are introduced on sub-grid scale. In order to solve this issue, Pollard and DeConto (2012b) introduced such a constraint in the PennState3d model, which makes use of the analytical approach by Schoof (2007): The steady-state GL flux in a two-dimensional set-up with horizontal coordinate x without thermomechanical coupling (i.e. fixed rate factor A) can be analytically computed as

$$Q_{\mathrm{S}} = \left(\frac{A\,(\rho g)^{n+1}\,(1-\rho/\rho_{\mathrm{oc}})^{n}}{4^{n}C}\right)^{\frac{1}{m+1}} \left(\frac{\overline{\tau}}{\tau_{\mathrm{f}}}\right)^{\frac{n}{m+1}} H_{\mathrm{g}}^{\frac{m+n+3}{m+1}} \tag{2.31}$$

where $\overline{\tau}$ is the mean longitudinal stress just downstream from the GL,

$$\tau_{\mathrm{f}} = 0.5\,\rho\,g\,H_{\mathrm{g}}\,(1-\rho/\rho_{\mathrm{oc}}) \tag{2.32}$$

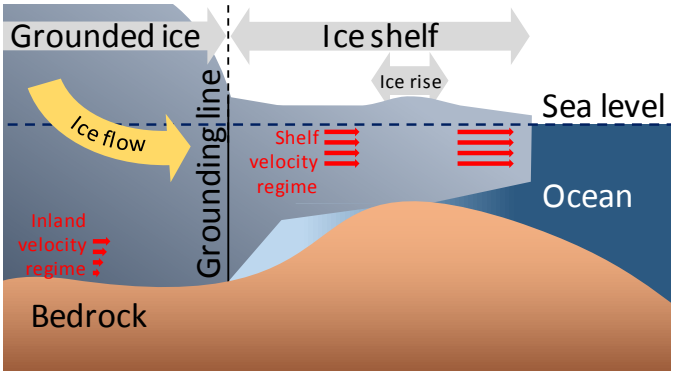

Figure 2.3
Transition from inland ice to shelf ice. The ice shelf buttresses the ice sheet at the grounding line e.g. by the back stress from ice rises.

is the unbuttressed stress corresponding to the height of the ice column above sea level (freeboard height), and H_g is the ice thickness at the GL where the floating criterion 2.28 is exactly at the edge:

$$H_\mathrm{g} = \rho / \rho_\mathrm{oc}\, s_\mathrm{rsl} \ . \tag{2.33}$$

The $(\overline{\tau}/\tau_\mathrm{f})^{\frac{n}{m+1}}$ term in Eq. 2.31 incorporates the buttressing that the ice shelf provides to the ice sheet via the back stress from ice rises (see below) and islands, from lateral compression or from side drag (see Figure 2.3). The GL flux given by Eq. 2.31 yields the vertically averaged horizontal velocity $\overline{v}_\mathrm{g}$:

$$\overline{v}_\mathrm{g} = Q_\mathrm{S} / H_\mathrm{g} \ . \tag{2.34}$$

In order to approximate the GL dynamics in a Full-Stokes solution by the otherwise rather inert SIA/SSA solution, Pollard and DeConto (2012b) use Eq. 2.31 to constrain the velocity field at the GL and so to enhance the GL dynamics. This implies the transition from the two-dimensional case considered in Eq. 2.31 to three dimensions and the consideration of a vertically averaged rate factor $\overline{A}$. The modeled SIA/SSA GL flux in (horizontal) i-direction ($i \in \{x, y\}$) is computed from the modeled ice thickness and the modeled vertically averaged velocity $\overline{v}_{\mathrm{m},i}$ not using Eq. 2.31 at the sub-grid GL position where Eq. 2.33 is fulfilled:

$$Q_{\mathrm{m},i} = \overline{v}_{\mathrm{m},i}\, H_\mathrm{g} \ . \tag{2.35}$$

Then, comparison with the constraint $Q_{\mathrm{S},i}$ yields either GL advance or retreat according to an *ad-hoc* rule:

- $Q_{\mathrm{S},i} < Q_{\mathrm{m},i}$ means that more ice is transported over the GL than necessary to maintain the GL at its present position. This leads to grounded ice outwards from the present GL and thus to GL advance. In order to model this, $\overline{v}_{\mathrm{g},i}$ is set as new $\overline{v}_{\mathrm{m},i}$ at the first floating grid point downstream from the subgrid GL position.

- If it is in contrast $Q_{\mathrm{S},i} > Q_{\mathrm{m},i}$, then there is not enough ice crossing the GL in i-direction to maintain its position. Consequently, the GL will retreat from this position. This is modeled by applying $\overline{v}_{\mathrm{g},i}$ as new value for $\overline{v}_{\mathrm{m},i}$ at the last grounded grid point upstream from the subgrid GL position.

Sub-grid pinning points

An important feature for slowing down the ice flow in ice shelves, and thus providing back stress and buttressing at the GL, are ice rises and pinning points (Favier et al., 2012; Siegert et al., 2013). Both appear where the bathymetry below sea level is shallow enough that the ice is grounded (Figure 2.3). In the case of ice rises, the ice at such a site grounds there permanently until it becomes too thin. Pinning points are characterized by their non-permanent influence on the ice dynamics due to alternating periods of grounding and floating. If the spatial (and temporal) extent of such features is large enough to be captured by the spatial grid and time stepping, their influence on the ice dynamics is naturally modeled.

The PennState3d model also accounts for the influence of pinning points on sub-grid scale in Antarctica: In the ice shelves, the basal drag $\tau_{B,x}$ and $\tau_{B,y}$ in Eqs. 2.26 and 2.27, which would occur if the ice was fully grounded, is multiplied by $0.5 \times \max\left(0, 1 - \frac{h_{\mathrm{w}}}{\delta B}\right)$, which stands for the grid cell's fractional area of grounding. Here, $h_{\mathrm{w}} = s_{\mathrm{rsl}} - \rho/\rho_{\mathrm{oc}}\, H$ is the water column between the ice-shelf base and the ocean bottom and δB is the standard devation of the BEDMAP2 bed elevations (Fretwell et al., 2013) within the coarser model grid box.

2.3 Solid-Earth dynamics

The loading and unloading of continents and ocean floor by advancing and retreating ice sheets during glacial cycles forces the glacial-isostatic adjustment (GIA), which is the redistribution of mass in the Earth's interior due to these loading changes and the associated surface deformation, gravity field changes, and migration of coastlines. While the elastic response of the lithosphere is following instantaneously after a change in the loading, the viscoelastic rheology of the Earth's interior delays the response of the associated mantle flow by hundreds or thousands of years (Haskell, 1935). In the scope of this thesis, solid-Earth dynamics shall always refer to the relaxation in response to such changes in the surface load. Other dynamical processes such as thermodynamically driven convection in the Earth's mantle or plate tectonics (e.g. Turcotte and Schubert, 2002) are not considered here except for adopting characteristic parameterizations for the structure of the Earth in regions of interest such as the Antarctic.

2.3.1 Continuum-mechanical approach to solid-Earth relaxation

Similarly to the ice dynamical problem, the mathematical description relies on continuity equations and a constitutive equation. The model domain, i.e. an initially spherical Earth, will be described in the Lagrangian frame which is the natural approach if one is interested in the displacement of the Earth's surface from an initial state (cf. Figure 2.4). The spherical Earth shall be considered as incompressible and hydrostatically pre-stressed. The changes of the gravity field due to mass redistribution are important in terms of their effect on sea level, but also on the redistribution itself. The incompressibility can be expressed by a divergence-free displacement field of the interior and the surface of the Earth, $\vec{U}$:

$$\operatorname{div} \vec{U} = 0 \ . \tag{2.36}$$

The evolution of the stress $\underline{\boldsymbol{\mathcal{T}}}$ (in terms of the Lagrangian increment of the Cauchy stress tensor in the Earth), displacement, and the gravitational potential increment ϕ_1 can be described by the linearized balance of linear momentum without inertial contributions,

$$\operatorname{div} \underline{\boldsymbol{\mathcal{T}}} - \rho_0 \operatorname{grad} \phi_1 - \operatorname{div} \left(\rho_0 \, \vec{U} \right) \vec{g}_0 + \operatorname{grad} \left(\rho_0 \, \vec{U} \cdot \vec{g}_0 \right) = 0 \ , \tag{2.37}$$

and Poisson's equation for ϕ_1,

$$\frac{1}{4\pi G} \operatorname{div} \operatorname{grad} \phi_1 + \operatorname{div} \left(\rho_0 \, \vec{U} \right) = 0 \ . \tag{2.38}$$

Here, the density ρ_0 is considered as unperturbed and only radially varying $\rho_0(\vec{R}) = \rho_0(R)$ with R being the distance from the Earth centre to $\vec{R}$. With only radially varying ρ_0, the initial gravitational acceleration $\vec{g}_0$ is also a function of R only and has only a radial component: $\vec{g}_0 = -g_0(R)\vec{e}_R$ with $\vec{e}_R$ being the unit vector pointing radially outwards; $\vec{g}_0$ is related to the unperturbed gravitational potential ϕ_0 by

$$\vec{g}_0 = -\operatorname{grad} \phi_0 \ . \tag{2.39}$$

Newton's gravitational constant is $G = 6.67384 \times 10^{-11}$ m^3/kg/s^2. The gravitational potential $\phi = \phi_0 + \phi_1$ is the sum of the unperturbed potential ϕ_0 and the increment ϕ_1. Eqs. 2.37 and 2.38 hold for small perturbations (Wu and Peltier, 1982; Wolf, 1991; Martinec, 2000). The gravity potential is not a material quantity and usually decribed in the Eulerian frame.

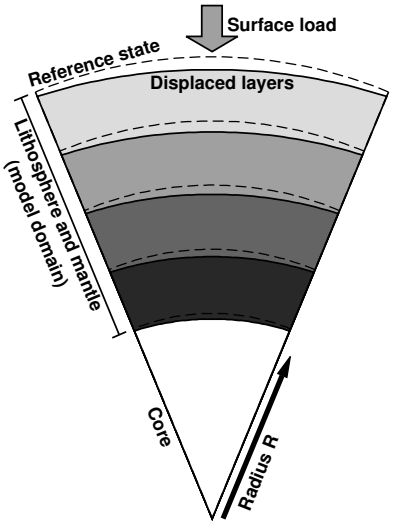

Figure 2.4
Exemplary cross section through the deformed Earth under a surface load vs. the unloaded reference state (dashed). The model domain (lithosphere and the Earth's mantle, see below) is indicated.

A material discontinuity along an internal surface Σ demands the following boundary conditions on Σ (Longman, 1962, 1963; Farrell, 1972; Martinec, 2000):

$$\vec{U}^{+} = \vec{U}^{-} \tag{2.40}$$

$$\vec{n} \cdot \underline{\boldsymbol{T}}^{+} = \vec{n} \cdot \underline{\boldsymbol{T}}^{-} \tag{2.41}$$

$$\phi_1^{+} = \phi_1^{-} \tag{2.42}$$

$$\left(\operatorname{grad} \phi_1 + 4\,\pi\,G\,\rho_0\,\vec{U}\right)^{+} \cdot \vec{n} = \left(\operatorname{grad} \phi_1 + 4\,\pi\,G\,\rho_0\,\vec{U}\right)^{-} \cdot \vec{n}\ . \tag{2.43}$$

Here, the superscript '+' denotes the respective quantity on the outward side of Σ, whereas the superscript '$-$' denotes the same quantity on the inward side. These boundary conditions imply that the displacement is continuous (Eq. 2.40), and likewise the normal stress components (Eq. 2.41) and the incremental potential (Eq. 2.42). Additionally, Eq. 2.43 yields differentiability of the potential.

The viscoelastic deformation and gravity change is induced by a changing surface load σ which is described as a boundary condition at the surface of the Earth. As described in Section 2.3.2, the load σ is computed from the weight of ice and ocean columns at any point $\Omega = (\varphi, \lambda)$ (φ: geographical longitude; λ: latitude), has the dimension of an surface mass density [kg/m^2] and acts as a stress in radial direction, i.e. in direction of the gravitational force ($\vec{n} = \vec{e}_R$). Then, on the Earth's surface S_{E}, Eq. 2.41 takes the form

$$\vec{e}_R \cdot \underline{\boldsymbol{T}}^{-} \cdot \vec{e}_R = -g\,\sigma \ \text{ and} \tag{2.44}$$

$$\underline{\boldsymbol{T}}^{-} \cdot \vec{e}_R - \left(\vec{e}_R \cdot \underline{\boldsymbol{T}}^{-} \cdot \vec{e}_R\right) \vec{e}_R = 0\ . \tag{2.45}$$

The boundary condition for the potential gradient (Eq. 2.43) on S_E reads:

$$[\mathrm{grad}\,\phi_1]^+ \cdot \vec{e}_R + 4\,\pi\,G\,\sigma = \left(\mathrm{grad}\,\phi_1 + 4\,\pi\,G\,\rho_0(R_\mathrm{E})\vec{U}\right)^- \cdot \vec{e}_R \ . \tag{2.46}$$

Here, $R_\mathrm{E} = 6371$ km is the Earth's radius, and $g = g_0(R_\mathrm{E})$ is the gravitational acceleration at the surface as also used in Section 2.2.

The second important boundary is the core–mantle boundary S_CMB. The core shall be considered as fluid so that it can be taken into account only via the interface with the Earth's mantle. Then, the respective conditions at this boundary demand a continuous normal component of the displacement and of the stress as well as a free-slip condition (Martinec, 2000), so that the following relations hold on S_CMB:

$$\vec{n} \cdot \vec{U}^+ = \vec{n} \cdot \vec{U}^- \tag{2.47}$$

$$\vec{n} \cdot \underline{\boldsymbol{\mathcal{T}}}^+ \cdot \vec{n} = \vec{n} \cdot \underline{\boldsymbol{\mathcal{T}}}^- \cdot \vec{n} \tag{2.48}$$

$$\underline{\boldsymbol{\mathcal{T}}} \cdot \vec{n} - (\vec{n} \cdot \underline{\boldsymbol{\mathcal{T}}} \cdot \vec{n})\,\vec{n} = 0 \ . \tag{2.49}$$

Linear Maxwell viscoelasticity

Just as in the case of ice dynamics (Section 2.2), a constitutive equation for the viscoelastic behaviour of the solid Earth is required. Here, a Maxwell viscoelastic rheology shall be considered. The evolution of the shear stresses $\underline{\boldsymbol{\mathcal{T}}}$ and the pertubation pressure P, i.e. the deviations from hydrostatic pressure, can be formulated as (Martinec, 2000):

$$\dot{\underline{\boldsymbol{\mathcal{T}}}} = \dot{\underline{\boldsymbol{\mathcal{T}}}}_\mathrm{e} - \frac{\mu}{\eta}\,(\underline{\boldsymbol{\mathcal{T}}} - P\,\underline{\mathbb{1}}) \tag{2.50}$$

with the stress associated with the elastic deformation

$$\underline{\boldsymbol{\mathcal{T}}}_\mathrm{e} = P\,\underline{\mathbb{1}} + 2\,\mu\,\underline{\boldsymbol{\mathcal{E}}} \ . \tag{2.51}$$

Here, $\underline{\boldsymbol{\mathcal{E}}} = (\mathrm{grad}\,\vec{U} + (\mathrm{grad}\,\vec{U})^\mathrm{T})/2$ is the deviatoric shear strain. The material parameters are elastic shear modulus μ and viscosity η. Analogously to the respective constitutive equation for ice 2.8, pressure variations (given by P) do not cause deformation; therefore, P appears separately in Eqs. 2.50 and 2.51.

The respective initial condition for $\underline{\boldsymbol{\mathcal{T}}}$ and $\underline{\boldsymbol{\mathcal{E}}}$ under the assumption of hydrostatic equilibrium in the Earth's interior is:

$$\underline{\boldsymbol{\mathcal{T}}}^0 = 2\,\mu\,\underline{\boldsymbol{\mathcal{E}}}^0 \ . \tag{2.52}$$

The simplest realization of a Maxwell viscoelastic body consists of one spring (elastic component) and one viscous damper (viscous component) in series. Then the ratio of the elastic and viscous parameters directly defines the characteristic time scale for relaxation:

$$\tau_\mathrm{r} = \eta/\mu \quad . \tag{2.53}$$

The stratification of the Earth's interior as well as the possibility of lateral flow, however, implies a complex spectrum of relaxation times (Peltier and Andrews, 1976).

There are empirical relations for relating the viscosity η and the temperature as well as other state variables in the Earth's mantle (van der Wal et al., 2013) comparable to the respective flow law for ice (Eq. 2.9), but the common approach in GIA models is to apply prescribed viscosities in the Earth's mantle. This is also due to the fact that thermodynamics are not considered in the solid-Earth dynamics here.

Uniqueness of the solution

The above equations need additional constraints so that the displacement field $\vec{U}$ is unique (Cathles, 1975). The applied uniqueness condition here implies that the centre of mass of the Earth is fixed in the origin of the reference frame and no net rotation of the body is allowed:

$$\int_{B_\mathrm{E}} \rho_0 \, \vec{U} \, \mathrm{d}V = 0 \quad \text{and} \quad \int_{B_\mathrm{E}} \left(\vec{e}_R \times \rho_0 \, \vec{U} \right) \, \mathrm{d}V = 0 \quad . \tag{2.54}$$

Here, B_E stands for the complete model domain, i.e. the modeled Earth's mantle and crust. The uniqueness condition 2.54 is applied in terms of an additional term in the energy functional (Appendix B.1), which is introduced in the context of the weak formulation (Section 2.3.3).

2.3.2 Surface loading

The surface load σ is the driving boundary condition (cf. Eqs. 2.44 and 2.46) for the system described above. The sea-level equation (SLE; Farrell and Clark, 1976) provides a scheme to consistently solve for changes of the sea surface and ocean bathymetry, as well as coastline migration and the related changes in σ while conserving the planet's water mass. This section first introduces important quantities, then explains the general handling of the surface load σ, and finally addresses the SLE.

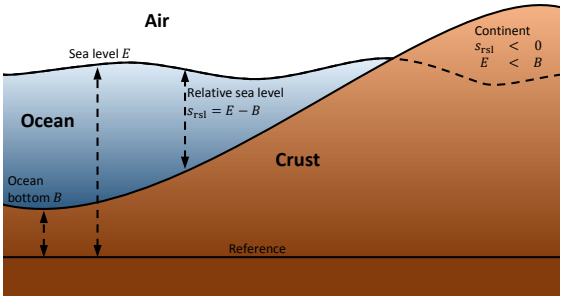

Figure 2.5
On the definition of sea level E, ocean bottom topography B, and relative sea level s_{rsl}. Via its coincidence with an equipotential surface of the gravity field, the geoid (see below), the sea surface is also defined on continents.

Sea level measures and related quantities

A static ocean, as it will be considered here, is characterized by the sea surface, or sea level, $E(\Omega, t)$, and the ocean bottom $B(\Omega, t)$ identical to the bedrock topography as introduced in Section 2.2, both measured as radial distances from a given reference (e.g. the Earth's centre of mass, or any surface defined for the complete Ω-domain such as the sea level $E_0 \equiv 0$ at a specified time t_0). This situation is illustrated in Figure 2.5. The relative sea level (RSL) stands for the ocean depth and can be calculated as

$$s_{\mathrm{rsl}} = E - B \quad . \tag{2.55}$$

The bathymetry ζ gives the elevation of the Earth's surface above sea level, i.e.

$$\zeta = B - E = -s_{\mathrm{rsl}} \quad . \tag{2.56}$$

Negative values of s_{rsl} ($\zeta > 0$) indicate land masses, whereas positive values of s_{rsl} ($\zeta < 0$) indicate oceans (Figure 2.5). The global coastlines are given by $s_{\mathrm{rsl}} = \zeta = 0$.

Later considerations depend on wether a given location Ω is covered with ocean / floating ice or land / grounded ice at time t. The ocean function $\mathcal{O}(\Omega, t)$ is defined as

$$\mathcal{O}(\Omega, t) = \begin{cases} 1 \;\text{ if }\; \zeta(\Omega, t) + \frac{\rho}{\rho_{\mathrm{oc}}} H(\Omega, t) < 0 \;\; \text{(Ocean)} \\ 0 \;\text{ if }\; \zeta(\Omega, t) + \frac{\rho}{\rho_{\mathrm{oc}}} H(\Omega, t) \geq 0 \;\; \text{(Land)} \end{cases} \quad , \tag{2.57}$$

and therefore binarily distinguishes between these two situations. Here, ρ is the ice density, ρ_{oc} is the ocean water density, and H is the ice thickness. The consideration of $\rho/\rho_{\mathrm{oc}}\, H$ is due to the facts that (1) the existence of ice which is floating ($0 < H < -\rho_{\mathrm{oc}}/\rho\, \zeta(\Omega, t)$) on the ocean does not change the weight of the respective ocean column and (2) grounded ice ($H \geq \rho_{\mathrm{oc}}/\rho\, \zeta(\Omega, t)$ and $H > 0$) displaces the complete water column and thus expulses the ocean from the respective site if

$\zeta < 0$. If $\zeta \geq 0$, then the grounded ice is grounded above sea level so that there would be no ocean in any case.

Ice and ocean load

The following considerations are based on Hagedoorn et al. (2007). The actual surface mass density σ_{abs} can be computed as the weight of the respective ice or ocean columns:

$$\sigma_{\mathrm{abs}}(\Omega, t) = -\rho_{\mathrm{oc}}\, \zeta(\Omega, t)\, \mathcal{O}(\Omega, t) + \rho\, H(\Omega, t)\, (1 - \mathcal{O}(\Omega, t)) \tag{2.58}$$

Adopting this scheme for computing the respective solid-Earth response, however, implies a situation where there is no ocean and no ice on Earth at the initial time t_0 ($\sigma_{\mathrm{abs}}(\Omega, t_0) \equiv 0$). If instead the Earth is assumed to be in equilibrium with respect to some (steady) load $\sigma_{\mathrm{abs}}(\Omega, t_0) = \sigma_{\mathrm{abs},0}(\Omega)$, then the difference in the load

$$\sigma(\Omega, t) = \sigma_{\mathrm{abs}}(\Omega, t) - \sigma_{\mathrm{abs},0}(\Omega) \quad , \tag{2.59}$$

which is mainly given by the change in ice thickness $\Delta H = H - H_0$ and change in relative sea level $\Delta s_{\mathrm{rsl}} = -\Delta\zeta = \zeta_0 - \zeta$, is actually driving the solid-Earth dynamics as given by Eqs. 2.44 and 2.46. Here, H_0 and ζ_0 (and below $\mathcal{O}_0$) are the respective quantities at t_0.

If for a given site Ω and a given time t, $\mathcal{O}(\Omega, t) = \mathcal{O}_0(\Omega)$ holds, i.e. either initial ocean is also ocean at time t or initial land is also land at time t (branches A and D in Figure 2.6), then

$$\sigma(\Omega, t) = \rho_{\mathrm{oc}}\, \Delta s_{\mathrm{rsl}}(\Omega, t)\, \mathcal{O}(\Omega, t) + \rho\, \Delta H(\Omega, t)\, (1 - \mathcal{O}(\Omega, t)) \quad , \tag{2.60}$$

meaning that only the respective changes in the ocean load (in terms of Δs_{rsl}) or in the ice load (in terms of ΔH) affect $\sigma(\Omega, t)$.

If, however, $\mathcal{O}(\Omega, t) \neq \mathcal{O}_0(\Omega)$, one has to take into account the missing weight of the replaced ice or water column and the complete weight of the present water or ice column: If $\mathcal{O}_0(\Omega) = 0$ and $\mathcal{O}(\Omega, t) = 1$ (grounded ice or land becomes floating ice or ocean; branch B in Figure 2.6), then

$$\sigma(\Omega, t) = -\rho\, H_0(\Omega) - \rho_{\mathrm{oc}}\, \zeta(\Omega, t) \tag{2.61}$$

because the initial ice load in $\sigma_{\mathrm{abs},0}$ is gone and the complete water column now acts as ocean load.

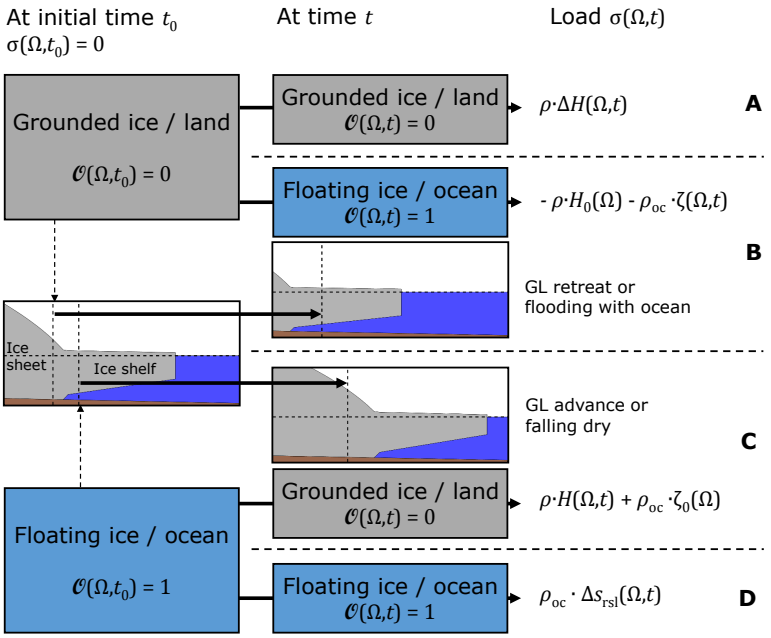

Figure 2.6
Scheme for computing the load σ depending on the ice/ocean distribution at the initial time t_0 and at time t. Note that the sketches refer to a situation including a migrating grounding line. However, migrating coastlines alone (without ice present at Ω but with shallower ocean instead) also lead to situations where σ has to be computed as in branch B (flooding) or branch C (falling dry).

If $\mathcal{O}_0(\Omega) = 1$ and $\mathcal{O}(\Omega, t) = 0$ (floating ice or ocean becomes grounded ice or land; branch C in Figure 2.6), then

$$\sigma(\Omega, t) = \rho\, H(\Omega, t) + \rho_{\mathrm{oc}}\, \zeta_0(\Omega) \tag{2.62}$$

because the complete ice column – including possible initially floating portions, which would not be represented by ΔH only – acts on the surface whereas the initial ocean load present in $\sigma_{\mathrm{abs},0}$ is gone.

The sea-level equation

Initially proposed by Farrell and Clark (1976), the SLE and its features have been discussed and further developed by e.g. Clark et al. (1978), Peltier et al. (1978), Mitrovica and Peltier (1991), Johnston (1993), Lambeck (1993), Peltier (1994), Milne and Mitrovica (1998), Milne et al. (1999), Johnston and Lambeck (1999), Kendall et al. (2005), Hagedoorn et al. (2007), and Melini et al. (2010). The SLE is based on the assumption of a conserved global water mass and the coincidence of the ocean surface E with an equipotential surface of the gravity field, the geoid. This approach implies a static ocean – ignoring the effects of dynamic processes in the ocean and the atmosphere such as ocean currents or atmospheric pressure variations on sea level. The object of the SLE, namely the change in RSL Δs_{rsl}, is necessary for the computation of the surface load σ (Eqs. 2.60 and 2.61). In turn,

σ determines the evolution of the ocean surface and bottom and therefore Δs_{rsl}, which makes the SLE nonlinear.

Here, Δs_{rsl} is split into a uniform part $\Delta s_{\mathrm{rsl}}^{\mathrm{UF}}$, which depends on Ω only via the ocean function, and a non-uniform part $\Delta s_{\mathrm{rsl}}^{\mathrm{NU}}$ capturing all changes due to surface displacement $U_{\mathrm{S}}(\Omega, t) = U(R_{\mathrm{E}}, \Omega, t)$ (the radial component of $\vec{U}$ at the Earth's surface) and the displacement of the referential equipotential surface $e(\Omega, t)$. The latter is computed from the incremential gravitational potential ϕ_1 according to the Bruns formula (Heiskanen and Moritz, 1967)

$$e(\Omega, t) = -\phi_1(R_{\mathrm{E}}, \Omega, t)/g \quad . \tag{2.63}$$

The SLE reads

$$\Delta s_{\mathrm{rsl}}(\Omega, t) = \Delta s_{\mathrm{rsl}}^{\mathrm{UF}}(\Omega, t) + \Delta s_{\mathrm{rsl}}^{\mathrm{NU}}(\Omega, t) \tag{2.64}$$

with

$$\Delta s_{\mathrm{rsl}}^{\mathrm{UF}}(\Omega, t) = -\frac{\rho\, \Delta V_{\mathrm{Ice}}(t) + \rho_{\mathrm{oc}}\, \Delta V_{\mathrm{oc}}^{\mathrm{NU}}(t)}{\rho_{\mathrm{oc}}\, A_{\mathrm{oc}}(t)} \cdot \mathcal{O}(\Omega, t) \tag{2.65}$$

and

$$\begin{aligned} \Delta s_{\mathrm{rsl}}^{\mathrm{NU}}(\Omega, t) = \quad & [e(\Omega, t) - U_{\mathrm{S}}(\Omega, t)]\, \mathcal{O}(\Omega, t) \\ & -\zeta(\Omega, t_0)\, [\mathcal{O}(\Omega, t) - \mathcal{O}_0(\Omega)] \quad . \end{aligned} \tag{2.66}$$

U_{S} and e (or ϕ_1, respectively) are solved for when addressing the viscoelastic Earth as explained above. The displacement of the referential equipotential surface e and the uniform contribution to the RSL $\Delta s_{\mathrm{rsl}}^{\mathrm{UF}}$ make up the changes of the sea surface, or the equipotential surface of the gravity field coinciding with the sea surface (geoid),

$$E(\Omega, t) = E(\Omega, t_0) + e(\Omega, t) + \Delta s_{\mathrm{rsl}}^{\mathrm{UF}} \quad , \tag{2.67}$$

whereas the surface displacement is directly related to the surface topography:

$$B(\Omega, t) = B(\Omega, t_0) + U_{\mathrm{S}}(\Omega, t) \quad . \tag{2.68}$$

The remaining quantities in Eqs. 2.64 – 2.66 are explained in the following. ΔV_{Ice} is the global volume change in grounded ice:

$$\Delta V_{\mathrm{Ice}}(t) = \int_{S_{\mathrm{E}}} \Big[H(\Omega, t)\ (1 - \mathcal{O}(\Omega, t)) - H_0(\Omega)\ (1 - \mathcal{O}_0(\Omega)) \Big]\, \mathrm{d}S \tag{2.69}$$

with S_{E} representing the complete angular domain of the Earth's surface. The mean global sea-level variations which occur because of variations in grounded ice volume ΔV_{Ice} are refered to as eustatic sea-level variations.[i] The term $\Delta V_{\mathrm{oc}}^{\mathrm{NU}}(t)$ is the surface integral of $\Delta s_{\mathrm{rsl}}^{\mathrm{NU}}$, which is the non-uniform change of RSL. The ocean area A_{oc} can be easily obtained from the ocean function:

$$A_{\mathrm{oc}}(t) = \int_{S_{\mathrm{E}}} \mathcal{O}(\Omega, t)\, \mathrm{d}S \quad . \tag{2.70}$$

The second contribution in Eq. 2.66, $\zeta(\Omega, t_0)\,[\mathcal{O}(\Omega, t) - \mathcal{O}_0(\Omega)]$, accounts for migrating coastlines as it is nonzero only if $\mathcal{O}(\Omega, t) \neq \mathcal{O}_0$.

When simulating the sea level through the past (where the actual bathymetry is not known) towards present-day, the past evolution should be consistent with the final (known) present-day bathymetry as e.g. the ocean function and the oceanic loading in flooded areas are affected by the initial bathymetry ζ_0. Therefore, the simulation through the respective period (e.g. one glacial cycle) is performed in an iterative manner (Peltier, 1994; Mitrovica and Milne, 2003; Kendall et al., 2005): Starting the simulation from a first-guess initial bathymetry, the deviation of the modeled and the observed present-day bathymetry is used to correct this first-guess initial bathymetry, from which the sea-level evolution is then simulated again. This procedure is repeated until the bathymetry is converged. This approach is discussed in detail in Chapter 5.

2.3.3 The solid-Earth model VILMA

The solid-Earth model VILMA has been developed by Martinec (2000) with further development by Hagedoorn et al. (2007), Klemann et al. (2008), and Klemann and Martinec (2011). It has been benchmarked with other GIA models by Spada et al. (2011). In the following, the mathematical approach and its numerical implementation will be briefly introduced. More details are given in Appendices B.1 and B.2.

Weak formulation

Most solid-Earth models use a normal-mode approach to the time evolution (Peltier, 1974; Spada et al., 1992; Sabadini and Vermeersen, 2004), where the solution is computed in the Laplace domain. The advantage of the model VILMA is based on formulating the problem in a weak sense (Křížek and Neittaanmäki, 1990) –

[i] Note that also non-glacial hydrology or groundwater reservoir fluctuations in principal contribute to eustasy.

allowing an explicit time scheme, which makes the exchange of fields between an ice-sheet model and and the solid-Earth model straightforward and far less computationally expensive compared to the normal-mode approach (Section 2.4). The weak formulation of the initial boundary value problem described in Section 2.3.1 comprises the identification of certain functions $\vec{U}$, ϕ_1, and P which fulfil the initial condition given by Eq. 2.52 and a given variational equality, which is based on considerations of the mechanical energy budget of the solid Earth. An overview over this variational approach is given in Appendix B.1.

The spectral–finite-element approach

The spherical shape which has been assumed for an adequate representation of the Earth gives rise to the use of spherical coordinates and of surface spherical harmonics for treating the angular dependencies of the field variables. The radial dependencies of $\vec{U}$, ϕ_1, and P are treated by finite elements. This approach of treating angular dependencies spectrally by spherical harmonics and radial dependencies by finite-elements is often refered to as spectral–finite-element approach. Appendix B.2 gives more details. The numerical model needs a finite discretization in radial direction as well as a cut-off Legendre degree $j_{\max}$ for the spherical-harmonic representation of $\vec{U}$, ϕ_1, P, and σ, implying that contributions from higher degrees j are neglected. This cut-off degree is chosen to be $j_{\max} = 256$ in all experiments in this thesis.

Sea-level equation

The SLE as discussed in Section 2.3.2 is solved in the spatial domain. This means that at every time step, the respective quantities, namely surface displacement $U_{\mathrm{S}}(\Omega, t)$ and geoid displacement $e(\Omega, t)$, have to be converted from the angular spectrum to the spatial grid for the geographical coordinates $\Omega = (\varphi, \lambda)$, on which the SLE solver operates. Likewise, the computed spectrum $\sigma(\Omega, t)$ has to be converted into its spectral representation $\sigma_{jm}(t)$. The SLE solver has been implemented by Hagedoorn et al. (2007). The load σ is partially delayed by one time step (Hagedoorn et al., 2007): The load at sites Ω where $\mathcal{O}(\Omega, t^{i+1}) = 1$ (ocean) is computed from the respective sea-level state at t^i because it is determined by the Earth's response and therefore cannot be solved for explicitly without iteration. The load at sites with $\mathcal{O}(\Omega, t^{i+1}) = 0$ (ice / land) is always up to date, i.e. it refers to the input at t^{i+1}.

The spatial (Ω-)grid on which the SLE solver operates is a Gauss-Legendre grid, because this is optimal for the conversion from the spatial to the spectral domain. It has 1024×512 nodes, leading to a grid spacing of roughly 0.35°. The

number of grid-points allows for an alias-free spherical-harmonic cut-off degree $j_{\max} = 512$ if the viscosity is only radially varying (Sneeuw, 1994), or for $j_{\max} = 340$ if $\eta = \eta(R, \Omega)$ (Martinec, 1989). The chosen lower value $j_{\max} = 256$ is due to the computing efficiency and justified by the low-pass filtering by the lithosphere. The SLE solver requires an initial bathymetry ζ_0 so that the cases indicated in Figure 2.6 can be distinguished and the load σ can be computed consistently.

Earth rotation

The linear momentum balance considered in Eq. 2.37 does not account for Earth rotation. However, the redistribution of ice and ocean masses on glacial time scales as well as the related mass transport in the Earth's interior affects the inertia tensor of the rotating Earth and therefore also the rotation itself. The effect of Earth rotation on surface displacement and sea level has been studied e.g. by Nakiboglu and Lambeck (1980), Wu and Peltier (1984), Ricard et al. (1993), Vermeersen and Sabadini (1996), Milne and Mitrovica (1998), Johnston and Lambeck (1999), and Martinec and Hagedoorn (2005). The rotational deformation is neglected here, but the effect of the changing rotation on gravity is captured by superimposing the related incremental rotational potential Ψ on the incremental gravitational potential when computing the displacement of the referential equipotential surface e, so that Eq. 2.63 reads:

$$e = -\left(\phi_1 + \Psi\right)/g \quad . \tag{2.71}$$

Martinec and Hagedoorn (2005) and Hagedoorn (2005) implemented rotation of the Earth in VILMA according to this approach. The MacCullagh formula (e.g. Kellogg, 1929) allows for the derivation of changes of the inertia tensor relative to the initial configuration from the coefficients F_{20} and F_{21} of the gravitational potential. The resulting change of the rotation axis affects the rotational potential in terms of Ψ, which then contributes to the geoid displacement e. The changes of the potential are restricted to the $j = 2 \;/\; m \in \{-1, 0, 1\}$ coefficents. Note that Ψ only captures effects from the mass transport given by σ in the numerical implementation, whereas the deviation of the Earth from a sphere is unconsidered in the treatment of rotational changes (Martinec and Hagedoorn, 2005).

2.3.4 Earth representation in VILMA

The Earth's density and elastic structure (the latter in terms of the shear modulus μ) are assumed as only radially varying parameters $\rho_0 = \rho_0(R)$ (see above) and $\mu = \mu(R)$. The viscosity η shall be laterally varying in principal $\eta = \eta(R, \Omega)$. Lateral gradients of the viscosity are critical when comparing model results with

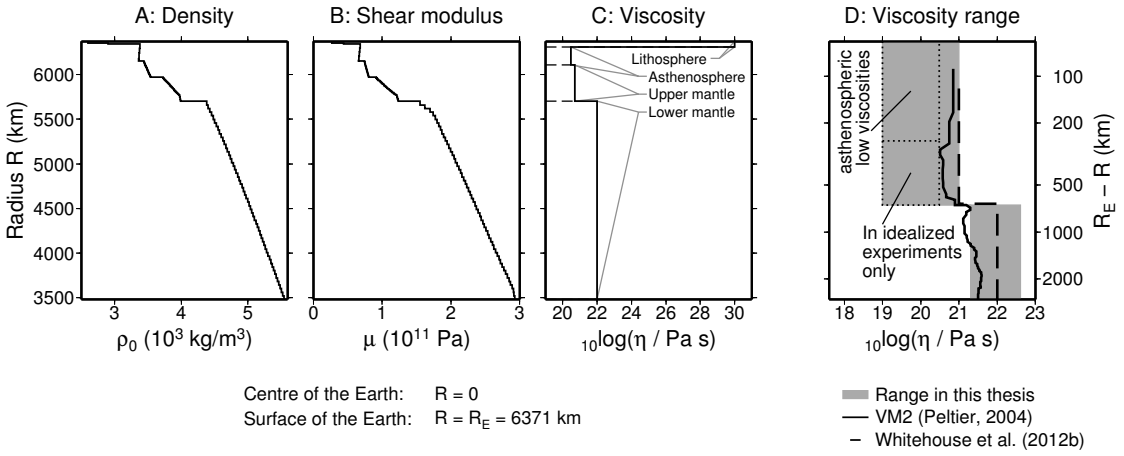

Figure 2.7
A: Radial density distribution ρ_0 according to the Preliminary Earth Reference Model (PREM; by Dziewonski and Anderson, 1981); B: PREM shear modulus μ; C: exemplary 4-layer viscosity structure. D: The considered viscosity range in this thesis (grey shading). Note the logarithmic scale for depth $R_\mathrm{E} - R$. For reference, the VM2 distribution (Peltier, 2004) and the optimal distribution for Antarctica by Whitehouse et al. (2012b) are shown. The upper dotted box indicates low viscosities for modeling the West Antarctic rift (Chapter 4). The lower box indicates the low range for the idealized experiment in Section 3.2.

geological RSL data (Kaufmann et al., 1997; Spada et al., 2006; Austermann et al., 2013). Here, the focus is more on the time scales of the near-field response (i.e. close to a climate-driven ice sheet) than on the interpretation of sea-level observations in some distance from the ice sheet. Therefore, lateral viscosity variations are not considered in the scope of this thesis.

In the experiments carried out within the scope of this thesis, the Earth is divided into three or four radial layers w.r.t. the viscosity layering. The number of layers depends on the applicability of a low-viscous asthenospheric layer. The layers are from the Earth surface to the mantle–core boundary:

- an elastic lithosphere with thickness h_L ranging between 120 km and 30 km, parameterized by a viscosity $\eta_L = 1{\times}10^{30}$ Pa s, which is practically infinite,
- an asthenospheric layer with thickness $h_\mathrm{A} = 200$ km and partially low viscosities η_A between $1{\times}10^{19}$ Pa s and $1{\times}10^{21}$ Pa s,
- the upper mantle ranging from the lower surface of the asthenosphere to the depth of 670 km with viscosities η_UM between $1{\times}10^{19}$ Pa s and $1{\times}10^{21}$ Pa s, and
- the lower mantle covering the remaining radial distance up to the mantle–core boundary at 2891 km depth with viscosity η_LM ranging between $2{\times}10^{21}$ Pa s

and $4{\times}10^{22}$ Pa s.

In general, the values of the piecewise constant viscosity are monotonically increasing with depth below surface, except for the elastic lithosphere, i.e.

$$\eta_{\mathrm{A}} \leq \eta_{\mathrm{UM}} \leq \eta_{\mathrm{LM}} \quad . \tag{2.72}$$

The Earth's radial distribution of the density $\rho_0(R)$ and of the shear modulus $\mu(R)$ are taken from the Preliminary Earth Reference Model (PREM) by Dziewonski and Anderson (1981). The PREM density and shear modulus structure as well as an exemplary viscosity structure is shown in Figure 2.7A–C. Figure 2.7D shows the range of the used viscosity values together with values from the literature. Note that μ and η are only relevant in the range illustrated in Figure 2.7 ($R \geq 3480$ km $\hat{=}$ core–mantle boundary), whereas the density in the Earth's core is still necessary to calculate the initial gravity $\vec{g}_0(R)$.

2.3.5 The thin-plate approximation ELRA as a common approach in ice-sheet modeling

The continuum-mechanical approach to solid-Earth relaxation on glacial timescales as discussed above is computationally expensive, especially if the Earth's response is not treated in the time domain as e.g. in the case of VILMA, but in the Laplace domain. There is, however, a cheaper method for treating solid-Earth dynamics when modeling ice-sheet dynamics (e.g. Le Meur and Huybrechts, 1996; Huybrechts et al., 2011; Greve et al., 2011; Pollard and DeConto, 2012b; Maris et al., 2014). This method comprises two assumptions.

Firstly, the elastic lithosphere is considered as a thin plate with infinite horizontal extension. Then, the surface deformational response U_q to a point load q fulfils the following differential equation (Brotchie and Silvester, 1969):

$$D\frac{\mathrm{d}^4}{\mathrm{d}r_q^4}U_q(r) = q - \rho_{\mathrm{a}}\, g\, U_q(r_q) \;, \tag{2.73}$$

i.e. the load is compensated by the lithospheric flexure (left-hand side of Eq. 2.73) and the buoyancy $\rho_{\mathrm{a}}\, g\, U_q(r_q)$. Here, r_q is the distance to the point load, D is the flexural rigidity (composite of lithospheric shear modulus, lithosphere thickness and Poisson ratio, see Eqs. 2.77 and 2.78), ρ_{a} is asthenospheric density, and g is again gravitational acceleration. In the literature, the asthenospheric density is mostly chosen to be $\rho_{\mathrm{a}} = 3300$ kg/m^3. With the radius of relative stiffness,

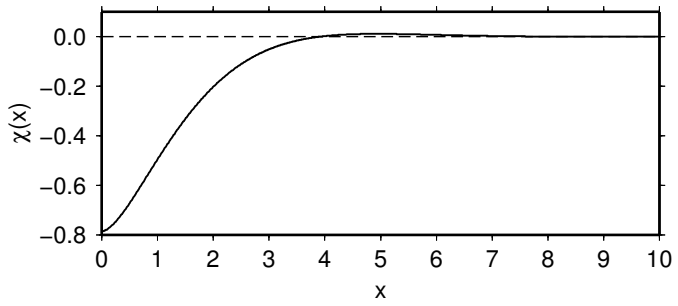

Figure 2.8
The Kelvin function of zeroth order as it appears in Eqs. 2.74 and 2.75. Note that both the Kelvin function χ and its argument (not to be confused with the Cartesian coordinate x in this thesis) are dimensionless.

$L_\mathrm{r} = (D/\rho_\mathrm{a}/g)^{0.25}$, the solution U_q of Eq. 2.73 can be written as

$$U_q(r_q) = \frac{q\, g\, L_\mathrm{r}^2}{2\,\pi\, D}\chi(r_q/L_\mathrm{r}) \quad , \tag{2.74}$$

where χ is the Kelvin function of zeroth order (Abramowitz and Stegun, 1964, cf. Figure 2.8). With $q = \sigma\, \mathrm{d}x\, \mathrm{d}y$, Eq. 2.74 yields the equilibrium deformation pattern U_eq as defined by the surface load σ:

$$\begin{aligned} U_\mathrm{eq}(x,y,t) &= \frac{g\, L_\mathrm{r}^2}{2\,\pi\, D} \int \sigma(x',y',t)\, \chi(r'/L_\mathrm{r})\, \mathrm{d}x'\, \mathrm{d}y' \quad \text{with} \\ r' &= r'(x,y,x',y') = \sqrt{(x-x')^2 + (y-y')^2} \quad . \end{aligned} \tag{2.75}$$

This equilibrium deformation pattern U_eq, however, is not reached instantaneously as it is delayed by the viscous mantle flow. The second assumption is that this delay can be modeled by one *a priori* relaxation time τ_r, so that the deformation U_S at time t can be described as

$$\frac{\mathrm{d}U_S}{\mathrm{d}t} = -\frac{U_S - U_\mathrm{eq}}{\tau_\mathrm{r}} \quad , \tag{2.76}$$

where U_eq is computed from σ at every time t. Then, Eq. 2.68 yields the updated bedrock topography. Eq. 2.76 is typically solved on the ice-sheet model's grid for ice thickness H, as σ is mainly produced by the changes in H.

The evolution of the Earth's surface when considering ELRA for solid-Earth dynamics is then based on the two ELRA parameters, namely the flexural rigidity of the lithosphere D and the relaxation time of asthenosphere and mantle τ_r.

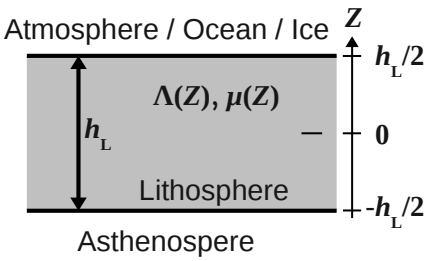

Figure 2.9
Reference for calculating the flexural rigidity for a given lithospheric thickness h_L and elastic parameters $\Lambda(Z)$ and $\mu(Z)$ according to Eq. 2.77.

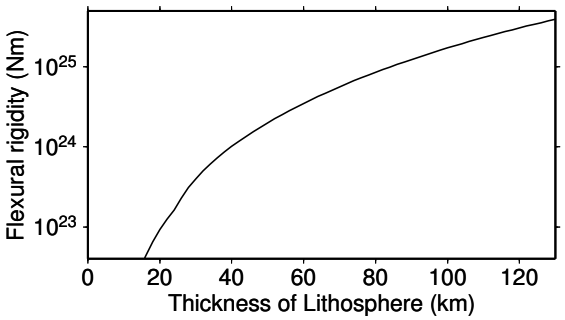

Figure 2.10
Relation between lithospheric thickness h_L and flexural rigidity D following Eqs. 2.77 and 2.78 with shear modulus μ from PREM and $\nu = 1/2$ (incompressible).

Comparability of ELRA and VILMA parameters

A comparison of results from the continuum mechanical approach of VILMA and the ELRA approximation requires a certain comparability of the applied parameters. This is not straightforward for the relaxation time τ_r, as it can at best represent one single peak of the more realistic relaxation spectrum for a given Earth structure in VILMA. The flexural rigidity D, however, can be related to the lithospheric thickness h_L and the elastic structure of the lithosphere in terms of Lamé's first and second parameters Λ and μ (Lambeck and Nakiboglu, 1980):

$$D = 4 \int_{-h_\mathrm{L}/2}^{h_\mathrm{L}/2} \frac{\mu(Z)\,(\Lambda(Z) + \mu(Z))}{\Lambda(Z) + 2\,\mu(Z)}\, Z^2 \,\mathrm{d}Z \quad . \tag{2.77}$$

Note that Lamé's second parameter μ is the shear modulus as introduced in Eqs. 2.50 and 2.51. The vertical coordinate Z is relative to the centre of the lithospheric layer (Figure 2.9). Lamé's first parameter can be expressed in terms of μ and the Poisson ratio ν:

$$\Lambda = \frac{2\,\mu\,\nu}{1 - 2\,\nu} \quad . \tag{2.78}$$

In an incompressible medium as it is assumed for the VILMA Earth, it is $\nu = 1/2$. Therefore, D is given by the PREM shear modulus structure alone when it shall be compared to h_L in VILMA. The resulting relation between h_L and D when considering PREM is shown in Figure 2.10.

Sea level in ELRA

The ELRA approach operates on a horizontally infinitely extended Earth surface. Therefore, it cannot consistently account for sea-level feedbacks as it provides no solution of the global gravity field and (self-)attraction of ice and ocean masses (Section 2.3.2). The common way to account for ice–sea-level interactions, for example in the separation of grounded and floating ice in Eq. 2.28, is to consider only eustatic sea-level contributions as they appear in Eq. 2.65,

$$\Delta s_{\mathrm{rsl}}^{\mathrm{eu}} = -\frac{\rho\, \Delta V_{\mathrm{Ice}}}{\rho_{\mathrm{oc}}\, A_{\mathrm{oc}}} \quad . \tag{2.79}$$

Without considering the sea-level evolution in terms of the SLE, the ocean area A_{oc} must be assumed constant or prescribed as a function of continentally stored ice volume $A_{\mathrm{oc}}(V_{\mathrm{Ice}})$ because migrating coastlines and the related change of ocean area are not treated. The change in RSL in the ELRA approach is then composite of eustatic sea-level variations and the bedrock deformation:

$$\Delta s_{\mathrm{rsl}}^{\mathrm{ELRA}}(x, y, t) = \Delta s_{\mathrm{rsl}}^{\mathrm{eu}}(t) - U_{\mathrm{S}}(x, y, t) \quad . \tag{2.80}$$

The change in grounded ice volume (ΔV_{Ice}) consists of 'internal' changes from the ice sheet which is modeled by the respective ice-sheet model and of 'external' changes which are prescribed and stem from ice sheets outside the model domain. Changes in oceanic loading within the ice-sheet model domain due to changes in the water column from sea-level rise in the ice shelf and ocean areas are also accounted for. This is, however, inconsistent as the ocean spreads much farther than the model domain actually is. Therefore, far field effects from oceanic loading are neglected, and the ocean floor response at the model domain margins is underestimated.

2.3.6 Phenomenology of GIA related processes

Characteristics of geoid displacement and surface displacement

The flexural behaviour of the Earth yields a shift of the Earth's surface response to longer wave-lengths when compared to the forcing load σ. This results from the low-pass filtering characteristics of the elastic lithosphere: A sharply defined point load causes a smooth deformation pattern (see also Eq. 2.74 and Figure 2.8 in the ELRA approach). The thicker the lithosphere, the more short-wavelength signal in the σ signal will be filtered in the Earth's deformational response. The geoid displacement e is even smoother as it can be inferred e.g. from the comparison of present-day GIA signals in terms of surface displacement and geoid displacement

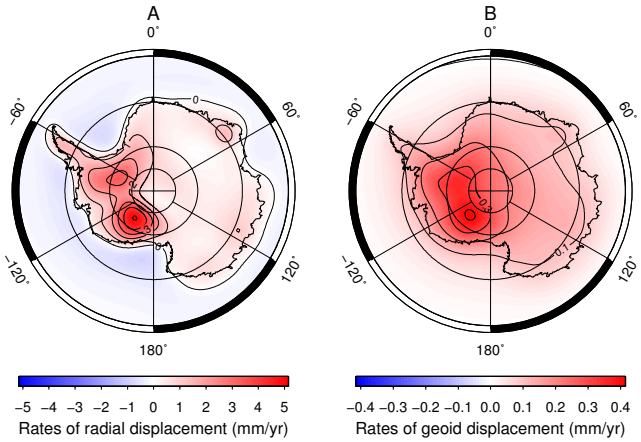

Figure 2.11
Estimated present-day rates of GIA related surface displacement $\partial U_S(\Omega,t)/\partial t$ (A) and geoid displacement $\partial E(\Omega,t)/\partial t$ (B) in Antarctica. The estimate is based on GIA modeling and adjustment to GRACE gravimetry and GPS data (AGE1b in Sasgen et al., 2013). Note the different magnitudes in the colorscale for rates of surface displacement and geoid displacement.

rates (Figure 2.11). The comparison also shows that the magnitude of surface deformation is about 10 times larger than that of geoid displacement at sites where load changes have initiated the GIA such as in the Antarctic. Far-field sites yield a lower ratio between geoid and surface deformation response.

The surface deformational response U_S is limited by the submergence of the respective lithospheric segment into the asthenosphere if one assumes that the buoyancy force alone compensates the load:

$$|U_S(\Omega,t)| \leq \frac{\sigma(\Omega,t)}{\rho_a} \quad . \tag{2.81}$$

In the case of ice loading, it is $\sigma = \rho\,\Delta H$ (Section 2.3.2). This yields a limit

$$\left|\frac{U_S(\Omega,t)}{\Delta H(\Omega,t)}\right| \leq \frac{\rho}{\rho_a} \approx \frac{1}{3} \quad . \tag{2.82}$$

The equality in 2.82 is, however, only given, if all compensating effects from the lithospheric flexure are neglected. As this is not the case here, the inequality applies.

Self-consistent sea-level evolution on glacial time scales

The SLE as described in Section 2.3.2 yields a gravitationally consistent description of sea level by accounting for the attraction of ocean water by ice mass, by mantle mass, and by the redistribution of ocean water to the resulting geoid surface (self-attraction). Figure 2.12 gives an example of the consistent sea-level evolution during the deglaciation of an ice sheet:

A Before deglaciation, an ice sheet surrounded by oceans is situated on a conti-

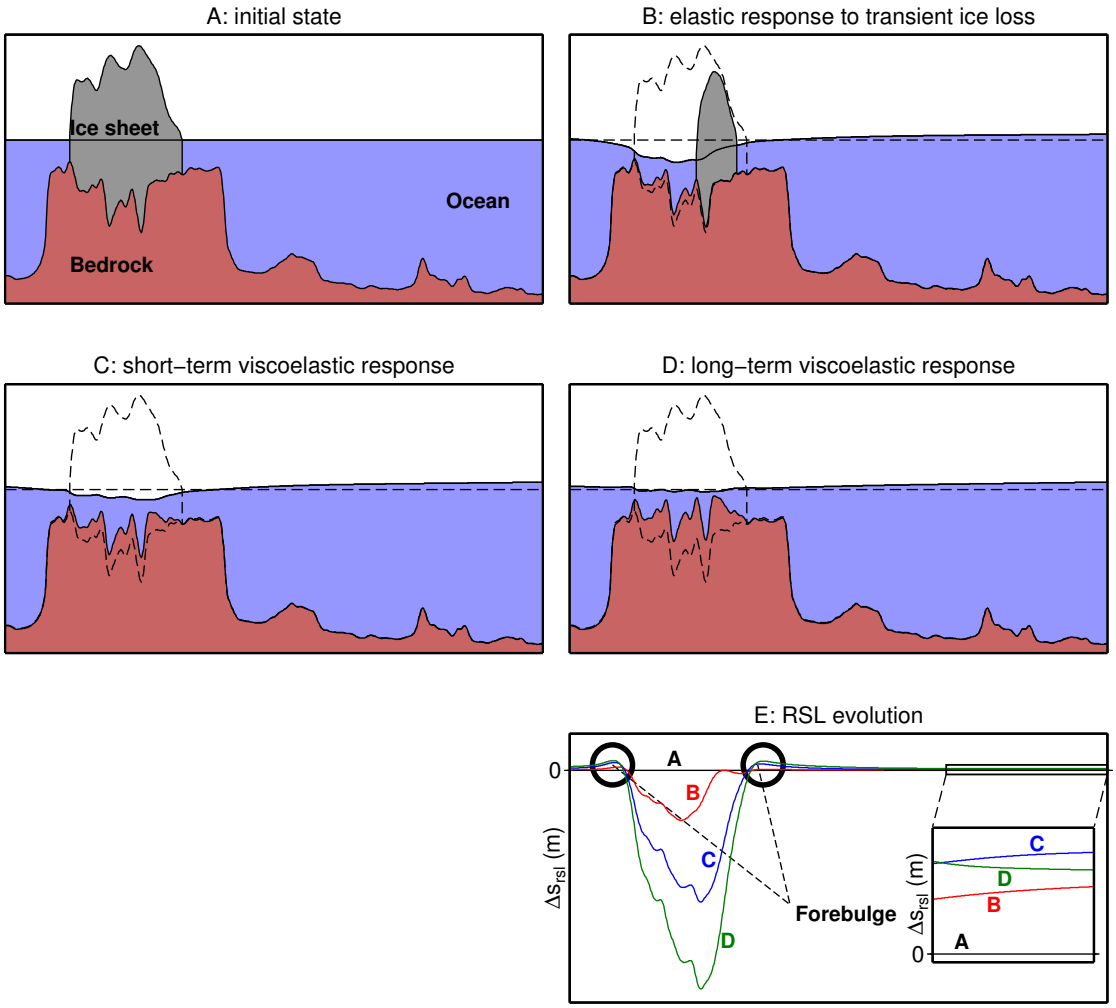

Figure 2.12
Schematic overview of the consistent sea-level evolution during and after deglaction. A: initial state with an ice sheet surrounded by oceans. Frames B–D show the situation of sea level and deformed bedrock during ice loss (B), some time after the the ice loss (C) and in the final steady situation (D). The dashed lines in B–D indicate the initial situation. E: RSL changes along the transect at the times considered in A–D. See main text for explanations. Note that the sea-level rise and fall are exaggerated by a factor of ∼40 in frames B–D. This amplification is not applied in frame E. Therefore, the eustatic sea-level rise in the far field can only be identified in the additional zoomed frame in E. See main text for an explanation of the forebulge formation.

nental shelf. In the depicted example, as well as in all later experiments, the solid Earth is considered to be in hydrostatic equilibrium with the loading by the present ice and ocean load, and sea level E and ocean bottom B are referenced to E_0.

B Warmer climate conditions cause retreat of the ice sheet. While the ice sheet loses mass, the Earth responds instantaneously to this unloading: The Earth surface rebounds due to elastic deformation; the retreat of the ice masses leads to less attraction of ocean water, which is why the sea level falls in the vicinity of the ice sheet. The sea level in the far-field rises due to the additional water from the melting ice sheet (eustasy) and from the drop of sea level around the ice sheet.

C Transient GIA implies the ongoing rebound of the Earth surface, which consequently gains in altitude. As this is accompanied by the accumulation of mantle material below the uplifting area, the gravity field in this area becomes stronger again, and the sea level rises w.r.t. stage B.

D In the final steady state, the surface rebound and the sea level are at their post-glacial maximum positions in the vicinity of the former ice sheet. The amplitudes of surface deformation around the former ice sheet, however, are larger than those of sea level (see above), so that the RSL falls from stage B through D – even if the sea level rises in the ice sheet's periphery w.r.t. stage B. This is not well captured by Figure 2.12A–D due to the exaggeration of sea-level rise and fall, but visible in frame E, which shows RSL changes without amplification of the sea-level amplitudes. The drop of far-field RSL from stage C to D, visible in the zoomed frame in E, is the so-called 'equatorial ocean syphoning' effect (Mitrovica and Peltier, 1991): Ocean water is drained from far-field sites into the subsiding forebulge areas (see below) in peripheral regions of the former ice sheet.

Another feature which cannot be seen in Figure 2.12 is hydro-isostasy (e.g. Lambeck and Chappell, 2001): For example, the rising RSL in the far field loads the underlying Earth surface at the ocean bottom, which likewise responds by elastic and viscoelastic deformation leading to subsidence of the ocean bottom. The magnitude is naturally lower than in the periphery of ice sheets because RSL changes and their associated weights are lower than e.g. a change of 4000 m in ice thickness for a continental ice sheet. Note that there is already a viscoelastic response (i.e. GIA) during deglaciation (e.g. in Figure 2.12B), as the ice goes into the ocean gradually.

Peripheral forebulge formation

The lithospheric flexure as well as the material flow in the mantle imply the formation of a peripheral forebulge around the load centers (Turcotte and Schubert, 2002): The subsidence of the Earth's surface under a growing ice sheet is accompanied by uplift in a belt in some hundreds of kms distance to the load margin, depending on the flexural characteristics of the lithosphere and the size of the load. When the subsided Earth rebounds again, the formerly uplifted forebulge areas subside again. Such forebulge formation can for instance be identified in Figure 2.11A as negative signal around Antarctica, or in Figure 2.12E as a peripheral RSL increase.

2.4 Coupling of ice and solid-Earth dynamics

With the single continuum mechanical systems of ice dynamics and solid-Earth dynamics including their numerical implementation treated in Sections 2.2 and 2.3, this section now describes and evaluates the technical aspects of their coupling. The explicit time scheme in the VILMA model[ii] allows for a straightforward strategy when exchanging the relevant fields between the ice-sheet models and VILMA. The two models run forward in time from a common initial time. In each coupling interval of length Δt_{C}, the coupling procedure as illustrated in Figure 2.13 is performed:

1. The ice-sheet model runs from coupling time step t to the next one, $t + \Delta t_{\mathrm{C}}$. Two different approaches are chosen for the two ice-sheet models:
   - The ice-sheet model RIMBAY extrapolates the Earth response between two coupling time steps t and $t + \Delta t_{\mathrm{C}}$ linearly in time.
   - The ice-sheet model PennState3d updates the Earth response at t and $t + \Delta t_{\mathrm{C}}$ and inbetween assumes zero changes. This second strategy is adopted from Gomez et al. (2013) who also use PennState3d.
2. The changes in ice thickness ΔH are handed over from the respective ice-sheet model to VILMA.
3. VILMA runs from t to $t + \Delta t_{\mathrm{C}}$ while interpolating ΔH linearly in time. By this design of the coupling, the ice-sheet model is always ahead compared to VILMA.
4. The solid-Earth response is handed over to the ice-sheet model. Two different (but equivalent) approaches are chosen:

[ii] The coupling with ELRA is considered straightforward as the ELRA equations are solved directly on the ice-sheet model's spatial grid.

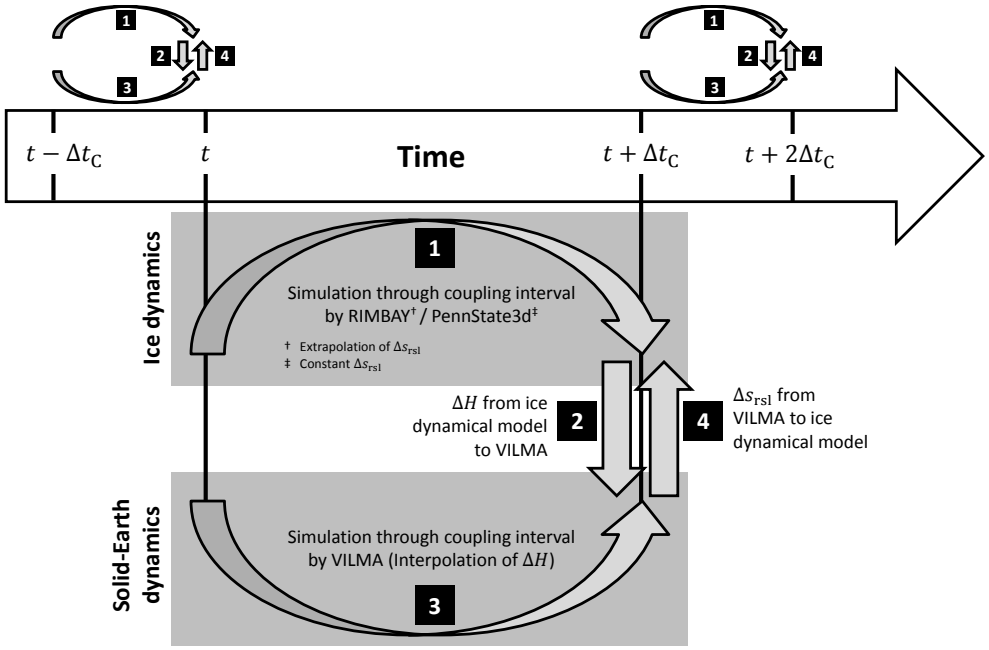

Figure 2.13
Schematic overview over the successive steps for coupling VILMA and the ice-sheet models. Steps 1–4 are according to the main text.

- For RIMBAY, the RSL changes are not handed as one, but subdivided into the radial displacement pattern $U_S(\Omega, t)$ and the changes of the sea surface $e(\Omega, t) + \Delta s_{rsl}^{UF}$, so that the bedrock topography B and the sea level E in the ice-sheet model can be updated according to Eqs. 2.67 and 2.68.
- For PennState3d, Δs_{rsl} is handed over as one pattern and applied as $B = B_0 - \Delta s_{rsl}$. This implies that the sea level E technically does not change in time: $E \equiv E_0 (\equiv 0)$.

The main difference between handing over the RSL as one field or subdivided into surface deformation and sea surface is that in the latter case, one could distinguish between effects that do not feedback with gravity and those who do. An example for a non-feedbacking effect could be that of a changing bedrock slope on the ice velocities, which should not be affected by local changes of the geoid height. These are, however, small compared to the surface displacement. The main interaction mechanism studied in this thesis, namely that between ocean depth and GL migration (see Section 1.1.3), is not affected by the way of handing over the RSL changes from VILMA to the respective ice-sheet model.

Method	ΔV_{Ice} (10^6 km^3)			ΔV_{rsl} (10^5 km^3)			S_{ROI}
	I	V	Diff.	V	I	Diff.	
R1	1.140	1.150	0.9%	−2.632	−2.626	0.2%	$\lambda \leq -76.5°$
R2	−0.512	−0.509	0.7%	2.509	2.504	0.2%	(*)
R3	−3.020	−3.022	0.0%	−3.005	−3.012	0.2%	$\lambda \leq -64.8°$

Table 2.2
Evaluation of the three regridding methods: (1) Ice volumes corresponding to the original (I; standing for 'ice-sheet model') and regridded (V; standing for VILMA) ΔH-fields as illustrated by Figures 2.14A, 2.15A–C, and 2.16A–C. (2) RSL volumes corresponding to the original (V) and regridded (I) Δs_{rsl}-fields as illustrated in Figures 2.14B, 2.15D, and 2.16D. For both quantities, the relative differences between original and regridded values are also given. The values for ΔV_{Ice} and ΔV_{rsl} are obtained from Eq. 2.83 by considering S_{ROI} as given in the table (λ: geographical latitude). Note that for R1, it is effectively $H \equiv \Delta H$, and Δs_{rsl} is substituted by the bedrock deformation U_{S} when computing V_{rsl} (cf. caption in Figure 2.14).
(*) latitude: $|\lambda| \leq 8.07°$; longitude: $|\varphi - 270°| \leq 8.26°$

2.4.1 Regridding

The regridding of the ΔH- and the Δs_{rsl}-fields is necessary because the ice-sheet models operate on a regional Cartesian grid with coordinates (x, y), whereas VILMA operates on a global Gauss-Legendre grid for the geographical longitude φ and latitude λ. Depending on the setting of the ice-sheet model domain, the regridding is performed differently. In the following, the respective interpolation methods are outlined and evaluated. For the latter, single examples of the exchanged fields from the experiments in the upcoming chapters are plotted for visual comparison. Additionally, the integrated values of the respective fields,

$$\begin{pmatrix} \Delta V_{\mathrm{Ice}} \\ \\ \Delta V_{\mathrm{rsl}} \end{pmatrix} = \int_{S_{\mathrm{ROI}}} \begin{pmatrix} \Delta H \\ \\ \Delta s_{\mathrm{rsl}} \end{pmatrix} \mathrm{d}S \ , \tag{2.83}$$

are compared in Table 2.2. Here, S_{ROI} stands for the 'regions of interest'. In the case of ΔV_{Ice}, S_{ROI} could be the respective model domains of RIMBAY/PennState3d and VILMA, if no ice outside the ice-sheet model domain is considered. For ΔV_{rsl}, however, a region has to be defined which is completely included in the non-global RIMBAY/PennState3d model domains, so that the two respective values from the regional Cartesian grid and the global Gauss-Legendre grid can be compared (see Table 2.2 for specification).

In Section 3.1, the rotational symmetry of the ice sheet allows to linear interpolate the ice thickness in latitudinal direction. The interpolation of the Earth

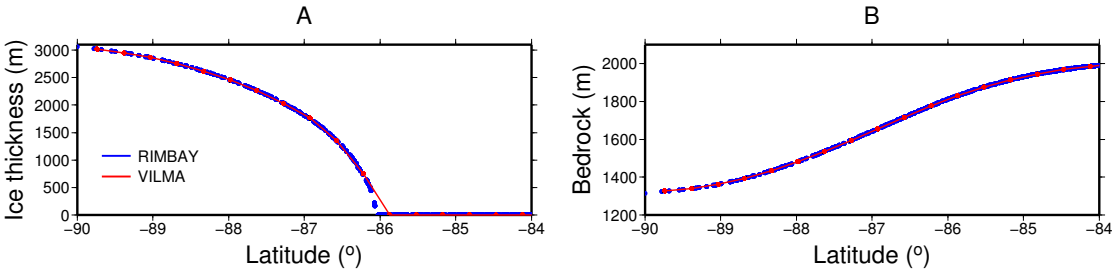

Figure 2.14
Regridding method R1: Ice thickness H (A) and bedrock topography B (B) as a function of latitude in the rotationally symmetric set-up as considered in Section 3.1 before and after the regridding. Note that all grid points in RIMBAY are plotted, whereas the fields are evaluated along only one longitudinal node in VILMA due to the rotational symmetry. The respective quantities are illustrated at the end of Period 1 in the simulation featuring the S12 Earth. The blue dots refer to the fields in RIMBAY and the red lines to the fields in VILMA. Here, H and ΔH are equal ($H \equiv 0$ at the initial time). Sea-level changes are not considered in the respective experiment; consequently, the radial surface displacement U_{S}, or the resulting deformed bedrock topography is the considered quantity for solid-Earth response.

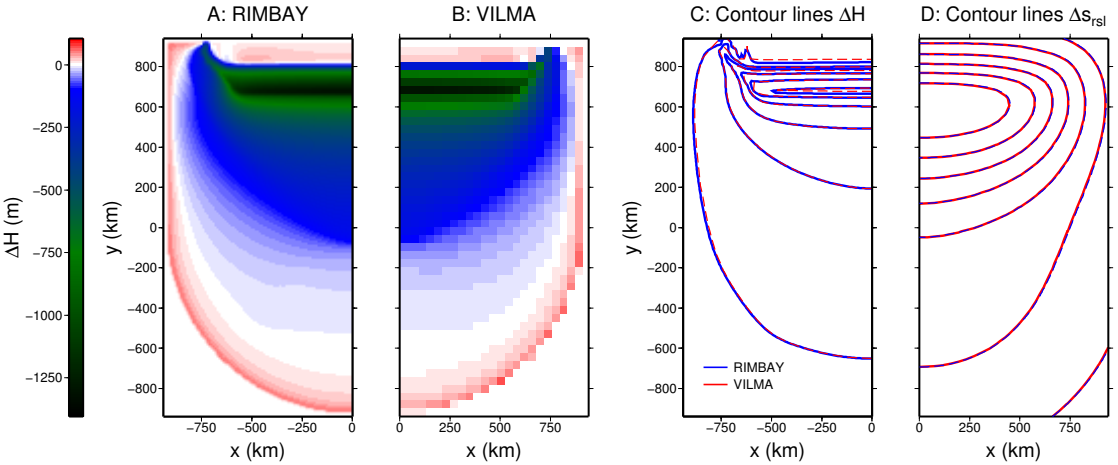

Figure 2.15
Regridding method R2: Changes in ice thickness ΔH (A, B, C) and RSL Δs_{rsl} (D) in the equatorially centered set-up as considered in Section 3.2 (after 15 kyr under `S120` forcing on the `VE_L100_M21` Earth). A: color-coded ΔH in RIMBAY. B: color-coded ΔH in VILMA. C: Contour lines of ΔH every 250 m in RIMBAY (blue) and VILMA (red). D: Contour lines of Δs_{rsl} every 20 m in VILMA (red) and RIMBAY (blue). Note that the ice-sheet model domain covers -940 m $\leq x \leq$ 940 m, but the symmetry w.r.t. the y-axis allows for plotting only half of it in every frame. Note also that the VILMA data are plotted in a latitude/longitude frame with $261.485° \leq \varphi \leq 278.515°$ and $|\lambda| \leq 8.45362°$ overlying the x-y-frame.

response at the ice-sheet model grid nodes is performed using the bi-cubic interpolation scheme provided by the Generic Mapping Tool software (Wessel and Smith, 1991). In the scope of this section, this regridding method (effectively including the methods for the two regridding directions) is labeled as 'R1'. Figure 2.14 exemplarily shows the intercomparison between the original and the regridded data for both directions.

The idealized ice sheet studied in Section 3.2 is centered at the equator. Therefore, the Gauss-Legendre grid is almost equidistant in x and y coordinates with a resolution of $\sim$39 km ($\hat{=}$ four times the ice-sheet model's resolution). Changes in the ice thickness ΔH are regridded to the Gauss-Legendre grid by Delaunay triangulation (Wessel and Smith, 1991), whereas the regridding of Δs_{rsl} is again performed by bicubic interpolation (see above). These combined two regridding methods are labeled as 'R2'. Figure 2.15 shows a respective exemplary intercomparison of original and regridded fields.

The simulations of the Antarctic Ice Sheet in Chapters 4 and 5 imply that the ice-sheet model domain again covers the South Pole as in Section 3.1. Here, however, the rotational symmetry is naturally not given. The triangulation for the regridding of ΔH is also not feasible as it suffers from the difference in grid node density in VILMA and PennState3d. Instead, for every VILMA-grid point (φ, λ), the two including PennState3d grid points in x-direction ($x_1 \leq x(\varphi, \lambda) \leq x_2$) and the two including points in y-direction ($y_1 \leq y(\varphi, \lambda) \leq y_2$) are used to bilinearly interpolate in x- and y-direction:

$$\begin{aligned} \Delta H(\varphi, \lambda) &= \sum_{i=1}^{2} \sum_{j=1}^{2} w_{x_i}\, w_{y_j}\, \Delta H(x_i, y_j) \quad \text{with} \\ w_{x_i} &= 1 - \left| \frac{x(\varphi, \lambda) - x_2}{x_1 - x_2} \right| \quad \text{and likewise for } w_{y_j}\ . \end{aligned} \tag{2.84}$$

The regridding of Δs_{rsl} is based on a similar scheme where Δs_{rsl} is interpolated at (x, y) from the VILMA output at the two longitudinal points φ_1 and φ_2 and latitudinal points λ_1 and λ_2 with $\varphi_1 \leq \varphi(x, y) \leq \varphi_2$ and $\lambda_1 \leq \lambda(x, y) \leq \lambda_2$. These bilinear methods are labeled as 'R3'. See Figure 2.16 for exemplary regridding results.

It is obvious from Figures 2.14, 2.15, and 2.16, that the regridding of Δs_{rsl} from the Gauss-Legendre VILMA grid to the Cartesian grid works well in terms of a visual comparison. The related integrated volumes ΔV_{rsl} deviate by 0.2% (Table 2.2), which also indicates an adequate performance of the respective methods.

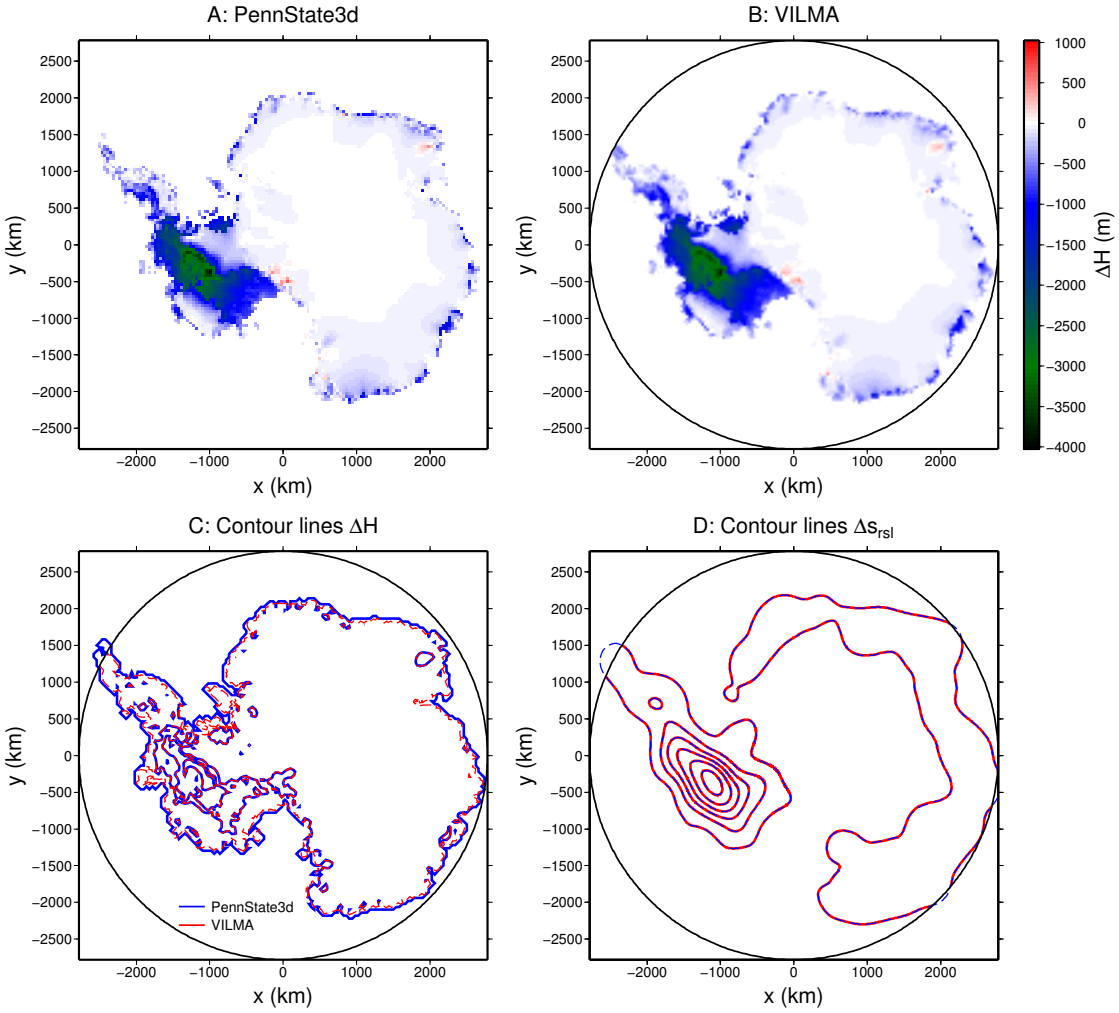

Figure 2.16
Regridding method R3: Changes in ice thickness ΔH (A, B, C) and RSL Δs_{rsl} (D) for the Antarctic Ice Sheet (AIS) after 20 kyr of warming climate forcing (Section 4). As in Figure 2.15, A and B show color-coded ΔH in PennState3d and VILMA, and C and D show contour lines of ΔH and Δs_{rsl}. The VILMA data in B, C, and D are plotted only in the area included by the black line indicating $\lambda = -64.81°$. They are plotted by stereographically projecting the geographical coordinates which coincides with the (x, y)-coordinates for the AIS in PennState3d. Note that in the PennState3d model, the non-equal area characteristic of the stereographic projection is compensated by a spatially varying grid cell area.

The regridding of ΔH is not as precise as the regridding of Δs_{rsl}, as it can be seen at the ice sheet's margin in Figure 2.14A, where the ice loss peaks in Figure 2.15C and at the margins of the Antarctic Ice Sheet in Figure 2.16C. This is due to the lower resolution in latitudinal direction in the case of the polar centered ice sheets (Figures 2.14 and 2.16) and the generally lower resolution in the equator-centered ice sheet (Figure 2.15). A higher resolution of the Gauss-Legendre grid would not yield better representation of the ice masses in VILMA as even the 1024×512 grid points are not fully captured by the harmonic cut-off degree $j_{\max} = 256$ (see Section 2.3.3).

The quality of the regridding is, however, also effected by the characteristics of the regridded fields: The smooth Earth response Δs_{rsl} allows for a better regridding than the H- or ΔH-fields with more sharply defined edges and peaks. Despite these differences and characteristics, the integrated values of the exchanged ΔH-fields differ by less than 1% for all three presented methods (Table 2.2) which also indicates adequate regridding results.

2.4.2 Length of the coupling interval

The time step for the coupling is chosen to be $\Delta t_{\mathrm{C}} = 50$ yr. In a set-up similar to the one described in Section 3.1 (rotationally symmetric, alternating ice-sheet growth and shrinking), the exchanged ice thickness differs by less than 0.1 m and the exchanged RSL differs by less than 1 m from a run where the respective fields are exchanged every time step of the two models (5 yr). The choice of $\Delta t_{\mathrm{C}} = 50$ yr is also in accordance with Gomez et al. (2012) and yields a much higher temporal resolution for the coupling than other studies in this field (van den Berg et al., 2008; Gomez et al., 2013; de Boer et al., 2014).

This high temporal resolution for the coupling is remarkable because the normal-mode approach in most solid-Earth models, i.e. the operation in the Laplace domain, makes the coupling with an ice-sheet model disproportionally expensive if the coupling time steps are dense. The additional cost for coupling in the present case (using VILMA), where the two models run ahead in time only delayed by Δt_{C}, is rather small as it is only due to the resources for handing over the respective fields from one model to the other and vice versa, and there is no integration over the complete preceding load history necessary at each coupling time step as it is when employing the normal-mode approach.

3 Analysis of the feedback mechanisms in simplified situations

– Comparison between ELRA and VILMA

3.1 Solid-Earth behaviour in coupled simulations

This section and the respective conclusions in Section 3.3 as well as the related supplementary material in Appendix C is based on and in large parts is literally taken from

H. Konrad, M. Thoma, I. Sasgen, V. Klemann, D. Barbi, K. Grosfeld, and Z. Martinec. The deformational response of a viscoelastic solid earth model coupled to a thermomechanical ice sheet model. *Surv. Geophys.*, 35(6):1441–1458, 2014. doi: 10.1007/s10712-013-9257-8.

The final publication is available at link.springer.com.

To date, common approaches in either GIA or ice-sheet modeling do not account for the feedbacks between ice and Earth dynamics as described in Section 1.1 in their full complexity: GIA models typically use predefined deglaciation patterns inferred from sea level indicators and geological evidence (e.g. Peltier, 2004), from geomorphological evidence (e.g. Ivins and James, 2005), or from thermomechanical ice-sheet modeling without direct coupling to the later used solid Earth model (e.g. Whitehouse et al., 2012a,b). Often, deglaciation histories are inferred simultaneously with optimizing for a specific viscoelastic stratification of the solid Earth, e.g. in the case of the commonly used global load history/viscosity distribution ICE-5G/VM2 (Peltier, 2004). Consequently, there is an inconsistency when applying the glacial history to a different set of Earth model parameters, or when assessing the respective results against additional observational data which can only be solved by spatially or temporally modifying the deglaciation history (Bassett et al., 2005). On the other hand, ice-sheet models typically adopt a simple parameterization for the adjustment of the solid Earth consisting of an elastic lithospheric plate and a relaxing asthenosphere (ELRA) (Section 2.3.5) which describes solid-Earth deformation in an inadequate way, as it will be shown in this context.

Le Meur and Huybrechts (1996) found that the bedrock deformation by ELRA is suffient in terms of modeling the volume of the Antarctic Ice Sheet by comparing it to a simulation featuring a self-gravitating viscoelastic Earth model (SGVEM) comparable to VILMA. The authors, however, excluded sea-level feedbacks. Contrary to that, van den Berg et al. (2008) found that e.g. the stored ice volume in Fennoscandia at the Last Glacial Maximum is underestimated by at least 30% when employing an ELRA model instead of a SGVEM for solid Earth deformation. The greatest drawback of the ELRA approximation is that it does not allow representing local sea level; by this, it is missing a process (Section 1.1.3) considered important in the evolution of the ice sheets through glacial times (Gomez et al., 2012, 2013).

Here, results on the feedbacks between ice dynamics and solid-Earth dynamics obtained from coupling a three-dimensional thermomechanical ice-sheet model to solid-Earth models of varying complexity are presented. The focus is on the SMB-altitude feedback (Section 1.1.1) and on the bedrock–velocity-field feedback (Section 1.1.2). The effect on the solid-Earth deformation is assessed for a simplified ice-sheet geometry and glaciation scenario. The aim of the study is threefold: (i) to test the new coupled system and evaluate its performance, (ii) to derive optimal parameters for ELRA and (iii) identify the limitations of the computationally more efficient ELRA approach.

It has already been stated by van den Berg et al. (2008) that the optimal choice for ELRA parameters depends on the load dimension. Consequently, aim (ii), for which mainly ice volume, ice thickness, and ice velocities, are analysed, is considered less important than aim (iii). For the latter, bedrock deformation patterns and the respective rates directly beneath the ice sheet and at peripheral sites are addressed in order to find systematic differences between the ELRA approach and VILMA. The consideration of peripheral sites is also motivated by the availability of e.g. geodetic data against which simulations could be validated in realistic scenarios.

3.1.1 Scenario

In this study, the ice-sheet model RIMBAY (Section 2.2.3) is employed. In the simplified set-up, basal melting or sliding are prohibited, i.e. the ice is frozen to the bedrock within the entire model domain. The flow rate factor A in the flow law (Eq. 2.13) is multiplied by a flow-enhancement factor (Pattyn, 2003) with a value of 3, which has no implications in the synthetic environment apart from affecting the final equilibrium geometry and the time to reach it. The spatial resolution of

Label	h_{L}	η_{UM}	η_{LM}
VM2	90 km	4×10^{20} Pa s	2×10^{21} Pa s
S12	90 km	4×10^{20} Pa s	4×10^{22} Pa s

Table 3.1
Considered viscosity distributions for VILMA consisting of an upper mantle (UM) and a lower mantle (LM) layer (Section 2.3.4). VM2 is simplified after Peltier (2004); S12 is taken from Sasgen et al. (2012); h_{L} stands for thickness of lithosphere.

the Cartesian grid is 25 km × 25 km in the horizontal plane and 41 vertical layers. The time step is 10 years when VILMA is considered, otherwise it is 20 years.

The radial resolution in VILMA is 5 km in the upper 420 km, 10 km in the next 250 km and 40 km up to the core-mantle boundary (2890 km depth). Beyond this transition, it is 60 km. The time step is chosen to be 25 years. For the radially varying viscosity structure, a simplified version of the VM2 viscosity distribution (Peltier, 2004) and a viscosity distribution, which was found optimal for fitting GIA signatures over the northern Hemisphere (Sasgen et al., 2012), henceforth referred to as S12, are employed (see Table 3.1). Both viscosity distributions feature the same thickness of the lithosphere (90 km) and differ only in the value for the averaged lower mantle viscosity, which is considerably higher in S12 (4×10^{22} Pa s) compared to VM2 (2×10^{21} Pa s).

In this study, also the ELRA parameterization (Section 2.3.5) is employed and the respective deformational patterns are compared to the continuum-mechanically obtained results from VILMA. The chosen values for the relaxation time τ_{r} are 1 kyr, 3 kyr, 5 kyr, and the used values for flexural rigidity D are 1×10^{25} N m, 2×10^{25} N m, and 3×10^{25} N m. According to Eq. 2.77, these values correspond to a thickness of lithosphere of 84 km, 105 km, and 119 km, respectively.

A simplified, rotationally symmetric set-up for the ice-sheet forcing is employed, starting from an initial state with zero ice and a flat bedrock. The initial bedrock altitude in the RIMBAY domain is uniformly 2000 m. Surface temperature T_S depends on altitude of the ice-sheet surface S, latitude λ, and time t:

$$T_S(x,y,t) = T_0 - A_S \cdot S(x,y,t) + A_\lambda \cdot (\lambda(x,y) + 90^\circ) + T_{\mathrm{f}}(t) \tag{3.1}$$

with $T_0 = 8.9034$°C, $A_S = 9.14 \cdot 10^{-3}$ °C/m, and $A_\lambda = 1.20 \cdot 10^{-2}$ °C/°. The temporal evolution of T_{f} is listed in Table 3.2. Note that the ice divide, i.e. in this symmetric scenario the centre of the ice sheet, will be situated at the South Pole ($\lambda = -90^\circ$) when coupled to VILMA.

Period	Time (kyr)	T_f (°C)	$\dot{b}_{S,\mathrm{f}}$ (m/yr)	B_f (m/yr/(°)^2)
1	0 – 150	0	−4.00	0.37093
2	150 – 300	5	−3.75	0.49457
3	300 – 450	0	−4.00	0.37093

Table 3.2
Time dependence of forcing parameters: T_f (offset for surface temperature), $\dot{b}_{S,\mathrm{f}}$ (offset for surface mass balance), and B_f (parameter for surface mass balance – latitude relation): Three periods of 150 kyr length are defined: Period 1 and 3 are colder with less ablation compared to Period 2.

The SMB $\dot{b}_S$, consisting of accumulation rate $\dot{b}_{S,+}$ and ablation rate $\dot{b}_{S,-}$, depends on surface temperature, latitude, and time:

$$\begin{aligned} \dot{b}_{S,+}(x,y,t) &= B_T \left(T_S(x,y,t) - T_\mathrm{v}\right)^2 + \dot{b}_{S,0} \\ \dot{b}_{S,-}(x,y,t) &= \max\left\{0\,,\ \dot{b}_{S,\mathrm{f}}(t) + B_\mathrm{f}(t)\cdot\left(90+\lambda(x,y)\right)^2\right\} \\ \dot{b}_S(x,y,t) &= \dot{b}_{S,+}(x,y,t) - \dot{b}_{S,-}-(x,y,t) \end{aligned} \tag{3.2}$$

with $T_\mathrm{v} = -60$°C, $\dot{b}_{S,0} = 0.1$ m water equivalent (WE)/yr, and $B_T = 1.5\cdot 10^{-4}$ m WE/yr/(°C)^2. The parameters $\dot{b}_{S,\mathrm{f}}$ and B_f are also listed in Table 3.2.

The temporal variations of T_f, $\dot{b}_{S,\mathrm{f}}$, and B_f are subdivided into three periods, namely a cool, low-ablation period, in which the ice sheet builds up, succeeded by a warmer high-ablation period, which is then again followed by a cool period with the same conditions as in the first period (Table 3.2). The length of each period is set to 150 kyr, as after that time a steady state is reached in terms of ice-sheet geometry and bedrock deformation. This set-up is chosen in order to quantify effects from partial deglaciation (warm period) and long-term behaviour (final cold period). The decrease of surface temperature and thus accumulation rate with increasing surface altitude is characteristic and will provide a realistic picture of how the solid-Earth response to glacial loading increases the achieved maximum volume of an ice sheet.

The mininum surface temperatures reached by this parameterization (Table C.1 in Appendix C) are comparable to the EISMINT benchmark experiment A by Payne et al. (2000). The choice for a temperature difference of 5°C between cold and warm periods has also been applied by Payne et al. (2000) in experiment B. It is also justified by the findings at the Vostok ice core (Petit et al., 1999) showing a

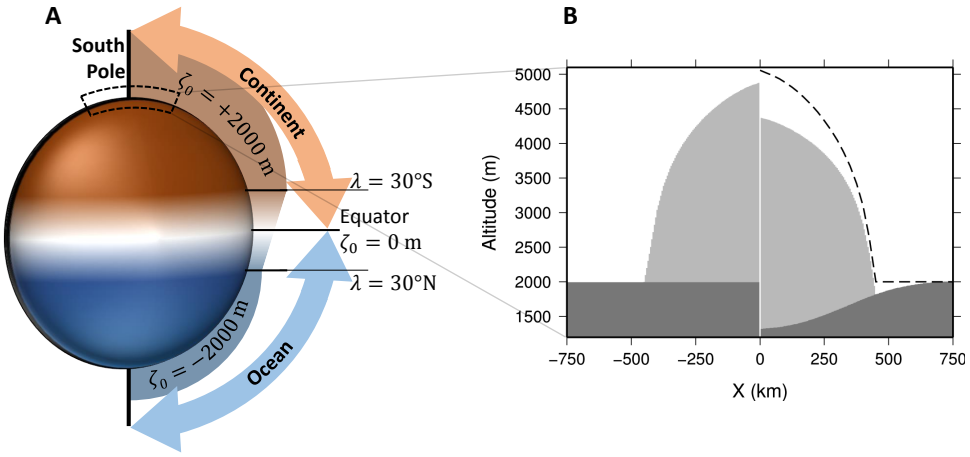

Figure 3.1
A: Initial global bathymetry (Section 2.3.2); the RIMBAY domain at the South Pole is indicated by the dashed segment. B: Geometry of the ice sheet at the end of Period 1 (in steady state) along a radial cross section. Left ($x < 0$): rigid Earth without deformation; right ($x > 0$): VILMA VM2 as an example for the non-rigid Earth simulations. The light grey area is the ice sheet. The dark grey area is the bedrock. The dashed black line shows ice thickness (referenced to 2000 m) such that the difference in ice thickness between the rigid and the non-rigid Earth is visible.

temperature difference between 2°C and 8°C w.r.t. present-day during the last ice age. The relation between surface temperature and accumulation rate is similar to the one in Huybrechts (1993) for Antarctica. The ablation rate is chosen such that a stable ice-sheet geometry can build up without expansion over the model domain's boundaries.

The initialization of VILMA requires an initial global bathymetry (Section 2.3.3). Here, a simple, longitudinally symmetric bathymetry consisting of three areas (Figure 3.1A) is applied: A continent with uniform altitude (2000 m – according to the initial bedrock altitude in the ISM domain) between $\lambda = -90°$ and $\lambda = -30°$, an ocean between $\lambda = 30°$ and $\lambda = 90°$ with uniform depth (−2000 m), and a linear transition between these two areas (from $\lambda = -30°$ to $\lambda = 30°$). The relatively large continent, on which the ice sheet builds up, corresponds to the infinite extension of the ELRA Earth. As the ice volume stored in the ice sheet is rather small and the ocean is remote from this ice sheet, the influence of the SLE solver in VILMA reduces to the conservation of the planetary water mass.

A cross section trough the steady-state solution at the end of Period 1 of the rigid Earth model and the VILMA VM2 model simulation is shown in Figure 3.1B.

3.1.2 Results

Differences in the forcing SMB, ice volume and extreme values of ice thickness and bedrock deformation

According to Eqs. 3.1 and 3.2 the surface mass balance (SMB) is decreasing with surface elevation. Consequently, the steady-state ice sheet on a rigid Earth, i.e. without any coupling to solid-Earth deformation, is driven by a lower SMB than those on a non-rigid Earth, where the ice sheet subsides due to its weight on the solid Earth (Table C.1 in Appendix C). This, again, results in less maximum ice thickness and less ice volume (see Figure 3.2) for a rigid Earth.[iii] The higher ice volume in the case of a non-rigid Earth is also related to the inward depression that holds the ice from flowing out.

The largest bedrock depression (at the centre of the load, i.e. at the ice divide) strongly depends on the flexural rigidity values D in the ELRA cases (Figure 3.3). In steady state, a relatively thin lithosphere ($D = 1{\times}10^{25}$ N m) causes a by ∼26% (cold periods) to ∼33% (warm period) stronger bedrock depression compared to a more rigid lithosphere ($D = 3{\times}10^{25}$ N m). If the load was larger, the depression at the load center would tend to a hydrostatic equilibrium and, so, would be less sensitive to the considered value of D (e.g. Watts, 2001). As there is also more ice (∼2% in volume and ∼2.7% in maximum ice thickness) in the thin lithosphere case, and as more ice induces a stronger depression, there is a positive feedback occurring in this situation. The small gain in ice thickness (2.7%) compared to ∼30% larger bedrock depression, however, indicates that this is a rather secondary effect.

The comparison of steady-state ice volume, maximum ice thickness, and maximum bedrock depression for the rigid Earth, ELRA and the VILMA Earth model yields the following principal findings:

1. The difference in VILMA VM2 and VILMA S12 are negligible after equilibrium state is reached. As the lithospheric structure is the same in both simulations, these can only result from small differences in ice thickness through the transient phases that end up in a slightly different steady-state ice sheet. During the transient phases, small delays in maximum bedrock depression occur due to the different lower mantle viscosities (Figure 3.3).
2. The medium ELRA lithosphere ($D = 2{\times}10^{25}$ N m) is best in overall fitting the ice volume, the maximum ice thickness, and the maximum bedrock depression of the VILMA runs.

[iii] As the three periods cover 150 kyr each, which exceeds the chosen values for τ_r by far, the focus lies on the values $\tau_r = 5$ kyr. Other values for τ_r are considered only when transient behaviour is discussed.

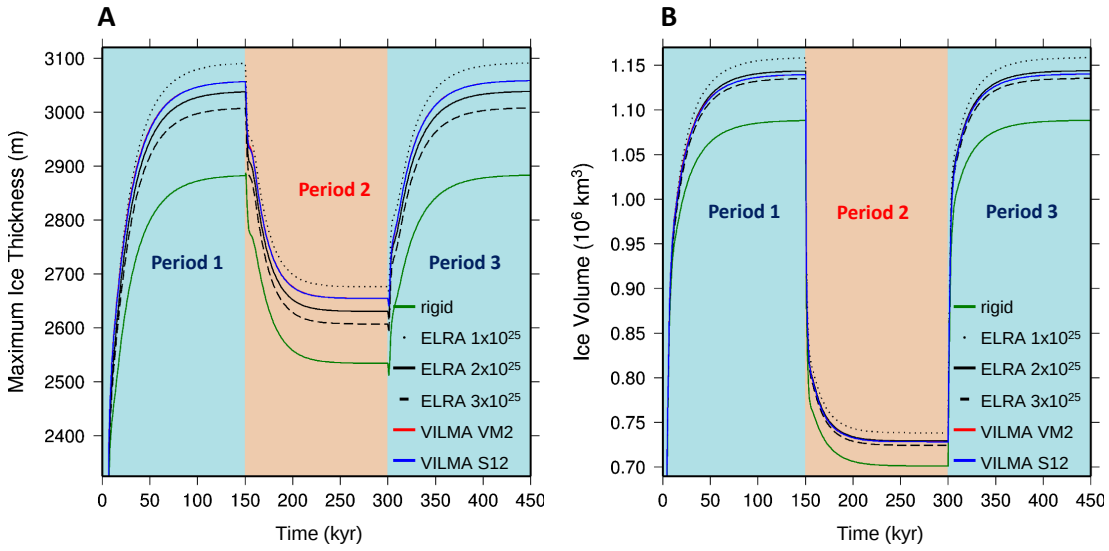

Figure 3.2
Time series of maximum ice thickness (A) and ice volume (B). Note that the lines for VILMA VM2 and S12 plot on top of each other.

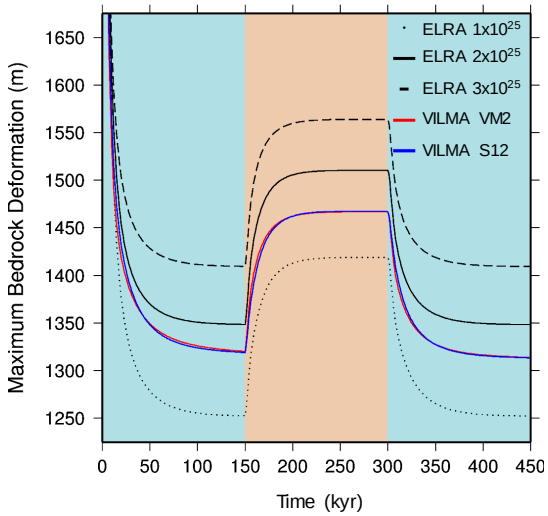

Figure 3.3
Time series of maximum bedrock deformation, i.e. at the ice divide. Note that the 'rigid Earth' run, for which deformation is zero, is not shown.

Run	$\overline{v}_\mathrm{h}$ Period 2		$\overline{v}_\mathrm{h}$ Period 3	
rigid Earth	55.5 m/yr	(-12.7%)	40.7 m/yr	(-5.2%)
ELRA $D = 1{\times}10^{25}$ N m	62.0 m/yr	(-2.5%)	43.4 m/yr	(-0.9%)
ELRA $D = 2{\times}10^{25}$ N m	62.4 m/yr	(-1.9%)	43.3 m/yr	(-1.1%)
ELRA $D = 3{\times}10^{25}$ N m	62.6 m/yr	(-1.6%)	43.2 m/yr	(-1.3%)
VILMA S12	63.6 m/yr	(0.0%)	44.0 m/yr	(0.0%)
VILMA VM2	63.6 m/yr		44.0 m/yr	

Table 3.3
Comparison of horizontally averaged horizontal velocities $\overline{v}_\mathrm{h}$ between VILMA S12, ELRA and rigid Earth runs. Due to the symmetry, the horizontal velocity field is directed radially and outward. The numbers in brackets give the relative deviation from the VILMA VM2 run. The Period 2 values are taken at $x = 350$ km and $t = 299$ kyr). The Period 3 values are taken at $x = 400$ km and $t = 449$ kyr. These are the outermost grid nodes with non-zero ice thickness, where the ice is fastest. The ELRA runs are those with $\tau_\mathrm{r} = 5$ kyr.

3. Although ELRA with the thinnest lithosphere ($D = 1{\times}10^{25}$ N m) lies closer to the VILMA runs in terms of maximum ice thickness and maximum bedrock depression, the thickest lithosphere ($D = 3{\times}10^{25}$ N m) reproduces the VILMA ice volumes better.

4. During the warm period, the ELRA with the thin lithosphere is even closer in maximum ice thickness to the medium ELRA lithosphere, while they deviate in comparable magnitude (but opposite sign) in maximum bedrock depression.

The comparison can be retraced in detail in Table C.2 in Appendix C. These relations are found insensitive to a higher SMB gradient w.r.t. the surface temperature in Eq. 3.2.

Effect of the solid-Earth representation on the velocity field

The findings on the ice velocity field at the end of Period 2 (299 kyr) and Period 3 (449 kyr), when it is in steady state, are summarized in Table 3.3. The effect of the VILMA Earth on the flow field in the ice body is small compared to ELRA. The maximum deviations in mean horizontal velocity (i.e. averaged over depth) do not exceed 2.5%. Along a whole radial cross section, the mean absolute deviation in mean horizontal velocity of the ELRA runs from the VILMA runs does not exceed 0.2 m/yr. The differences between the two VILMA runs are again negligible. The maximum velocities in the ice sheet on a rigid Earth are considerably lower compared to any non-rigid Earth, due to smaller SMB.

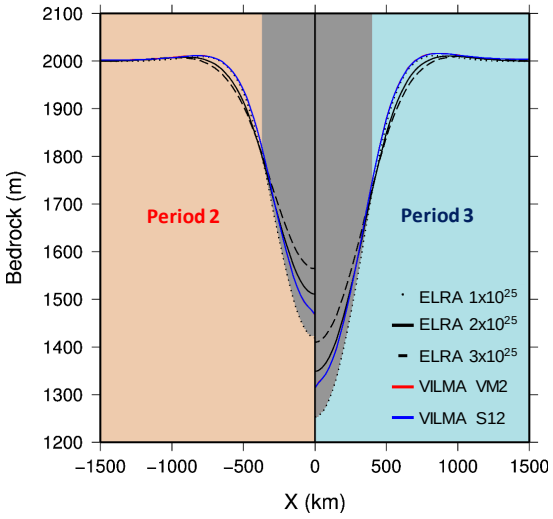

Figure 3.4
Bedrock at the end of Period 2 (299 kyr – left) and of Period 3 (449 kyr – right) along a radial cross section; the grey shaded part is covered by the ice sheet. Note that bedrock initially equals 2000 m and that the 'rigid Earth' run, for which deformation is zero, is not shown.

Run	max $\lvert\Delta_{\mathrm{bed}}\rvert$ (m)		mean $\lvert\Delta_{\mathrm{bed}}\rvert$ (m)	
ELRA $D = 1{\times}10^{25}$ N m	77.1	56.7	21.1	13.4
ELRA $D = 2{\times}10^{25}$ N m	33.6	43.6	12.6	11.1
ELRA $D = 3{\times}10^{25}$ N m	89.3	97.0	24.4	21.2
VILMA S12	1.2	0.3	0.7	0.2

Table 3.4
Maximum and mean of absolute deviations in bedrock deformation ($\lvert\Delta_{\mathrm{bed}}\rvert$) from the VILMA VM2 in steady state. The first value is for the cold periods, the second for the warm period. The ELRA runs are those with $\tau_{\mathrm{r}} = 5$ kyr.

The shape of the deformed bedrock

Figure 3.4 provides a view on the deformed bedrock along a radial cross section at the end of Period 2 (299 kyr, displayed for $x < 0$) and Period 3 (449 kyr, displayed for $x > 0$) – for both times the ice divide is located at $x = 0$. It becomes visible that bedrock deformation from ELRA compared to VILMA differs not only in amplitude, but also in shape. In particular, the peripheral forebulge is less pronounced for the ELRA Earth, except for the $D = 1{\times}10^{25}$ N m where, however, the bedrock depression at the load center is overestimated. Table 3.4 summarizes the deviations in bedrock deformation during steady state from the VILMA VM2 run. The $D = 2{\times}10^{25}$ N m ELRA Earth deviates least from the VILMA runs, which again lie very close to each other due to the same value of lithosphere thickness and elasticity. The minimum deviation between the medium lithosphere ELRA and the VILMA runs is also the reason for the best fit in ice volume and ice thickness as it controls the overall surface conditions via the atmospheric forcing.

As before, the ELRA run with $D = 3{\times}10^{25}$ N m deviates the most from the VILMA runs.

Transient forebulge behaviour

Although the systematic differences between ELRA and the VILMA appear negligible when evaluating the ice-dynamical quantities such as ice thickness and ice volume, a closer look at the peripheral forebulge structure reveals considerable differences in the bedrock deformation. Figure 3.5A, 3.5B, and 3.5C show time series of forebulge height, forebulge position, and distance of the inflection point (I) of the deformed bedrock profile from the forebulge maximum (M). The latter is a measure for the flexure of the lithosphere: small values imply a steeper bedrock, larger ones a smooth bedrock. In order to make the relation between the forebulge height (Figure 3.5A) and its migration (Figure 3.5B) clear, forebulge profiles at several times during the partial unloading following the onset of Period 2 and the spatial path of the forebulge peak for the two VILMA runs and one ELRA run are shown in Figure 3.5D.

The position of the forebulge maximum along the x-axis mostly depends on the lithospheric parameterization and varies by ∼50 km with the load (i.e. closer to the ice divide in the warmer periods) in each run. Forebulge height is obtained by considering positive deviations of the deformed bedrock from the initial altitude of 2000 m. The exponential characteristic of the ELRA dynamics (Eq. 2.76) is clearly visible. The thicker the ELRA lithosphere is, the less forebulge height is reached. The steepness in the ELRA runs, which is rather independent from the loading, increases with greater flexural rigidity (smaller values of M – I Distance means steeper bedrock slope): ∼510 km for $D = 1{\times}10^{25}$ N m; ∼600 km for $D = 2{\times}10^{25}$ N m; ∼660 km for $D = 3{\times}10^{25}$ N m. It shows no transient behaviour opposed to the VILMA runs, which also feature slightly different values in the cold and warm periods.

In general, best agreement with the VILMA runs is achieved by the thinnest lithosphere ($D = 1{\times}10^{25}$ N m) in terms of forebulge peak position and bedrock steepness. This is in contrast to the ice dynamical results, which are in best agreement for the $D = 2{\times}10^{25}$ N m lithosphere. For the VILMA runs, the temporal evolutions of S12 and VM2 forebulges differ strongly when the load changes; the forebulge height of S12 overshoots the one of VM2, which generally shows a rather smooth evolution.

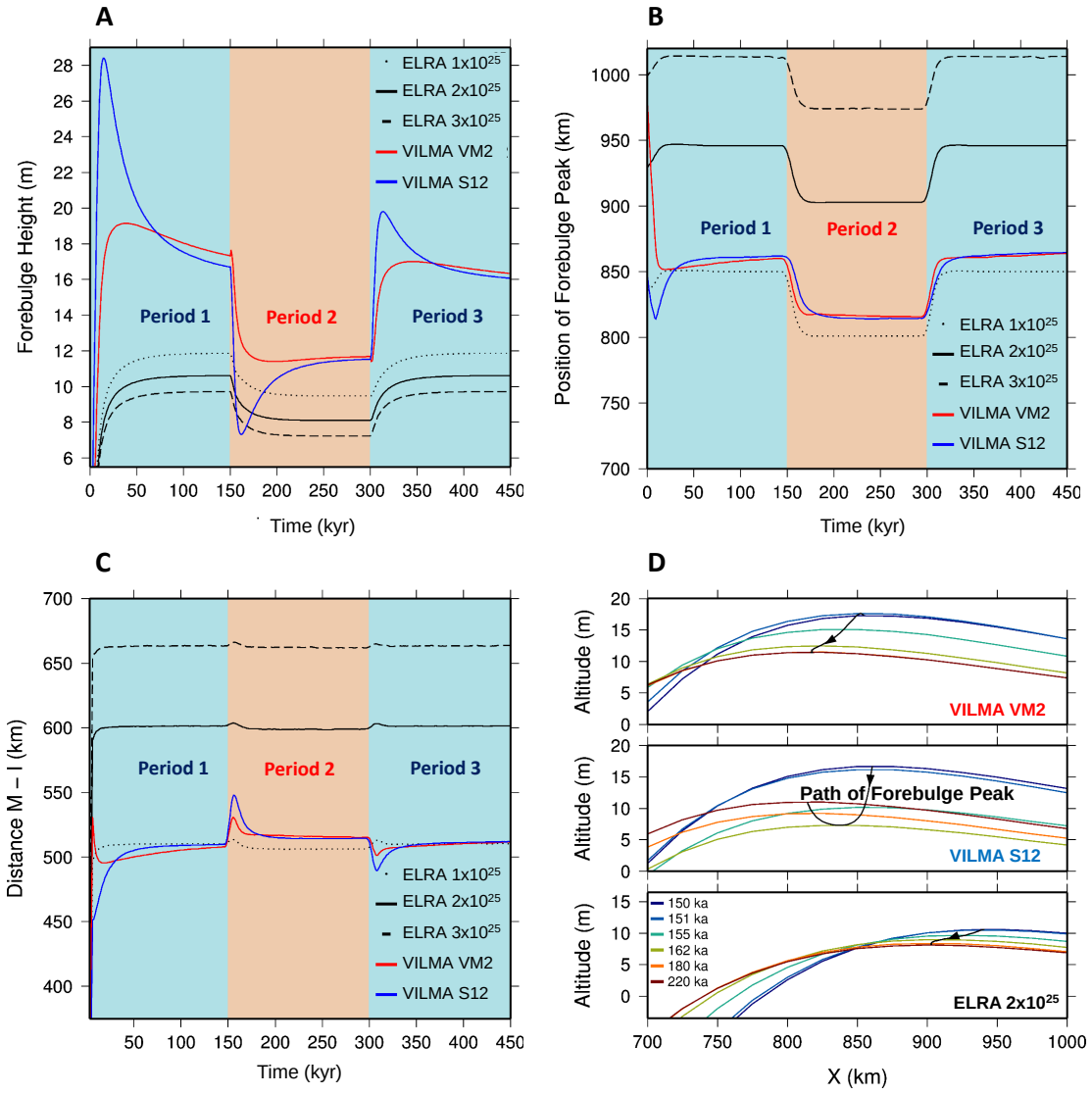

Figure 3.5
A: Time series of forebulge height (deviation from the initial altitude of 2000 m). B: Time series of forebulge position, i.e. distance of the forebulge maximum from the ice divide. C: Time series of the distance from point of inflection of the bedrock profile (I) to the forebulge maximum (M), which is a measure for the flexure of the lithosphere (see main text). D: Forebulge profiles at different times (radial cross sections) after the onset of Period 2 where the interplay between forebulge peak height and migration is shown for the VILMA runs (top: VM2; centre: S12) and one ELRA run (bottom: $D = 2{\times}10^{25}$ N m $-\ \tau_r = 5$ kyr). Note that also the path of the forebulge peak during its evolution in time is shown in black.

Bedrock deformation rates following the load changes

The bedrock deformation rates (BDR) – i.e. subsidence rates (BDR<0) and uplift rates (BDR>0) – illustrate the different transient behaviours of the solid Earth. Figure 3.6A and 3.6B show BDR at the ice divide (with $\tau_r = 5$ kyr in the ELRA runs in A and $\tau_r = 3$ kyr in B). As the maximum bedrock deformation is reached at approximately the same time in the ELRA runs with the same value of τ_r, but the maximum value itself varies with flexural rigidity D (Figure 3.3), the rates at the ice divide are highest for $D = 1{\times}10^{25}$ N m and lowest for $D = 3{\times}10^{25}$ N m.

The absolute BDR values in the ELRA cases also depend on the relaxation time τ_r. Here, large systematic differences between ELRA and VILMA can be found: The $\tau_r = 5$ kyr ELRA runs underestimate the maximum amplitude of the BDR in the first build-up phase (Period 1, except for $D = 1{\times}10^{25}$ N m) whereas the runs with $\tau_r = 3$ kyr reproduce this amplitude quite well (again except for $D = 1{\times}10^{25}$ N m), and the decay behaviour towards zero BDR is closer to the one in the VILMA runs for $\tau_r = 3$ kyr. Then, at the onset of the remaining two periods, when the change in load is smaller than directly at the beginning of the experiment, the $\tau_r = 3$ kyr runs overestimate the BDR amplitudes and the rates decay too fast, whereas the $\tau_r = 5$ kyr results show better consistency with VILMA.

Figure 3.6C shows BDR at horizontal position $x = 450$ km, which is beyond the ice sheet but close to its margin. Note that only $\tau_r = 5$ kyr is considered here. The order of the ELRA BDR is reversed; due to the different lithospheric deflections, the thinnest ELRA Earth ($D = 1{\times}10^{25}$ N m) has lowest absolute BDR. Here, the ELRA runs rather overestimate the BDR rates in Period 1 and then underestimate them in Period 2 and 3. The decay of the ELRA BDR towards zero is too slow compared to the VILMA results.

Figure 3.6D shows BDR at the position of the maximum forebulge height (varies in time along the x-axis; see Figure 3.5B), representing the temporal derivatives of the respective graphs in Figure 3.5A. Here, the deviations between ELRA and VILMA and between the two VILMA runs are comparably large. While the ELRA forebulges do not show much dynamical behaviour at all (see also Figure 3.5), the transient behaviour of the VILMA runs is more complex. For S12, the BDR changes sign from negative to positive in the forebulge region within a warm/cold period (see also Figure 3.5A). It is also visible that ELRA with only one relaxation time, while being sufficient for the ice dynamics, is a too simple Earth model parameterization for describing forebulge relaxation. The ELRA parameterization thus proves its major drawback as it is not applicable when predicting geological or geodetic observables in the peripheral regions of the ice sheet.

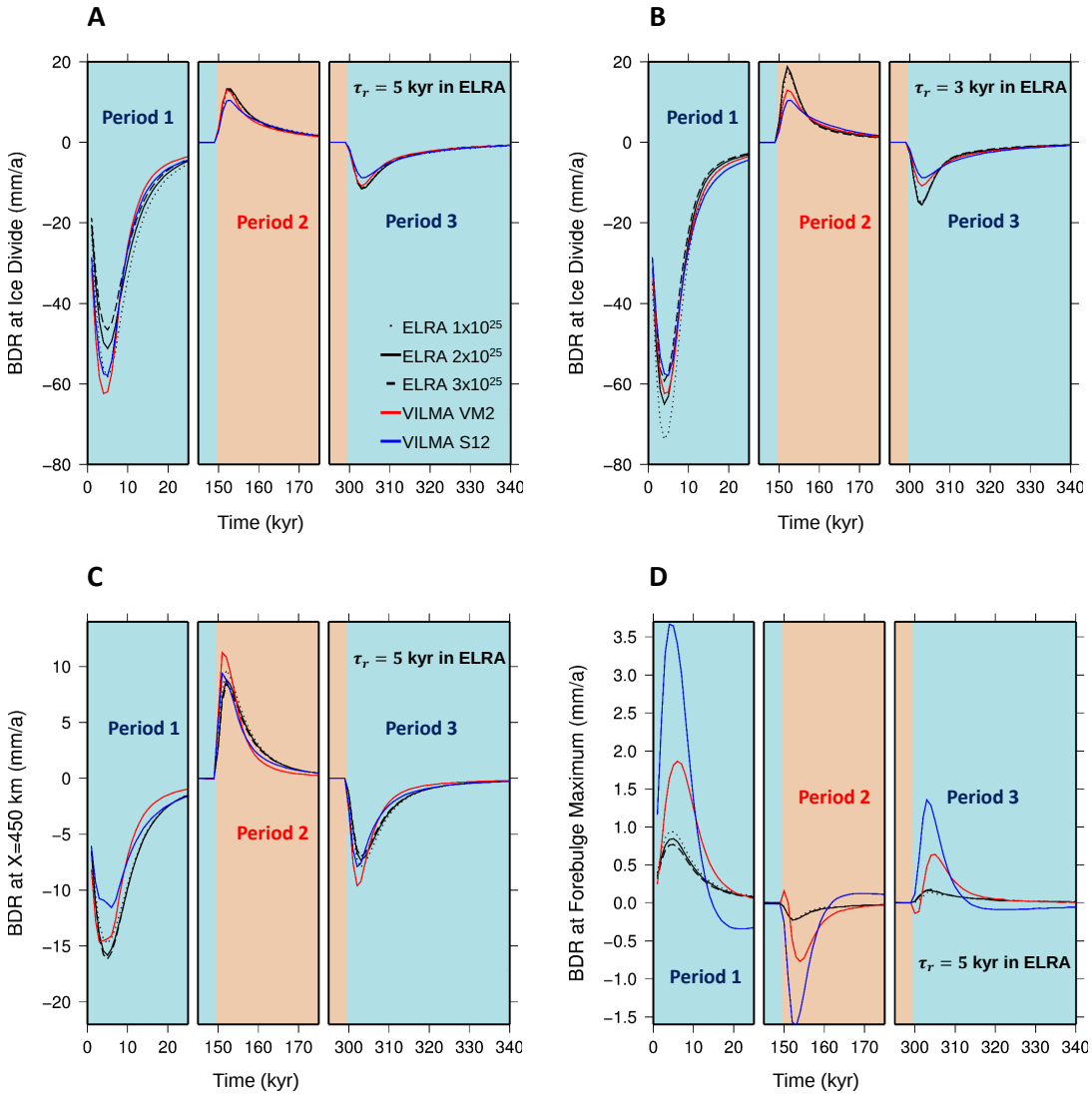

Figure 3.6
A: Bedrock deformation rates (BDR) at the ice divide ($x = 0$ km); B: Bedrock deformation rates (BDR) at the ice divide ($x = 0$ km) with $\tau_r = 3$ kyr for the ELRA runs; C: BDR at $x = 450$ km (ice free at any time, but close to the ice sheet's margin); D: BDR at the position of maximum forebulge height. Note that the plotted periods ($0 - 25$ kyr, $145 - 175$ kyr, $295 - 340$ kyr) are zooms to times around the transitions between cold and warm periods. Except for B with $\tau_r = 3$ kyr, the ELRA runs are those with $\tau_r = 5$ kyr.

3.1.3 Discussion

In accordance with Le Meur and Huybrechts (1996), the effect of a complex, continuum-mechanical solid-Earth model such as VILMA on the ice dynamics is found to be approximated by ELRA. Ice volume, ice thickness and ice velocities in the less complex solid Earth model ELRA are very close to the quantities in the VILMA runs; depending on the choice of the elastic parameter D, deviations of $\sim$0.1% in volume can be achieved. Therefore, the feedback of GIA with the atmospheric forcing depending on the surface altitude (Section 1.1.1) is satisfactorily accounted for by ELRA if the parameters are calibrated for a similar scenario with a complex viscoelastic Earth model.

The optimal parameters, however, depend on the size of the loading ice sheet and have to be determined for each scenario independently (van den Berg et al., 2008). In this sense, this simplified case study is not representative for larger ice sheets with a more complex geometry and glaciation history. In the present scenario, a best fit of stored ice volume to the VM2 and S12 viscosity structures could be obtained by setting the elastic parameter to $D = 2\times10^{25}$ N m. This value corresponds to 105 km thickness of lithosphere. As rather the $D = 1\times10^{25}$ N m (84 km thickness) lithosphere would match the 90 km lithospheric thickness in the VILMA simulations, the physical meaning of the lithospheric parameter D suffers from the thin-plate approximation in the ELRA approach.

Also, in this simplified set-up, only velocities resulting from ice deformation have been allowed for. In the case of a more realistic ice sheet, regions with extensive basal sliding might be more affected by GIA-induced changes of the bedrock slopes.

There are systematic discrepancies between the ELRA approximation and fully coupled simulations including VILMA in terms of solid-Earth deformation, relevant in particular in the periphery of the ice sheet, where observational constraints on GIA exist for real ice sheets, such as crustal uplift/subsidence velocities from GPS measurements, or paleo sea-level indicators. For including such data in the analysis of a coupled ice-sheet / solid-Earth simulation, the ELRA parameterization is not sufficiently precise and the more complex approach of a SGVEM such as VILMA is required; forebulge elevation might be underestimated (Figure 3.5A), whereas vertical crustal velocities beyond the ice sheet might be overestimated or underestimated, depending on the temporal change in loading (Figure 3.6).

The main drawback of the ELRA approach in this respect is the inconsistency of the elastic parameter w.r.t. the VILMA lithosphere: While the $D = 2\times10^{25}$ N m lithospere fits the VILMA runs best in terms of ice volume due to a better fit of

solid-Earth deformation in the ice-covered area, the $D = 1{\times}10^{25}$ N m lithospere reproduces the shape and the behaviour of solid-Earth deformation much better beyond the ice sheet (see also Figure 3.4). Additionally, features of a multi-layer viscosity structure such as the prominent forebulge dynamics due to the large contrast between upper and lower mantle viscosity in S12 cannot be captured by ELRA.

The possibility of a viscoelastic layering of the Earth that is more complex than the considered two-layer distributions in the Earth's mantle also represent an advantage of VILMA. A more complex stratification of viscoelastic parameters is expected to lead to more deviations on short wave-length and introduce even more deviations from the ELRA Earth.

3.2 Sea level and grounding-line migration in coupled simulations

With the SMB-feedback (Section 1.1.1) treated in the previous section and the bedrock–velocity feedback (Section 1.1.2) determined to be of minor importance and difficult to quantify, this section will address the feedback between sea level and grounding line (GL) dynamics, particularly in the case of an ice-sheet subject to the Marine Ice Sheet Instability (MISI – Section 1.1.3) – similar to Gomez et al. (2012). The focus will be on an extended analysis of the influence of the Earth model parameters on the ice-sheet / shelf dynamics.

In a geometrically simplified ice-sheet scenario (Figure 3.7), the sensitivity of the GL positioning to the viscoelastic structure of the underlying solid Earth is investigated, in particular to the thickness of the lithosphere and to upper mantle viscosity. Starting from an ice-sheet / shelf configuration in steady state, the coupled RIMBAY/VILMA system is subject to a forcing by sea-level rise from ice melting on a remote continent – similar to the Antarctic Ice Sheet under the influence of northern hemispheric melt-water pulses during the deglaciation after the Last Glacial Maximum – as well as to changes in the boundary conditions at the ice-sheet surface and at the ice-sheet–bedrock interface. Additionally, the ELRA model instead of VILMA is applied in order to find the limitations of the former w.r.t. GL dynamics.

3.2.1 Scenario

A thermomechanical coupling of ice viscosity to temperature (e.g. Hooke, 1981) is not considered here in order to minimize the number of effects that can be seen in

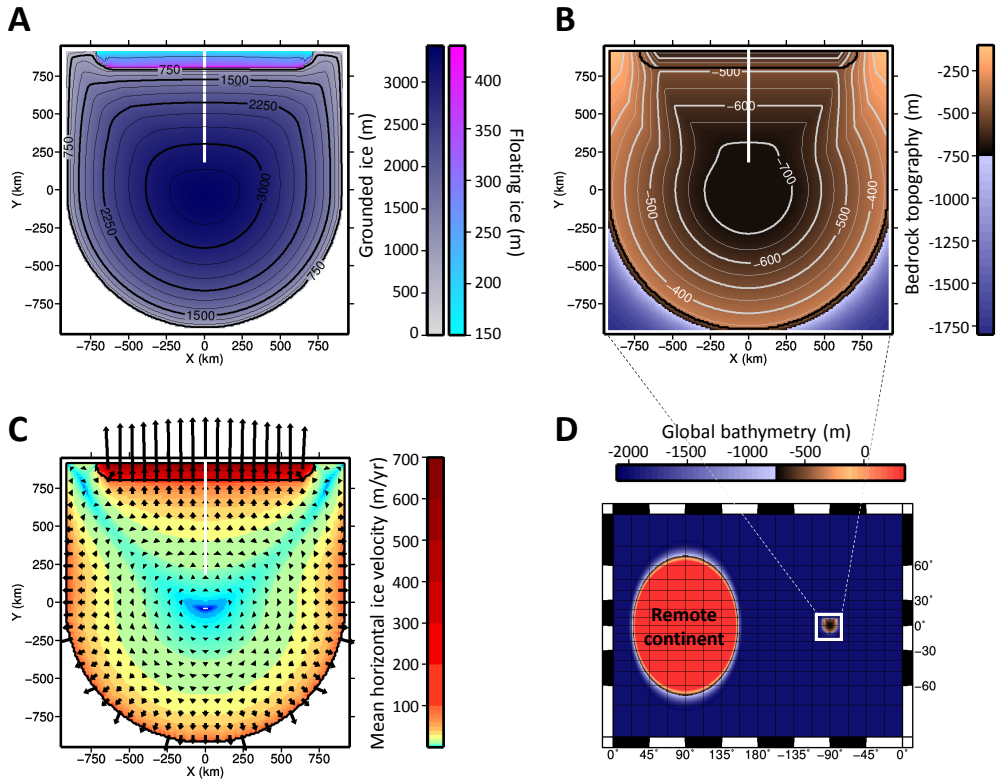

Figure 3.7
Initial set-up; A: Ice thickness; note the different color scales for grounded and floating ice. B: Bedrock topography; the topography is referenced to sea level at t=0. C: Mean horizontal ice velocities; in B and C, the black lines mark the transition between grounded ice, floating ice, and ocean (cf. A). The white line at $x = 0$ indicates the cross section along which the results are analyzed. D: Global bathymetry featuring the RIMBAY domain (-90° longitude), a remote circular continent (+90° longitude; in Mercator projection appearing as elliptical), and an ocean.

the later results. Instead, a constant rate factor A for Glen's Flow law (Eq. 2.9) is applied. As an advance w.r.t. Section 3.1, the sliding law given by Eq. 2.21 is employed with the initial value $C = 10^7$ Pa $(\mathrm{m/s})^{1/3}$ for the basal friction coefficient. The applied parameterization for basal melt rates in the floating areas ($\dot{b}_B^{\mathrm{shelf}}$) follows Beckmann and Goosse (2003):

$$\dot{b}_B^{\mathrm{shelf}} = A_{\mathrm{eff}} \frac{\rho_{\mathrm{oc}}\, c_{\mathrm{oc}}}{\rho L_{\mathrm{Ice}}}\, \gamma_T\, (T_{\mathrm{oc}} - T_{\mathrm{fp}}) \tag{3.3}$$

where the freezing point temperature at the ice-shelf base T_{fp} is computed as (Foldvik and Kvinge, 1974)

$$T_{\mathrm{fp}} = 0.0939^{\circ}\mathrm{C} - 0.057^{\circ}\mathrm{C}\,(\mathrm{PSU})^{-1}\, S_{\mathrm{oc}} - 7.64 \times 10^{-4}\,^{\circ}\mathrm{C\,m^{-1}}\, z_{\mathrm{bsl}}. \tag{3.4}$$

label	h_{L} (km)	η_{UM} (Pa s)	η_{LM} (Pa s)	μ
`VE_L035_M19`	35	1×10^{19}	1×10^{22}	PREM
`VE_L100_M19`	100	1×10^{19}	1×10^{22}	PREM
`VE_L035_M21`	35	1×10^{21}	1×10^{22}	PREM
`VE_L100_M21`	100	1×10^{21}	1×10^{22}	PREM
`RIGID`	–	1×10^{30}	1×10^{30}	1×10^{20} Pa

Table 3.5
Solid-Earth rheologies used in this study; the controlling parameters are thickness of lithosphere h_{L}, upper mantle viscosity η_{UM}, lower mantle viscosity η_{LM}, and the shear modulus μ; see Section 2.3.4. Note that the values for the `RIGID` Earth are practically infinite.

Here, z_{bsl} is the depth below sea level of the lower ice-shelf edge. The tuning parameter A_{eff} in Eq. 3.3 specifies the 'effective melting area'. The remaining quantities in Eqs. 3.3 and 3.4 are the ocean water density ρ_{oc} (cf. also Section 2.3.2), the specific heat of ocean water $c_{\mathrm{oc}} = 3974$ J (kg °C)$^{-1}$, the latent heat of the ice–water transition $L_{\mathrm{Ice}} = 333.5$ kJ kg^{-1}, the ocean temperature $T_{\mathrm{oc}} = -1.7$°C, the salinity $S_{\mathrm{oc}} = 35$ PSU, and the exchange velocity $\gamma_T = 10^{-4}$ m/yr.

Ice-berg calving is treated as follows: the calving front, where the ice shelves do not only share a vertical boundary with the ocean, but also a horizontal one, can only retreat but not advance in the model. Retreat occurs if the ice thickness at the calving front goes down to zero. Advance should occur if more ice flows over the horizontal ice-ocean interface than is actually calving (or melting). This is, however, not modeled. Instead, all ice that is flowing over the interface is assumed to have calved off and by that has gone into the ocean.

The RIMBAY domain is resolved with a 10 km × 10 km Cartesian grid.

In this study, five different sets of solid-Earth parameters are applied (Table 3.5). Four of them are three-layered, obtained by combining a thin or a thick lithosphere ($h_{\mathrm{L}} = 35$ km vs. 100 km) with a low-viscous or a high-viscous upper mantle ($\eta_{\mathrm{UM}} = 1\times10^{19}$ Pa s vs. 1×10^{21} Pa s). In these cases, the lower mantle has a viscosity of $\eta_{\mathrm{LM}} = 1\times10^{22}$ Pa s. Additionally, by applying practically infinite values for the viscosity (1×10^{30} Pa s) and the shear modulus (1×10^{20} Pa), the effects of a rigid (i.e. non-deforming) Earth, which allows only for gravitational feedbacks, are investigated. This rigid-Earth case (labeled as `RIGID`) is the only exception within this thesis from the usage of radial shear modulus μ from PREM (Dziewonski and Anderson, 1981). The labels for viscoelastic rheologies (`VE`) are made up of sub-labels: `L035` and `L100` indicating the lithosphere thickness, and `M19` and `M21` indicating the logarithm of upper mantle viscosity.

ELRA run No	D (N m)		τ_r (yr)	Corresponding VE layering
1	1×10^{23}	(20 km)	20	VE_L035_M19
2	2.5×10^{24}	(54 km)	20	VE_L035_M19
3	1×10^{23}	(20 km)	500	VE_L035_M19
4	2.5×10^{24}	(54 km)	500	VE_L035_M19
5	1×10^{25}	(84 km)	1000	VE_L100_M21
6	3×10^{25}	(119 km)	1000	VE_L100_M21
7	1×10^{25}	(84 km)	5000	VE_L100_M21
8	3×10^{25}	(119 km)	5000	VE_L100_M21

Table 3.6
ELRA parameters: The viscoelastic layering (Table 3.5), to which the respective ELRA run is compared, is indicated. The bracketed values give the lithospheric thickness corresponding to D according to Eq. 2.77.

The results from the coupled model are compared with simulations featuring the ELRA approximation for solid-Earth dynamics (Section 2.3.5). The values for the flexural rigidity D are chosen to encompass the 35 km and 100 km lithosphere in the viscoelastic simulations. Eq. 2.77 is applied to find the relation between D and h_L. The values $D = 1\times10^{23}$ N m and $D= 2.5\times10^{24}$ N m include the 35 km lithosphere, while $D = 1\times10^{25}$ N m and $D = 3\times10^{25}$ N m comprise the 100 km lithosphere. For the relaxation time, $\tau_r = 20$ yr and $\tau_r = 500$ yr are chosen for comparison with the low-viscous upper mantle and $\tau_r = 1000$ yr and $\tau_r = 5000$ yr for the high-viscous upper mantle. The combinations of these ELRA parameters are listed in Table 3.6.

Steady state set-up

The steady-state set-up comprises an ice shelf which is confined at three sides by an ice sheet (Figures 3.7A, B, and C). This ice-sheet geometry is reached after 60 kyr of initialization under constant SMB conditions of 0.2 m WE ice accumulation per yr and a surface temperature of -15°C. The bedrock topography is designed symmetrically with regard to the y-axis and features an inward slope such that a GL perturbation will cause further retreat (MISI; cf. Section 1.1.3). The melting rates in the ice shelf areas are forced to be close to zero compared to the accumulation rate by setting the adjustment parameter in Eq. 3.3 to $A_{\text{eff}} = 0.001$ m^2. The solid Earth is in rest at $t = 0$ (hydrostatic equilibrium).

VILMA requires a global bathymetry $\zeta(\Omega, t = 0)$ for initialization (Section 2.3.3). The applied bathymetry (Figure 3.7D) incorporates the RIMBAY domain

Scenario	h^{f} (m)	$\Delta V_{\mathrm{Ice}}^{\mathrm{f}}$ (km^3)	$t_{\mathrm{start}}/t_{\mathrm{end}}$ (yr)	$\dot{b}_S$ (m WE/yr)	A_{eff} (m^2)	C (Pa (m/s)$^{1/3}$)
`S120`	120	-4.8×10^7	100/1300	0.2*	10^{-3}*	1.0×10^{7}*
`S150`	150	-5.9×10^7	100/1600	0.2*	10^{-3}*	1.0×10^{7}*
`S180`	180	-7.1×10^7	100/1900	0.2*	10^{-3}*	1.0×10^{7}*
`ACCU`	0*	0*	100/600	0.1	10^{-3}*	1.0×10^{7}*
`BASL`	0*	0*	100/600	0.1	0.01	0.7×10^{7}

Table 3.7
Applied forcing scenarios: The forced equivalent sea-level rise h^{f} corresponds to the ice volume removed from the remote continent $\Delta V_{\mathrm{Ice}}^{\mathrm{f}}$ – cf. Eq. 2.79. Start and end time refer to the melting pulse from the remote continent (`S120`, `S150`, `S180`) or to the interval for linear decrease of the accumulation rate to the given value (`ACCU`, `BASL`). $\dot{b}_S$ is the model domain-wide SMB, A_{eff} is the tuning parameter for basal melting in the shelf regions (Eq. 3.3), and C is the basal friction coefficent. Asterisk-indexed values are unchanged.

continent at the equator with the y-axis of the RIMBAY domain coinciding with the meridian at $\phi = -90°(270°)$ longitude (positive y-axis points to the North Pole; positive x-axis points eastward). A remote continent (circular with radius $r_{\mathrm{cont}} = 7000$ km and altitude $\zeta_{\mathrm{cont}} = 300$ m above sea level) is equatorially centered as an antipode to this continent at $\phi = +90°$. The remaining part of the planet is deep ocean (ζ_{ocean} = -2000 m) and distance-weighted interpolations between continental altitudes and deep ocean depth in transition zones around the two continents.

Forcing

The steady-state ice-sheet/shelf configuration is forced out of its equilibrium with a) rising sea level, b) decreased accumulation rate (in terms of changing SMB), or c) decreased accumulation rate and changed conditions at the base of both the ice shelf and the grounded ice. The sea level forcing is applied by removing a uniform ice layer from the remote continent when handing the global ice thickness field from RIMBAY to VILMA: In the three scenarios `S120`, `S150`, and `S180`, the ice is removed at a constant rate of 0.1 m equivalent sea-level (ESL) per yr from the remote continent starting at $t = 100$ yr until the maximum forcing of $h^{\mathrm{f}} = 120$ m ESL, 150 m ESL, or 180 m ESL, respectively, is reached, coinciding with a respective ice volume $\Delta V_{\mathrm{Ice}}^{\mathrm{f}}$ (cf. Eq. 2.79). For the ELRA-based simulations, the rates are directly applied as sea-level rise, together with the sea-level rise from the retreating modeled ice sheet. The applied rate of global sea-level rise is approximately twice as large as the highest rates during the last deglaciation (meltwater pulse 1A: 20 m in ∼500 yr – Weaver et al. (2003)). This high value, as well as the

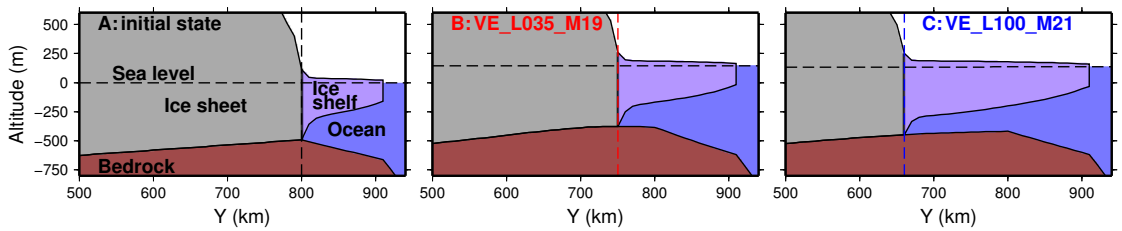

Figure 3.8
Cross sections through the ice-sheet geometry at time $t = 0$ (A) and after 8000 yr for the `VE_L035_M19` simulation (B) and the `VE_L100_M21` simulation (C) at $x = 0$ for the `S120` forcing. The GL positions correspond to the vertical dashed lines.

high amplitudes of more than 120 m ESL are due to the relatively low sensitivity of the ice-sheet model to sea-level rise (see below).

In the fourth scenario (`ACCU`), a linear decrease in the accumulation rate from 0.2 m WE/yr to 0.1 m WE/yr is realized between $t = 100$ yr and $t = 600$ yr. The fifth scenario (`BASL`) addresses the basal parameters in RIMBAY. It adopts the `ACCU` accumulation rate change together with an increased parameter A_{eff} in Eq. 3.3 (sub-shelf melting increases to values of > 0.18 m WE/yr) as well as reduced basal friction at $t = 0$. The applied forcing scenarios are summarized in Table 3.7.

3.2.2 Results

General findings

In all scenarios with a viscoelastically adjusting solid Earth, the forced GL retreat decelerates and eventually ceases. Figure 3.8 shows the initial geometry and the final geometry for the `VE_L035_M19` and `VE_L100_M21` simulations under the `S120` forcing along the cross section coinciding with the y-axis of the RIMBAY domain (Figure 3.7). Here, a first effect of the viscoelastic layering of the solid-Earth on the ice dynamics becomes visible: a more localized and faster uplift of the solid Earth (`VE_L035_M19` – B) leads to less GL retreat than a long-wave and slower response (`VE_L100_M21` – C). The backward slopes at the GL, however, at least partially remain. This is not surprising as GL retreat is treated in a three-dimensional set-up here. Consequently, GL stability is not only determined by the bedrock gradient, but also by the stress field in the ice body (Gudmundsson et al., 2012; Gudmundsson, 2013).

Figure 3.9 shows the GL retreat along the central cross section over 15 or 20 kyr, respectively, for the five applied forcing scenarios and the five VILMA parameteri-

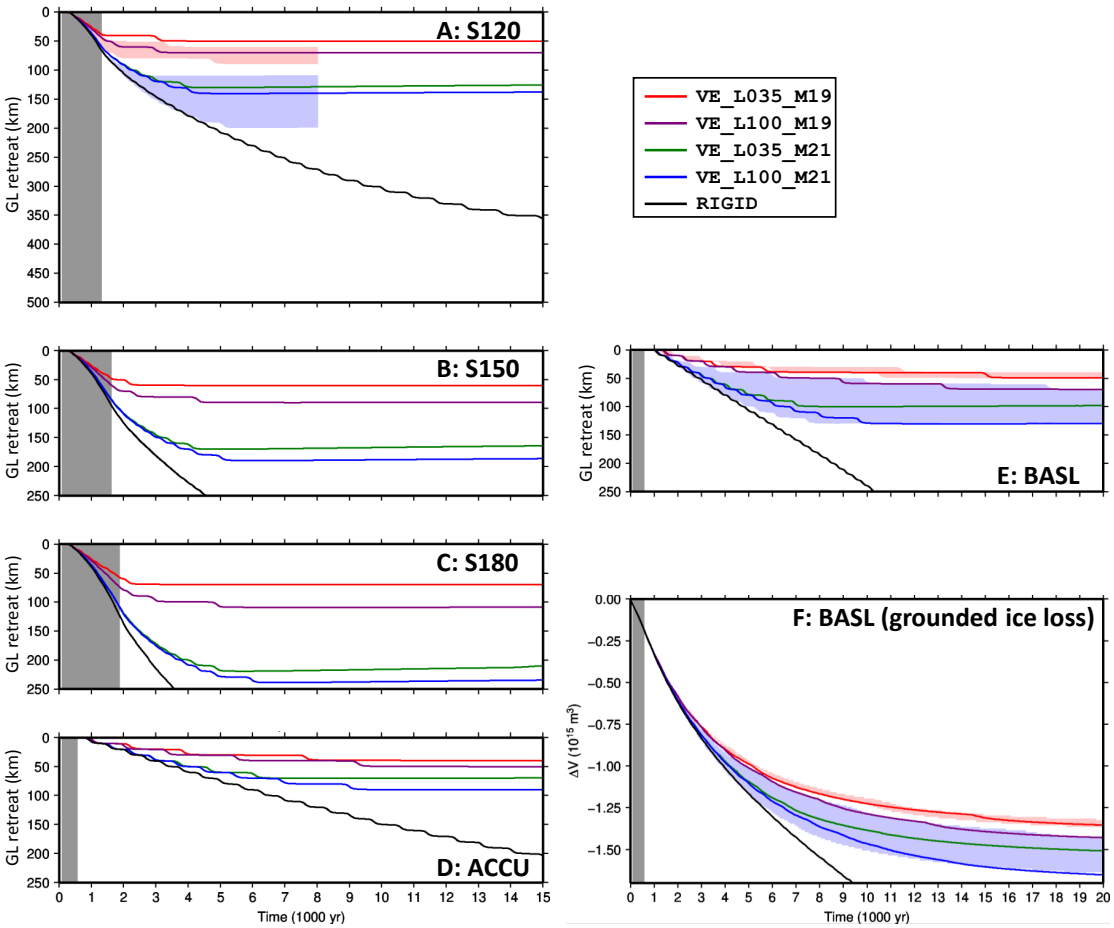

Figure 3.9
Time series of GL retreat for the `S120` (A), `S150` (B), `S180` (C), `ACCU` (D), and `BASL` (E) forcing scenarios. The GL retreat refers to the intersection of GL and the cross section at $x = 0$ (Figure 3.7). F: Loss of grounded ice volume of the modeled ice sheet. The grey areas mark the periods of gradual melting on the remote continent and thus the forced sea-level rise (`S120`, `S150`, `S180`), or the time interval of decreasing accumulation rate (`ACCU`, `BASL`). The red shaded areas in the `S120` and `BASL` frames indicate the results spanned by the applied ELRA parameters corresponding to the `VE_L035_M19` layering (Table 3.6). The blue shaded area shows the respective comparative ELRA results for the `VE_L100_M21` layering. Note that the time series in E and F show data until $t = 20$ kyr, whereas it is only 15 kyr in A–D.

Scenario	VE_L035_M19	VE_L100_M19	VE_L035_M21	VE_L100_M21
S120	50	70	130	140
S150	60	90	170	190
S180	70	110	220	240
ACCU	40	50	70	90
BASL	50	70	100	130

Table 3.8
Maximum distances covered by the GL retreat in km along the $x = 0$ cross section. As the numbers refer to the maximum retreat, they do not include the re-advance for VE_L035_M21 and VE_L100_M21 as shown in Figure 3.12 and so the numbers given here are not necessarily from the final steady-state for the M21 simulations.

zations. The stepwise GL retreat, as it can be seen in the time series of GL retreat, is a feature of the numerical approach to the GL migration. The GL – and thus the whole ice sheet – on the RIGID Earth is not yet in steady state at the end of the illustrated time spans in all five forcing scenarios. On a viscoelastically adjusting Earth, the GL retreat has stopped before $t = 7$ kyr (S120, S150, S180), or $t = 10$ kyr (ACCU) and $t = 15$ kyr (BASL). The exact number depends on the viscoelastic layering and the forcing strength. At this stage, only maximum GL retreat during each experiment is discussed, which does not necessarily mean that the ice sheet is in a steady state again. Below, the possibility of GL re-advance after reaching the maximum GL retreat distance, leading to a final position which is again closer to the initial position, will be discussed.

There are notable systematic differences between the viscoelastic settings: The fast adjusting, low-viscous upper mantle makes the VE_L035_M19 and VE_L100_M19 simulations less sensitive in terms of final GL position along the y-axis to the GL retreat forcing than the VE_L035_M21 and VE_L100_M21 runs with the high-viscous upper mantle, i.e. the time to regain a stable state is shorter. Additionally, in both of these subgroups, the thinner lithosphere (L035) leads to less GL response to the forcing. The maximum retreat distances along the cross section are listed in Table 3.8. It is also visible that simulations with a low-viscous upper mantle are less sensitive to an increase in forcing: the maximum retreat positions under the S120 and S180 forcings differ only by 20/40 km, while the higher upper mantle viscosity leads to respective differences of 90/100 km.

Comparison with ELRA under the S120 forcing

Figure 3.9A shows the results of the ELRA simulations under the S120 forcing with different choices for the flexural rigidity D and the relaxation time τ_r. Overall, the

ELRA simulations are similar to those with the real viscoelastic coupling in terms of the effect on the GL retreat: The faster and more local the solid Earth can adjust to the unloading by a GL retreat, the less sensitive the ice sheet responds to the forcing.

Here, however, the ELRA approach reveals shortcomings by a considerably higher sensitivity to the applied forcing: While the `VE_L100_M21` results are included by the respective ELRA results and thus consistency in terms of GL retreat and ice volume loss is given, the comparison of `VE_L035_M19` to the respective ELRA results indicates that the ice sheet with solid-Earth response by ELRA is more sensitive to the forcing even in the case of extremely low values for the relaxation time τ_r and flexural rigidity D. The ELRA results in this parameter range seem more appropriate for the `VE_L100_M19` with its thicker lithosphere than for the `VE_L035_M19` case. This is due to the higher sea level in the ELRA runs as a consequence of only accounting for eustatic sea-level rise (cf. Gomez et al., 2013).

This higher sensitivity to sea-level rise in the ELRA approach can be found more indirectly in the comparison of the 'well-fitted' `VE_L100_M21` results with those from ELRA: Figure 3.10 shows the RSL at the GL as it retreats for `VE_L100_M21` and two respective ELRA simulations. The time markers along the graphs show that the RSL falls faster in the ELRA simulations in general and so should provide earlier stability. The coverage of the `VE_L100_M21` results by the ELRA in the case of the `S120` forcing results must then be due to the overestimation of sea-level rise.

Comparison with ELRA under the `BASL` forcing

In the scenarios without externally forced sea-level rise, the `BASL` scenario shall be evaluated exemplarily in terms of ELRA and VILMA differences. The main difference to the sea-level forced scenarios is that the forcing does not only affect the ice sheet directly at the GL, but that the whole ice sheet shrinks and, due to the changes in the basal parameters, changes its geometry. The ice flow is accelerated by the decrease in basal friction, such that more ice is transported towards the margins. The overall unloading of the continent due to the shrinkage (volume time series in Figure 3.9F) leads to considerable uplift that stabilizes the GL to some extent even before it starts to retreat.

The `VE_L035_M19` und the respective ELRA simulations (red shading) are consistent in this scenario (Figure 3.9E) in terms of the inclusion of the `VE_L035_M19` results by the ELRA results. Due to the small increase in sea level from melting of the ice sheet, which results in less than 4 m eustatic sea-level rise for the ELRA runs No 1–4 (see Table 3.6 for the numbering), the above drawback concerning

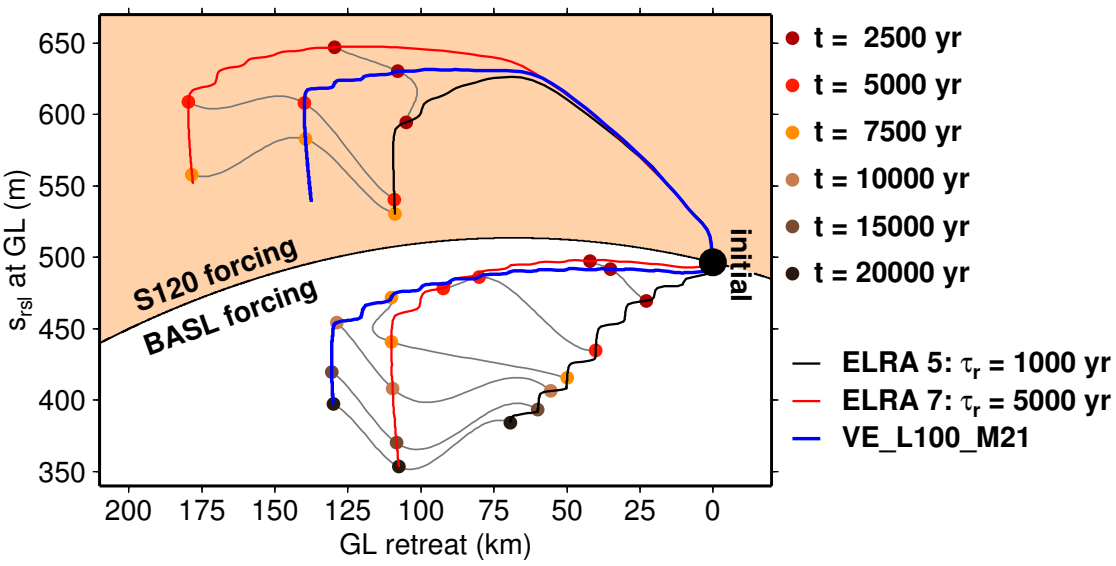

Figure 3.10
Relation between Δs_{rsl} at the GL and GL position along the central cross section in the `S120` (orange background) and `BASL` (white background) forcing scenarios for the `VE_L100_M21` Earth and two of the corresponding ELRA parameterizations (No. 5 and 7; cf. Table 3.6). All simulations start from the same initial state; consequently, all graphs are to be read from the black marker at approximately (0 km, 500 m). At given times (color-coded dots), the ELRA and VILMA graphs are connected by grey lines.

non-consistent sea-level rise is of minor importance.

The same comparison for the `VE_L100_M21` simulation and the respective ELRA runs (No 5–8), however, shows a clear preference towards $\tau_{\mathrm{r}} = 5000$ yr: While $\tau_{\mathrm{r}} = 1000$ yr to 5000 yr reproduce the `VE_L100_M21` results under the `S120` forcing, different τ_{r} parameters need to be chosen to encompass the combination of `VE_L100_M21` layering and `BASL` forcing. As for the `S120` forcing, the respective graphs in Figure 3.10 show a faster RSL fall at the GL in the ELRA simulations. In the `BASL` scenario, this relatively fast Earth response is not compensated by an overestimated sea-level rise as in `S120` so that the slower relaxation of the solid Earth effectively yields more GL retreat for the `VE_L100_M21` simulation.

Relation between ice dynamical and solid-Earth time scales

A feature of the simulations with a low-viscous upper mantle is the significantly increasing time span between two discrete GL steps in the model. These are partially of the order of several thousand years in the presented scenarios, whereas the high-viscous upper mantle runs feature a smooth and modest increase of the time intervals before the next GL step. As already mentioned above, the stepwise character is a numerical feature, but the long time spans in the case of low upper

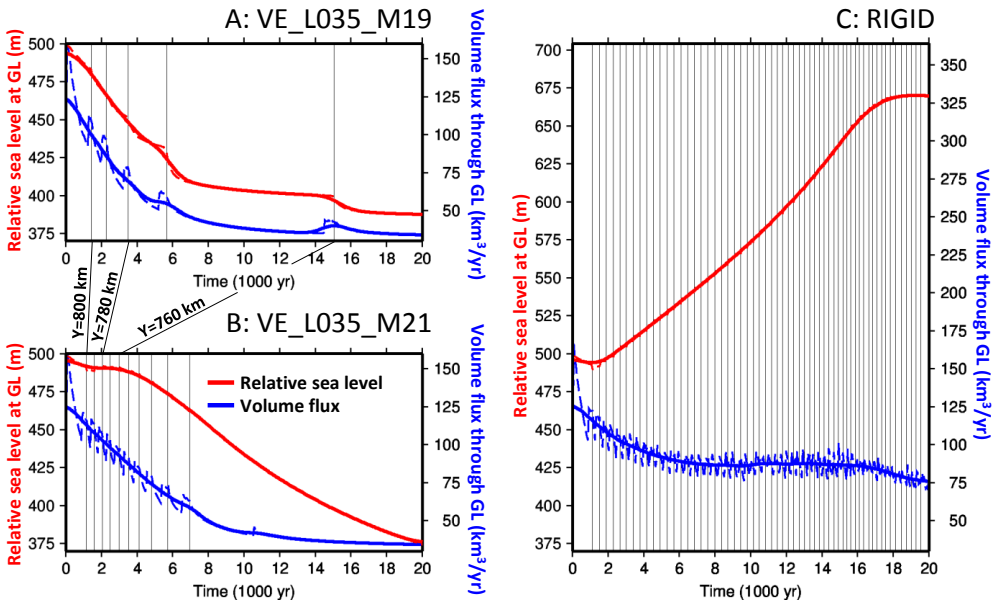

Figure 3.11
Time series of RSL at the GL (red; left ordinate) and GL flux (blue; right ordinate) for the `BASL` scenario on the `VE_L035_M19` Earth (A), on the `VE_L035_M21` Earth (B) and on the `RIGID` Earth (C). Each black vertical line indicates when the GL passes one of the y-grid nodes at $x = 0$. The GL flux is the integrated flux from the inland ice into the ice-shelf area. The GL retreat is w.r.t. the central cross section ($x = 0$). The dashed lines show the originally modeled data; the solid thick lines are obtained from these by running mean application and, hence, are less disturbed by numerical effects of the discrete GL retreat.

mantle viscosity still contains a physical message, as will be discussed here.

The `BASL` scenario serves as a prominent example for comparing the time scales of solid-Earth relaxation and ice-flow adjustment to the changed conditions for the thin lithosphere runs `VE_L035_M19` and `VE_L035_M21` and for the `RIGID` Earth. Figure 3.11 shows the time series of RSL at the GL (again along the central cross section) and GL flux integrated along the whole GL confining the ice shelf for these three runs. In order to not focus on numerical aspects of GL migration, the smoothened time series (solid, thick lines; obtained as running mean) are considered. Three issues concerning the phenomena shown in Figure 3.11 can be highlighted:

1. There is a GIA-induced fall of RSL at the GL in the viscoelastic runs: Following the GL retreat, there is unloading around the GL and thus bedrock uplift and sea-level fall. This is not the case for the `RIGID` Earth, where a steady increase of RSL occurs due to the backward sloping design of the bedrock geometry until flatter areas are reached ($t \approx 16$ kyr).

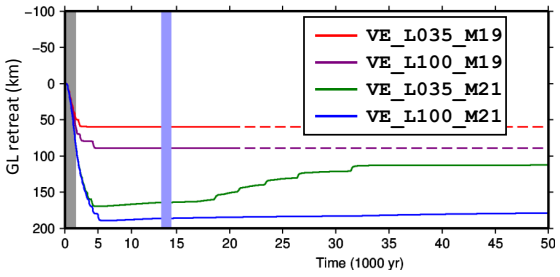

Figure 3.12
Time series of GL retreat along the central cross section for the `S150` scenario for 50 kyr (Figure 3.9B: 15 kyr). The blue shading marks the break between the two time axis parts with different scales. The dashed parts in the `VE_L035_M19` and `VE_L100_M19` time series are extrapolated.

2. The time intervals between two GL steps are equal over the whole time span for the `RIGID` run (distance between neighbouring vertical black lines), indicating an almost constant GL retreat velocity of $\sim$ 25 m/yr. In the viscoelastic runs, these time intervals get larger due to the partial adjustment to the unloading. This transition to longer time intervals is a very modest and smooth one in the `VE_L035_M21` run, whereas the time to cover the last 10 km distance in the `VE_L035_M19` run is longer than 9 kyr.
3. The integrated GL flux is much higher in the `RIGID` simulation as a constantly high amount of ice is transported from the inland to the shelf. In the case of a viscoelastically adjusting Earth, the GL flux decreases as the ice dynamics approaches a steady state. After the GL retreat is decelatered such that there is no more GL migration on grid scale, the GL flux decays towards the limit of $\sim$34 km^3/yr. In the case of the `VE_L035_M21` layering, the respective time scale is much smaller than the one of RSL relaxation (high-viscous upper mantle). In the case of the `VE_L035_M19` layering, the respective time scales appear to be of similar magnitude.

The slow adjustment of RSL in the case of a high-viscous upper mantle has further implications on the GL migration. Figure 3.12 shows time series of GL retreat along the central cross section for the `S150` scenario extending the time span shown in Figure 3.9B. Here, a gradual GL re-advance of the GL on the `VE_L035_M21` Earth starts after the maximum distance is reached at $t \approx 5$ kyr. After approximately 19 kyr, the GL re-advance reaches the grid scale and ends up at a final distance of 113 km away from the initial position and 57 km from the maximum retreat position. This prominent re-advance is, however, a feature of the deformational response of the thin lithosphere: a comparable evolution cannot be found for the `VE_L100_M21` simulation before $t = 50$ kyr although a sub-grid scale re-advance occurs.

3.2.3 Discussion

The general finding, that viscoelastic deformation can decelerate and stop GL retreat, is in accordance with Gomez et al. (2012). The actual evolution through

time depends on the solid-Earth parameters, namely thickness of lithosphere and mantle viscosity. The first one determines how localized the solid Earth responds to the unloading caused by an ice mass loss. As a more localized response leads to a more effective compensation of the former backward slopes, GL stability is reached at sites closer to the initial GL location. Mantle viscosity, in contrast, affects the time scale on which the solid Earth reacts to the change in the loading: the fast response of a low-viscous upper mantle also leads to GL stability at closer sites than the slower response of a high-viscous mantle and so to less GL retreat and ice mass loss.

In this scenario, the mantle viscosity and the related time scales of solid-Earth response have the dominant impact on maximum GL retreat (Table 3.8) compared to lithosphere thickness. One should, however, state that the grounded ice flow is rather slow in this scenario compared to present-day Antarctic ice streams, that feed the surrounding shelf areas (e.g. $\sim$500 m/yr in the catchment area of the Ross Ice Shelf (Thomas et al., 2013) vs. less than 150 m/yr here). Compared to that, the ice flow in this scenario is potentially less controlled by the underlying bedrock topography.

The initial magnitude of the backward slope also affects the time to reach stability. An ice sheet on a slope of different steepness might then also be more sensitive to lithospheric thickness as it is the case in this scenario. The possibility of GL re-advance yields a greater importance for the lithosphere thickness in later parts of the system's evolution in time.

The common method to account for a coupling between ice and solid-Earth dynamics, the ELRA method, shows similar behaviour as the RIMBAY/VILMA simulations, but has a major drawback when it comes to sea-level implications. The SLE is not solved within the ELRA approach. The one possible way of accounting for sea-level rise or fall on glacial-interglacial time scales is to account for eustatic sea level only. By that, the local sea level is overestimated (due to neglecting the reduced gravitational attraction following the ice mass loss), and by that also the ice sheet's response to sea-level change is amplified. The overestimated sea level could potentially be compensated by an adequate choice of ELRA parameters (faster and more localized adjustment). The physical meaning of τ_r and D, however, would suffer even more from that. The adjustment of the ELRA parameters and the assessment against SGVEM simulations is an important issue even without the requirement of modeling ice-sheet/sea-level interactions (van den Berg et al., 2008; Konrad et al., 2014). The comparison of results from the `VE_L035_M19` and `VE_L100_M21` simulations to results from respective ELRA simulations shows

that the *a priori* relaxation times in ELRA have to be chosen shorter than the related relaxation spectrum of a SGVEM in order to adequately model GL retreat in a sea-level rise scenario in general.

The relation between the time scales of solid-Earth relaxation and ice-flow adjustment is also very important for the retreat characteristics and potential re-advance of the GL. A slowly adjusting solid Earth stabilizes the disintegrating ice sheet gradually (`VE_L035_M21` graphs in Figure 3.11). Depending on the GL retreat velocity and on the delay of the solid-Earth response, the GL can even overshoot the later steady-state position and – after stopping further down-slope – re-advance when the delayed fall of RSL creates the necessary conditions (Figure 3.12). This, however, also depends on the lithosphere thickness: The thick lithosphere in the `VE_L100_M21` simulation and the related long-wavelength pattern of RSL fall prevent the GL from re-advancing.

A fast adjusting solid Earth interacts with the ice sheet in a more complex way. Depending on the ice-rheological parameters and the stress field in the ice, it takes the ice dynamics a certain time to adjust to new boundary conditions. In the case shown in Figure 3.11, these new conditions comprise the new SMB and the changed basal conditions (`BASL`), as well as the constantly adjusting ice-sheet geometry due to GL retreat. If the Earth beneath the ice sheet adjusts faster than or with similar time scales as the ice flow adjusts to the new conditions, the approach towards the final steady state becomes very slow. This manifests numerically in the long time spans between to grid-scale GL retreat events.

A general feature of the presented results is the insensitivity to the applied forcing: The GL covers 240 km at most – under the most unrealistic condition of a 180 m rise of global mean sea level within less than 2000 yr (Table 3.8). Although this might be attributed to the specific set-up, it points at the inert representation of the GL, if this is not treated beyond the application of the SIA on the one and SSA on the other side of the GL and the floating criterion to seperate these two areas (cf. Section 2.2.4). This drawback hinders clearer conclusions w.r.t. the relation of time scales of the ice and the Earth.

3.3 Conclusions

3.3.1 The applicability of ELRA

In accordance with a previous study (Le Meur and Huybrechts, 1996), it has been found in Section 3.1 that the feedback of ice sheets with the solid Earth via the

SMB and the surface elevation of the ice sheet (Section 1.1.1) can be reasonably approximated by the ELRA approach. Still, an optimal fit to the ice-dynamical results from a fully coupled simulation (here: RIMBAY/VILMA) needs a revision of the ELRA parameters as their physical meaning is compromised by the simplicity of the ELRA assumptions w.r.t. the lithospheric and mantle dynamics. Even in the cases of small deviations between ELRA and VILMA in terms of the ice dynamical response, the application of VILMA has the strong advantage that the quality of the solid-Earth response and the related feedbacks only depends on the quality of the applied viscoelastic Earth parameters. Also, a global consideration of glacial dynamics can be performed gravitationally consistently with the ice-sheet model coupled to VILMA.

The complex flexural behaviour of the lithosphere, as well as the mantle relaxation can be approximated by ELRA only in a rather crude way: Considerable systematic differences between VILMA and the ELRA model exist in the peripheral region of the ice sheet, and so it can be concluded that a fully coupled system may improve the interpretation of observations such as sea-level indicators or GPS data w.r.t. ELRA.

The simplified Earth dynamics of the ELRA approach yield an essential conceptual drawback when it comes to the feedback of ice sheets with the solid Earth via the GL positioning and sea level (Section 3.2). Firstly, ELRA does not allow treating sea level gravitationally consistently, which leads to a possible overestimation of the related effects. Secondly, the dependence of the relaxation time on the load dimension and the viscoelastic stratification can be of great importance, when it comes to GL migration in a MISI scenario; the usage of a single *a priori* relaxation time in ELRA, despite the wavelength-dependent relaxation spectrum associated with a more realistic Earth model description, introduces a bias in the evolution of the grounded ice, particularly if the ELRA parameters are not carefully tuned. Already in the simplified ice-sheet/shelf set-up in Section 3.2, it is difficult to define ELRA parameters, such that the effects from overestimated local RSL, inaccurate surface deformation and mantle relaxation are minimized. The problem becomes even more important for the simulation of an ice-sheet history (e.g. Antarctica, see Chapter 5) through glacial cycles, as the ice sheet's response is sensitive to both sea-level variations and atmospheric condititions.

To avoid these drawbacks, a coupled model system such as RIMBAY/VILMA or that by Gomez et al. (2012, 2013) or de Boer et al. (2014) should be used, as it self-consistently accounts for sea-level variations and surface deformations.

3.3.2 The studied feedbacks and the model system

The three feedbacks introduced in Section 1.1 have been treated to different extent in idealized model situations. In these simplified situations, the differences in the Earth representation – be it due to application of different approaches (ELRA vs. VILMA) or due to different choices for the viscoelastic parameters – lead to larger or more systematic differences in the ice dynamical evolution when the feedback between the ice and the Earth via RSL and GL dynamics is involved. In particular, the fast adjustment of an Earth with low mantle viscosities, as well as the high amplitudes of deformation of a relatively thin lithosphere yield a stronger negative feedback on GL migration than higher mantle viscosities and thicker lithospheric layers. Consequently, the remaining chapters will focus on this feedback and respective regions of the Antarctic Ice Sheet (AIS) where extensive GL motion can be expected: The future of the West Antarctic Ice Sheet (WAIS) as a part of the ice sheet that is vulnerable due to the MISI is investigated in Chapter 4. Chapter 5 presents results on modeling the last glacial cycle with its important transitions from floating to grounded ice and back again in today's ice shelves.

During the work on this thesis, it has been recognized that RIMBAY's rather insensitive GL dynamics also applies when modeling the AIS in a warmer (future) environment or through the last glacial cycle. It was identified, that this is likely caused by the inaccurate representation of the real stress state in the vicinity of the GL by SIA and SSA as pointed by Pattyn et al. (2012, 2013). The improved GL dynamics developed by Pollard and DeConto (2012b) based on the work of Schoof (2007) (Section 2.2.4) yield the possibility to achieve a more appropriate representation of the relation between GL motion and solid-Earth relaxation. With the kind provision of the respective numerical model by David Pollard, an advance towards realistic simulations of the AIS could be undertaken within the framework of this project, presented in Chapters 4 and 5.

4 The West Antarctic Ice Sheet in a warming climate

– Possible stabilization by a rapid solid-Earth response

4.1 The West Antarctic Ice Sheet: A glaciologically and tectonically sensitive region

The West Antarctic Ice Sheet (WAIS) is in large parts grounded below sea level on an inward deepening bedrock (e.g. Fretwell et al., 2013). This setting (Figure 4.1E) makes it susceptible to the Marine Ice Sheet Instability (MISI) mechanism (Section 1.1.3). Geological observations give rise to the assumption of a much smaller WAIS in past interglacials (Mercer, 1968; Scherer et al., 1998). The question of future instability and the related global sea-level contribution of the WAIS has been adressed e.g. by Oppenheimer (1998), Conway et al. (1999), Joughin and Alley (2011), or by Nowicki et al. (2013) and Bindschadler et al. (2013) within the scope of the SeaRISE experiments (although the latter two are not solely focussed on the WAIS). While the forcing in some of the applied scenarios in Nowicki et al. (2013) is strong enough to let the WAIS collapse within the next 500 years, Bindschadler et al. (2013) find that forcing the Antarctic Ice Sheet (AIS) with a combination of oceanic and atmospheric warming and enhanced basal sliding in accordance with IPCC AR5 scenarios (Stocker et al., 2013) does not lead to a collapse of the WAIS within the considered 500 years.

There have been many recent studies addressing the current extent of mass loss in the Amundsen Sea embayment (King et al., 2012; Sasgen et al., 2013; Rignot et al., 2014; Mouginot et al., 2014; Joughin et al., 2014b; Sutterley et al., 2014) which find the WAIS has exhibited a strong loss of ice mass along the Amundsen Sea coast in the past years to decades. Geologically based studies show evidence of ice loss in this area through earlier stages of the holocene (Johnson et al., 2014; Hillenbrand et al., 2013). Favier et al. (2014) find that Pine Island Glacier in the Amundsen Sea embayment retreats mainly due to the MISI and will continue to do so at least in the next decades.

All respective studies on the future WAIS instability that considered numerical modeling of the ice dynamics have been performed with simple representations of

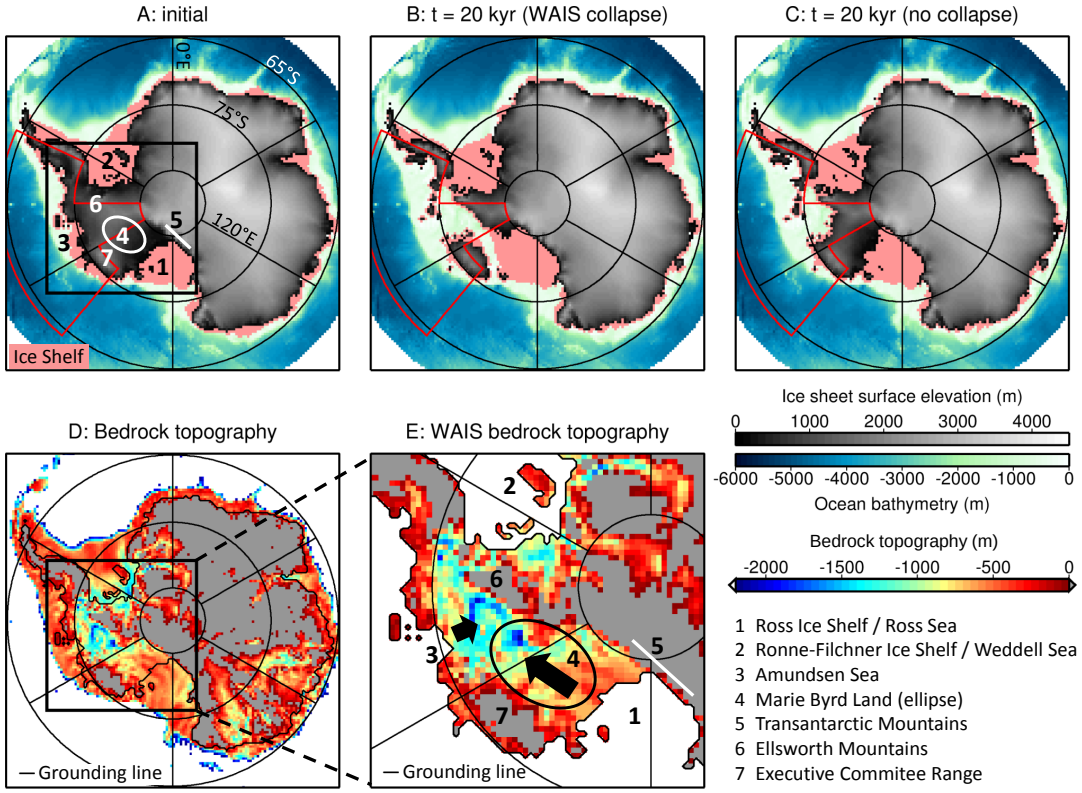

Figure 4.1
A: Antarctic Ice Sheet surface elevation after 200 kyr of initialization (corresponding to present-day observations – cf. Appendix D, Figure D.2). Ice shelves are indicated in light red; the bathymetry of the surrounding ocean is also colorcoded. B: AIS geometry after 20 kyr in the case of the WAIS collapse (medium forcing on the $h_{\mathrm{L}} = 60$ km / $\eta_{\mathrm{A}} = 3{\times}10^{19}$ Pa s Earth; see Section 4.3.1 for details). C: The same as B but for a parameter choice of the simulation leading to no WAIS collapse ($h_{\mathrm{L}} = 60$ km / $\eta_{\mathrm{A}} = 1{\times}10^{19}$ Pa s). Note the breakthrough from the Amundsen Sea to the Ross Ice Shelf in B. D: Present-day bathymetry (BEDMAP2 by Fretwell et al., 2013). Bedrock above sea level is indicated in grey. E: Zoom to the WAIS as indicated by the black squares in the A and D. Here, the bathymetry is only shown where the ice is grounded. The two black arrows indicate the main regions where the MISI can be expected in a future retreat of the WAIS: The bedrock deepens from the Amundsen Sea Coast and from the Ross Ice Shelf towards Marie Byrd Land. The red line in A, B, and C includes the Amundsen Sea Sector to which the oceanic forcing is applied.

the solid Earth response such as ELRA to changes in the ice load (e.g. Appendix in Bindschadler et al., 2013). On the basis of the mechanism explained in Section 1.1.3, recent studies, however, have proven the importance of the bedrock and local sea-level response to the migrating GL when the stability of a marine-based ice sheet is concerned (Gomez et al., 2010, 2012, Section 3.2 in this thesis).

The tectonic structure of Antarctica and the West Antarctic rift system in particular have been investigated in the past by seismic tomography and other geophysical methods. The East Antarctic Ice Sheet rests on a continental cratonic lithosphere and mantle (Morelli and Danesi, 2004), whereas the WAIS is situated on a rifted system with possibly much lower values of elastic lithosphere thickness and asthenosphere viscosity (Behrendt, 1999; Groh et al., 2012; Accardo et al., 2014) and associated high geothermal heat flux and subglacial volcanism, specifically in the Amundsen Sea Embayment and Marie Byrd Land (Schroeder et al., 2014; Lough et al., 2013). A relatively soft asthenosphere and thin lithosphere in the West Antarctic rift system should allow for a faster response of the solid Earth to a change in surface load. By this, the tectonical setting in West Antarctica bears the potential to play a crucial role in the future evolution of the WAIS. Based on the work of Gomez et al. (2012) and Section 3.2 of this thesis, the hypothesis of this study is that considering a correspondingly soft solid-Earth rheology may increase the stability of the WAIS and delay its potential future collapse in a warming climate.

In the context of this study, the collapse of the WAIS will be defined as the occurence of an open-ocean or ice-shelf connection from the Amundsen Sea Sector to the Ross Sea and to the Weddell Sea as it is shown in Figure 4.1B. Remaining parts of the WAIS are mainly grounded above sea level, as e.g. around the Ellsworth Mountains and the Executive Commitee Range (Figure 4.1E).

4.2 Outline of the experiments

To check the hypothesis of the solid-Earth relaxation stabilizing the WAIS, the following perturbation experiment are performed. The AIS is run to a steady state w.r.t. the present-day SMB, as well as oceanic and geothermal heat fluxes. The ice dynamics of the modern AIS are clearly not in a steady state as the ice sheet is losing mass at rates of ∼70–114 Gt/yr (King et al., 2012; Shepherd et al., 2012; Sasgen et al., 2013; Gunter et al., 2014). The steady state under present-day conditions is considered a reasonable approximation as common approaches to obtain a non-equilibrium initial state representative for present-day would require simulations through one or more glacial cycles (as e.g. summarized in Table 2 by

Bindschadler et al., 2013), which would be computationally costly and imply different initial conditions for each Earth stucture.

The solid Earth is assumed to be in rest (hydrostatic equilibrium); this is justified as the AIS would otherwise respond to adjustments in the solid Earth, contradicting the assumption of steady-state ice dynamics. In the case of the solid Earth, this assumption is valid: For example, Adhikari et al. (2014) find that the post-glacial rebound due to the unloading following the Last Glacial Maximum at ~ 20 kyr before present is outweighed by the response to expected future changes already after 100 yr from present-day.

Perturbations from this equilibrium are then simulated by prescribing higher air and ocean temperatures in and around Antarctica. The resulting loss of grounded ice is accompanied by the delayed solid-Earth response. In a final experiment, the additional impact of melt water from the Greenland Ice Sheet (GrIS) and the glaciers beyond Antarctica and Greenland on the WAIS stability is evaluated.

4.2.1 Set-up of AIS dynamics

Present-day AIS representation and forcing

For this and the following investigations, the PennState3d–VILMA coupled model is employed. The ice-sheet model's horizontal resolution in the presented experiments is 40 km. The simulations are started from present-day conditions: Initial bedrock and ice thickness from the BEDMAP2 data set (Fretwell et al., 2013), initial surface mass balance by van de Berg et al. (2006), and surface temperatures by Comiso (2000) are applied. Liquid water due to melting or rainfall on the surface of the AIS occurs only in limited coastal regions (Kuipers Munneke et al., 2012). Therefore, the SMB is sufficiently described by the surface accumulation field.

As argued by Pollard and DeConto (2012b), geothermal heat flux is prescribed in a simple pattern with colder East Antarctica and warmer West Antarctica, rather than more detailed data sets by Shapiro and Ritzwoller (2004) or Fox Maule et al. (2005), which differ significantly from each other. Basal friction conditions in terms of the basal friction coefficent (cf. Eq. 2.21) are applied as they have been inverted from present-day surface velocities (Pollard and DeConto, 2012a). The input data which have been listed here are illustrated in Appendix D.1.

Following Martin et al. (2011), the melting of ice under the ice shelves $\dot{b}_B^{\text{shelf}}$ is

parameterized as

$$\dot{b}_B^{\text{shelf}} = \frac{K_{\text{B}} K_T \rho_{\text{oc}} c_{\text{oc}}}{\rho L_{\text{Ice}}} \left| T_{\text{oc}} - T_{\text{fp}} \right| \left(T_{\text{oc}} - T_{\text{fp}} \right) \quad . \tag{4.1}$$

Here, T_{oc} is the ocean temperature and K_{B} is a basin-dependent scaling factor. The freezing point T_{fp} at the lower surface of the ice shelf is again given by Eq. 3.4. The transfer factor is $K_T = 15.77$ m/yr/K. The distributions of T_{oc} and K_{B} are described in Pollard and DeConto (2012b).

Ice-berg calving as an ice-loss mechanism at the vertical ice–ocean interface is parameterized on the basis of upstream ice thickness and the divergence of the horizontal velocities. Another such mechanism is the melting of ice below sea level along the vertical ice–ocean interface. The treatment follows the description for melting below the ice shelves in Eq. 4.1 and is scaled as a surface process by the respective ice column below sea level and the respective grid cell area.

Changing climatic conditions for the AIS

During the simulations, the boundary conditions change as the ice thickness evolves. This concerns for example basal sliding, whereever a change from floating to grounded ice or vice versa (GL migration) can be observed. Smoother transitions are expected for changing sub-shelf melting rates in the case of a thickening or thinning ice shelf given by Eqs. 3.4 and 4.1, as well as by a climate-related change of the ocean temperature ΔT_{oc}. The latter is either zero (during initialization) or, in the following experiment, given by a constant positive offset representing a warmer ocean with respect to the initial conditions.

The upper surface conditions are also subject to change in the case of a changing ice thickness and a changing climate. The surface temperature is computed as

$$T_S = T_S^{\text{PD}} - \gamma \left(S - S^{\text{PD}} \right) + \Delta T_{\text{at}} \tag{4.2}$$

where T_S^{PD} and S^{PD} are observations of present-day surface temperature (from Comiso, 2000) and surface elevation (from Fretwell et al., 2013). The consideration of the lapse rate $\gamma = 0.008°\text{C/m}$ models the decrease of temperature with increasing surface elevation in the atmosphere. As for external ocean temperature changes, the external atmospheric temperature change ΔT_{at} is zero for AIS initialization and positive and constant for the simulation of a warming climate. Eq. 4.2 is applied as boundary condition for the temperature field, but also used

to update the SMB:

$$\dot{b}_S = \dot{b}_S^{\mathrm{PD}} \times 2^{\left(T_S - T_S^{\mathrm{PD}}\right)/10°\mathrm{C}} \ , \tag{4.3}$$

which models the feedback between SMB and bedrock deformation (Section 1.1.1). Additional changes of $\dot{b}_S$ arise from meltwater percolation and run-off at warmer sites. It is modeled by a so-called Positive-Degree-Day (PDD) scheme (e.g. Huybrechts and Oerlemans, 1990).

Initialized AIS

The differences between present-day ice thickness and GL and the final steady-state AIS after 200 kyr of initialization are rather small (Appendix D, Figures D.2 and D.3). Hence, it is assumed that the steady state is a reasonable representation of the present-day AIS. During the initialization, all feedbacks with the solid Earth and gravity are neglected, meaning that neither bedrock deformation nor sea-level variations are allowed.

4.2.2 Solid-Earth set-up

In this study, a radially-symmetric 4-layer solid Earth is assumed, consisting of a lower mantle (viscosity $\eta_{\mathrm{LM}} = 2{\times}10^{22}$ Pa s), an upper mantle ($\eta_{\mathrm{UM}} = 5{\times}10^{20}$ Pa s), a 200 km asthenospheric layer with the potential for low viscosity values between $\eta_{\mathrm{A}} = 1{\times}10^{19}$ Pa s and $5{\times}10^{20}$ Pa s, and an elastic lithosphere with practically infinite viscosity and thickness h_{L} varying between 40 km and 120 km (summarized in Figure 4.2). The values for upper and lower mantle viscosity are consistent with Klemann et al. (2008) and Klemann and Martinec (2011) and lie between the values which were found optimal to explain geological or space-geodetic data all over Antarctica as reported by Whitehouse et al. (2012b) and Ivins et al. (2013). The highest values for asthenosphere viscosity of $\eta_{\mathrm{A}} = 5{\times}10^{20}$ Pa s – reducing the Earth structure to three layers without low viscosities in the asthenosphere – and lithospheric thickness of $h_{\mathrm{L}} = 120$ km are chosen to roughly represent the cratonic setting of East Antarctica. The eight combinations of

$$\begin{aligned} \eta_{\mathrm{A}}(\text{Pa s}) &\in \{1 \times 10^{19},\ 3 \times 10^{19},\ 1 \times 10^{20},\ 3 \times 10^{20}\} \text{ and} \\ h_{\mathrm{L}}(\text{km}) &\in \{40,\ 60,\ 80\} \ , \end{aligned} \tag{4.4}$$

which are given in Figure 4.2, are meant to represent the rifted system of West Antarctica. The lower bound for the asthenosperic viscosity ($1{\times}10^{19}$ Pa s) equals the upper bound for other rifts as investigated by Schotman and Vermeersen (2005); hence, the associated short time scales of solid-Earth relaxation are probably not underestimated drastically, if at all. It is also in accordance with Kaufmann

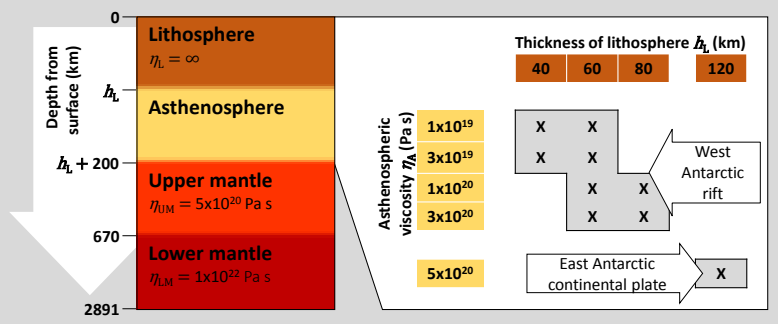

Figure 4.2
Applied one-dimensional viscoelastic settings: The West Antarctic rift system is modeled by relatively low values for the thickness of the lithosphere between 40 km and 80 km and for the viscosity in the asthenosphere between 1×10^{19} Pa s and 3×10^{20} Pa s. The East Antarctic continental plate is exemplarily modeled by a 120 km lithosphere and 5×10^{20} Pa s viscosity for both asthenosphere and the upper mantle. The considered combinations are marked by a cross in the matrix.

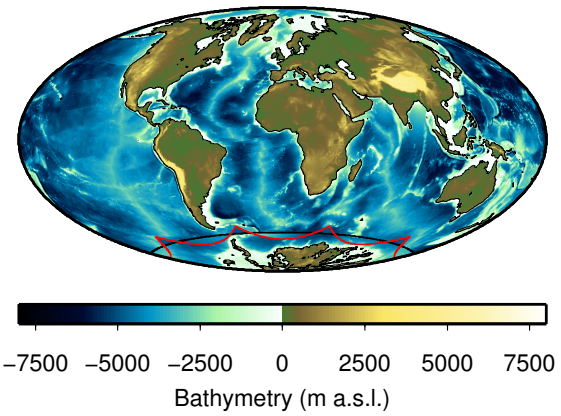

Figure 4.3
Global present-day bathymetry according to the ETOPO1 data set (Amante and Eakins, 2009) north of the thick black line and the re-gridded BEDMAP2 data set (Fretwell et al., 2013) south of it. The red line includes the model domain of the ice-sheet model.

et al. (2005), who apply a viscosity gradient in the upper mantle (100 km to 450 km depth) from 1×10^{21} Pa s along the Transantarctic Mountains to $\sim3\times10^{18}$ along the Amundsen Sea coast based on seismic tomography, and with van der Wal et al. (2015), who find values for the viscosity in the asthenosphere between 1×10^{18} Pa s and $\sim1\times10^{21}$ Pa s for West Antarctica. The upper bound (3×10^{20} Pa s) yields a transition to a three-layered Earth with $\eta_{\mathrm{A}} = \eta_{\mathrm{UM}} = 5 \times 10^{20}$ Pa s.

Global bathymetry initialization

An initial global bathymetry $\zeta_0(\Omega)$ (Section 2.3.2) has to be provided to the SLE solver in VILMA. The commonly applied ETOPO1 bathymetry (Amante and Eakins, 2009) is considered here. The Antarctic region is substituted by the

BEDMAP2 data set (Fretwell et al., 2013) after it has been regridded to the SLE solver's Gauss-Legendre grid as explained in Section 2.4.1. The respective present-day bathymetry is shown in Figure 4.3.

4.2.3 Perturbations of the steady state

Atmospheric and oceanic perturbation

The applied forcing consists of instantaneous atmospheric and oceanic warming by ΔT_{at} and ΔT_{oc}, respectively, at present day ($t = 0$). Via Eqs. 4.3 and 4.1 and the PDD scheme, this leads to higher rates of snow precipitation and melt water run-off on the ice-sheet surface (ΔT_{at}) and higher rates of ice-shelf melting at the ice–ocean interface.

The ocean temperature increase ΔT_{oc} is applied to the Amundsen Sea Sector only, where the WAIS is most vulnerable due to the upwelling of warm circumpolar deep water (e.g. Thomas et al., 2004; Thoma et al., 2008; Jacobs et al., 2011), and where oceanic warming in the present and in the future is also most likely (Bindschadler et al., 2013). The definition of the Amundsen Sea Sector in terms of geographical coordinates (cf. Figure 4.1) follows Pollard and DeConto (2012b). An equal warming in the strongly protected oceanic caverns under the large Ross Ice Shelf and Ronne-Filchner Ice Shelf are unrealistic (Bindschadler et al., 2013), although particularly the temperature of ocean water below the Ronne-Filchner Ice Shelf may also increase in the future (Hellmer et al., 2012).

Three different forcing scenarios are considered: A weak forcing with $\Delta T_{\mathrm{oc}} = 1.2°\mathrm{C}/\Delta T_{\mathrm{at}} = 2.4°\mathrm{C}$, a medium forcing with $\Delta T_{\mathrm{oc}} = 1.4°\mathrm{C}/\Delta T_{\mathrm{at}} = 2.8°\mathrm{C}$, and a strong forcing with $\Delta T_{\mathrm{oc}} = 2.0°\mathrm{C}/\Delta T_{\mathrm{at}} = 4.0°\mathrm{C}$. Ligtenberg et al. (2013) report an increase of the 2 m air temperature over Antarctica by 2.4–5.3°C until 2200 AD obtained from regional climate modeling, depending on the respective IPCC AR5 scenario (Stocker et al., 2013), which approximately corresponds to the span of the chosen values for ΔT_{at}. The related change of SMB in this study might differ, however, as it is simply parameterized by Eq. 4.3 and the PDD scheme. Timmermann and Hellmer (2013) report ∼1°C of ocean warming in the Amundsen Sea area from 2010 to 2200 under different IPCC AR5 scenarios.

Sea level rise from Greenland and glaciers

The GrIS stores $\sim 2.96 \times 10^6$ km^3 of ice or ∼7.4 m of equivalent sea level (ESL) (Bamber et al., 2013). In order to create a deglaciation history of the present GrIS,

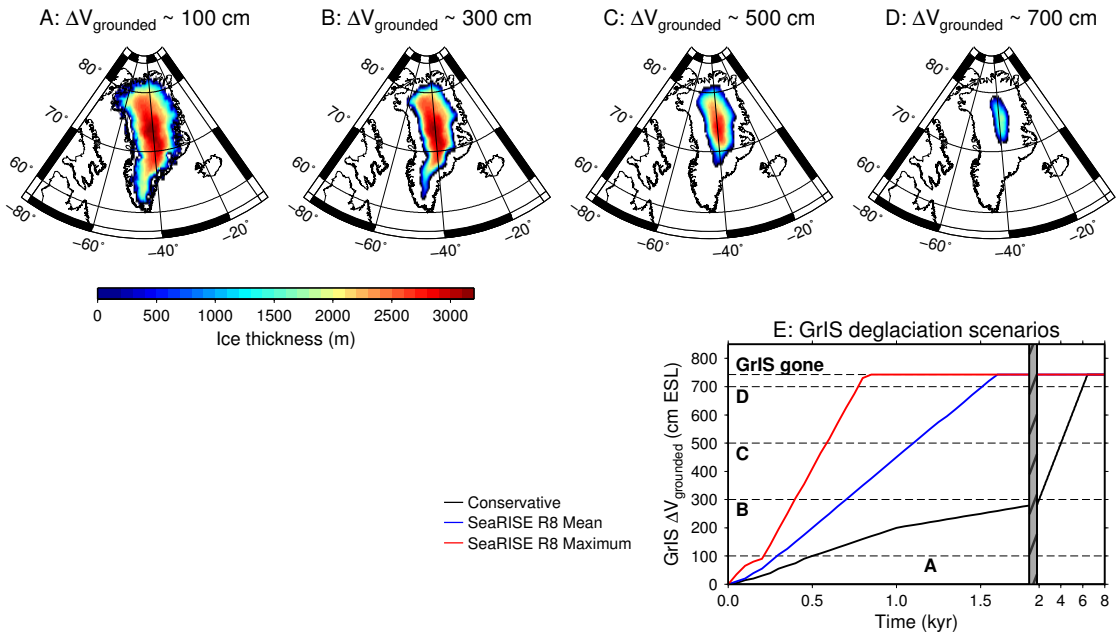

Figure 4.4
GrIS deglaciation history; A–D: ice thickness for a given ice volume loss (in cm ESL). E: Time series of ice loss according to three deglaciation scenarios. The two fast deglaciation scenarios (red and blue) are based on the SeaRISE R8 experiments (Bindschadler et al., 2013). The horizontal dashed lines indicate states of the GrIS as they are illustrated in A–D. Note the different scale of the time axis after 2 kyr in E.

the present-day mass loss pattern by Sørensen et al. (2011) obtained from ICESat[iv] laser altimetry data is applied to the Greenland ice distribution until a given volume loss is reached. The mass loss naturally occurs mainly at the margins of the ice sheet. Snap shots of the deglaciation at given volumes are shown in Figure 4.4A–D.

The rates at which the GrIS discharges ice into the oceans are partially taken from the SeaRISE R8 experiment (Bindschadler et al., 2013) in which e.g. maximum and mean ESL contributions at $t = 100$ yr, 200 yr and 500 yr are listed. These have been extrapolated until the GrIS has completely vanished (red and blue in Figure 4.4E). In the case of the maximum contributions (red curve), the GrIS is gone within the first 850 yr. The mean scenario (blue curve) takes 1600 yr. A more conservative scenario has been defined which leads to a complete vanishing of the GrIS after 6450 yr (black curve).

The complete global glacier inventory has been estimated to contain ice of 0.6 m ESL (Radić and Hock, 2010), 0.43 m ESL (Huss and Farinotti, 2012), or 0.35 m

[iv] Ice, Cloud and Land Elevation Satellite

ESL (Grinsted, 2013). Due to data availability, the values of Radić and Hock (2010) have been used here to create a global glacier ice distribution on the SLE solver's Gauss-Legendre grid. This distribution and its genesis on the basis of Radić and Hock (2010) can be found in Appendix D.3. Note that glaciers in Antarctica and Greenland are excluded here as they are considered by either the description above (Greenland) or the explicit ice dynamical modeling (Antarctica). Consequently, the global glacier volume considered here amounts to ∼0.4 m ESL. In the experiments with sea-level rise from non-Antarctic locations, the glaciers are assumed to melt with uniform rates within the first 2000 yr of the experiments or to stay in its present state (i.e. no melting). It is important to note that the mass loss of the GrIS and the other glaciated regions is not dynamically modeled, but prescribed as an additional far-field sea-level forcing of the AIS by adding the respective ΔH-fields during the coupling procedure (Section 2.4).

4.3 Results

4.3.1 Dependence of the WAIS stability on the solid-Earth structure

The results discussed in this section are obtained without additional sea-level forcing from the GrIS or the glacier melting, but solely by increasing atmospheric and oceanic temperatures according to the classifications above (weak, medium, strong). A preliminary study, in which sea-level or solid-Earth deformation feedbacks have not been taken into account, showed that the GL dynamics in the PennState3d model are behaving chaotically if extended GL retreat is involved as it is in the case of the WAIS collapse. Therefore, the timing of the potential WAIS collapse cannot be determined by single simulations but rather ensembles with different initial states (see Appendix D.4 for details of the preliminary study). In order to keep the computational cost in a reasonable range, the weakly forced scenarios ($\Delta T_{\mathrm{oc}} = 1.2°\mathrm{C}$, $\Delta T_{\mathrm{at}} = 2.4°\mathrm{C}$) are computed only once with initialization time $\Delta t_{\mathrm{ini}} = 200$ kyr. This is justified as the WAIS does not collapse under this forcing, regardless of the Earth-model parameters. If the WAIS collapse occurs (medium and strong forcing), the time series of grounded ice volume are computed from such ensembles based on different initialization times.

In the case of the strong forcing, a fast collapse occurs which outweighs the effect of the chaotic behaviour; therefore, the respective ensembles are small (six samples). The sample results support the assumption of small scattering in the case of a fast collapse (cf. Figure D.6J–R in Appendix D). The same argument does not necessarily hold for the medium forcing. Therefore, the ensemble is chosen

to be larger (41 samples). The individual results show a broader scattering and therefore yield a larger formal variability (Figure D.6A–I).

In all simulations, the oceanic and atmospheric warming leads to loss of grounded ice, specifically in the WAIS. However, a complete collapse of the WAIS does not necessarily occur in all simulations. Independently from the applied solid-Earth set-up, the weak forcing does not lead to a collapse of the WAIS in the above terms, i.e. a break-through from the Amundsen Sea to the Ross Ice Shelf. The strong forcing leads to the collapse before $t = 20$ kyr, again independent from the Earth structure. Under the medium forcing, however, the WAIS reacts differently, depending on the Earth structure. Figure 4.1B and C illustrate the final states after 20 kyr in the case of a collapsing or stable WAIS.

Figures 4.5 and 4.6 exemplarily provide a more detailed insight into the situations before the potential collapse and after 20 kyr in these two simulations (medium forcing; $h_{\mathrm{L}} = 60$ km; $\eta_{\mathrm{A}} = 3{\times}10^{19}$ Pa s or $1{\times}10^{19}$ Pa s). The time 'before the collapse' is defined to be the time at which the ice sheet reaches the value $V_{\mathrm{grounded}} = 24.34{\times}10^{6}$ km^3 for grounded ice volume. This value is arbitrarily chosen with the requirement that it is close to the steady-state volume achieved later in the case of the stable WAIS (here: $\eta_{\mathrm{A}} = 1{\times}10^{19}$ Pa s). The times, at which the two simulations reach this value, differ by 1.6 kyr. This is (1) due to the chaotic behaviour (Appendix D.4) and (2) due to the stabilizing effects of the softer asthenosphere ($\eta_{\mathrm{A}} = 1{\times}10^{19}$ Pa s). For a better comparison and to avoid misinterpreting the effect caused by the chaotic behaviour, the common value for V_{grounded} is preferred over the same time.

Figure 4.5 shows the differences in ice thickness with respect to the initial state before the potential collapse (A: $\eta_{\mathrm{A}} = 3{\times}10^{19}$ Pa s at $t = 5$ kyr; B: $\eta_{\mathrm{A}} = 1{\times}10^{19}$ Pa s at $t = 6.6$ kyr), and after 20 kyr (D: $\eta_{\mathrm{A}} = 3{\times}10^{19}$ Pa s; E: $\eta_{\mathrm{A}} = 1{\times}10^{19}$ Pa s), as well as the respective differences between the simulations based on the two Earth structures (C and F). Figure 4.6 illustrates the changes in RSL at the same times and the respective differences for the two different asthenosphere viscosities.

The change of ice thickness before a potential collapse (Figure 4.5A,B) does not differ very much between the simulations with different asthenosphere viscosity (Figure 4.5C). The larger differences occur along the Transantarctic Mountains, where also the Ross Ice Shelf GL differs most. In both cases, there is already a small open-ocean (or ice-shelf) connection from the Amundsen Sea to the Weddell Sea. The respective changes in RSL, however, yield a shallower ocean depth ($\sim$80 m at the peak) in the already collapsed Amundsen Sea embayment in the

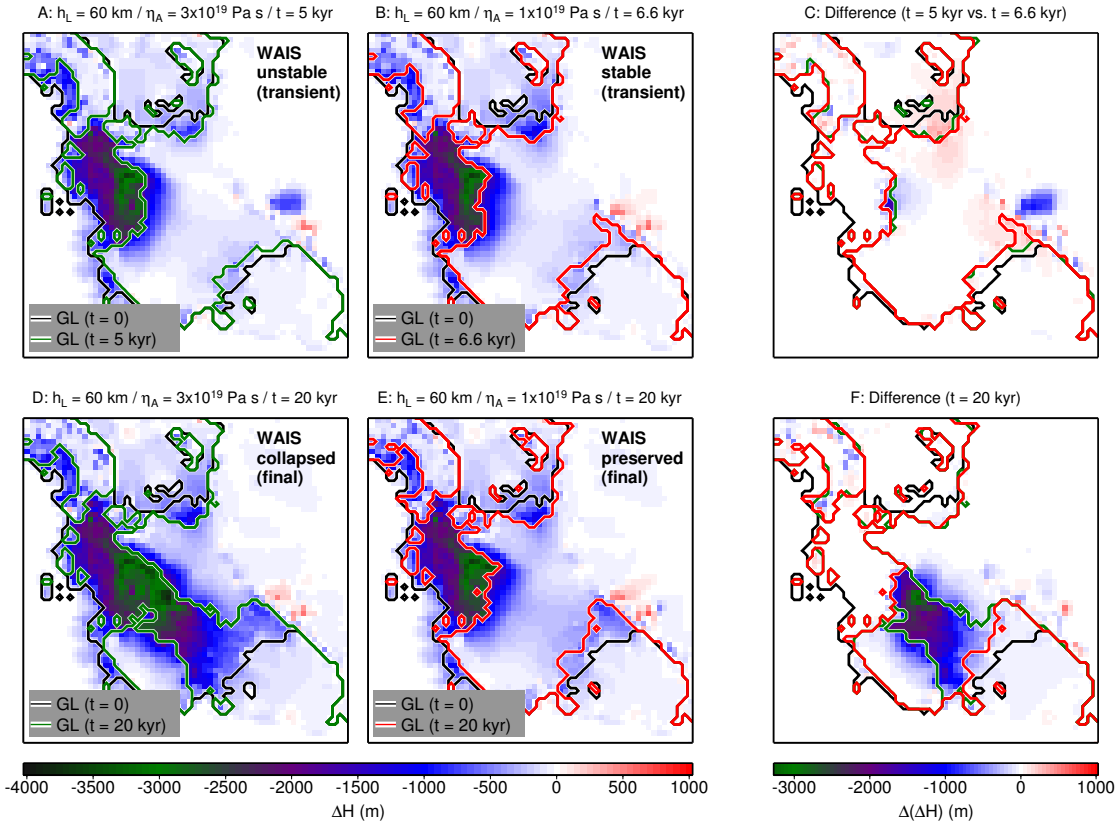

Figure 4.5
A: Change of ice thickness (ΔH) in the medium forcing scenario with the $h_{\mathrm{L}} = 60$ km / $\eta_{\mathrm{A}} = 3{\times}10^{19}$ Pa s Earth structure at $t = 5$ kyr. B: The same for $\eta_{\mathrm{A}} = 1{\times}10^{19}$ Pa s and $t = 6.6$ kyr (see main text for the chosen times). In both cases, the WAIS has mainly retreated from the former Amundsen Sea coastline. C: Difference between the ΔH-fields in A and B. D: The same as A at $t = 20$ kyr; the break-through from the Amundsen Sea to the Ross Ice Shelf is evident here (WAIS collapsed). E: The same as B at $t = 20$ kyr; no break-through (WAIS preserved). F: Difference between the ΔH-fields in D and E. Please note that the colors of the GLs in C and F refer to the respective colors for GLs in A and B, or D and E, respectively. The labels in the upper right corner of A, B, D, and E mark the specific situations as representatives in the later discussion (e.g. Figure 4.7). The illustrated region of Antarctica is the same as in Figure 4.1E

.

case of $\eta_{\mathrm{A}} = 1{\times}10^{19}$ Pa s (Figure 4.6C). This is due to (1) the faster asthenospheric response (lower viscosity) and (2) the advanced timing (6.6 kyr vs. 5 kyr) so that the respective uplift is strong enough to prevent the WAIS from further collapse.

After 20 kyr, the WAIS has collapsed in the case of $\eta_{\mathrm{A}} = 3{\times}10^{19}$ Pa s (Figure 4.5D): All ice is lost in Marie Byrd Land. In contrast to that, the ice thickness is almost the same as after 6.6 kyr on the $\eta_{\mathrm{A}} = 1{\times}10^{19}$ Pa s Earth. The respective RSL

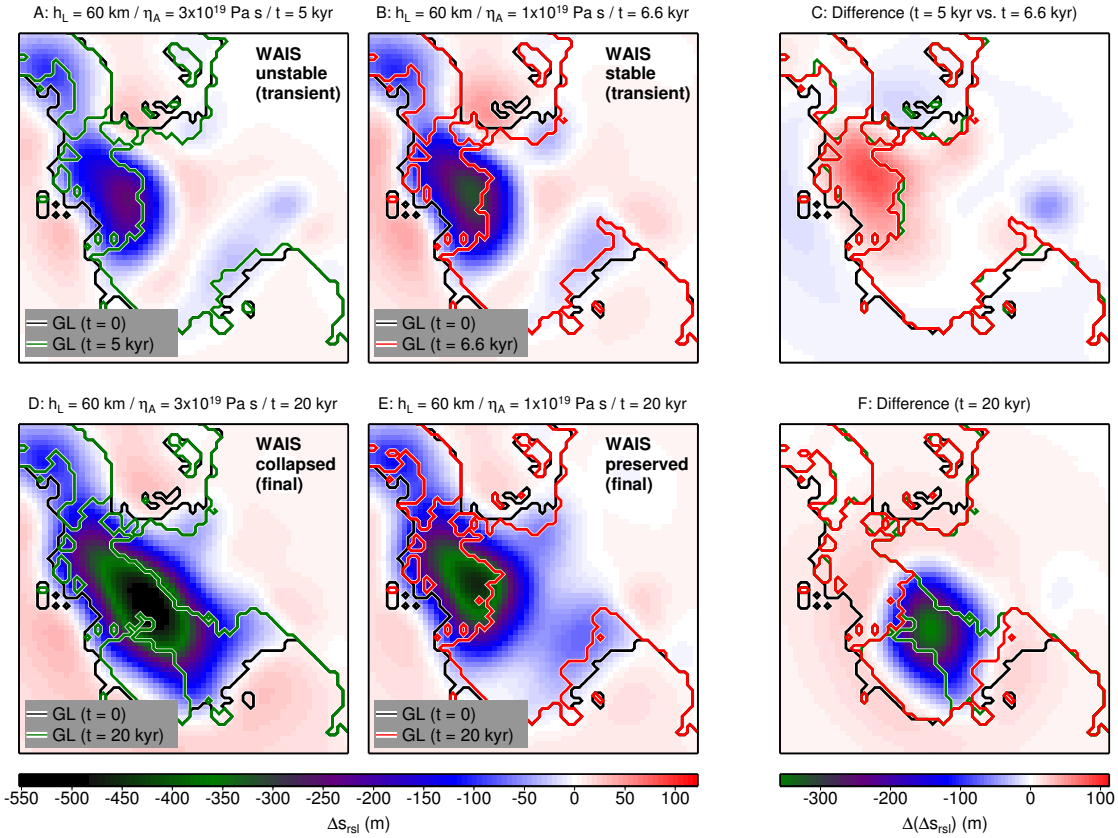

Figure 4.6
The same as Figure 4.5 for RSL change (Δs_{rsl}). Note that negative values in A, B, D, and E indicate decrease of ocean depth/bedrock uplift. Positive values in C and F indicate a shallower ocean/higher uplift for $\eta_{\mathrm{A}} = 1{\times}10^{19}$ Pa s. In A and B, the RSL response to the retreat from the Amundsen Sea coast is evident. The high RSL response spreads all over Marie Byrd Land in the case of a collapse (D), whereas the RSL pattern does not change so much from earlier stages in the case of a preserved WAIS (B vs. E). Still, the RSL is stronger after 20 kyr than after only 6.6 kyr of relaxation.

changes now yield a shallower ocean in Marie Byrd Land for $\eta_{\mathrm{A}} = 3{\times}10^{19}$ Pa s, but this is simply due to the loss of more grounded ice compared to $\eta_{\mathrm{A}} = 1{\times}10^{19}$ Pa s and the associated unloading of the Earth.

The (in-)stability is directly related to the magnitude of the RSL response to the ice retreat in the Amundsen Sea embayment. An important feature within each ensemble in the mediumly forced scenario is that the WAIS stability depends solely on the Earth structure as discussed here. Different initial states lead to a different timing of grounded ice loss but do not affect the general feature of collapse or stability (cf. Appendix D.5).

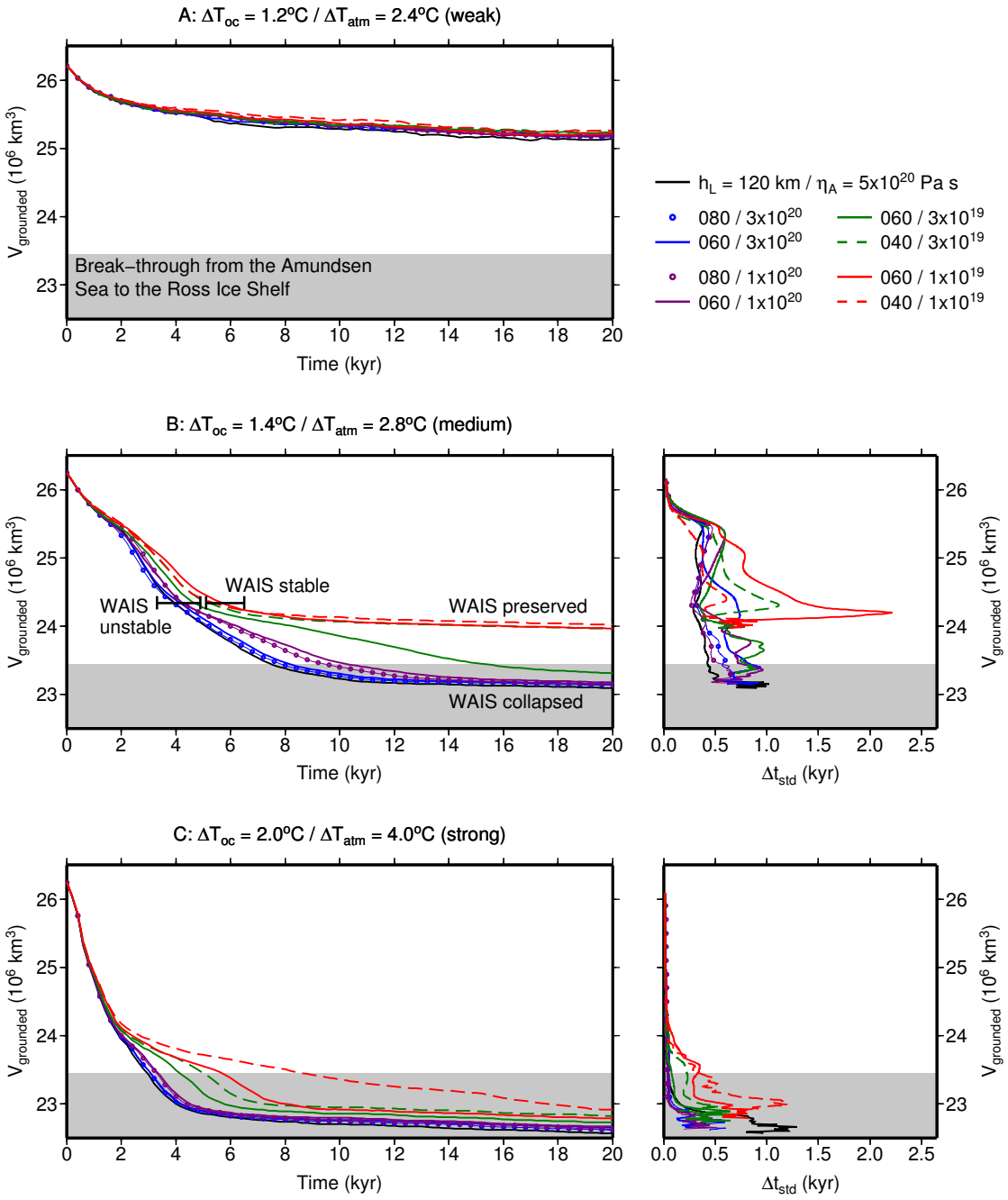

Figure 4.7
Time series of grounded ice for the various simulations. A: weak forcing; B: medium forcing; C: strong forcing. The right frames in B and C give the 1σ-variability of the time to reach a given volume of grounded ice (see main text). The grey shading indicates the volume at which the break-through from the Amundsen Sea to the Ross Ice Shelf occurs. The labels in B refer to the respective exemplary situations shown in Figures 4.5 and 4.6 (black horizontal line: $V_{\mathrm{grounded}} = 24.34{\times}10^6$ km^3 – see main text).

Evolution of grounded ice volume

The left frames in Figure 4.7 show the time series of grounded ice volume for the three forcing scenarios. As an ensemble is created for a given Earth structure in the cases of the medium forcing (B) and the strong forcing (C), the time series on the left handside show the mean evolution $V_{\mathrm{grounded}}(t)$ of the ensembles. The break-through from the Amundsen Sea to the Ross Ice Shelf only occurs if the grounded ice volume drops to $\sim 23.5\times10^6$ km^3 or below, indicated by the grey shading in Figure 4.7. Note, however, that the respective loss of $\sim 3\times10^6$ km^3 of grounded ice does not only come from the WAIS as the atmospheric warming is applied to the whole AIS.[v] With a collapsed WAIS indicated by this threshold for grounded ice volume, the general stability in the weakly forced scenario and the general collapse in the strongly forced one are obvious from Figure 4.7.

The threshold also indicates the dependency of the collapse on the Earth structure as discussed above under the medium forcing. The WAIS is finally preserved in the simulations with $h_{\mathrm{L}} = 40$ km / $\eta_{\mathrm{A}} = 3\times10^{19}$ Pa s, $h_{\mathrm{L}} = 60$ km / $\eta_{\mathrm{A}} = 1\times10^{19}$ Pa s, and $h_{\mathrm{L}} = 40$ km / $\eta_{\mathrm{A}} = 1\times10^{19}$ Pa s. When passing the empirical $V_{\mathrm{grounded}} = 24.34\times10^6$ km^3 threshold (see above), the WAIS state is either 'stable' (Figure 4.5B) or 'unstable' (Figure 4.5A) as marked by the labels in Figure 4.7B. The final ($t = 20$ kyr) difference in grounded ice volume between the AIS with the 'WAIS preserved' and the 'WAIS collapsed' is $\sim 0.9\times10^6$ km^3 or an additional equivalent sea-level rise by 2.25 m in the 'WAIS collapsed' case. Again, the 'collapsed' and 'preserved' labels refer to the respective situations in Figure 4.5. The combination of $h_{\mathrm{L}} = 60$ km and $\eta_{\mathrm{A}} = 3\times10^{19}$ Pa s yields a slow collapse towards an ice-free WAIS. Likewise, the $h_{\mathrm{L}} = 40$ km / $\eta_{\mathrm{A}} = 1\times10^{19}$ Pa s Earth structure (the 'softest' combination in terms of the thinnest lithosphere combined with the lowest viscosity in the asthenosphere) exhibits ongoing ice loss under the strong forcing and thus unfinished collapse even after the illustrated 20 kyr.

On the temporal uncertainty

The right frames in Figure 4.7B and C show the standard deviation in timing for each Earth structure, which has been calculated from the ensemble as

$$\Delta t_{\mathrm{std}}(t) = \left| \frac{\mathrm{d}V_{\mathrm{grounded}}(t)}{\mathrm{d}t} \right|^{-1} \Delta V_{\mathrm{std}}(t) \tag{4.5}$$

[v] In the most extreme scenario (strong forcing, East Antarctic solid-Earth representation), 2.58×10^6 km^3 of grounded ice are drained from the WAIS and the Antarctic Peninsula.

with the standard deviation $\Delta V_{\mathrm{std}}(t)$ at a given time t. The monotonous loss of grounded ice then yields the inverse relations $t(V_{\mathrm{grounded}})$ and $\Delta t_{\mathrm{std}}(V_{\mathrm{grounded}})$.

The temporal scattering should not be considered at times when the grounded ice volume already approaches its final value. Then, Eq. 4.5 naturally yields large values for Δt_{std} due to the low values for the derivative $\mathrm{d}V_{\mathrm{grounded}}/\mathrm{d}t$. These are not of interest because all samples of one ensemble are approaching their new steady states which do not differ very much in volume. This applies for example for the $\Delta t_{\mathrm{std}} = 2.5$ kyr peak in the case of the medium forcing on the $h_{\mathrm{L}} = 60$ km / $\eta_{\mathrm{A}} = 1{\times}10^{19}$ Pa s Earth at $V_{\mathrm{grounded}} \approx 24.2{\times}10^{6}$ km^3 (red solid line in Figure 4.7B). The spread of the volume loss timing (right frames in Figure 4.7B and C), are largest in the medium forcing scenario. The respective ensembles (Appendix D, Figure D.6A–I) show a certain drift into an apparent steady state above $V_{\mathrm{grounded}} = 25{\times}10^{6}$ km^3, from which a larger ice loss with broadly scattered timing occurs. This leads to first peaks in the $\Delta t_{\mathrm{std}}(V_{\mathrm{grounded}})$ relation for almost all Earth structures in the case of the medium forcing. By this, the temporal uncertainty during the transient ice loss ranges between 0.5 and 1.5 kyr. The timing does not scatter if the volume loss occurs fast ($\Delta t_{\mathrm{std}} < 0.1$ kyr in the strongly forced scenario for all Earth structures before approaching the final state).

Delay of the WAIS collapse by a soft Earth structure

The mere comparison of the timing of the collapse also yields large differences as it can already be inferred from the time series in Figure 4.7B and C. Here, an extended analysis for the medium and the strong forcing and two values of grounded ice is shown in Figure 4.8. These two values are $V_{\mathrm{grounded,1}} = 24.5{\times}10^{6}$ km^3, which is reached long before the collapse and corresponds to an AIS state that is comparable to the ones shown in Figure 4.5A and B (depending on whether a collapse occurs in the future), and $V_{\mathrm{grounded,2}} = 23.5{\times}10^{6}$ km^3, which corresponds roughly to the break-through from the Amundsen Sea to the Ross Ice Shelf (see above). The times are taken from the mean time series which are illustrated in Figure 4.7B and C. The respective variability is indicated by the error bars.

The time to reach the earlier state ($V_{\mathrm{grounded,1}}$) spreads much less for different Earth structures, particularly in the case of the strong forcing (Figure 4.8B), than the time to reach the break-through $V_{\mathrm{grounded,2}}$, which is increasing with softer Earth structures due to the slow decay of the WAIS in these cases. In the mediumly forced scenario, the value $V_{\mathrm{grounded,2}} = 23.5{\times}10^{6}$ km^3 associated with the WAIS collapse is reached between ∼7 and 14 kyr after the onset of the forcing. Under the strong forcing, this value is reached between 3 and 8 kyr.

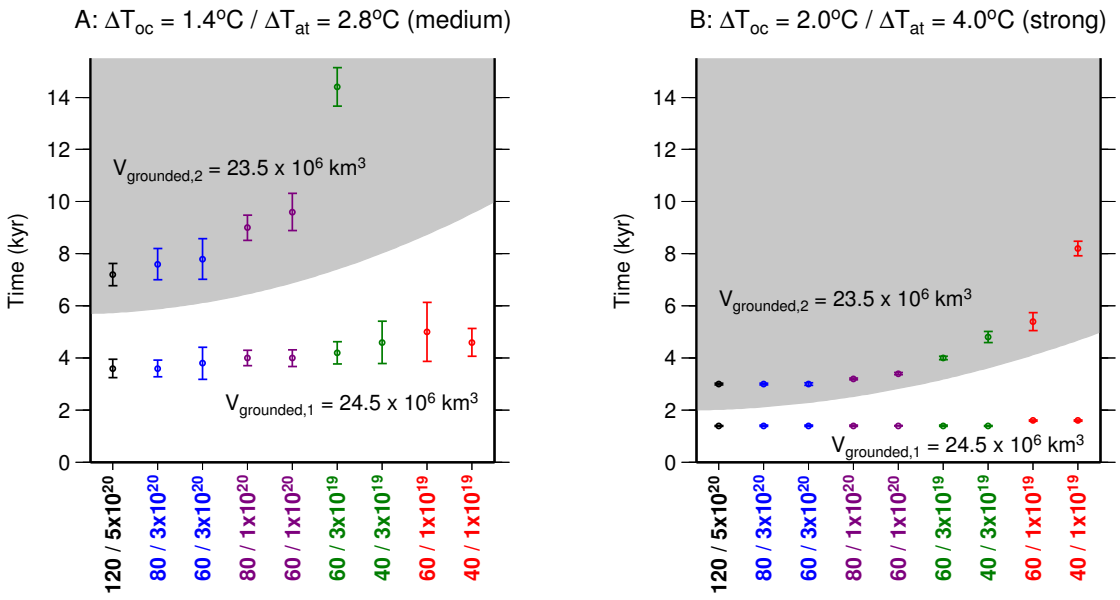

Figure 4.8
Timing incl. 1σ variability (error bars) for two values of grounded ice volume $V_{\mathrm{grounded},1} = 24.5{\times}10^6$ km^3 (white background; before the potential collapse, roughly corresponding to Figures 4.5A,B and 4.6A,B) and $V_{\mathrm{grounded},2} = 23.5{\times}10^6$ km^3 (grey background; roughly coinciding with the break-through from the Amundsen Sea to the Ross Ice Shelf) for all Earth structures (indicated as h_{L} / η_{A} along the abcissa) under the medium (A) and the strong (B) forcing. The larger error bars in the mediumly forced simulation are due to the broader scattering (see main text). Note the similar timing of $V_{\mathrm{grounded},1}$ for all Earth structures, especially in B, and the larger spreading towards later times in the case of softer Earth structures for $V_{\mathrm{grounded},2}$. As the WAIS does not collapse for the three softest Earth structures in the mediumly forced scenario, the respective times for $V_{\mathrm{grounded},2}$ are not defined (A).

In the following, the temporal delay for a given volume $V_{\mathrm{grounded},k}$ ($k = 1, 2$ – see above) between two Earth structures i and j, i.e. the difference in time to reach this value of grounded ice volume, is discussed:

$$\Delta t_{\mathrm{delay},ijk} = t_i(V_{\mathrm{grounded},k}) - t_j(V_{\mathrm{grounded},k}) \tag{4.6}$$

These differences are considered significant, if

$$\Delta t_{\mathrm{delay},ijk} > \sqrt{\left(\Delta t_{\mathrm{std},i}(V_{\mathrm{grounded},k})\right)^2 + \left(\Delta t_{\mathrm{std},j}(V_{\mathrm{grounded},k})\right)^2} \tag{4.7}$$

with Δt_{std} defined in Eq. 4.5. The respective values for the delay are shown in Appendix D.6. They can, however, be directly inferred from Figure 4.8. In the following, only differences, which are significant in the above sense, are discussed.

$V_{\text{grounded},1} = 24.5{\times}10^6$ km^3 is reached during the WAIS GL retreat in the mediumly forced scenario between 0.7 and 1.5 kyr later in the case of an asthenosphere viscosity $\eta_{\text{A}} < 3{\times}10^{20}$ Pa s when compared to the $\eta_{\text{A}} \geq 3{\times}10^{20}$ Pa s results. A comparison between simulations with $\eta_{\text{A}} \leq 1{\times}10^{20}$ Pa s is only significant for the most differing Earth structures in that range: $h_{\text{L}} = 40$ km / $\eta_{\text{A}} = 1{\times}10^{19}$ Pa s yields a delay of 0.7 kyr w.r.t the simulations with $\eta_{\text{A}} = 1{\times}10^{20}$ Pa s. Differences in the lithospheric thickness do not lead to significant delay for any of the values for asthenosphere viscosity. In the strongly forced scenario, $V_{\text{grounded},1} = 24.5{\times}10^6$ km^3 is reached almost at the same time in all simulations with a delay not exceeding 0.2 kyr.

The second illustrated value $V_{\text{grounded},2} = 23.5{\times}10^6$ km^3 (break-through from the Amundsen Sea to the Ross Ice Shelf; see above) is not reached under the medium forcing in the simulations featuring the three softest Earth structures which consequently give no results. For the same forcing, the collapse in the $\eta_{\text{A}} = 1{\times}10^{20}$ Pa s simulations is delayed by 1.1 to 2.4 kyr when compared to a stiffer asthenosphere. The gradual decay of the WAIS in the case of the $h_{\text{L}} = 60$ km / $\eta_{\text{A}} = 3{\times}10^{19}$ Pa s Earth (Figure 4.7B) leads to a delay of the collapse of more than 4.7 kyr. Again, differences in lithospheric thickness alone do not provide a significant delay. The strong forcing, which causes the WAIS collapse for all applied Earth structures, yields temporal delays that are almost all significant in the above sense. Here, the delay between $\eta_{\text{A}} = 3{\times}10^{20}$ Pa s and $\eta_{\text{A}} = 1{\times}10^{20}$ Pa s becomes very small (≤ 0.5 kyr), whereas a softer asthenosphere $\eta_{\text{A}} \leq 3{\times}10^{19}$ Pa s implies a delay between 0.8 and 5.2 kyr. Within this range of low viscosities, for which the delay is up to 4 kyr, the values for η_{A} are very important for the exact timing of the WAIS collapse. Here, differences in the lithospheric thickness also provide significant and rather long delays of the collapse of 0.8 kyr ($\eta_{\text{A}} = 3{\times}10^{19}$ Pa s) or 2.6 kyr ($\eta_{\text{A}} = 1{\times}10^{19}$ Pa s).

4.3.2 Impact of additional sea-level rise

To this point, all results have been obtained without considering sea-level rise from the GrIS or glacier melting. Additional experiments are now evaluated, for which the weak or the medium atmospheric/oceanic forcing is employed together with an additional sea-level forcing caused by the decay of the GrIS at variable rates (Figure 4.4E) and the glacier melting. The strong atmospheric/oceanic forcing is omitted here because the WAIS collapses even without further forcing. The additional efforts do not aim at a similar analysis of the delay of the WAIS collapse, etc. but only at the general impact of far-field sea-level rise in Antarctica on the WAIS stability. Therefore, only the Earth structures featuring the 60 km

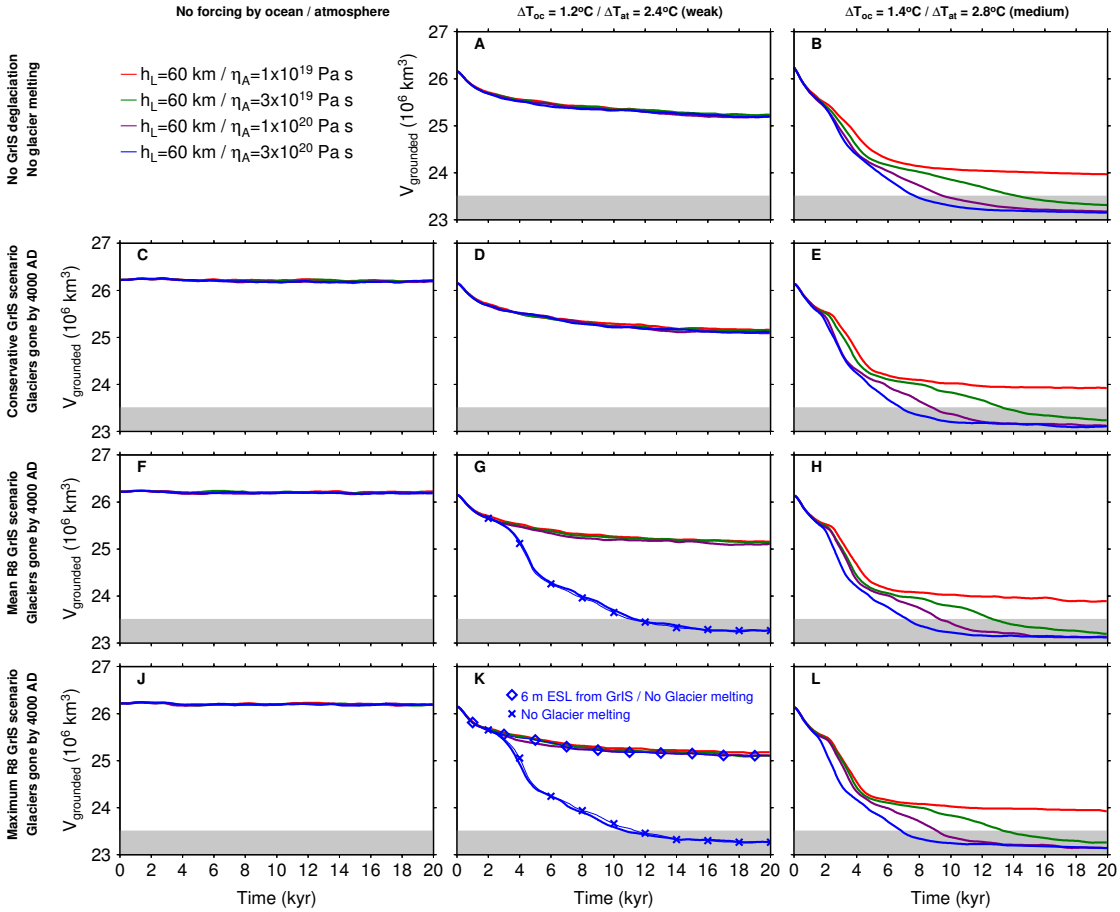

Figure 4.9
Time series of the AIS grounded ice volume for different forcing scenarios. In each column, the forcing from atmospheric and oceanic warming is the same (left: no forcing, center: weak forcing, right: medium forcing). In each row, the sea-level forcing is the same (top: no forcing, second: conservative GrIS melting, third: mean R8 SeaRISE melting, bottom: maximum R8 SeaRISE melting). In the three bottom rows, all glaciers are vanished by $t = 2000$ yr. The frames A and B correspond to the times series in Figure 4.7A and B. Note, however, that only Earth structures with $h_{\mathrm{L}} = 60$ km are considered here. Frames G and K show exceptions from the sorting of the forcing scenarios by rows and columns: The blue lines with cross markers are obtained by applying the row-specific GrIS melting but no glacier melting. The blue line with diamond markers is obtained without glacier melting and the GrIS only contributing 6 m ESL instead of a complete melting (7.4 m ESL). Note that all results except those in A and B have been obtained from single simulations instead of larger ensembles. As in Figure 4.7, the grey shading indicates roughly where the break-through from the Amundsen Sea coast to the Ross Ice Shelf occurs.

lithosphere are considered and the results are not based on larger ensembles but on single runs. This is justified, as whether there is collapse or not is determined by one representative sample.

The results are summarized in Figure 4.9. Note that Figure 4.9A,B correspond to Figure 4.7A,B. The left column in Figure 4.9 shows the results in the case of sea-level rise but no atmospheric or oceanic warming. It is obvious that the steady-state AIS is not responding to the sea-level rise – no matter at which rate it occurs. The right column (medium atmospheric and oceanic warming) shows no differences with varying sea-level forcing: In each frame, the WAIS is only stable if $\eta_{\mathrm{A}} = 1{\times}10^{19}$ Pa s. The center column (weak atmospheric and oceanic warming) shows that the WAIS is preserved, independently from the Earth structure, if no additional sea-level rise occurs (A) or the GrIS decays slowly (D).

If, however, the GrIS decays fast (mean or maximum R8 scenario – frames G and K), the stiffest asthenosphere considered here ($\eta_{\mathrm{A}} = 3{\times}10^{20}$ Pa s – thick blue lines without cross or diamond markers) does not sufficiently compensate the GL retreat, so that the WAIS collapses. This is not the case for any lower value of the asthenosphere viscosity. The GrIS amplitude of $\sim$7.4 m is important for the collapse of the WAIS: The blue diamond markers in K show that the WAIS is stable if the GrIS contributes only 6 m of ESL, even if at the highest rate, instead of melting completely. An additional test revealed that the sea-level contribution from glacier melting beyond Greenland has no impact on the results with $\eta_{\mathrm{A}} = 3{\times}10^{20}$ Pa s and a fast decay of the GrIS (blue crosses in G and K).

4.4 Discussion

The ice loss after the onset of the perturbation in the first stage of the experiments is governed by the strength of the forcing: No differences arise from the different Earth structures in this first stage. If the forcing is weak enough (cf. the weakly forced scenario), this stage covers rather the whole time span over which the AIS is studied here, because only little GL retreat is involved. A stronger forcing that leads to substantial GL retreat in the WAIS shows larger differences in the loss of grounded ice after $\sim$2 kyr.

In the further evolution, the solid-Earth response to the GL retreat becomes crucial, as it determines if the WAIS collapse can be prevented by a fast solid-Earth response. The solid Earth's potential for prevention of the collapse depends on the specific Earth structure and the forcing strength: The stronger the forcing, the softer the Earth is required to provide stability to the WAIS. After exceeding a

certain threshold, even the softest considered solid-Earth layering cannot prevent the WAIS from collapsing. Nevertheless, the delay of the WAIS collapse imposed by a fast solid-Earth response can easily be greater than 4 kyr.

The lithospheric thickness only leads to significant differences in the decay scheme of the WAIS in the presence of a low asthenosphere viscosity. Then, a thinner lithosphere yields WAIS stability where a thicker does not ($\eta_A = 3\times10^{19}$ Pa s under the medium forcing), or it delays the collapse by 0.8 kyr ($\eta_A = 3\times10^{19}$ Pa s under the strong forcing) or 2.6 kyr ($\eta_A = 1\times10^{19}$ Pa s under the strong forcing).

If sea-level rise from the GrIS[vi] is considered in addition to atmospheric and oceanic warming, the WAIS becomes more vulnerable if the asthenosphere viscosity is close to the upper limit of the range employed here. This is, however, only the case if the atmospheric and oceanic warming is too weak to force the WAIS collapse on its own. The occurence of the WAIS collapse triggered by the GrIS melting under the preconditioning of a warmer atmosphere and Amundsen Sea (Figure 4.9G,K) points on the necessity to apply a reasonable representation of the solid Earth when studying the future of the WAIS. Vice versa, the consideration of a relatively stiff Earth structure calls for an adequate representation of far-field sea level from possible melt water sources when the future stability of the WAIS is concerned.

The collapse-triggering effect of the GrIS melting in an otherwise stable WAIS situation does obviously not occur in the case of a softer Earth structure: The $\eta_A = 1\times10^{19}$ Pa s Earth under the medium atmospheric and oceanic forcing is not affected by any rate of GrIS melting (Figure 4.9B,E,H,L). Such a soft structure allows an easy compensation of additional increase of the ocean water column.

The main question then is, which solid-Earth structure should be considered to assess the occurrence or the timing of the WAIS collapse. The relevant region is of course that which reacts most to the loss of grounded ice as e.g. illustrated in Figure 4.6D and E, i.e. the hinterland of the Amundsen Sea coast and Marie Byrd Land. Earlier studies on Antarctic GIA mostly applied a mean one-dimensional Earth structure suitable for whole Antarctica (e.g. Whitehouse et al., 2012b; Ivins et al., 2013), or focused on regions which are relatively far apart and tectonically separated from the West Antarctic rift (e.g. Nield et al., 2012, 2014). Consequently, there is currently no explicit reference for the adjustment of viscoelastic parameters to GIA-related observations such as long-term trends in GPS-detected

[vi] According to Section 4.3.2, the GrIS melting alone has the same effects as GrIS and glacier melting combined. Therefore, the glacier melting is negligible in this context.

surface uplift around the Amundsen Sea Coast. Groh et al. (2012) suggest lower viscosities compared to standard models for Antarctica in the region of interest to explain the observed high rates of viscoelastic vertical motion along the Amundsen Sea coast. Based on this suggestion, the range of asthenosphere viscosities in the present study seems feasible.

Even if the Earth's softness under Marie Byrd Land was overestimated by the $\eta_A \leq 3{\times}10^{19}$ Pa s asthenosphere, the results from a $\eta_A = 1{\times}10^{20}$ Pa s asthenosphere would still yield a delay of the collapse of 1.1 to 2.4 kyr compared to an Earth set-up that fits to a mean parameterization of the whole Antarctic continent. It should be emphasized, however, that for the applicability of the $\eta_A \leq 3{\times}10^{19}$ Pa s results, the respective Earth structure does not have to fit all over Antarctica or even to the Earth beneath the whole WAIS, but only to the Earth in the hinterland of the Amundsen Sea coast and the Western parts of Marie Byrd Land in order to create the RSL response illustrated in Figure 4.6E timely for a stabilization or at least the respective delay (depending on the strength of the forcing).

4.5 Conclusions

On the basis of the presented results, it can be concluded that the solid Earth exerts an important control on the possibility and the timing of a WAIS collapse, as a consequence of the MISI. While the first stage of ice loss is purely governed by the extent of atmospheric and oceanic warming, the interaction of the ice sheet and the solid Earth becomes important in later stages: A very soft tectonic structure below Marie Byrd land might even yield WAIS stability if the climatic warming does not exceed a certain threshold. If the forcing of the future AIS is strong enough to cause a collapse, a soft Earth structure still yields a slower decay of the WAIS. Ignoring this softer setting might lead to up to 5 kyr earlier timing of the collapse in respective model-based estimations, which is of the order of the time which it takes for the WAIS to collapse (3 kyr to 14 kyr). Sea-level rise caused by melt water from the GrIS may induce collapse for stiff Earth structures, even if the forcing is moderate enough that the WAIS is stable without additional sea-level forcing. In contrast, softer Earth structures easily compensate the additional forcing. Finally, a very soft astenosphere, makes the leads to stability unaffected by the sea-level rise from the GrIS.

5 Antarctic Ice Sheet dynamics through the last glacial cycle

– Influence of the Earth structure and implications of the paleo bathymetry state

5.1 On paleo bathymetry initialization

In the experiments in Chapter 4, the prescription of the initial bathymetry ζ_0 is straightforward: The initial time t_0 refers to present-day, for which data sets of the bedrock topography and ocean bathymetry are available (Section 4.2.2). A simulation that starts in the past and ends at present-day, however, demands a more thorough approach, because the (initial) paleo bathymetry is not known. Typically, a first guess for the paleo bathymetry is applied and then corrected in an iterative manner (grey cycle in Figure 5.1) so that finally the simulation ends with the present-day bathymetry (Peltier, 1994; Mitrovica and Milne, 2003; Kendall et al., 2005). This paleo bathymetry initialization is necessary because the migrating coastlines change both the oceanic and the glacial loading, and thus the residual deformation at present-day. Therefore, the initialized paleo bathymetry depends on the applied viscoelastic structure of the Earth.

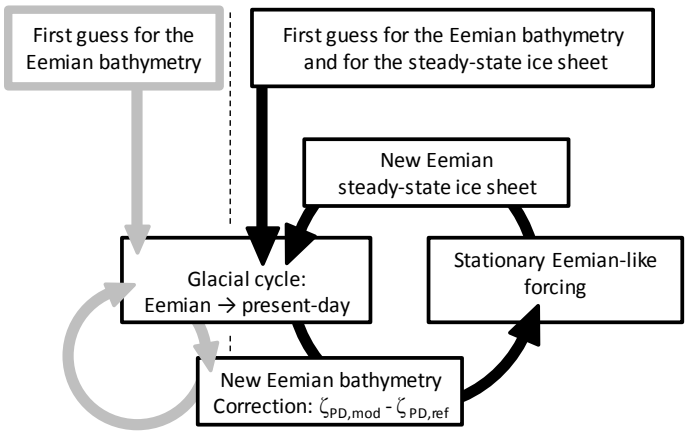

Figure 5.1
Schematic overview over the bathymetry iteration: The grey loop (left of the black dashed line) corresponds to the initialization as it is common in sea-level modeling (Section 5.1). The black loop (right) incorporates the ice-sheet initialization as described in Section 5.3. $\zeta_{\mathrm{PD,mod}}$ refers to the modeled present-day bathymetry, whereas $\zeta_{\mathrm{PD,ref}}$ stands for the reference present-day bathymetry (here based on ETOPO1 and BEDMAP2; Figure 4.3).

The initialization of the paleo bathymetry also affects the ice dynamics via changes in the ocean depth and the bedrock-topography elevation.[vii] However, this initialization was not considered in the ice-dynamics, as long as the SLE was not involved (as in Gomez et al., 2013; de Boer et al., 2014). There have been many simulation studies of ice-sheet dynamics over past glacial cycles or parts of the last glacial cycle, in which the representation of the Earth has been varied in some sense. For instance, Le Meur and Huybrechts (1996), van den Berg et al. (2008), and Olaizola et al. (2012) tested several approaches to solid-Earth dynamics. Maris et al. (2014) varied the relaxation time τ_r of the ELRA approach (Section 2.3.5). There is, however, no study focussing on the effect of paleo bathymetry adjustment to the present-day bathymetry.

As stated above, the inferred paleo bathymetry depends on the applied Earth structure. This study aims at a qualitative understanding of the effect of a consistent paleo bathymetry initialization on the dynamics of the AIS during the last glacial cycle.

5.2 Experiment set-up

The general set-up of the AIS simulation follows the description in Section 4.2.1. The prescribed atmospheric and oceanic temperature offsets as well as the sea-level forcing from the northern hemispheric ice sheets, the initial AIS geometry, the applied Earth structures and the paleo bathymetry iteration are explained below. The simulated glacial cycle starts in the last interglacial, the Eemian ($t = t_0 = -123$ kyr), and ends at present-day ($t = 0$).

5.2.1 Atmospheric and oceanic forcing

The SMB depends on the atmospheric temperature according to the parameterization given in Eq. 4.3. As described by Pollard and DeConto (2012b), the temperature offset ΔT_{at} in Eq. 4.2 is linearly coupled to the isotopic composition of oxygen in marine sediments in terms of the global δ^{18}O-stack by Lisiecki and Raymo (2005) and to deviations of the annual insolation at 80°S from the present-day value (ΔQ_{80}; from Laskar et al., 2004):

$$\Delta T_{\mathrm{at}}(t) = -10^{\circ}\mathrm{C}\ \delta^{18}\mathrm{O}_{\mathrm{n}}(t) + 0.1^{\circ}\mathrm{C\ W^{-1}\ m^{2}}\ \Delta Q_{80}(t) \quad , \tag{5.1}$$

[vii] For the sake of an easier reading, the term '(bedrock) topography' will not be used in the following even if changes in the bathymetry correspond to changes in the bedrock topography.

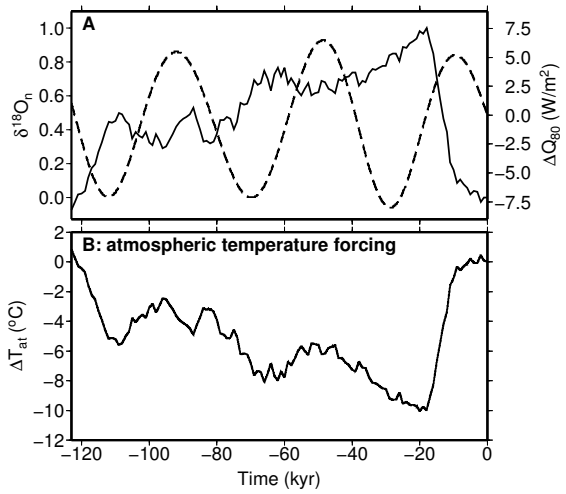

Figure 5.2
A: Time series of normalized benthic δ^{18}O (solid line; left ordinate) according to Lisiecki and Raymo (2005) and insolation changes relative to present-day at 80°S (dashed line; right ordinate) according to Laskar et al. (2004) during the last glacial cycle ($t = 0$ stands for present-day; $t = -123$ kyr stands for the Eemian interglacial). B: Resulting atmospheric temperature forcing (Eq. 5.1).

where $\delta^{18}\mathrm{O_n}$ is the normalized δ^{18}O value with $\delta^{18}\mathrm{O_n} = 1$ standing for Last Glacial Maximum (LGM) conditions and $\delta^{18}\mathrm{O_n} = 0$ standing for modern climate conditions. The $\delta^{18}\mathrm{O_n}$ and ΔQ_{80} time series as well as the resulting atmospheric temperature forcing ΔT_{at} according to Eq. 5.1 are shown in Figure 5.2.

The distribution of the oceanic temperature offset, which is applied all around the AIS (in contrast to the experiments in Chapter 4), follows the temperature changes at 400 m depth according to Liu et al. (2009): The closest grid point of their oceanic global circulation model is used to supply ocean temperature in the parameterization of basal melting rates (Eq. 4.1) at each ice-model grid point. As Liu et al. (2009) provide data only for the transition from LGM to the Holocene, the respective changes ΔT_{oc} at times before LGM are chosen according to equal values of globally stacked δ^{18}O (Lisiecki and Raymo, 2005) in this period.

5.2.2 Sea-level forcing by ice-mass variation outside Antarctica

During the last glacial cycle, the sea-level lowstand exceeded 100 m w.r.t. present-day (e.g. Rohling et al., 1998; Lambeck and Chappell, 2001) and by that also affected the evolution of the AIS (e.g. Pollard and DeConto, 2009). These contributions are in principal accounted for by adding ice-thickness changes from the ICE-5G ice history (Peltier, 2004) at sites remote from Antarctica when handing over the ΔH-field to VILMA (Section 2.4). The time series of the ICE-5G grounded ice volume and the equivalent sea level as well as sampled spatial distributions of ice thickness in the northern hemisphere are shown in Figure 5.3.

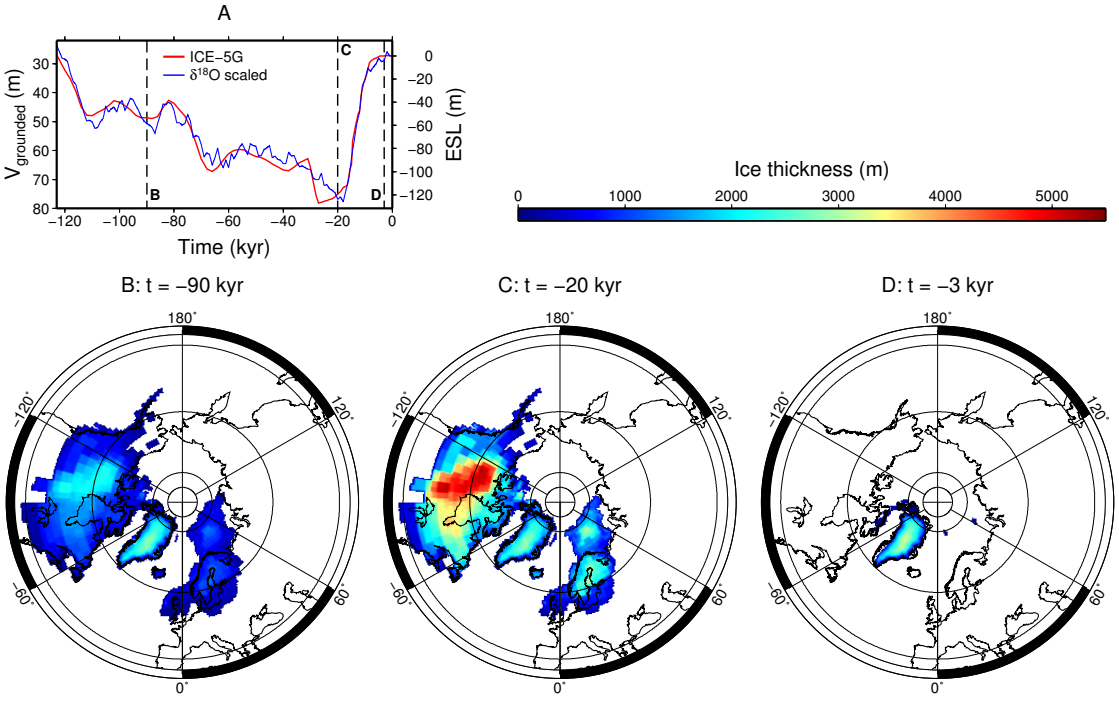

Figure 5.3
A: Time series of grounded ice volume and equivalent sea level in ICE-5G (red) and the scaled δ^{18}O-stack (blue). The vertical black lines indicate the times for which the ICE-5G northern hemispheric ice thickness is plotted in B (during glaciation), C (Last Glacial Maximum), and D (Holocene).

During the global glaciation (from −123 kyr to −40 kyr), the respective ICE-5G ice thickness changes ΔH are scaled such that eustatic sea-level contributions from the dynamically modeled AIS and the remaining ICE-5G ice distribution coincide with the sea level according to the δ^{18}O-stack by Lisiecki and Raymo (2005) (scaled to 125 m sea-level lowstand at LGM and 0 m sea-level contributions at present-day). From −40 kyr to present-day, the ICE-5G non-Antarctic ice thickness changes are used without scaling them as the obervations of paleo sea-level evolution, upon which ICE-5G is based, are denser and more reliable during the global deglaciation.

5.2.3 Earth structure

Four different Earth structures are applied in this study. In accordance with the chosen values in Chapter 4, two structures represent the East Antarctic continental plate (labeled 'stiff') or the West Antarctic rift system (labeled 'soft'). Two additional Earth structures, deviating largely from the former ones towards high viscosities (labeled 'very stiff') and low viscosities ('very soft') in the astheno-

Label	h_{L} (km)	η_{A} (Pa s)	η_{UM} (Pa s)	η_{LM} (Pa s)	Label 2
very soft	60	3×10^{19}	3×10^{20}	1×10^{22}	060 / 0003 / 0030 / 1000
soft	60	1×10^{20}	5×10^{20}	1×10^{22}	060 / 0010 / 0050 / 1000
stiff	120	5×10^{20}	5×10^{20}	1×10^{22}	120 / 0050 / 0050 / 1000
very stiff	120	1×10^{21}	1×10^{21}	2×10^{22}	120 / 0100 / 0100 / 2000

Table 5.1
Parameters of the four adopted viscosity structures: thickness of the lithosphere (h_{L}), viscosity of the asthenosphere (η_{A}), of the upper mantle (η_{UM}) and of the lower mantle (η_{LM}). See Section 2.3.4. The 'Label 2' column summarizes the parameters with the viscosity values represented by the mantissa w.r.t. 10^{19} Pa s for later reference in the legends of the graphics.

sphere and the mantle, are also considered. As in the Earth structures considered in Chapter 4, the asthenosphere extends to 200 km below the elastic lithosphere in the cases where $\eta_{\mathrm{A}} \neq \eta_{\mathrm{UM}}$. The respective values are listed in Table 5.1. Note that the very soft Earth structure is not representative for any larger fraction of Antarctica, whereas the very stiff Earth structure has been found optimal for the interpretation of observations in Antarctica by Whitehouse et al. (2012b).

5.3 Initial ice-sheet geometry and paleo bathymetry initialization

The Eemian sea-level highstand has likely reached ∼8 m above today's mean sea level (e.g. Kopp et al., 2009). A smaller grounded ice volume in the West Antarctic is assumed to have contributed to this highstand (Mercer, 1968; Scherer et al., 1998; Dutton and Lambeck, 2012). To account for this contribution, the AIS geometry from a final steady state from Chapter 4 with a collapsed WAIS is considered as a general initial setting. Likewise, the respective resulting global bathymetry – featuring shallower oceans under the collapsed WAIS (Figure 4.6D) for example – is applied as the first guess for the Eemian initial bathymetry ζ_0.

The iterative procedure for adjusting the paleo bathymetry is outlined in Figure 5.1 (black cycle). Starting from the initial setting as discussed above, the glacial cycle experiment is performed. Consequently, for iteration step 1 the initial bathymetry and the AIS geometry are the same for all four Earth structures. The differences between the final bathymetry at $t = 0$ and the actual present-day bathymetry (ETOPO1 (Amante and Eakins, 2009) / BEDMAP2 (Fretwell et al., 2013); cf. Figure 4.3) are considered for correcting the bathymetry for the SLE solver and the ice-sheet model in the Eemian.

With this corrected bathymetry, stationary Eemian climate conditions are applied to the first-guess Eemian AIS without solid-Earth or sea-level response in order to reach a new steady state after 50 kyr consistent with the new Eemian bathymetry to start the glacial cycle from. This is done in order to exclude effects of the sudden change of the bathymetry on the ice dynamics at the beginning of the glacial cycle in the next iteration step. The new Eemian steady state depends on the Earth structure as it depends on the bathymetry correction. Therefore, also the GL positioning differs from one Earth structure to the other.

The alternation of glacial-cycle forcing and stationary forcing with iteratively corrected bathymetry is repeated in order to achieve a convergence of the final model bathymetry towards the present-day bathymetry and by that also a convergence of the Eemian paleo bathymetry towards its formerly unknown representation. With the Eemian paleo bathymetry converged, the SLE is ultimately solved consistently with the AIS dynamics during the glacial cycle. In accordance with Gomez et al. (2013) and de Boer et al. (2014), the Eemian bathymetry in iteration step 3 is considered to have converged sufficiently. The convergence of the paleo bathymetry is discussed in detail in Appendix D.7. Here, it shall only be noted that the overall convergence is given. A certain alternation of the paleo bathymetry in the cases of the softer Earth structures due to the Eemian steady-state assumption is restricted to regions that are not of particular interest in this study.

In order to create an ensemble as in Chapter 4, ten slightly different initial states to start the glacial cycle simulation from are taken from the stationarily forced run before iteration step 3. For clarity, the term 'first-guess initial bathymetry' shall be used to refer to the Eemian initial bathymetry in iteration step 1 (henceforth IS1), whereas 'corrected initial bathymetry' shall refer to the Eemian initial bathymetry in iteration step 3 (henceforth IS3).

5.4 Results and Discussion

Figure 5.4 shows the time series of the ensemble mean of the grounded ice volume in the ten sample simulations per Earth structure from IS3 (solid lines) and the respective standard deviations (dashed lines) over the glacial cycle for the complete AIS, as well as the time series of grounded ice volume from IS1 (dotted; no ensemble but single results).

The general features of the time series are the fast gain of grounded ice from -123 kyr to -100 kyr, followed by a relative minimum of grounded ice at -90 kyr.

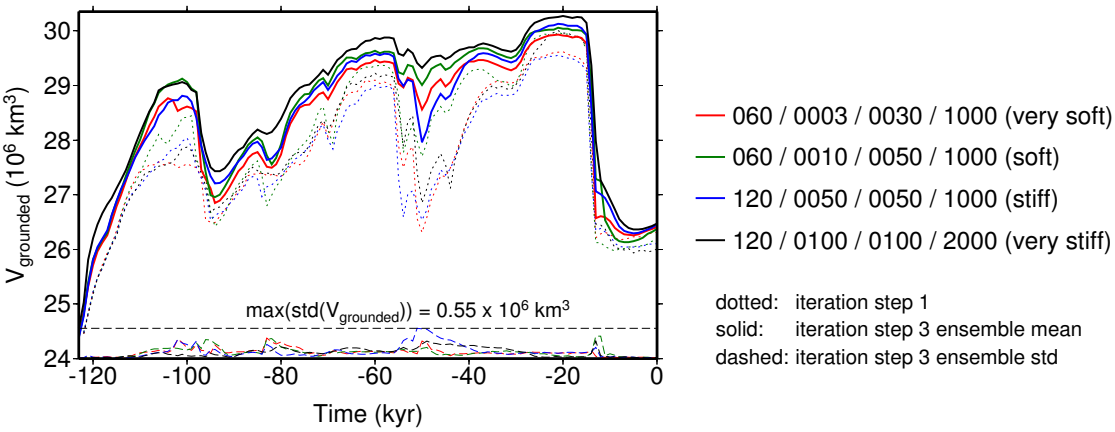

Figure 5.4
Time series of mean grounded ice volume per Earth structure in Antarctica inferred from the ensemble runs of iteration step 3 (IS3; solid lines) and from the single results from iteration step 1 (IS1; dotted lines). The dashed lines illustrate the respective IS3 ensemble standard deviation, referenced to the base of the frame. The single time series of the ensembles from IS3 are shown in Appendix D.8.

The subsequent re-gain of grounded ice is interrupted by minima at -82 kyr and -55 kyr. From -30 kyr to -15 kyr, the grounded ice volume is highest in each time series (LGM). Then, the substantial loss of grounded ice leads to the present-day state at $t = 0$.

In general, the different Earth structures group differently at different epochs during the glacial cycle. It can already be inferred from the standard deviation for the ensembles of IS3 in Figure 5.4 that the differences in one ensemble are partially larger than the differences between the ensemble means of two different Earth structures for IS3.

5.4.1 Differences between the iteration steps

The comparison between the single results from IS1 and the ensemble results from IS3 in Figure 5.4 shows that the iteration procedure inherently leads to a higher post-Eemian ice volume. The bathymetry characteristics for the two iteration steps and the averaged ice volumes are listed in Table 5.2. The individual results from IS1 and IS3 differ by up to 1.9×10^6 km^3. This maximum value is reached at -55 kyr, where the ice volumes determined for IS1 drop further than the volumes determined for IS3. On average, the four volume time series from IS1 and the fourty from IS3 differ by 0.7×10^6 km^3 over the whole glacial cycle.

The reason for the higher ice volumes in IS3 lies in the bathymetry correction:

	ζ_0 (Eemian)	ζ_{PD} (present-day)	$\overline{V}_{\mathrm{grounded}}$ (10^6 km^3)
IS1	equal for all Earth structures (first guess)	deviating from observations and depending on Earth structure	27.8±1.2
IS3	depending on Earth structure (corrected)	matching present-day observations ⇒ almost equal for all Earth structures	28.5±1.3

Table 5.2
Principal characteristics of the initial bathymetry and present-day bathymetry in iteration step 1 (IS1) and iteration step 3 (IS3) and the volume of grounded ice $\overline{V}_{\mathrm{grounded}}$ averaged over the glacial cycle and all simulations of the respective iteration step (regardless of the Earth structure; 4 simulations for IS1 and 40 simulations for IS3).

Figure 5.5 shows that the corrected initial bathymetry for IS3 implies a shallower ocean in the Eemian beyond the GL for all Earth structures. This is because the Earth in today's ice shelves and oceans around Antarctica has been loaded by the advancing AIS between the Eemian and the LGM (∼100 kyr of loading; with interruptions) and then unloaded again during the deglaciation after the LGM (∼20 kyr of unloading). The much longer loading period leads to more net subsidence before the LGM than there is net uplift since the LGM which shifts the corrected initial bathymetry to shallower oceans so that eventually the modeled present-day bathymetry matches the observed one.

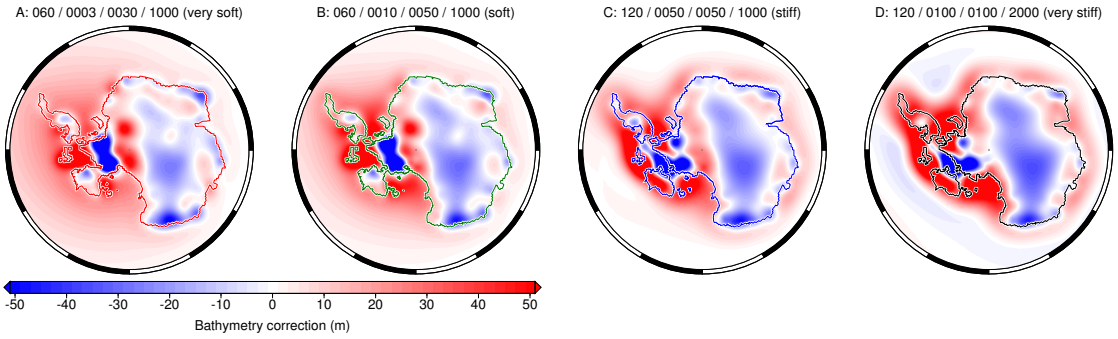

Figure 5.5
Corrected initial bathymetry ζ_0^{IS3} of iteration step 3 (IS3) w.r.t. the first-guess initial bathymetry ζ_0^{IS1} of iteration step 1 (IS1) for the four Earth structures. The convention is: $\zeta_0^{\mathrm{IS3}} - \zeta_0^{\mathrm{IS1}}$. This means that positive values around Antarctica stand for shallower initial oceans in IS3 compared to IS1. The Eemian GL in IS3, which depends on the Earth structure, particularly in the WAIS (cf. Section 5.3 and Appendix D.7), is also shown as coloured outlines.

5.4.2 Regional analysis of the glacial evolution

From here on, all discussed results are representing IS3. For a more regional evaluation of the results, the AIS is subdivided into four major parts by systematically combining drainage basins inferred from satellite observations (Zwally and Giovinetto, 2011) to larger entities. The four chosen areas are shown in Figure 5.6. They are

A the Filchner-Ronne Ice Shelf and its catchment – labeled as Filchner-Ronne Ice Shelf catchment (although this is imprecise in two senses: firstly, the ice shelf itself would not belong to its catchment; secondly, all today's Antarctic ice-shelf regions were covered with grounded ice at the LGM (e.g. Bentley et al., 2014) and therefore have been no ice shelves),

B the Ross Ice Shelf and its catchment (with the same imprecision concerning the label),

C the remaining parts of today's WAIS (mainly the Bellinghausen and Amundsen Sea coasts) and the Antarctic Peninsula, and

D the remaining parts of the East Antarctic Ice Sheet (EAIS), covering Dronning Maud Land, the Amery Ice Shelf and its catchment and Wilkes Land.

The outlines of the drainage basins by Zwally and Giovinetto (2011) have been extended from the present-day calving fronts such that they cover the continental shelf. By that, all grounded ice during the glacial cycle except for only a few grid cells in the outer LGM Peninsula ice sheet and except for the ice cap on the South Orkney Islands is captured in the four catchment areas. The time series of grounded ice in these four areas are shown in Figure 5.7. The results for the total AIS (Figure 5.4) are the sums of the respective results presented in these frames.

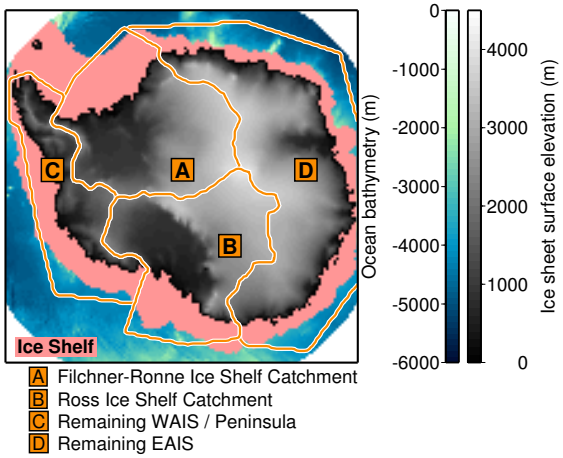

Figure 5.6
The four catchment areas (orange) defined according to the ice divides from Zwally and Giovinetto (2011) with the AIS surface elevation and ocean bathymetry at LGM. The catchments' labels (A–D) are in accordance with Figure 5.7 and the main text. Here, it can also be seen that the AIS extends much farther than in its present configuration (cf. Figure 4.1 in the previous chapter).

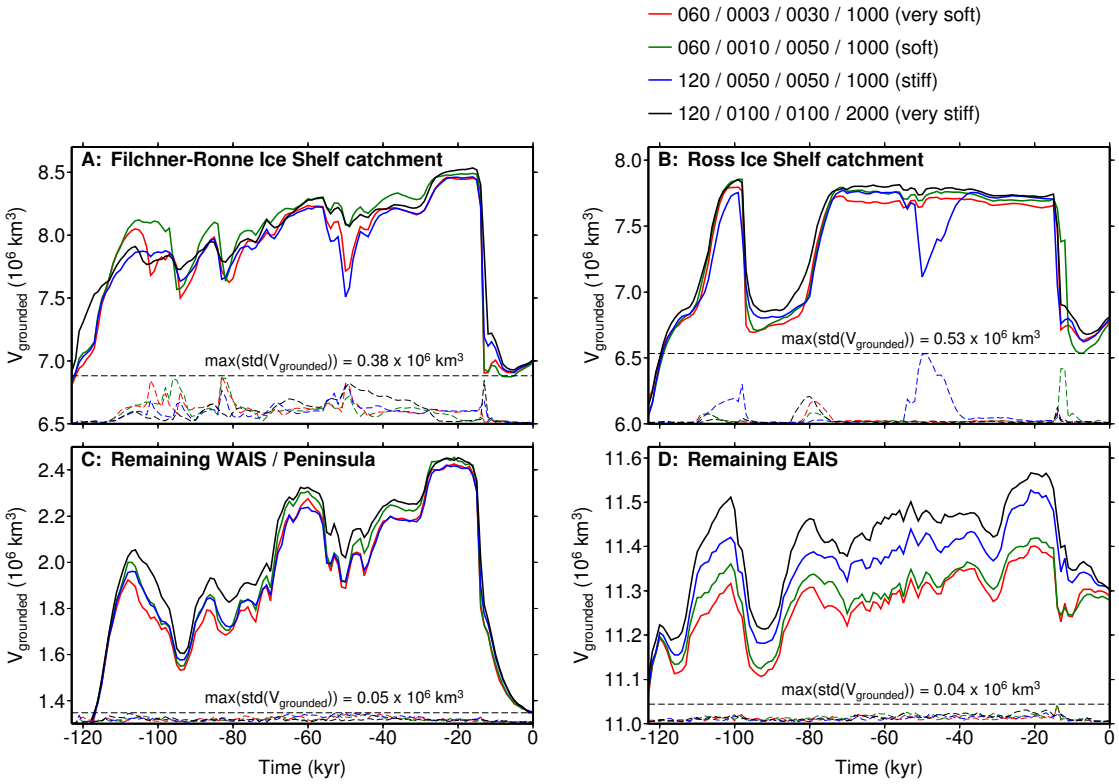

Figure 5.7
Time series of grounded ice volume of the IS3 ensemble mean (solid lines) and standard deviation (dashed; referenced to the frames' base) for each Earth structure in the four catchment areas outlined in Figure 5.6. The IS3 results in Figure 5.4 are the sums of those in A–D. The single time series of the ensembles from IS3 are shown in Appendix D.8.

The Filchner-Ronne Ice Shelf catchment (Figure 5.7A) yields very high variability between the ensemble members over the whole time span (see also in Figure D.9 in the Appendix). The size of the considered ensembles is probably too small for analysing the relations between grounded ice volume and the Earth structures.

The large variability of the results in the Filchner-Ronne Ice Shelf catchment can be attributed to the quasi-chaotic behaviour, which is also visible in the results concerning the future WAIS collapse (Chapter 4), and its interplay with the prominent features of the bathymetry in today's floating portions in this area such as the deep depression around the present-day GL (white cross in Figure 5.8A) and particularly the Thiel Trough on the Eastern ice-sheet–shelf boundary. The variability overlies most grounded ice variations induced by differences in the Earth structure.

Aside from the initial Eemian state (featuring the collapsed WAIS), the ice evolution in the Ross Ice Shelf catchment (Figure 5.7B) can be characterized by two states and relatively fast transitions between these two:

1. The GL is approximately at its present-day location (red line in Figure 5.8A,B), e.g. during the minimum reached around −90 kyr and (of course) at present-day ($t = 0$). This state is also reached in 50% of the ensemble simulations for the stiff Earth (Appendix D.8) around $t = -55$ kyr, which leads to the loss of grounded ice in the mean time series (blue in Figure 5.7B) and the peaking variability (0.53×10^6 km^3).
2. The GL is close to the continental margin (Figure 5.6; black line in Figure 5.8A,B), where further gain of grounded ice via GL advance is not possible. This state is reached above a threshold of $V_{\text{grounded}} \approx 7.75 \times 10^6$ km^3.

This simple and rather stable advance and retreat scheme is probably due to the smooth ocean bottom beneath today's Ross Ice Shelf (Figure 5.8A) compared to the Filchner-Ronne Ice Shelf with its prominent depressions and the associated rather chaotic GL migration (see above). It manifests in much less variability for the different Earth structures: The standard deviations are generally low, but peak whenever the results from the respective Earth deviate from the mean evolution. Examples are:

1. less grounded ice in the case of the stiff Earth (blue) before the first mininum at −90 kyr,
2. an earlier re-advance from this first minimum if the very stiff Earth (black) is considered,
3. the very prominent collapse of large grounded ice portions around −55 kyr on the stiff Earth (blue), and
4. the delayed loss of grounded ice following the LGM on the soft Earth (green).

The specific behaviour of item 3 will be the main focus of Section 5.4.3.

The ensembles yield a much lower absolute variability (factor 10) in the two other areas, the remaining WAIS/Peninsula (Figure 5.7C) and the remaining EAIS (D). The results in the remaining WAIS/Peninsula do not show a clear systematical grouping of the Earth structures: During the first 45 kyr, the soft and the stiff Earth are clustered, whereas the very soft (very stiff) Earth yields a smaller (larger) grounded ice volume. Then, the soft and the very stiff Earth are clustered, as well as the very soft and the stiff Earth, implying that no unique relation between the Earth's stiffness and the evolution of grounded ice volume applies here.

The evolution of grounded ice in the EAIS is systematically affected by the structure of the underlying solid Earth: The stiffer the Earth, the higher the stored volume of grounded ice. The variations of grounded ice volume in this area over the glacial cycle are, however, rather low compared to the other three regions where the grounded ice advances over large areas to reach the continental margin.

The positive relation between grounded ice volume in the remaining EAIS and the stiffness of the Earth can be understood as the superposition of the two following mechanisms.

1. The advancing grounded ice loads the Earth, which leads to subsidence around the GL. This subsidence acts as a negative feedback on further GL advance (Section 1.1.3). The negative feedback is less pronounced for stiffer Earth structures because of the lower amplitudes and longer time scales of the subsidence.
2. During the glacial cycle, the SMB is reduced due to the colder atmospheric environment. The subsequent unloading and uplift in central East Antarctica, remote from the GL and the respective sea-level effects, serves as a positive feedback on the SMB reduction (Section 1.1.1) as the atmospheric lapse rate (Eq. 4.2) leads to colder surface temperatures for an uplifting ice-sheet surface. The greater (and faster) crustal uplift of a softer Earth then leads to a larger SMB reduction, or smaller SMB, for softer Earth structures.

Both effects lead to greater volumes of grounded ice for stiffer Earth structures compared to softer Earth structures and explain the relation between the stiffness of the Earth and the ice volume in the remaining EAIS.

5.4.3 The Ross Ice Shelf catchment area around −55 kyr

The vulnerability of the grounded ice in today's Ross Ice Shelf around −55 kyr on a stiff Earth can intuitively be attributed to the slow Earth response: Prior to the collapse, the ocean temperatures and by that the sub-shelf melting rates increase which leads to thinning of the ice shelf. The weaker ice shelf provides less stability to the ice sheet, which forces the GL to retreat. This eventually leads to a collapse of the respective grounded portions in today's Ross Ice Shelf if the Earth is too stiff to stop this collapse via a relatively fast fall of RSL. This is in accordance with the findings in Chapter 4.

In contrast, the very stiff Earth (black) does not feature such collapses in any of the respective ensemble simulations, although this should be expected from this argumentation. A comprehensive explanation for this apparent contradiction is

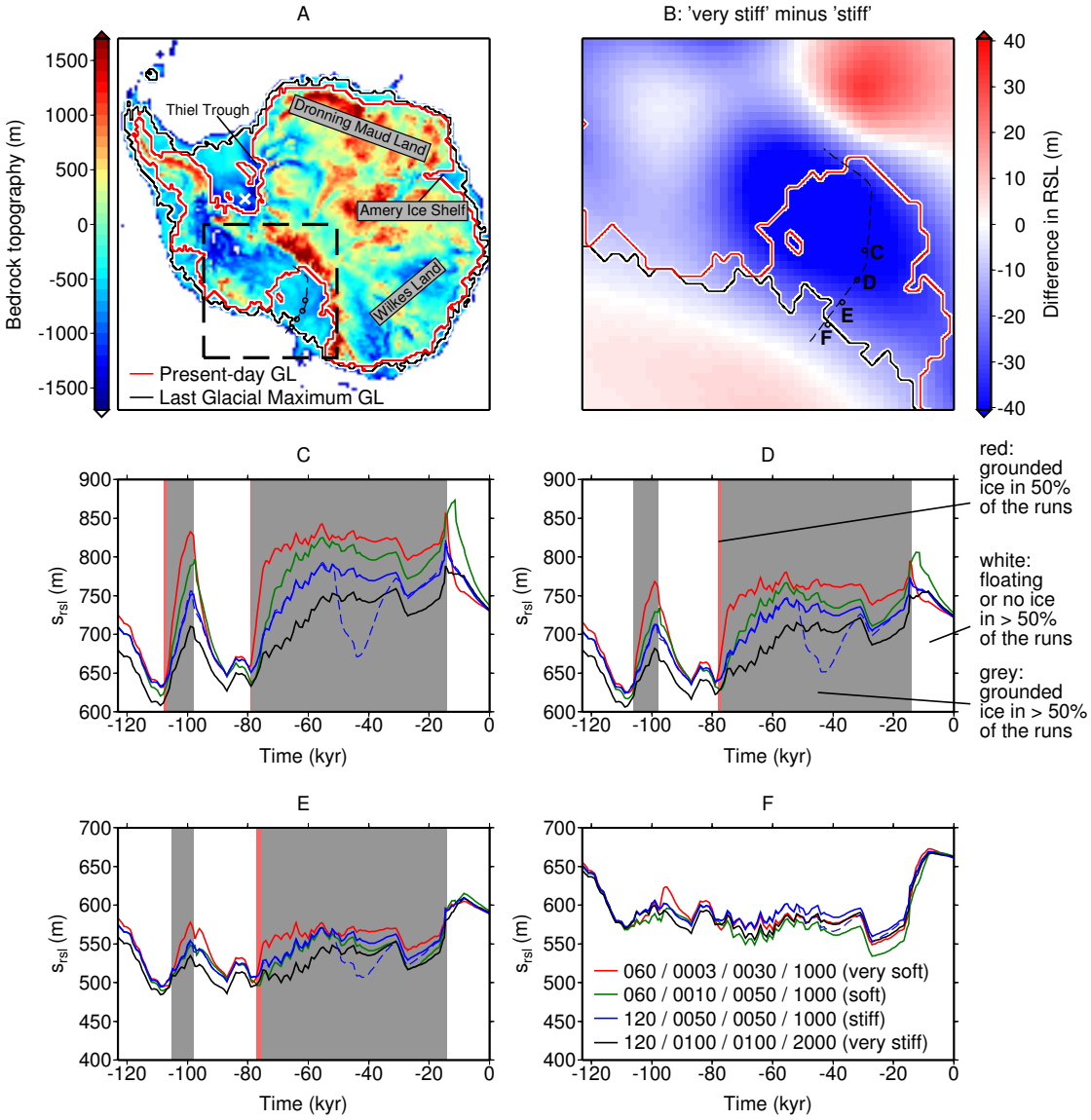

Figure 5.8
A: Overview of the present-day bathymetry around Antarctica. The geographical annotations are for reference in the main text. B: Difference in RSL between the very stiff and the stiff Earth (averaged from $t = -60$ kyr until $t = -56$ kyr – i.e. prior to the occasional collapse in the stiff Earth ensemble) in today's Ross Ice Shelf (black dashed square in A). A and B also show the LGM (black solid line) and present-day GL (red solid line) and an approximated flow line for times at which the ice in today's Ross Ice Shelf is grounded (thin black dashed line). C–F: Time series of RSL at the four points along the flow line indicated in A and B. The data are from one particular member of each ensemble. Grey background indicates mostly grounded ice (i.e. in the case of three or all Earth structures). In the same sense, the white background indicates mostly floating ice or ocean. The blue solid lines shows RSL for a member of the stiff Earth structure ensemble without collapse around −55 kyr; the blue dashed lines shows the same for a member featuring this collapse.

the evolution of the bathymetry during the glacial cycle: Figure 5.8B shows that the RSL in the very stiff Earth simulations is up to 50 m lower than in the stiff Earth simulations in today's Ross Ice Shelf prior to the occassional collapse at −55 kyr on the stiff Earth, i.e. the ocean (or – more generally - the bedrock below sea level) is deeper in the latter case.

The time series in Figures 5.8C–F show RSL along an approximated flow line in this area (indicated in Figure 5.8B). At any time, the ocean is deeper for a softer Earth in the interior of today's Ross Ice Shelf (C and D). The only exception is the potential collapse at $t = -55$ kyr on the stiff Earth (dashed blue) which leads to significant uplift and consequently RSL fall. In the outer parts (E and F), the different flexure of the 120 km and 60 km lithospheres also has an effect on the order of the Earth structures. The sea-level fingerprint of northern hemispheric ice-mass variations in principle also depends on the applied Earth structure but has been found to not affect the RSL evolution in the Ross Ice Shelf significantly (Appendix D.9).

The time series in Figure 5.8 also reveal that these differences are not only due to slower adjustment to the loading and unloading for stiffer Earth structures, but that they exist even in the Eemian ($t = -123$ kyr) and therefore are a feature of the bathymetry initialization. Figure 5.9 shows the deviation of the corrected initial bathymetry from the present-day bathymetry in Antarctica in terms of the average from the four Earth structures (A) and the deviations from this mean for the given Earth structures (B–E). The peak in the difference to present-day in West Antarctica (frame A) is due to the assumption of the WAIS collapse in the Eemian. In order to match the present-day bathymetry in today's shelf regions (Ross, Filchner-Ronne, Amery) as well as in the coastal regions all around Antarctica after the post-LGM retreat of grounded ice, a softer Earth structure requires a deeper ocean at the beginning of the experiment in these areas than a stiffer Earth structure does. Consequently, the very stiff Earth structure yields the shallowest ocean in today's shelf and coastal regions in the Eemian (Figure 5.9E). This shallower ocean, particularly in today's Ross Ice Shelf, is the reason for the stability of this area during the glacial cycle in the case of the very stiff Earth, despite the occasional collapse at −55 kyr on the stiff Earth.

Based on this result, another effect of the solid Earth on GL stability is proposed: The degree of the Earth's adjustment to the post-LGM deglaciation determines the corrected initial bathymetry via the iterative paleo bathymetry initialization, which in turn affects the past evolution of the ice sheet. By that and by the slower subsidence following the ice advance, a stiffer Earth can indirectly provide more

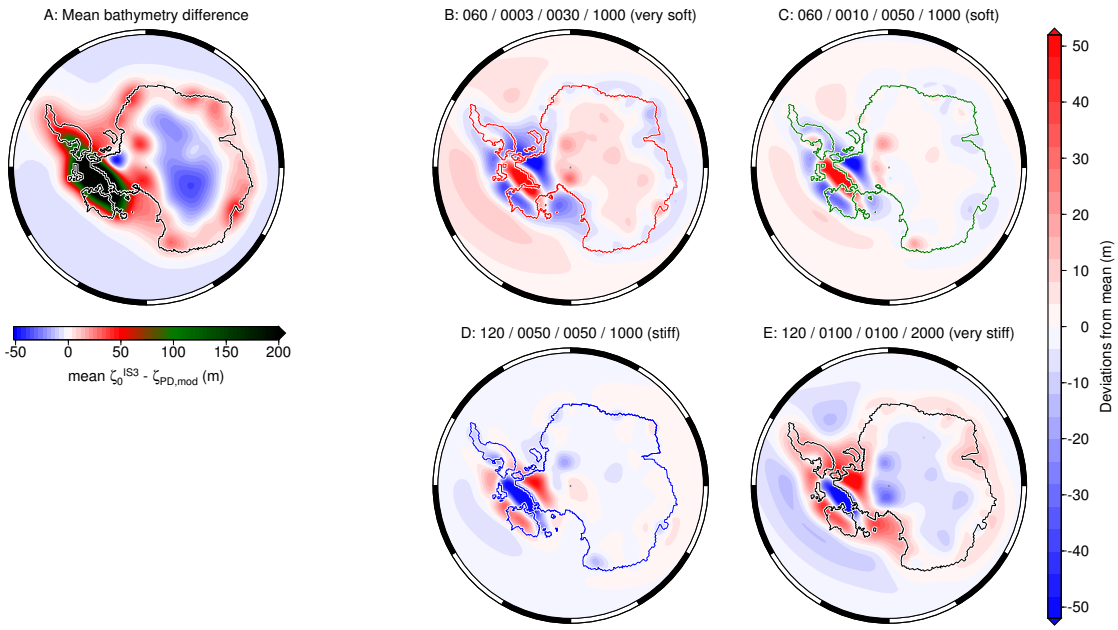

Figure 5.9
A: Difference between the corrected initial bathymetry (at $t = -123$ kyr) and the present-day bathymetry in Antarctica in terms of the mean from the four Earth structures in IS3. B–E: Deviations from the mean illustrated in A for the four Earth structures. Positive values beyond the GL (coloured lines) indicate shallower oceans compared to the mean. The initial Eemian GL positioning depends on the Earth structure, particularly in the WAIS, due to the assumption of an steady state of the AIS in the Eemian (cf. Section 5.3 and Appendix D.7).

stability to the GL via shallower oceans. The stability provided to the ice sheet by these shallower oceans leads to a hysteretic behaviour due to which a softer Earth is not necessarily providing more stability to the ice sheet.

5.4.4 Further potential stabilization by shallower oceans

The same process as discussed in Section 5.4.3 is likely responsible for the slight delay of the post-LGM ice retreat in today's Ross Ice Shelf in the case of the soft Earth (Figure 5.7B). In accordance with the findings in Chapter 4, the soft Earth structure allows for a relatively fast response to partial GL retreat and the associated unloading, which yields more stability than in the case of the stiff and the very stiff Earth. This argument alone also holds for the very soft Earth. In the latter case, however, the bedrock lies deeper below sea level prior to the post-LGM retreat (Figure 5.8C,D,E), which leads to an earlier deglaciation in this area.

It can be hypothesized that the evolution of grounded ice in the remaining

WAIS and the Peninsula (Figure 5.7C) is also affected by the Earth structure in the above sense which leads to the grouping of the results as discussed in Section 5.4.2. However, the results in this region are probably affected by the alternation of the bathymetry during the iterative procedure as discussed in Appendix D.7, so that a quantification of this effect on the results in this area requires a tighter convergence of the bathymetry and cannot be carried out here.

Likewise, the prominent loss of grounded ice on the stiff Earth in the Filchner-Ronne Ice Shelf catchment around −55 kyr (and its absence in the case of the very stiff Earth; Figure 5.7A) might be attributed to the above mechanism. Here, however, the high variability within each Earth structure ensemble prevents clearer conclusions.

5.5 Conclusions

In this chapter, it has been found that the initialization of the paleo bathymetry does not only affect the reconstruction of sea-level variability but also the paleo ice dynamics during the glacial cycle: In order to match the present-day bathymetry, the sequence of pre-LGM loading and post-LGM unloading requires shallower oceans around Antarctica in the Eemian. These lead to a more effective advance of the ice sheets into the continental shelf regions during the pre-LGM loading phase. By that, also the volume of grounded ice is affected during the glacial cycle. This effect is independent of the Earth structure as shown for the broad range of Earth models considered in this study. Consequently, a bias towards less grounded ice is introduced when not adjusting the paleo bathymetry.

In Section 3.2 and Chapter 4, a straightforward relation between the stability of a marine-based ice sheet and the softness of the underlying solid-Earth could be verified: The softer the Earth is, the more likely is a prevention of a collapse by the adjustment of the solid-Earth. However, only GL retreat from a given initial state was considered there. Here, additional contrary mechanisms have been found, which relate to the sequence of loading and unloading during the glacial cycle:

1. During the loading phase, the slower and (depending on the lithospheric thickness) smaller subsidence of a stiffer Earth structure implies shallower oceans compared to softer Earth structures. This effect also applies if no iterative initialization of the paleo bathymetry is considered.
2. In the corrected initial bathymetry, the adjacent oceans are shallower for stiffer Earth structures, as the post-LGM net uplift in the adjacent oceans is smaller for these stiffer Earth structures.

The shallower adjacent oceans in the case of stiffer Earth structures provide more stability to the marine-based ice sheet during the glacial cycle. Consequently, the evolution of grounded ice in a situation such as the −55 kyr interim warming is stabilized by solid-Earth adjustment in the cases of a very stiff or a very soft Earth rheology. For intermediate rheological structures, both stabilizing mechanisms may be too weak to act.

However, the actual evolution of Antarctic ice dynamics, depends rather on the climatic forcing than on the solid-Earth response to the ice-mass variations. For example, the occasional GL retreat at −55 kyr in today's Ross Ice Shelf in the stiff Earth ensemble occurs due to a prescribed increase of sub-shelf melting rates. As in Chapter 4 for the forced collapse of the WAIS, the strength of such a forcing determines if the stabilizing mechanisms of the coupling to the solid Earth are sufficient to provide stability to the ice dynamics. However, the evaluation of the forcing is not within the scope of this study.

The iterative adjustment of the paleo bathymetry as well as a thorough consideration of the determining parameters for the Earth structure must be strongly recommended for an exhaustive approach to modeling paleo ice dynamics, also when considering simpler approximations of the Earth response like ELRA (Section 2.3.5).

6 Summarizing conclusions and outlook

In this thesis, results from coupled numerical models for ice and solid-Earth dynamics including a gravitationally consistent description of sea level have been presented and analysed. The applied Maxwell-viscoelastic gravitationally self-consistent solid-Earth model (SGVEM), VILMA, belongs to the class of models which are commonly applied in GIA studies. Advantage could be taken of VILMA's explicit time scheme, allowing to inexpensively couple it to the applied ice-sheet models – a stand-alone characteristic of the presented coupled model system. The focus was on evaluating different feedback mechanisms, of which the relation between grounding-line (GL) positioning and relative sea level (RSL) proved most important. The significant impact of the solid-Earth representation on the ice dynamics, especially via the RSL evolution, has been identified for the various situations studied in this thesis.

Comparison of VILMA and ELRA

The feedback mechanisms were first studied in geometrically simplified situations in Chapter 3. Here, the results from the fully coupled model, featuring the SGVEM, have been compared to results from the simpler ELRA ('elastic lithosphere / relaxing asthenosphere') approach to solid-Earth relaxation. The ELRA approach assumes a thin-plate lithosphere, represented by its flexural rigidity and one *a priori* relaxation time for the viscous flow in the Earth's mantle instead of a full spectrum as implied in the continuum-mechanical approach of GIA models. Additionally, ELRA does not allow to incorporate spatial variations of sea level. Instead, the evolution of eustatic sea level is prescribed when employing ice-sheet models on centennial to millenial time scales to model the effect of rising and falling sea levels on ice dynamics. This rather overestimates the local sea-level evolution in the vicinity of ice sheets,

Section 3.1 focussed on the crustal deformation in the periphery of radially symmetric ice sheet. It was found that the Earth response to loading and unloading as modeled by the ELRA approach does not allow an unbiased interpretation of observational data from respective peripheral sites. From this, as well as from the SGVEM–ELRA comparison in Section 3.2, where the focus was on the stabilization of a retreating GL by falling RSL (see below), it could be concluded that the

tuning of the ELRA parameters is ambiguous: In general, the ELRA solid-Earth response can approximate the response by a SGVEM (cf. Le Meur and Huybrechts, 1996); however, this tuning depends on the applied loading, and therefore does not capture the complexity of the coupled ice/Earth system (cf. van den Berg et al., 2008). The results in Section 3.2 particularly indicated that the consideration of eustatic sea level, together with the fixed value for the *a priori* ELRA relaxation time, may lead to significant biases for GL retreat.

Stabilization of marine-based ice sheets by the solid-Earth response in GL retreat scenarios

The scenario in Section 3.2 was designed to particularly study the ice-sheet stabilization during the Marine Ice Sheet Instability (MISI) by the RSL fall associated with the solid-Earth unloading after the onset of GL retreat (cf. Gomez et al., 2012). It was found that mantle viscosity and lithosphere thickness significantly influence the extent of GL retreat in this scenario: Lower mantle viscosities imply faster solid-Earth uplift and hence faster RSL fall, leading to less GL retreat; a thinner lithosphere allows for higher amplitudes of RSL fall, which also leads to less GL retreat ('stabilization by RSL fall').

As presented in Chapter 4, this effect is confirmed to be relevant for realistic geometries and forcing scenarios. Within a range of moderate atmospheric and oceanic warming, the response of a soft Earth structure, adequate for the West Antarctic rift system, may restrain GL retreat in the marine-based portions of the West Antarctic Ice Sheet (WAIS). The WAIS collapses under the same climatic forcing if stiffer Earth structures are employed. Prescribing a stronger warming of atmosphere and oceans forces the WAIS collapse even under the assumption of soft Earth structures. In such cases, the response of a soft Earth structures still leads to considerable delay of the WAIS collapse compared to stiffer Earth structures.

Significance of the Earth structure in simulations through glacial cycles

In contrast to the pure GL retreat scenarios in Section 3.2 and Chapter 4, the ice dynamics of the Antarctic Ice Sheet (AIS) through the last glacial cycle consist also of extensive GL advance prior to LGM. The alternation of GL advance and retreat and the resulting solid-Earth loading and unloading lead to a contrary effect of stabilization depending on the viscosity structure; stiffer Earth structures yield shallower oceans in the direct vicinity of Antarctica during the loading period which stabilizes the growth and maintenance of the ice sheet ('stabilization by lower precollapse RSL'). This effect is amplified by the iterative reconstruction of the paleo bathymetry for the last interglacial (the Eemian), which is necessary

to match present-day observations of the bathymetry at the end of the simulation: The post-LGM uplift in today's ice shelves of Antarctica is smaller for stiffer Earth structures and therefore requires shallower oceans in the Eemian.

The stabilization by lower precollapse RSL (provided by stiffer Earth structures) interferes with the stabilization by RSL fall (provided by softer Earth structures): Both mechanisms naturally imply a destabilization by the respective opposite Earth structure range. Consequently, it depends largely on the strength and time scales of the forcing whether one of the stabilizing mechanisms applies.

Feedbacks with the solid Earth in view of the actual forcing mechanisms for ice-sheet dynamics

Ice dynamics are in general driven by changes in the atmospheric and oceanic environment of an ice sheet. The effects of the solid-Earth response on ice dynamics are of second order. An example is the WAIS collapse discussed in Chapter 4; above a certain threshold of atmospheric and oceanic warming, the collapse will occur even in the presence of low viscosities in the asthenosphere and a thin lithosphere. The delaying effect of a soft solid-Earth structure under such climate conditions, as it is visible in the respective results, will possibly be canceled by an even stronger forcing (not simulated here): As the WAIS GL could potentially retreat on shorter time scales, the RSL could presumably not fall fast enough in response to this retreat, so that significant delay of the GL retreat does not occur even in the case of softer Earth structures.

As indicated by the analysis in Section 3.2, the feedback between GL migration and RSL does not only depend on the Earth structure, but also on the rates at which the GL retreats. Consequently, a quantitative assessment of the second-order effects (the Earth structure's stabilizing effect on a marine-based ice sheet) in general also requires an adequate representation of the first-order effect in the numerical model (a realistic sensitivity of the modeled GL w.r.t. the applied forcing mechanisms). This is given for the simulations of the AIS in this thesis according to the PennState3d model's performance in the MISMIP benchmarking experiments (Pattyn et al., 2012, 2013).

In the considered forcing ranges, which also include the sea-level rise by GrIS melt water in Antarctica and its impact on the WAIS stability in Chapter 4 or the pre-LGM interim warming of oceans in Chapter 5, the ice sheet is situated at a tipping point where the second-order effects of the time scales and amplitudes of RSL fall define the tendency of the future evolution.

6.1 Perspectives for future studies

The findings on the future and past evolution of the Antarctic Ice Sheet (AIS) in this thesis could be specified or improved in several ways, concerning the initial states of the model system, the prescription of the driving boundary conditions for ice dynamics, the inclusion of geological constraints or a more rigorous consideration of the viscosity distribution in the Earth's interior. Specific suggestions are given in the following.

The future stability of the WAIS and its relation to the underlying solid Earth has been studied in terms of the perturbation experiments in Chapter 4 implying a steady-state AIS at present-day and a parameterized climatic warming, which forces the AIS out of its equilibrium. An expensive spin-up through one or more glacial cycles in order to start from non-steady present-day conditions, as well as the prescription of the future climate conditions such as sub-shelf ocean warming or changing surface mass balance based on projections by respective numerical models (e.g. Timmermann and Hellmer, 2013; Ligtenberg et al., 2013), would provide a more realistic future evolution of the AIS. A more complete approach would also include a dynamic coupling to an oceanic global circulation model as available for the ice-sheet model RIMBAY (Barbi et al., 2014). This would allow to clearer determine the relevance of the WAIS stabilization by solid-Earth deformation.

Geological observations of ice extent for the period before LGM could help to verify, falsify, or constrain the pre-LGM characteristics in the evolution of the AIS as discussed in Chapter 5, such as the -55 kyr retreat event in the Ross Sea in the case of the stiff Earth, or the unsteady pre-LGM evolution in the Weddell Sea. However, geological data in Antarctica refer rather to the post-LGM deglaciation (e.g. Bentley et al., 2014) than to the time before LGM, so that an improved insight into the specified pre-LGM dynamics is unlikely. Additional conclusions could potentially be drawn w.r.t. the Eemian state of the AIS in relation to the underlying Earth structure and the existence of the WAIS in the Eemian in particular by considering longer periods for the simulations, e.g. two or three glacial cycles instead of only one.

Advancing from the radially varying viscosity distributions $\eta(R)$ in the SGVEM to a three-dimensional distribution of viscosities $\eta(\Omega, R)$ (Klemann et al., 2008) would allow to simultaneously consider the relevant tectonic features in Antarctica, mainly the West Antarctic rift system and the East Antarctic craton. This would allow to assess the significance of the discussed stabilizing effects separately for the WAIS and the EAIS. In simulations through the past towards present-day, the consideration of realistic lateral viscosity variations might improve the under-

standing of today's observations of GIA in terms of uplift or subsidence rates as well as horizontal motion of the Earth's surface.

Beyond the Antarctic Ice Sheet

The Pleistocene ice sheets in the northern Hemisphere are assumed to have interacted extensively with the oceans, just as the AIS. Consequently, the feedbacks with the RSL should also be an important aspect of their evolution, particularly in the case of the controversial Barents Sea Ice Sheet (Ingólfsson and Landvik, 2013) or the Laurentide Ice Sheet, from which large amounts of ice have been discharged into the oceans during Heinrich events (MacAyeal, 1993; Calov et al., 2002). A more rigorous approach to the glacial/interglacial evolution of ice sheets could be to dynamically model the major northern hemispheric ice sheets and the AIS while synchronously coupling their dynamics to the global solid-Earth and sea-level response modeled by the SGVEM as by de Boer et al. (2014). Together with a laterally varying viscosity distribution mentioned above, which represents the global tectonic setting, the connections of the global ice sheets as well as their interaction with the RSL could be modeled consistently and allowing new insights on the controls on the ice-sheet evolution.

Bibliography

M. Abramowitz and I.A. Stegun. *Handbook of Mathematical Functions with Formulas, Graphs, and Mathematical Tables*. Dover, 1964.

N.J. Accardo, D.A. Wiens, S. Hernandez, R.C. Aster, A. Nyblade, A. Huerta, S. Anandakrishnan, T. Wilson, D.S. Heeszel, and I.W.D. Dalziel. Upper mantle seismic anisotropy beneath the West Antarctic Rift System and surrounding region from shear wave splitting analysis. *Geophys. J. Int.*, 2014. doi: 10.1093/gji/ggu117.

S. Adhikari, E.R. Ivins, E. Larour, H. Seroussi, M. Morlighem, and S. Nowicki. Future Antarctic bed topography and its implications for ice sheet dynamics. *Solid Earth*, 5(1):569–584, 2014. doi: 10.5194/se-5-569-2014.

C. Amante and B.W. Eakins. Etopo1 1 arc-minute global relief model: Procedures, data sources and analysis. *NOAA Technical Memorandum NESDIS NGDC*, 24, 2009. doi: 10.7289/V5C8276M.

A. Arakawa and V.R. Lamb. Computational design of the basic dynamical processes of the UCLA general circulation model. In J. Chang, editor, *Methods in Computational Physics*, pages 173–265. Academic Press, New York, 1977.

J. Austermann, J.X. Mitrovica, K. Latychev, and G.A. Milne. Barbados-based estimate of ice volume at Last Glacial Maximum affected by subducted plate. *Nature Geosci.*, 6:553–557, 2013. doi: 10.1038/ngeo1859.

J.L. Bamber, J.A. Griggs, R.T.W.L. Hurkmans, J.A. Dowdeswell, S.P. Gogineni, I. Howat, J. Mouginot, J. Paden, S. Palmer, E. Rignot, and D. Steinhage. A new bed elevation dataset for Greenland. *The Cryosphere*, 7(2):499–510, 2013. doi: 10.5194/tc-7-499-2013.

D. Barbi, G. Lohmann, K. Grosfeld, and M. Thoma. Ice sheet dynamics within an earth system model: downscaling, coupling and first results. *Geosci. Model Dev.*, 7(5):2003–2013, 2014. doi: 10.5194/gmd-7-2003-2014.

S.E. Bassett, G.A. Milne, J.X. Mitrovica, and P.U. Clark. Ice Sheet and Solid Earth Influences on Far-Field Sea-Level Histories. *Science*, 309(5736):925–928, 2005. doi: 10.1126/science.1111575.

A. Beckmann and H. Goosse. A parameterization of ice shelf-ocean interaction for climate models. *Ocean Model.*, 5(2):157–170, 2003. doi: 10.1016/S1463-5003(02)00019-7.

J.C. Behrendt. Crustal and lithospheric structure of the West Antarctic Rift System from geophysical investigations – a review. *Global Planet. Change*, 23(1–4):25–44, 1999. doi: 10.1016/S0921-8181(99)00049-1.

M.J. Bentley, C. Cofaigh, and the RAISED Consortium. A community-based geological reconstruction of Antarctic Ice Sheet deglaciation since the Last Glacial Maximum. *Quat. Sci. Rev.*, 100(0):1–9, 2014. doi: 10.1016/j.quascirev.2014.06.025.

S. Bettadpur. *GRACE Level-2 Gravity Field Product User Handbook*. Center for Space Research, The University of Texas at Austin, CSR-GR-03-01, 2012.

R.A. Bindschadler, S. Nowicki, and the SeaRISE participants. Ice-sheet model sensitivities to environmental forcing and their use in projecting future sea level (the SeaRISE project). *J. Glaciol.*, 59(214):195–224, 2013. doi: 10.3189/2013JoG12J125.

J.F. Brotchie and R. Silvester. On Crustal Flexure. *J. Geophys. Res.*, 74(22):5240–5252, 1969. doi: 10.1029/JB074i022p05240.

R. Calov, A. Ganopolski, V. Petoukhov, M. Claussen, and R. Greve. Large-scale instabilities of the Laurentide ice sheet simulated in a fully coupled climate-system model. *Geophys. Res. Lett.*, 29(24):69–69, 2002. doi: 10.1029/2002GL016078.

L.M. Cathles. *The Viscosity of the Earth's Mantle*. Princeton University Press, 1975.

J.A. Clark, W.E. Farrell, and W.R. Peltier. Global changes in postglacial sea level: A numerical calculation. *Quatern. Res.*, 9(3):265–287, 1978. doi: 10.1016/0033-5894(78)90033-9.

J.C. Comiso. Variability and Trends in Antarctic Surface Temperatures from In Situ and Satellite Infrared Measurements. *J. Climate*, 13(10):1674–1696, 2000. doi: 10.1175/1520-0442(2000)013<1674:VATIAS>2.0.CO;2.

H. Conway, B.L. Hall, G.H. Denton, A.M. Gades, and E.D. Waddington. Past and Future Grounding-Line Retreat of the West Antarctic Ice Sheet. *Science*, 286(5438):280–283, 1999. doi: 10.1126/science.286.5438.280.

K.M. Cuffey and W.S.B. Paterson. *The Physics of Glaciers*. Elsevier Science, 4th edition, 2010. ISBN 9780080919126.

B. de Boer, P. Stocchi, and R.S.W. van de Wal. A fully coupled 3-D ice-sheet – sea-level model: algorithm and applications. *Geosci. Model Dev. Discuss.*, 7(3): 3505–3544, 2014. doi: 10.5194/gmdd-7-3505-2014.

G.H. Denton, T.J. Hughes, and W. Karlén. Global ice-sheet system interlocked by sea level. *Quat. Res.*, 26(1):3–26, 1986. doi: 10.1016/0033-5894(86)90081-5.

A. Dutton and K. Lambeck. Ice Volume and Sea Level During the Last Interglacial. *Science*, 337(6091):216–219, 2012. doi: 10.1126/science.1205749.

A.M. Dziewonski and D.L. Anderson. Preliminary reference Earth model. *Phys. Earth Planet. Inter.*, 25(4):297–356, 1981. doi: 10.1016/0031-9201(81)90046-7.

R.W. Fairbridge. Eustatic changes in sea level. *Phys. Chem. Earth*, 4:99–185, 1961.

W. Farrell and J. Clark. On postglacial sea level. *Geophys. J. Astr. Soc.*, 46: 647–667, 1976. doi: 10.1111/j.1365-246X.1976.tb01252.x.

W.E. Farrell. Deformation of the Earth by surface loads. *Rev. Geophys.*, 10(3): 761–797, 1972. doi: 10.1029/RG010i003p00761.

L. Favier, O. Gagliardini, G. Durand, and T. Zwinger. A three-dimensional full Stokes model of the grounding line dynamics: effect of a pinning point beneath the ice shelf. *The Cryosphere*, 6(1):101–112, 2012. doi: 10.5194/tc-6-101-2012.

L. Favier, G. Durand, S.L. Cornford, G.H. Gudmundsson, O. Gagliardini, F. Gillet-Chaulet, T. Zwinger, A.J. Payne, and A.M. Le Brocq. Retreat of Pine Island Glacier controlled by marine ice-sheet instability. *Nature Clim. Change*, 4(2): 117–121, 2014. doi: 10.1038/nclimate2094.

A. Foldvik and T. Kvinge. Conditional instability of sea water at the freezing point. *Deep-Sea Res.*, 21(3):169–174, 1974. doi: 10.1016/0011-7471(74)90056-4.

C. Fox Maule, M.E. Purucker, N. Olsen, and K. Mosegaard. Heat Flux Anomalies in Antarctica Revealed by Satellite Magnetic Data. *Science*, 309(5733):464–467, 2005. doi: 10.1126/science.1106888.

P. Fretwell, H.D. Pritchard, and the BEDMAP2 Consortium. Bedmap2: improved ice bed, surface and thickness datasets for Antarctica. *The Cryosphere*, 7(1): 375–393, 2013. doi: 10.5194/tc-7-375-2013.

C.F. Gauß. *Bestimmung des Breitenunterschiedes zwischen den Sternwarten von Göttingen und Altona.* Vandenhoeck und Ruprecht, 1828.

J.W. Glen. The Creep of Polycrystalline Ice. *Proc. Roy. Soc. A*, 228(1175):519–538, 1955. doi: 10.1098/rspa.1955.0066.

N. Gomez, J.X. Mitrovica, P. Huybers, and P.U. Clark. Sea level as a stabilizing factor for marine-ice-sheet grounding lines. *Nature Geosci.*, 3(12):850–853, 2010. doi: 10.1038/ngeo1012.

N. Gomez, D. Pollard, J.X. Mitrovica, P. Huybers, and P.U. Clark. Evolution of a coupled marine ice sheet–sea level model. *J. Geophys. Res.*, 117:F01013, 2012. doi: 10.1029/2011JF002128.

N. Gomez, D. Pollard, and J.X. Mitrovica. A 3-D coupled ice sheet – sea level model applied to Antarctica through the last 40 ky. *Earth Planet. Sci. Lett.*, 384:88–99, 2013. doi: 10.1016/j.epsl.2013.09.042.

R. Greve and H. Blatter. *Dynamics of Ice Sheets and Glaciers*. Advances in Geophysical and Environmental Mechanics and Mathematics. Springer Berlin Heidelberg, 2009. ISBN 978-3-642-03414-5. doi: 10.1007/978-3-642-03415-2_5.

R. Greve, F. Saito, and A. Abe-Ouchi. Initial results of the SeaRISE numerical experiments with the models SICOPOLIS and IcIES for the Greenland ice sheet. *Ann. Glaciol.*, 52(58):23–30, 2011. doi: 10.3189/172756411797252068.

A. Grinsted. An estimate of global glacier volume. *The Cryosphere*, 7(1):141–151, 2013. doi: 10.5194/tc-7-141-2013.

A. Groh, H. Ewert, M. Scheinert, M. Fritsche, A. Rülke, A. Richter, R. Rosenau, and R. Dietrich. An investigation of Glacial Isostatic Adjustment over the Amundsen Sea sector, West Antarctica. *Global Planet. Change*, 98–99(0):45–53, 2012. doi: 10.1016/j.gloplacha.2012.08.001.

G. H. Gudmundsson, J. Krug, G. Durand, L. Favier, and O. Gagliardini. The stability of grounding lines on retrograde slopes. *The Cryosphere*, 6(6):1497–1505, 2012. doi: 10.5194/tc-6-1497-2012.

G.H. Gudmundsson. Ice-shelf buttressing and the stability of marine ice sheets. *The Cryosphere*, 7(2):647–655, 2013. doi: 10.5194/tc-7-647-2013.

B.C. Gunter, O. Didova, R.E.M. Riva, S.R.M. Ligtenberg, J.T.M. Lenaerts, M.A. King, M.R. van den Broeke, and T. Urban. Empirical estimation of present-day Antarctic glacial isostatic adjustment and ice mass change. *The Cryosphere*, 8 (2):743–760, 2014. doi: 10.5194/tc-8-743-2014.

J. Hagedoorn. *Glaziale Isostasie und rezente Meeresspiegeländerung*. PhD thesis, Geodätisches Institut, Universität Stuttgart, 2005.

J.M. Hagedoorn, D. Wolf, and Z. Martinec. An estimate of global mean sea-level rise inferred from tide-gauge measurements using glacial-isostatic models consistent with the relative sea-level record. *Pure Appl. Geophys.*, 164(4):791–818, 2007. doi: 10.1007/s00024-007-0186-7.

N.A. Haskell. The Motion of a Viscous Fluid Under a Surface Load. *J. Appl. Phys.*, 6(8):265–269, 1935. doi: 10.1063/1.1745329.

J.D. Hays, J. Imbrie, and N.J. Shackleton. Variations in the Earth's Orbit: Pacemaker of the Ice Ages. *Science*, 194(4270):1121–1132, 1976. doi: 10.1126/science.194.4270.1121.

W.A. Heiskanen and H. Moritz. *Physical Geodesy*. W.H. Freeman, 1967.

H.H. Hellmer, F. Kauker, R. Timmermann, J. Determann, and J. Rae. Twenty-first-century warming of a large Antarctic ice-shelf cavity by a redirected coastal current. *Nature*, 485(7397):225–228, 2012. doi: 10.1038/nature11064.

C. Hillenbrand, G. Kuhn, J.A. Smith, K. Gohl, A.G.C. Graham, R.D. Larter, J.P. Klages, R. Downey, S.G. Moreton, M. Forwick, and D.G. Vaughan. Grounding-line retreat of the West Antarctic Ice Sheet from inner Pine Island Bay. *Geology*, 41(1):35–38, 2013. doi: 10.1130/G33469.1.

R.L. Hooke. Flow law for polycrystalline ice in glaciers: Comparison of theoretical predictions, laboratory data, and field measurements. *Rev. Geophys.*, 19(4): 664–672, 1981. ISSN 1944-9208. doi: 10.1029/RG019i004p00664.

M. Huss and D. Farinotti. Distributed ice thickness and volume of all glaciers around the globe. *J. Geophys. Res.*, 117(F4), 2012. ISSN 2156–2202. doi: 10.1029/2012JF002523.

P. Huybrechts. Glaciological Modelling of the Late Cenozoic East Antarctic Ice Sheet: Stability or Dynamism? *Geogr. Ann. Phys. Geogr.*, 75(4):221–238, 1993. URL `http://www.jstor.org/stable/521202`.

P. Huybrechts. Sea-level changes at the LGM from ice-dynamic reconstructions of the Greenland and Antarctic ice sheets during the glacial cycles. *Quat. Sci. Rev.*, 21(1):203–231, 2002.

P. Huybrechts and J. Oerlemans. Response of the Antarctic ice sheet to future greenhouse warming. *Clim. Dynam.*, 5(2):93–102, 1990. doi: 10.1007/BF00207424.

P. Huybrechts, H. Goelzer, I. Janssens, E. Driesschaert, T. Fichefet, H. Goosse, and M.-F. Loutre. Response of the Greenland and Antarctic Ice Sheets to multi-millennial greenhouse warming in the Earth system model of intermediate complexity LOVECLIM. *Surv. Geophys.*, 32(4-5):397–416, 2011. doi: 10.1007/s10712-011-9131-5.

J. Imbrie, E.A. Boyle, S.C. Clemens, A. Duffy, W.R. Howard, G. Kukla, J. Kutzbach, D.G. Martinson, A. McIntyre, A.C. Mix, B. Molfino, J.J. Morley, L.C. Peterson, N.G. Pisias, W.L. Prell, M.E. Raymo, N.J. Shackleton, and J.R. Toggweiler. On the Structure and Origin of Major Glaciation Cycles 1. Linear Responses to Milankovitch Forcing. *Paleoceanography*, 7(6):701–738, 1992. doi: 10.1029/92PA02253.

Ó Ingólfsson and J.Y. Landvik. The Svalbard–Barents Sea ice-sheet – Historical, current and future perspectives. *Quat. Sci. Rev.*, 64(0):33–60, 2013. doi: 10.1016/j.quascirev.2012.11.034.

E.R. Ivins and T.S. James. Antarctic glacial isostatic adjustment: a new assessment. *Antarct. Sci.*, 17(4):541–553, 2005. doi: 10.1017/S0954102005002968.

E.R. Ivins, T.S. James, J. Wahr, E.J.O. Schrama, F.W. Landerer, and K.M. Simon. Antarctic contribution to sea level rise observed by GRACE with improved GIA correction. *J. Geophys. Res.*, 118(6):3126–3141, 2013. doi: 10.1002/jgrb.50208.

S.S. Jacobs, A. Jenkins, C.F. Giulivi, and P. Dutrieux. Stronger ocean circulation and increased melting under Pine Island Glacier ice shelf. *Nature Geosci.*, 4(8):519–523, 2011. doi: 10.1038/ngeo1188.

J.S. Johnson, M.J. Bentley, J.A. Smith, R.C. Finkel, D.H. Rood, K. Gohl, G. Balco, R.D. Larter, and J.M. Schaefer. Rapid Thinning of Pine Island Glacier in the Early Holocene. *Science*, 343(6174):999–1001, 2014. doi: 10.1126/science.1247385.

P. Johnston. The effect of spatially non-uniform water loads on prediction of sea-level change. *Geophys. J. Int.*, 114(3):615–634, 1993. doi: 10.1111/j.1365-246X.1993.tb06992.x.

P. Johnston and K. Lambeck. Postglacial rebound and sea level contributions to changes in the geoid and the Earth's rotation axis. *Geophys. J. Int.*, 136(3):537–558, 1999. doi: 10.1046/j.1365-246x.1999.00738.x.

I. Joughin and R.B. Alley. Stability of the West Antarctic ice sheet in a warming world. *Nature Geosci.*, 4(8):506–513, 2011. doi: 10.1038/ngeo1194.

I. Joughin, B.E. Smith, D.E. Shean, and D. Floricioiu. Brief Communication: Further summer speedup of Jakobshavn Isbrae. *The Cryosphere*, 8(1):209–214, 2014a. doi: 10.5194/tc-8-209-2014.

I. Joughin, B.E. Smith, and B. Medley. Marine Ice Sheet Collapse Potentially Under Way for the Thwaites Glacier Basin, West Antarctica. *Science*, 344(6185): 735–7–38, 2014b. doi: 10.1126/science.1249055.

G. Kaufmann and K. Lambeck. Mantle dynamics, postglacial rebound and the radial viscosity profile. *Phys. Earth Planet. Int.*, 121(3–4):301–324, 2000. doi: 10.1016/S0031-9201(00)00174-6.

G. Kaufmann, P. Wu, and D. Wolf. Some effects of lateral heterogeneities in the upper mantle on postglacial land uplift close to continental margins. *Geophys. J. Int.*, 128(1):175–187, 1997. doi: 10.1111/j.1365-246X.1997.tb04078.x.

G. Kaufmann, P. Wu, and E.R. Ivins. Lateral viscosity variations beneath Antarctica and their implications on regional rebound motions and seismotectonics. *J. Geodyn.*, 39(2):165–181, 2005. doi: 10.1016/j.jog.2004.08.009.

O. Kellogg. *Foundations of Potential Theory*. Springer, Berlin, 1929.

R.A. Kendall, J.X. Mitrovica, and G.A. Milne. On post-glacial sea level – II. Numerical formulation and comparative results on spherically symmetric models. *Geophys. J. Int.*, 161(3):679–706, 2005. doi: 10.1111/j.1365-246X.2005.02553.x.

M.A. King, R.J. Bingham, P. Moore, P.L. Whitehouse, M.J. Bentley, and G.A Milne. Lower satellite-gravimetry estimates of Antarctic sea-level contribution. *Nature*, 491:586–589, 2012. doi: 10.1038/nature11621.

V. Klemann and Z. Martinec. Contribution of glacial-isostatic adjustment to the geocenter motion. *Tectonophysics*, 511(3–4):99–108, 2011. doi: 10.1016/j.tecto.2009.08.031.

V. Klemann and D. Wolf. The eustatic reduction of shoreline diagrams: implications for the inference of relaxation-rate spectra and the viscosity stratification below Fennoscandia. *Geophys. J. Int.*, 162(1):249–256, 2005. doi: 10.1111/j.1365-246X.2005.02637.x.

V. Klemann, Z. Martinec, and E.R. Ivins. Glacial isostasy and plate motion. *J. Geodyn.*, 46(3–5):95–103, 2008. doi: 10.1016/j.jog.2008.04.005.

H. Konrad, M. Thoma, I. Sasgen, V. Klemann, D. Barbi, K. Grosfeld, and Z. Martinec. The deformational response of a viscoelastic solid earth model coupled

to a thermomechanical ice sheet model. *Surv. Geophys.*, 35(6):1441–1458, 2014. doi: 10.1007/s10712-013-9257-8.

R.E. Kopp, F.J. Simons, J.X. Mitrovica, A.C. Maloof, and M. Oppenheimer. Probabilistic assessment of sea level during the last interglacial stage. *Nature*, 462 (7275):863–867, 2009. doi: 10.1038/nature08686.

M. Křížek and P. Neittaanmäki. Finite Element Approximation of Variational Problems and Applications. J. Wiley, New York, 1990.

P. Kuipers Munneke, G. Picard, M.R. van den Broeke, J.T.M. Lenaerts, and E. van Meijgaard. Insignificant change in Antarctic snowmelt volume since 1979. *Geophys. Res. Lett.*, 39(1), 2012. doi: 10.1029/2011GL050207.

K. Lambeck. Glacial rebound of the British Isles – II. A high-resolution, high-precision model. *Geophys. J. Int.*, 115(3):960–990, 1993. doi: 10.1111/j.1365-246X.1993.tb01504.x.

K. Lambeck and J. Chappell. Sea Level Change Through the Last Glacial Cycle. *Science*, 292(5517):679–686, 2001. doi: 10.1126/science.1059549.

K. Lambeck and S. M. Nakiboglu. Seamount loading and stress in the ocean lithosphere. *J. Geophys. Res.*, 85(B11):6403–6418, 1980. doi: 10.1029/0JGREA000085000B11006403000001.

K. Lambeck, P. Johnston, and M. Nakada. Holocene glacial rebound and sea-level change in NW Europe. *Geophys. J. Int.*, 103(2):451–468, 1990. doi: 10.1111/j.1365-246X.1990.tb01784.x.

J. Laskar, P. Robutel, F. Joutel, M. Gastineau, A.C.M. Correia, and B. Levrard. A long-term numerical solution for the insolation quantities of the Earth. *Astron. Astrophys.*, 428(1):261–285, 2004. doi: 10.1051/0004-6361:20041335.

A.M. Le Brocq, A.J. Payne, and A. Vieli. An improved Antarctic dataset for high resolution numerical ice sheet models (ALBMAP v1). *Earth Syst. Sci. Data*, 2 (2):247–260, 2010. doi: 10.5194/essd-2-247-2010.

E. Le Meur and P. Huybrechts. A comparison of different ways of dealing with isostasy: examples from modeling the Antarctic ice sheet during the last glacial cycle. *Ann. Glaciol.*, 23:309–317, 1996.

E. Le Meur and P. Huybrechts. Present-day uplift patterns over Greenland from a coupled ice-sheet/visco-elastic bedrock model. *Geophys. Res. Lett.*, 25(21): 3951–3954, 1998. doi: 10.1029/1998GL900052.

S.R.M. Ligtenberg, W.J. van de Berg, M.R. van den Broeke, J.G.L. Rae, and E. van Meijgaard. Future surface mass balance of the Antarctic ice sheet and its influence on sea level change, simulated by a regional atmospheric climate model. *Clim. Dynam.*, 41(3–4):867–884, 2013. doi: 10.1007/s00382-013-1749-1.

L.E. Lisiecki and M.E. Raymo. A Pliocene-Pleistocene stack of 57 globally distributed benthic δ^{18}O records. *Paleoceanography*, 20(1), 2005. doi: 10.1029/2004PA001071.

Z. Liu, B.L. Otto-Bliesner, F. He, E.C. Brady, R. Tomas, P.U. Clark, A.E. Carlson, J. Lynch-Stieglitz, W. Curry, E. Brook, D. Erickson, R. Jacob, J. Kutzbach, and J. Cheng. Transient Simulation of Last Deglaciation with a New Mechanism for Bølling-Allerød Warming. *Science*, 325(5938):310–314, 2009. doi: 10.1126/science.1171041.

I.M. Longman. A Green's function for determining the deformation of the Earth under surface mass loads: 1. Theory. *J. Geophys. Res.*, 67(2):845–850, 1962. doi: 10.1029/JZ067i002p00845.

I.M. Longman. A Green's function for determining the deformation of the Earth under surface mass loads: 2. Computations and numerical results. *J. Geophys. Res.*, (2):485–496, 1963. doi: 10.1029/JZ068i002p00485.

A.C. Lough, D.A. Wiens, C. Grace Barcheck, S. Anandakrishnan, R.C. Aster, D.D. Blankenship, A.D. Huerta, A. Nyblade, D.A. Young, and T.J. Wilson. Seismic detection of an active subglacial magmatic complex in Marie Byrd Land, Antarctica. *Nature Geosci.*, 6(12):1031–1035, 2013. doi: 10.1038/ngeo1992.

D.R. MacAyeal. Binge/purge oscillations of the Laurentide Ice Sheet as a cause of the North Atlantic's Heinrich events. *Paleoceanography*, 8(6):775–784, 1993. doi: 10.1029/93PA02200.

M.N.A. Maris, B. de Boer, S.R.M. Ligtenberg, M. Crucifix, W.J. van de Berg, and J. Oerlemans. Modelling the evolution of the Antarctic ice sheet since the last interglacial. *The Cryosphere*, 8(4):1347–1360, 2014. doi: 10.5194/tc-8-1347-2014.

M.A. Martin, R. Winkelmann, M. Haseloff, T. Albrecht, E. Bueler, C. Khroulev, and A. Levermann. The Potsdam Parallel Ice Sheet Model (PISM-PIK) – Part 2: Dynamic equilibrium simulation of the Antarctic ice sheet. *The Cryosphere*, 5(3):727–740, 2011. doi: 10.5194/tc-5-727-2011.

Z. Martinec. Program to calculate the spectral harmonic expansion coefficients of the two scalar fields product. *Comput. Phys. Commun.*, 54(1):177–182, 1989. doi: 10.1016/0010-4655(89)90043-X.

Z. Martinec. Spectral-finite element approach to three-dimensional viscoelastic relaxation in a spherical Earth. *Geophys. J. Int.*, 142(1):117–141, 2000. doi: 10.1046/j.1365-246x.2000.00138.x.

Z. Martinec and J. Hagedoorn. Time-domain approach to linearized rotational response of a three-dimensional viscoelastic earth model induced by glacial-isostatic adjustment: I. Inertia-tensor perturbations. *Geophys. J. Int.*, 163(2): 443–462, 2005. doi: 10.1111/j.1365-246X.2005.02758.x.

D. Melini, G. Spada, and A. Piersanti. A sea level equation for seismic perturbations. *Geophys. J. Int.*, 180(1):88–100, 2010. doi: 10.1111/j.1365-246X.2009.04412.x.

J.H. Mercer. Antarctic ice and Sangamon sea level. *IAHS publications – red books*, 79:217–225, 1968. URL `http://iahs.info/uploads/dms/079020.pdf`.

G.A. Milne and J.X. Mitrovica. Postglacial sea-level change on a rotating Earth. *Geophys. J. Int.*, 133(1):1–19, 1998. doi: 10.1046/j.1365-246X.1998.1331455.x.

G.A. Milne, J.X. Mitrovica, and A.M. Forte. The sensitivity of glacial isostatic adjustment predictions to a low-viscosity layer at the base of the upper mantle. *Earth Planet. Sci. Lett.*, 154(1–4):265–278, 1998. doi: 10.1016/S0012-821X(97)00191-X.

G.A. Milne, J.X. Mitrovica, and J.L. Davis. Near-field hydro-isostasy: the implementation of a revised sea-level equation. *Geophys. J. Int.*, 139(2):464–482, 1999. doi: 10.1046/j.1365-246x.1999.00971.x.

J.X. Mitrovica and G.A. Milne. On post-glacial sea level: I. General theory. *Geophys. J. Int.*, 154(2):253–267, 2003. doi: 10.1046/j.1365-246X.2003.01942.x.

J.X. Mitrovica and W.R. Peltier. On postglacial geoid subsidence over the equatorial oceans. *J. Geophys. Res.*, 96(B12):20053–20071, 1991. doi: 10.1029/91JB01284.

A. Morelli and S. Danesi. Seismological imaging of the Antarctic continental lithosphere: a review. *Global Planet. Change*, 42(1–4):155–165, 2004. doi: j.gloplacha.2003.12.005.

J. Mouginot, E. Rignot, and B. Scheuchl. Sustained increase in ice discharge from the Amundsen Sea Embayment, West Antarctica, from 1973 to 2013. *Geophys. Res. Lett.*, 41(5):1576–1584, 2014. doi: 10.1002/2013GL059069.

S.M. Nakiboglu and K. Lambeck. Deglaciation effects on the rotation of the Earth. *Geophys. J. R. Astr. Soc.*, 62(1):49–58, 1980. doi: 10.1111/j.1365-246X.1980.tb04843.x.

F. Nansen. *The earth's crust, its surface-forms, and isostatic adjustment.* 1928.

G.A. Nield, P.L. Whitehouse, M.A. King, P.J. Clarke, and M.J. Bentley. Increased ice loading in the Antarctic Peninsula since the 1850s and its effect on glacial isostatic adjustment. *Geophys. Res. Lett.*, 39(17), 2012. doi: 10.1029/2012GL052559.

G.A. Nield, V.R. Barletta, A. Bordoni, M.A. King, P.L. Whitehouse, P.J. Clarke, E. Domack, T.A. Scambos, and E. Berthier. Rapid bedrock uplift in the Antarctic Peninsula explained by viscoelastic response to recent ice unloading. *Earth Planet. Sci. Lett.*, 397(0):32–41, 2014. doi: 10.1016/j.epsl.2014.04.019.

S. Nowicki, R.A. Bindschadler, and the SeaRISE participants. Insights into spatial sensitivities of ice mass response to environmental change from the SeaRISE ice sheet modeling project I: Antarctica. *J. Geophys. Res.*, 118(2):1002–1024, 2013. doi: 10.1002/jgrf.20081.

J.F. Nye. The Distribution of Stress and Velocity in Glaciers and Ice-Sheets. *Proc. Roy. Soc. A*, 239(1216):113–133, 1957. doi: 10.1098/rspa.1957.0026.

J. Oerlemans. Model experiments on the 100,000-yr glacial cycle. *Nature*, 287 (5781):430–432, 1980. doi: 10.1038/287430a0.

M. Olaizola, R.S.W. van de Wal, M.M. Helsen, and B. de Boer. An ice flow modeling perspective on bedrock adjustment patterns of the Greenland ice sheet. *The Cryosphere*, 6(6):1263–1274, 2012. doi: 10.5194/tc-6-1263-2012.

M. Oppenheimer. Global warming and the stability of the West Antarctic Ice Sheet. *Nature*, 393(6683):325–332, 1998. doi: 10.1038/30661.

D. Paillard. Glacial cycles: Toward a new paradigm. *Rev. Geophys.*, 39(3):325–346, 2001. doi: 10.1029/2000RG000091.

F. Pattyn. A new three-dimensional higher-order thermomechanical ice sheet model: Basic sensitivity, ice stream development, and ice flow across subglacial lakes. *J. Geophys. Res.*, 108(B8):2382, 2003. doi: 10.1029/2002JB002329.

F. Pattyn, C. Schoof, L. Perichon, R.C.A. Hindmarsh, E. Bueler, B. de Fleurian, G. Durand, O. Gagliardini, R. Gladstone, D. Goldberg, G.H. Gudmundsson, P. Huybrechts, V. Lee, F.M. Nick, A.J. Payne, D. Pollard, O. Rybak, F. Saito, and A. Vieli. Results of the Marine Ice Sheet Model Intercomparison Project, MISMIP. *The Cryosphere*, 6(3):573–588, 2012. doi: 10.5194/tc-6-573-2012.

F. Pattyn, L. Perichon, and the MISMIP3d participants. Grounding-line migration in plan-view marine ice-sheet models: results of the ice2sea MISMIP3d intercomparison. *J. Glaciol.*, 59(215):410–422, 2013. doi: 10.3189/2013JoG12J129.

A.J. Payne, P. Huybrechts, A. Abe-Ouchi, R. Calov, J.L. Fastook, R. Greve, S.J. Marshall, I. Marsiat, C. Ritz, L. Tarasov, and M.P.A. Thomassen. Results from the EISMINT model intercomparison: The effects of thermomechanical coupling. *J. Glaciol.*, 46(153):227–238, 2000. doi: 10.3189/172756400781820534.

W.R. Peltier. The impulse response of a Maxwell Earth. *Rev. Geophys.*, 12(4): 649–669, 1974. doi: 10.1029/RG012i004p00649.

W.R. Peltier. Ice Age Paleotopography. *Science*, 265(5169):195–201, 1994. doi: 10.1126/science.265.5169.195.

W.R. Peltier. Global glacial isostasy and the surface of the ice-age Earth: the ICE5G (VM2) model and GRACE. *Annu. Rev. Earth Pl. Sci.*, 32:111–149, 2004. doi: 10.1146/annurev.earth.32.082503.144359.

W.R. Peltier and J.T. Andrews. Glacial-isostatic adjustment – i. the forward problem. *Geophys. J. Int.*, 46(3):605–646, 1976. doi: 10.1111/j.1365-246X.1976.tb01251.x.

W.R. Peltier, W.E. Farrell, and J.A. Clark. Glacial isostasy and relative sea level: A global finite element model. *Tectonophysics*, 50(2–3):81–110, 1978. doi: 10.1016/0040-1951(78)90129-4.

W.R. Peltier, D.F. Argus, and R. Drummond. Space geodesy constrains ice age terminal deglaciation: The global ICE-6G_C (VM5a) model. *J. Geophys. Res*, 2014. doi: 10.1002/2014JB011176.

J.R. Petit, J. Jouzel, D. Raynaud, N.I. Barkov, J.-M. Barnola, I. Basile, M. Bender, J. Chappellaz, M. Davis, G. Delaygue, M. Delmotte, V.M. Kotlyakov, M. Legrand, V.Y. Lipenkov, C. Lorius, L. Pépin, C. Ritz, E. Saltzman, and M. Stievenard. Climate and atmospheric history of the past 420,000 years from the Vostok ice core, Antarctica. *Nature*, 399(6735):429–436, 1999. doi: 10.1038/20859.

D. Pollard and R.M. DeConto. Hysteresis in Cenozoic Antarctic ice-sheet variations. *Global Planet. Change*, 45(1–3):9–21, 2005. doi: 10.1016/j.gloplacha.2004.09.011.

D. Pollard and R.M. DeConto. Modelling West Antarctic ice sheet growth and collapse through the past five million years. *Nature*, 458(7236):329–332, 2009. doi: 10.1038/nature07809.

D. Pollard and R.M. DeConto. A simple inverse method for the distribution of basal sliding coefficients under ice sheets, applied to Antarctica. *The Cryosphere*, 6(5):953–971, 2012a. doi: 10.5194/tc-6-953-2012.

D. Pollard and R.M. DeConto. Description of a hybrid ice sheet-shelf model, and application to Antarctica. *Geosci. Model Dev.*, 5(5):1273–1295, 2012b. doi: 10.5194/gmd-5-1273-2012.

V. Radić and R. Hock. Regional and global volumes of glaciers derived from statistical upscaling of glacier inventory data. *J. Geophys. Res.*, 115(F1), 2010. ISSN 2156–2202. doi: 10.1029/2009JF001373.

Y. Ricard, G. Spada, and R. Sabadini. Polar wandering of a dynamic earth. *Geophys. J. Int.*, 113(2):284–298, 1993. doi: 10.1111/j.1365-246X.1993.tb00888.x.

E. Rignot, J. Mouginot, M. Morlighem, H. Seroussi, and B. Scheuchl. Widespread, rapid grounding line retreat of Pine Island, Thwaites, Smith, and Kohler glaciers, West Antarctica, from 1992 to 2011. *Geophys. Res. Lett.*, 41(10):3502–3509, 2014. doi: 10.1002/2014GL060140.

G.H. Roe and M.R. Allen. A comparison of competing explanations for the 100,000-yr Ice Age cycle. *Geophys. Res. Lett.*, 26(15):2259–2262, 1999. doi: 10.1029/1999GL900509.

E.J. Rohling, M. Fenton, F.J. Jorissen, P. Bertrand, G. Ganssen, and J.P. Caulet. Magnitudes of sea-level lowstands of the past 500,000 years. *Nature*, 394(6689):162–165, 1998. doi: 10.1038/28134.

R. Sabadini and B. Vermeersen. *Global Dynamics of the Earth: Applications of Normal Mode Relaxation Theory to Solid-Earth Geophysics*. Modern Approaches in Geophysics. Springer, 2004. ISBN 9781402012679.

I. Sasgen, Z. Martinec, and K. Fleming. Wiener optimal filtering of GRACE data. *Stud. Geophys. Geod.*, 50(4):499–508, 2006. doi: 10.1007/s11200-006-0031-y.

I. Sasgen, V. Klemann, and Z. Martinec. Toward the inversion of GRACE gravity fields for present-day ice-mass changes and glacial-isostatic adjustment in North America and Greenland. *J. Geodyn.*, 59–60:49–63, 2012. doi: 10.1016/j.jog.2012.03.004.

I. Sasgen, H. Konrad, E.R. Ivins, M.R. van den Broeke, J.L. Bamber, Z. Martinec, and V. Klemann. Antarctic ice-mass balance 2003 to 2012: regional reanalysis of GRACE satellite gravimetry measurements with improved estimate of glacial-isostatic adjustment based on GPS uplift rates. *The Cryosphere*, 7(5):1499–1512, 2013. doi: 10.5194/tc-7-1499-2013.

R.P. Scherer, A. Aldahan, S. Tulaczyk, G. Possnert, H. Engelhardt, and B. Kamb. Pleistocene Collapse of the West Antarctic Ice Sheet. *Science*, 281(5373):82–85, 1998. doi: 10.1126/science.281.5373.82.

C. Schoof. Ice sheet grounding line dynamics: Steady states, stability, and hysteresis. *J. Geophys. Res.*, 112(F3), 2007. doi: 10.1029/2006JF000664.

H.H.A. Schotman and L.L.A. Vermeersen. Sensitivity of glacial isostatic adjustment models with shallow low-viscosity earth layers to the ice-load history in relation to the performance of GOCE and GRACE. *Earth Planet. Sci. Let.*, 236 (3–4):828–844, 2005. doi: 10.1016/j.epsl.2005.04.008.

D.M. Schroeder, D.D. Blankenship, D.A. Young, and E. Quartini. Evidence for elevated and spatially variable geothermal flux beneath the West Antarctic Ice Sheet. *Proc. Natl. Acad. Sci. U.S.A.*, 111(25):9070–9072, 2014. doi: 10.1073/pnas.1405184111.

N.J. Shackleton. Oxygen isotopes, ice volume and sea level. *Quat. Sci. Rev.*, 6 (3–4):183–190, 1987. doi: 10.1016/0277-3791(87)90003-5.

N.M. Shapiro and M.H. Ritzwoller. Inferring surface heat flux distributions guided by a global seismic model: particular application to Antarctica. *Earth Planet. Sci. Lett.*, 223(1–2):213–224, 2004. doi: 10.1016/j.epsl.2004.04.011.

A. Shepherd, E.R. Ivins, and the IMBIE participants. A Reconciled Estimate of Ice-Sheet Mass Balance. *Science*, 338(6111):1183–1189, 2012. doi: 10.1126/science.1228102.

M. Siegert, N. Ross, H. Corr, J. Kingslake, and R. Hindmarsh. Late Holocene ice-flow reconfiguration in the Weddell Sea sector of West Antarctica. *Quaternary Sci. Rev.*, 78(0):98–107, 2013. doi: 10.1016/j.quascirev.2013.08.003.

M.J. Siegert and J.A. Dowdeswell. Numerical reconstructions of the eurasian ice sheet and climate during the late weichselian. *Quat. Sci. Rev.*, 23(11–13):1273–1283, 2004. doi: 10.1016/j.quascirev.2003.12.010.

N. Sneeuw. Global spherical harmonic analysis by least-squares and numerical quadrature methods in historical perspective. *Geophys. J. Int.*, 118(3):707–716, 1994. doi: 10.1111/j.1365-246X.1994.tb03995.x.

L.S. Sørensen, S.B. Simonsen, K. Nielsen, P. Lucas-Picher, G. Spada, G. Adalgeirsdottir, R. Forsberg, and C.S. Hvidberg. Mass balance of the Greenland ice sheet (2003–2008) from ICESat data – the impact of interpolation, sampling and firn density. *The Cryosphere*, 5(1):173–186, 2011. doi: 10.5194/tc-5-173-2011.

G. Spada, R. Sabadini, D.A. Yuen, and Y. Ricard. Effects on post-glacial rebound from the hard rheology in the transition zone. *Geophys. J. Int.*, 109(3):683–700, 1992. doi: 10.1111/j.1365-246X.1992.tb00125.x.

G. Spada, A. Antonioli, S. Cianetti, and C. Giunchi. Glacial isostatic adjustment and relative sea-level changes: the role of lithospheric and upper mantle heterogeneities in a 3-D spherical Earth. *Geophys. J. Int.*, 165(2):692–702, 2006. doi: 10.1111/j.1365-246X.2006.02969.x.

G. Spada, V.R. Barletta, V. Klemann, R.E.M. Riva, Z. Martinec, P. Gasperini, B. Lund, D. Wolf, L.L.A. Vermeersen, and M.A. King. A benchmark study for glacial isostatic adjustment codes. *Geophys. J. Int.*, 185(1):106–132, 2011. doi: 10.1111/j.1365-246X.2011.04952.x.

P. Stocchi and G. Spada. Influence of glacial isostatic adjustment upon current sea level variations in the mediterranean. *Tectonophysics*, 474(1–2):56–68, 2009. doi: 10.1016/j.tecto.2009.01.003.

P. Stocchi, C. Escutia, A.J.P. Houben, B.L.A. Vermeersen, P.K. Bijl, H. Brinkhuis, R.M. DeConto, S. Galeotti, S. Passchier, D. Pollard, and the Expedition 318 scientists. Relative sea-level rise around East Antarctica during Oligocene glaciation. *Nature Geosci.*, 6(5), 2013.

T.F. Stocker, D. Qin, G.-K. Plattner, M. Tignor, S.K. Allen, J. Boschung, A. Nauels, Y. Xia, V. Bex, and P.M. Midgley, editors. *Climate Change 2013: The Physical Science Basis. Contribution of Working Group I to the Fifth Assessment Report of the Intergovernmental Panel on Climate Change*. Cambridge University Press, 2013. doi: 10.1017/CBO9781107415324.

T.C. Sutterley, I. Velicogna, E. Rignot, J. Mouginot, T. Flament, M.R. van den Broeke, J.M. van Wessem, and C.H. Reijmer. Mass loss of the Amundsen Sea

Embayment of West Antarctica from four independent techniques. *Geophys. Res. Lett.*, 2014. doi: 10.1002/2014GL061940.

M. Thoma, A. Jenkins, D. Holland, and S. Jacobs. Modelling Circumpolar Deep Water intrusions on the Amundsen Sea continental shelf, Antarctica. *Geophys. Res. Lett.*, 35(18), 2008. doi: 10.1029/2008GL034939.

M. Thoma, K. Grosfeld, C. Mayer, and F. Pattyn. Interaction between ice sheet dynamics and subglacial lake circulation: a coupled modelling approach. *The Cryosphere*, 4(1):1–12, 2010. doi: 10.5194/tc-4-1-2010.

M. Thoma, K. Grosfeld, C. Mayer, and F. Pattyn. Ice flow sensitivity to boundary processes: A coupled model study in the Vostok Subglacial Lake area. *Ann. Glaciol.*, 53(60):173–180, 2012. doi: 10.3189/2012AoG60A009.

M. Thoma, K. Grosfeld, D. Barbi, J. Determann, S. Goeller, C. Mayer, and F. Pattyn. RIMBAY – a multi-approximation 3D ice-dynamics model for comprehensive applications: model description and examples. *Geosci. Model Dev.*, 7(1): 1–21, 2014. doi: 10.5194/gmd-7-1-2014.

R. Thomas, E. Rignot, G. Casassa, P. Kanagaratnam, C. Acuña, T. Akins, H. Brecher, E. Frederick, P. Gogineni, W. Krabill, S. Manizade, H. Ramamoorthy, A. Rivera, R. Russell, J. Sonntag, R. Swift, J. Yungel, and J. Zwally. Accelerated Sea-Level Rise from West Antarctica. *Science*, 306(5694):255–258, 2004. doi: 10.1126/science.1099650.

R. Thomas, B. Scheuchl, E. Frederick, R. Harpold, C. Martin, and E. Rignot. Continued slowing of the Ross Ice Shelf and thickening of West Antarctic Ice streams. *J. Glaciol.*, 59(217):838–844, 2013. doi: 10.3189/2013JoG12J122.

R.H. Thomas and C.R. Bentley. A model for holocene retreat of the west antarctic ice sheet. *Quatern. Res.*, 10(2):150–170, 1978. doi: 10.1016/0033-5894(78) 90098-4.

R. Timmermann and H.H. Hellmer. Southern Ocean warming and increased ice shelf basal melting in the twenty-first and twenty-second centuries based on coupled ice-ocean finite-element modelling. *Ocean Dynam.*, 63(9–10):1011–1026, 2013. doi: 10.1007/s10236-013-0642-0.

D.L. Turcotte and G. Schubert. *Geodynamics*. Cambridge University Press, 2002.

W.J. van de Berg, M.R. van den Broeke, C.H. Reijmer, and E. van Meijgaard. Reassessment of the Antarctic surface mass balance using calibrated output of a regional atmospheric climate model. *J. Geophys. Res.*, 111:D11104, 2006. doi: 10.1029/2005JD006495.

J. van den Berg, R.S.W. van de Wal, G.A. Milne, and J. Oerlemans. Effect of isostasy on dynamical ice sheet modeling: A case study for Eurasia. *J. Geophys. Res.*, 113:B05412, 2008. doi: 10.1029/2007JB004994.

W. van der Wal, A. Barnhoorn, P. Stocchi, S. Gradmann, P. Wu, M. Drury, and B. Vermeersen. Glacial isostatic adjustment model with composite 3-D Earth rheology for Fennoscandia. *Geophys. J. Int.*, 194(1):61–77, 2013. doi: 10.1093/gji/ggt099.

W. van der Wal, P.L. Whitehouse, and E.J.O. Schrama. Effect of GIA models with 3D composite mantle viscosity on GRACE mass balance estimates for Antarctica. *Earth Planet. Sci. Lett.*, 414(0):134–143, 2015. doi: 10.1016/j.epsl.2015.01.001.

D. Varshalovich, A.N. Moskalev, and V.K. Khersonskii. *Quantum theory of angular momentum*. World Scientific, 1989.

L.L.A. Vermeersen and R. Sabadini. Significance of the fundamental mantle rotational relaxation mode in polar wander simulations. *Geophys. J. Int.*, 127(2): F5–F9, 1996. doi: 10.1111/j.1365-246X.1996.tb04717.x.

A. B. Watts. *Isostasy and Flexure of the Lithosphere*. Cambridge University Press, 2001. ISBN 9780521006002.

A.J. Weaver, O.A. Saenko, P.U. Clark, and J.X. Mitrovica. Meltwater Pulse 1A from Antarctica as a Trigger of the Bølling-Allerød Warm Interval. *Science*, 299 (5613):1709–1713, 2003. doi: 10.1126/science.1081002.

J. Weertman. On the sliding of glaciers. *J. Glaciol.*, 3(21):33–38, 1957.

J. Weertman. Stability of the junction of an ice sheet and an ice shelf. *J. Glaciol.*, 13(67):3–11, 1974.

P. Wessel and W.H.F. Smith. Free software helps map and display data. *Eos Trans. AGU*, 72(41):441, 1991. doi: 10.1029/90EO00319.

P.L. Whitehouse, M.J. Bentley, and A.M. Le Brocq. A deglacial model for Antarctica: geological constraints and glaciological modelling as a basis for a new model of Antarctic glacial isostatic adjustment. *Quat. Sci. Rev.*, 32(0):1–24, 2012a. doi: 10.1016/j.quascirev.2011.11.016.

P.L. Whitehouse, M.J. Bentley, G.A. Milne, M.A. King, and I.D. Thomas. A new glacial isostatic adjustment model for Antarctica: calibrated and tested using observations of relative sea-level change and present-day uplift rates. *Geophys. J. Int.*, 190(3):1464–1482, 2012b. doi: 10.1111/j.1365-246X.2012.05557.x.

D. Wolf. Viscoelastodynamics of A Stratified, Compressible Planet: Incremental Field Equations and Short- and Long-Time Asymptotes. *Geophys. J. Int.*, 104 (2):401–417, 1991. doi: 10.1111/j.1365-246X.1991.tb02520.x.

P. Wu and W.R. Peltier. Viscous Gravitational Relaxation. *Geophys. J.R. Astr. Soc.*, 70:435–485, 1982.

P. Wu and W.R. Peltier. Pleistocene deglaciation and the Earth's rotation: a new analysis. *Geophys. J. R. Astr. Soc.*, 76(3):753–791, 1984. doi: 10.1111/j.1365-246X.1984.tb01920.x.

H. J. Zwally and M. B. Giovinetto. Overview and Assessment of Antarctic Ice-Sheet Mass Balance Estimates: 1992–2009. *Surv. Geophys.*, 32(4–5):351–376, 2011. doi: 10.1007/s10712-011-9123-5.

Acknowledgements/Danksagungen

An dieser Stelle möchte ich mich zunächst bei Ingo Sasgen für die tagtägliche Betreuung meiner Doktorarbeit bedanken, sei es aus dem Büro ein paar Schritte den Gang hinunter, sei es aus Kalifornien oder Pennsylvania. Sein Ohr und sein E-Mail-Postfach waren immer offen, seine Grundstimmung immer positiv und seine Ratschläge hinsichtlich der Ausrichtung meiner wissenschaftlichen Arbeit immer zielführend. Weiterhin bedanke ich mich bei Volker Klemann für die fruchtbaren Diskussionen, für die Hinweise auf die notwendigen Verbesserungen und die vielfältigen Implikationen meiner Arbeit und für die konstruktive Kritik an meinen zarten Visualisierungsversuchen. Ich habe in den vergangenen Jahren sehr gerne mit den beiden zusammen gearbeitet.

Maik Thomas danke ich für die Unterstützung meiner Arbeit und seine Begleitung als Betreuer sowie seine offene Tür.

Zdeněk Martinec, David Pollard, Malte Thoma, and Klaus Grosfeld supported me and my work with their numerical models for solid-Earth and ice dynamics, many discussions, advices and proofreadings, for which I am very grateful.

Ebenso möchte ich mich bei Jan Hagedoorn für das Korrekturlesen einer frühen Version bedanken.

Finanziert wurde mein Schaffen durch die Deutsche Forschungsgemeinschaft und die REKLIM Initiative (Regionale Klimaänderungen) der Helmholtzgemeinschaft. Im Rahmen dieser Initiative habe ich die Zusammenarbeit mit den Kollegen am Alfred-Wegener-Institut sehr zu schätzen gelernt.

Zuletzt möchte ich mich bei Anik und Johanna, meiner Familie, dafür bedanken, dass sie mir, insbesondere als diese Arbeit in ihren letzten Zügen lag, die notwendigen Freiheiten ließen, aber auch dafür, dass ich durch sie und für sie (fast) jeden Abend beim Arbeiten ein Ende gefunden habe.

Appendix

A Notation for vector and tensor operations

A^{T} – For a $m \times n$ matrix A (m, n: positive integers), the components of the transposed matrix A^{T} are $(A^{\mathrm{T}})_{ji} = A_{ij}$ with $i \in \{1, ..., m\}$ and $j \in \{1, ..., n\}$. A^{T} is $n \times m$.

$A \cdot B$ – The product of a $m \times n$ matrix A and a $n \times p$ matrix B is defined for each component as $(A \cdot B)_{ij} = \sum_{k=1}^{n} A_{ik} B_{kj}$ for $i \in \{1, ..., m\}$ and $j \in \{1, ..., p\}$. $A \cdot B$ is $m \times p$.

A^n – The above product also defines natural exponents for a quadratic $n \times n$ matrix A: $(A^2)_{ij} = (A \cdot A)_{ij} = \sum_{k=1}^{n} A_{ik} A_{kj}$, etc.

$\vec{a} \cdot \vec{b}$ – The scalar product of two vectors $\vec{a}$ and $\vec{b}$ from an n-dimensional vector space is $\vec{a} \cdot \vec{b} = \sum_{i=1}^{n} a_i b_i$. Its notation is inconsistent with the above definition of the matrix product: $\vec{a}$ and $\vec{b}$ are both $n \times 1$ matrices, so that a consistent notation would be $\vec{a}^{\mathrm{T}} \cdot \vec{b}$. The transposition is, however, dropped for an easier reading.

$\mathrm{tr}\, A$ – The trace of a (quadratic) $n \times n$ matrix A is defined as $\mathrm{tr} A = \sum_{i=1}^{n} A_{ii}$, i.e. the sum over the diagonal elements.

B Details on the solid-Earth model VILMA

B.1 Weak formulation of solid-Earth dynamics

By formulating the initial boundary value problem for solid-Earth dynamics (Section 2.3.1) in a weak sense (Křížek and Neittaanmäki, 1990), functions $\vec{U}$ (displacement field), ϕ_1 (incremental gravitational potential), and P (perturbation pressure) from specific function spaces (here combined in by $(\vec{U}, \phi_1, P) \in \mathscr{V}$) have to be found, which fulfil the initial condition in Eq. 2.52 and an appropriate variational equality. Martinec (2000) showed the equivalence of the weak and the strong formulation, the existence of the solution and its uniqueness. This section briefly outlines the approach by Martinec (2000).

The respective variational equality, that has to be fulfilled by the required solution $(\vec{U}, \phi_1, P)$ at time t^{i+1}, is

$$\delta\mathscr{E}(\vec{U}^{i+1}, \phi_1^{i+1}, P^{i+1}, \delta\vec{U}, \delta\phi_1, \delta P) = \delta\mathscr{F}^{i+1}(\delta\vec{U}, \delta\phi_1) \quad \forall(\delta\vec{U}, \delta\phi_1, \delta P) \in \mathscr{V} \ . \tag{B.1}$$

Here, $\delta\mathscr{E}$ is the variation of the energy functional $\mathscr{E}$ that can be written as

$$\begin{aligned} \delta\mathscr{E}(\vec{U}, \phi_1, P, \delta\vec{U}, \delta\phi_1, \delta P) &= \delta\mathscr{E}_{\mathrm{p}}(\vec{U}, P, \delta\vec{U}, \delta P) + \delta\mathscr{E}_{\mathrm{s}}(\vec{U}, \delta\vec{U}) \\ &\quad + \delta\mathscr{E}_{\mathrm{g}}(\vec{U}, \phi_1, \delta\vec{U}, \delta\phi_1) + \delta\mathscr{E}_{\mathrm{u}}(\vec{U}, \delta\vec{U}) \end{aligned} \tag{B.2}$$

with the respective variations of the functionals for pressure $\delta\mathscr{E}_{\mathrm{p}}$, elastic shear energy $\delta\mathscr{E}_{\mathrm{s}}$, gravitational energy $\delta\mathscr{E}_{\mathrm{g}}$, and uniqueness $\delta\mathscr{E}_{\mathrm{u}}$:

$$\delta\mathscr{E}_{\mathrm{p}}(\vec{U}, P, \delta\vec{U}, \delta P) = \int_{B_{\mathrm{E}}} \delta P \, \mathrm{div}\, \vec{U} \, \mathrm{d}V + \int_{B_{\mathrm{E}}} P \, \mathrm{div}\, \delta\vec{U} \, \mathrm{d}V \tag{B.3}$$

$$\delta\mathscr{E}_{\mathrm{s}}(\vec{U}, \delta\vec{U}) = 2 \int_{B_{\mathrm{E}}} \mu \, \mathrm{tr}\, (\underline{\boldsymbol{\mathcal{E}}} \cdot \delta\underline{\boldsymbol{\mathcal{E}}}) \, \mathrm{d}V \tag{B.4}$$

$$\begin{aligned} \delta\mathscr{E}_{\mathrm{g}}(\vec{U}, \phi_1, \delta\vec{U}, \delta\phi_1) &= \int_{B_{\mathrm{E}}} \rho_0 \, \delta\vec{U} \cdot \left(\vec{g}_0 \, \mathrm{div}\, \vec{U} - \mathrm{grad}\left(\vec{U} \cdot \vec{g}_0\right) + \mathrm{grad}\, \phi_1 \right) \mathrm{d}V \\ &\quad + \int_{B_{\mathrm{E}}} \left[\frac{1}{4\,\pi\,G} \, \mathrm{grad}\, \phi_1 + \rho_0 \, \vec{U} \right] \cdot \mathrm{grad}\, \delta\phi_1 \, \mathrm{d}V \end{aligned} \tag{B.5}$$

$$\delta\mathscr{E}_{\mathrm{u}}(\vec{U},\delta\vec{U}) = \left(\int_{B_{\mathrm{E}}} \rho_0\,\vec{U}\,\mathrm{d}V\right)\cdot\left(\int_{B_{\mathrm{E}}} \rho_0\,\delta\vec{U}\,\mathrm{d}V\right) + \left(\int_{B_{\mathrm{E}}} \left(\vec{e}_R\times\rho_0\,\vec{U}\right)\mathrm{d}V\right)\cdot\left(\int_{B_{\mathrm{E}}} \left(\vec{e}_R\times\rho_0\,\delta\vec{U}\right)\mathrm{d}V\right) \quad . \tag{B.6}$$

B_{E} stands for the whole Earth, whereas S_{E} stands for the Earth's surface; ρ_0 is the Earth's density; μ is the elastic shear modulus; $\vec{g}_0$ is the initial gravitational acceleration; $\vec{e}_R$ is the unity vector in radial direction; G is Newton's gravitational constant. In Eq. B.4, the variation of the strain rate tensor $\underline{\boldsymbol{\mathcal{E}}}$, $\delta\underline{\boldsymbol{\mathcal{E}}}$, is defined as

$$\delta\underline{\boldsymbol{\mathcal{E}}} = \frac{1}{2}\left[\mathrm{grad}\,\delta\vec{U} + \left(\mathrm{grad}\,\delta\vec{U}\right)^{\mathrm{T}}\right] \quad . \tag{B.7}$$

The right-hand side of the equality B.1 is the variation of the linear functional $\mathscr{F}^{i+1}$, which is given by

$$\delta\mathscr{F}^{i+1}(\delta\vec{U},\delta\phi_1) = -\int_{B_{\mathrm{E}}} \mathrm{tr}\left(\underline{\boldsymbol{\mathcal{T}}}^{\,i}_{\mathrm{v}}\cdot\delta\underline{\boldsymbol{\mathcal{E}}}\right)\mathrm{d}V + \int_{S_{\mathrm{E}}} \left(\vec{b}_0^{\,i+1}\cdot\delta\vec{U}^{i+1} + b_1^{i+1}\delta\phi_1^{i+1}\right)\mathrm{d}S \quad . \tag{B.8}$$

The first summand on the right-hand side of Eq. B.8 stands for the dissipative energy, for which the viscous part of the stress tensor at time t^i, $\underline{\boldsymbol{\mathcal{T}}}^{\,i}_{\mathrm{v}}$, can be considered as known. The second summand ensures the fulfilling of the surface boundary conditions given by the surface load σ,

$$\vec{b}_0 = -g\,\sigma\vec{e}_R \ \text{ and} \tag{B.9}$$

$$b_1 = \frac{1}{4\,\pi\,G}\left[\mathrm{grad}\,\phi_1\right]^{+}\cdot\vec{e}_R - \sigma \quad . \tag{B.10}$$

Here, g stands for the scalar gravitational acceleration at the Earth's surface.

B.2 The spectral–finite-element approach

The usage of spherical coordinates and spherical harmonics is motivated from the spherical shape of the model domain. The field quantities $\vec{U}$, ϕ_1, and P as discussed in Section 2.3 and Appendix B.1 can be expressed with spherical harmonics (and

likewise their variations):

$$\vec{U}(R,\Omega,t) = \sum_{j=0}^{\infty}\sum_{m=-j}^{j}\Big(U_{jm}(R,t)\vec{S}_{jm}^{(-1)}(\Omega)+V_{jm}(R,t)\vec{S}_{jm}^{(1)}(\Omega) + W_{jm}(R,t)\vec{S}_{jm}^{(0)}(\Omega)\Big) \tag{B.11}$$

$$\begin{pmatrix}\phi_1(R,\Omega,t)\\ P(R,\Omega,t)\end{pmatrix} = \sum_{j=0}^{\infty}\sum_{m=-j}^{j}\begin{pmatrix}F_{jm}(R,t)\\ P_{jm}(R,t)\end{pmatrix}Y_{jm}(\Omega)\ . \tag{B.12}$$

$Y_{jm}(\Omega)$ is the scalar spherical harmonics of Legendre degree j and order m; $\vec{S}_{jm}^{(\nu)}(\Omega)$, $\nu\in\{-1,0,1\}$, are the respective vector spherical harmonics. The tensor quantities $\underline{\boldsymbol{\mathcal{T}}}$, $\underline{\boldsymbol{\mathcal{T}}}_{\mathrm{v}}$, and $\underline{\boldsymbol{\mathcal{E}}}$ can likewise be expressed in terms of tensor spherical harmonics $\underline{\boldsymbol{\mathcal{Z}}}_{jm}^{(\nu)}(\Omega)$ with $1\le\nu\le 6$. A short overview of spherical harmonics is given in Section B.2.2.

The radial (R) dependencies are approximated by finite elements, namely by piecewise linear basis function $\Psi_k(R)$ in the case of $\vec{U}$, ϕ_1, $\delta\vec{U}$, and $\delta\phi_1$, and by piecewise constant basis functions $\xi_k(R)$ for P and δP where the index k enumerates the nodes of radial intervals from 1 to n_R+1: $0=R_1<R_2<\ldots<R_{n_R}<R_{n_R+1}=R_{\mathrm{E}}$. The linear basis functions are chosen by $\Psi_k(R_i)=\delta_{ki}$; the two non-zero linear basis functions in the interval $[R_k,R_{k+1}]$ are

$$\Psi_k(R)=\frac{R_{k+1}-R}{R_{k+1}-R_k}\qquad\text{and}\qquad\Psi_{k+1}(R)=\frac{R-R_k}{R_{k+1}-R_k} \tag{B.13}$$

The piecewise constant basis functions are

$$\xi_k(R)=\begin{cases}1 & \text{if } R\in[R_k,R_{k+1}]\\ 0 & \text{else}\end{cases}\ . \tag{B.14}$$

Then, the respective coefficients are

$$\begin{pmatrix}U_{jm}(R)\\ V_{jm}(R)\\ W_{jm}(R)\\ F_{jm}(R)\end{pmatrix} = \sum_{k=1}^{n_R+1}\begin{pmatrix}U_{jm}^k\\ V_{jm}^k\\ W_{jm}^k\\ F_{jm}^k\end{pmatrix}\Psi_k(R) \tag{B.15}$$

$$P_{jm}(R) = \sum_{k=1}^{n_R+1}P_{jm}^k\xi_k(R)\ . \tag{B.16}$$

By also expressing the surface load $\sigma(\Omega,t)$ by spherical harmonics,

$$\sigma(\Omega,t)=\sum_{j=0}^{\infty}\sum_{m=-j}^{j}\sigma_{jm}(t)\,Y_{jm}(\Omega)\ , \tag{B.17}$$

and assuming piecewise constant elastic modulus $\mu(R)$ and density $\rho_0(R)$ analogously to $P_{jm}(R)$ in Eq. B.16, the variational equality B.1 can be rearranged so that the solution can be found in terms of the coefficients U^k_{jm}, ..., P^k_{jm} in Eqs. B.15 and B.16. The numerical solution naturally requires not only a finite radial resolution given by n_R, but also a finite cut-off degree $j_{\max}$ for the spherical harmonics expansion, so that eventually, the numerical solution is:

$$\begin{aligned}\vec{U}(R,\Omega,t) &= \sum_{j=0}^{j_{\max}}\sum_{m=-j}^{j}\sum_{k=1}^{n_R+1}\Big(U^k_{jm}(t)\,\Psi_k(R)\,\vec{S}^{(-1)}_{jm}(\Omega) \\ &\qquad +V^k_{jm}(t)\,\Psi_k(R)\,\vec{S}^{(1)}_{jm}(\Omega)+W^k_{jm}(t)\,\Psi_k(R)\,\vec{S}^{(0)}_{jm}(\Omega)\Big) \qquad \text{(B.18)}\\ \phi_1(R,\Omega,t) &= \sum_{j=0}^{j_{\max}}\sum_{m=-j}^{j}\sum_{k=1}^{n_R+1}F^k_{jm}(t)\,\Psi_k(R)\,Y_{jm}(\Omega) \qquad \text{(B.19)}\\ P(R,\Omega,t) &= \sum_{j=0}^{j_{\max}}\sum_{m=-j}^{j}\sum_{k=1}^{n_R+1}P^k_{jm}(t)\,\xi_k(R)\,Y_{jm}(\Omega) \qquad \text{(B.20)}\end{aligned}$$

B.2.1 Time-differencing scheme for Maxwell-Viscoelasticity

With ρ_0 and μ varying only radially, it is convenient to apply an explicit Euler differencing scheme for solving Eq. 2.50. The Cauchy stress tensor is divided into the elastic part given by Eq. 2.51 and the remaining part related to viscous deformation $\underline{\boldsymbol{\mathcal{T}}}_{\rm v}$; then, Eq. 2.51 can be formulated as (Martinec, 2000):

$$\begin{aligned}\underline{\boldsymbol{\mathcal{T}}}^{\,i+1} &= \underline{\boldsymbol{\mathcal{T}}}^{\,i+1}_{\rm e}+\underline{\boldsymbol{\mathcal{T}}}^{\,i}_{\rm v} \ \text{ with} \qquad \text{(B.21)}\\ \underline{\boldsymbol{\mathcal{T}}}^{\,i}_{\rm v} &= \left[1-\frac{\mu}{\eta}\left(t^{i+1}-t^i\right)\right]\underline{\boldsymbol{\mathcal{T}}}^{\,i-1}_{\rm v}-2\,\mu\frac{\mu}{\eta}\left(t^{i+1}-t^i\right)\underline{\boldsymbol{\mathcal{E}}}^{\,i}\ . \qquad \text{(B.22)}\end{aligned}$$

The upper indices $i(+1)$ stand for the respective quantities at the given time step $i(+1)$.

Inserting Eq. B.21 in the equation for the linear momentum balance 2.37 yields a respective equation where $\underline{\boldsymbol{\mathcal{T}}}_{\rm e}$ and $\underline{\boldsymbol{\mathcal{T}}}_{\rm v}$ are also separated:

$$\mathrm{div}\,\underline{\boldsymbol{\mathcal{T}}}^{\,i+1}_{\rm e}-\rho_0\,\mathrm{grad}\,\phi^{i+1}_1-\mathrm{div}\left(\rho_0\vec{U}^{i+1}\right)\vec{g}_0+\mathrm{grad}\left(\rho_0\vec{U}^{i+1}\cdot\vec{g}_0\right)=-\mathrm{div}\,\underline{\boldsymbol{\mathcal{T}}}^{\,i}_{\rm v}\ . \tag{B.23}$$

At time t^{i+1}, $\underline{\boldsymbol{\mathcal{T}}}_{\mathrm{v}}^{\,i}$ is known as it can be calculated via Eq. B.22 from known fields $\underline{\boldsymbol{\mathcal{T}}}_{\mathrm{v}}^{\,i-1}$ and $\underline{\boldsymbol{\mathcal{E}}}^{i}$.

B.2.2 Spherical harmonics

The scalar, vector and tensor spherical harmonics are defined following Varshalovich et al. (1989). The scalar spherical harmonics for degree j and order m are given by

$$Y_{jm}(\Omega) = Y_{jm}(\varphi,\theta) = p_{jm}(\cos\,\theta)\, e^{\mathrm{i}m\varphi} \tag{B.24}$$

with $\theta = \pi/2 - \lambda$ being colatitude[viii], φ being longitude, p_{jm} being the associated Legendre polynomial of degree j and order m and i being the imaginary unit. It is

$$p_{jm}(\cos\,\theta) = (-\sin\,\theta)^m \sqrt{\frac{2\,j+1}{4\,\pi}\frac{(j-m)!}{(j+m)!}}\,\frac{\mathrm{d}^m}{\mathrm{d}(\cos\,\theta)^m}\,p_j(\cos\,\theta) \tag{B.25}$$

with the Legendre polynomial p_j of order j

$$p_j(\cos\,\theta) = \frac{1}{2^j\,j!}\,\frac{\mathrm{d}^j}{\mathrm{d}(\cos\,\theta)^j}\,\left((\cos\,\theta)^2-1\right)^j \quad . \tag{B.26}$$

The scalar spherical harmonics are orthonormal:

$$\int_{\Omega_0} Y_{jm}(\Omega)\,Y^*_{j'm'}(\Omega)\,\mathrm{d}\Omega = \delta_{jj'}\,\delta_{mm'} \quad . \tag{B.27}$$

Here, Ω_0 stands for the surface of the unit sphere, * marks the complex conjugate, and δ_{ij} is the Kronecker Delta, i.e. $\delta_{ij} = 1$ if $i = j$ and 0 else.

The vector spherical harmonics are defined on the basis of Y_{jm}:

$$\vec{S}^{(-1)}(\Omega) = \vec{e}_R\,Y_{jm}(\Omega) \quad , \tag{B.28}$$

$$\vec{S}^{(0)}(\Omega) = \vec{\nabla}_\Omega\,Y_{jm}(\Omega) \quad , \tag{B.29}$$

$$\vec{S}^{(1)}(\Omega) = \vec{L}_\Omega\,Y_{jm}(\Omega) \quad , \tag{B.30}$$

[viii] Note that for the sake of an easier reading, no difference shall be made between $\Omega = (\varphi,\theta)$ and $\Omega = (\varphi,\lambda)$, but imply that it is $\Omega = (\varphi,\lambda) = (\varphi,\lambda(\theta))$ or vice versa.

with the angular gradient operator

$$\vec{\nabla}_\Omega = \vec{e}_\theta \frac{\partial}{\partial \theta} + \vec{e}_\varphi \frac{1}{\sin\,\theta}\,\frac{\partial}{\partial \varphi} \tag{B.31}$$

and the operator

$$\vec{L}_\Omega = \vec{e}_R \times \vec{\nabla}_\Omega \quad . \tag{B.32}$$

With $\vec{S}^{(-1)}$ being parallel to the radial unit vector $\vec{e}_R$, the series

$$U(R,\Omega,t) = \sum_{j=0}^{\infty} \sum_{m=-j}^{j} U_{jm}(R,t)\, Y_{jm}(\Omega) \tag{B.33}$$

yields the radial displacement as it is used in the SLE (Section 2.3.2) and the coupling with the ice-sheet models (Section 2.4). For the definition of the tensor spherical harmonics see Martinec (2000) and Hagedoorn (2005).

C Additional material on the idealized scenarios

Run	$T_{S,\min}$ (°C)			$\dot{b}_{S,\max}$ (m we/yr)			$\dot{b}_{S,\mathrm{div}}$ (m we/yr)		
RE	−35.7	−27.5	−35.7	0.304	0.376	0.304	0.188	0.258	0.188
E1	−30.8	−23.5	−30.8	0.333	0.408	0.333	0.228	0.300	0.228
E2	−31.2	−23.9	−31.2	0.333	0.406	0.333	0.225	0.295	0.224
E3	−31.5	−24.2	−31.5	0.332	0.405	0.332	0.222	0.292	0.222
V. VM2	−31.1	−23.8	−31.1	0.333	0.407	0.333	0.225	0.297	0.226
V. S12	−31.1	−23.8	−31.1	0.333	0.407	0.333	0.225	0.297	0.226

Table C.1
Additional results from the experiments in Section 3.1: Minimum surface temperature, maximum surface mass balance (SMB) and SMB at the ice divide at the end of each period (149 kyr / 299 kyr / 449 kyr); 'we' stands for water equivalent. RE stands for 'rigid Earth'. En stands for the ELRA run with $D = n{\times}10^{25}$ N m. 'V. VM2/S12' stands for 'VILMA VM2/S12'. The ELRA runs are those with $\tau_\mathrm{r} = 5$ kyr.

Run	Δ_vol		$\Delta_{\max\ \mathrm{ice}}$		$\Delta_{\max\ \mathrm{bed}}$		
RE	−4.5	−3.7	−5.7	−4.5			
E1	1.6	1.4	1.1	0.8	9.0	(9.9)	9.0
E2	0.4	0.1	−0.6	−0.9	−5.0	(−4.2)	−8.2
E3	−0.4	−0.5	−1.6	−1.8	−13.9	(−13.1)	−18.2
V. S12	0.0	0.0	0.0	0.0	0.1	(0.2)	0.0

Table C.2
Additional results from the experiments in Section 3.1: Relative deviation of ice volume Δ_vol, maximum ice thickness ($\Delta_{\max\ \mathrm{ice}}$) and maximum bedrock depression ($\Delta_{\max\ \mathrm{bed}}$ in terms of deviation from the initial altitude of 2000 m) in steady state from the VILMA VM2 run (in percent). The first value is for the cold periods, the second for the warm period. In the case of $\Delta_{\max\ \mathrm{bed}}$, the first value refers to the first cold period (Period 1) and the bracketed value to the second cold period (Period 3). Negative signs mean that there is less volume, less ice at the ice divide, or less depression as in the chosen reference (VILMA VM2). The ELRA runs are those with $\tau_\mathrm{r} = 5$ kyr.

D Additional material on the AIS simulations

D.1 Input fields for the AIS

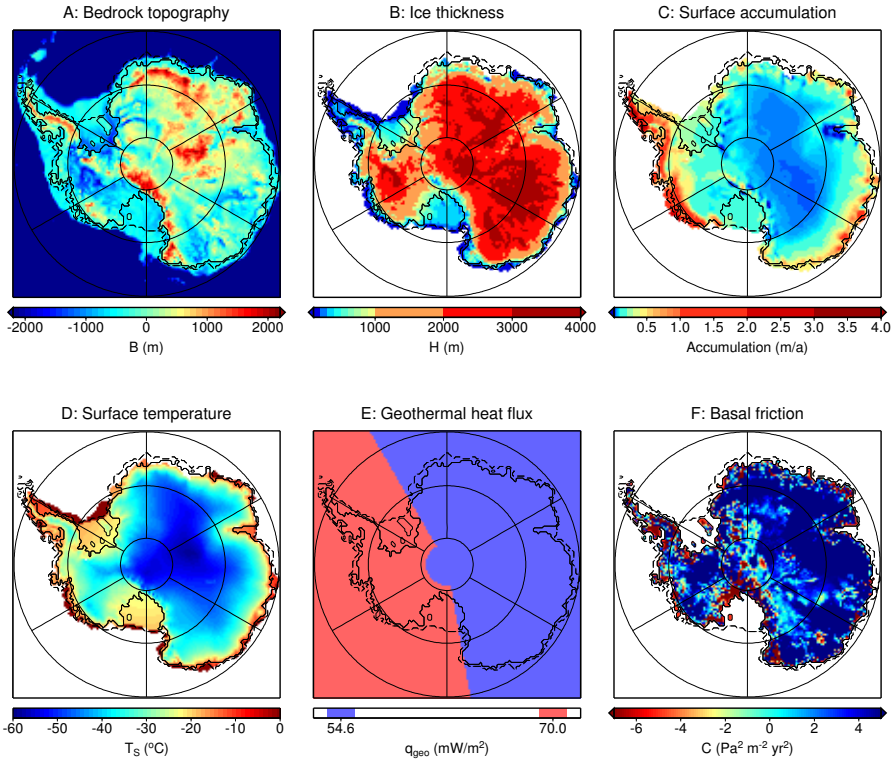

Figure D.1
Present-day geometry and boundary conditions of the AIS. A: BEDMAP2 bedrock topography. B: BEDMAP2 ice thickness (both from Fretwell et al., 2013). C: Surface accumulation (van de Berg et al., 2006). D: surface temperature (Comiso, 2000). E: Geothermal heat flux as employed by Pollard and DeConto (2012b). F: Basal friction coefficient C according to Pollard and DeConto (2012a) – cf. Eq. 2.21. Note that Pollard and DeConto (2012a,b) formulate the sliding law inversely w.r.t Eq. 2.21. The black solid line indicates the present-day grounding line. The black dashed line marks the present-day calving front.

D.2 Initialization of the present-day state

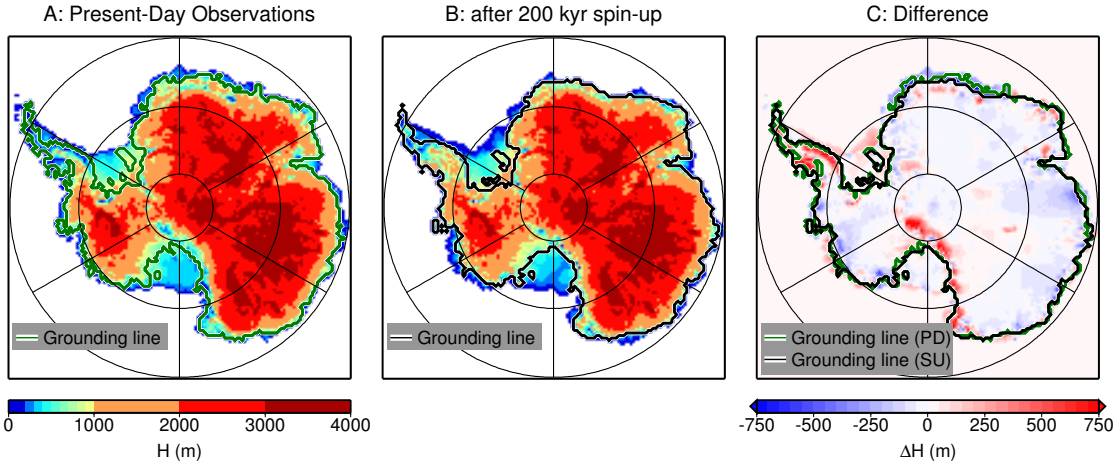

Figure D.2
A: Observations of present-day ice thickness (H_{PD}) on the AIS and the surrounding ice shelves as presented by Fretwell et al. (2013) at the ice-sheet model's resolution. This data set serves as input to the initialization run. B: Steady-state ice thickness after 200 kyr of initialization (H_0). C: Difference in ice thickness ($H_0 - H_{\mathrm{PD}}$). Larger differences occur in steep regions (Antarctic Peninsula, Transantarctic Mountains) where the sliding law might yield too low velocities for reproducing the thinner observed ice. In general, GL migration from A to B covers only few grid points. In the relevant area (WAIS), the major change is the straightening of the Ross Ice Shelf GL, which is a common evolution (Nowicki et al., 2013). Note the logarithmic colorscale in A and B and the open linear scale in C. 'PD' stands for 'present day'; 'SU' stands for 'after spin-up'.

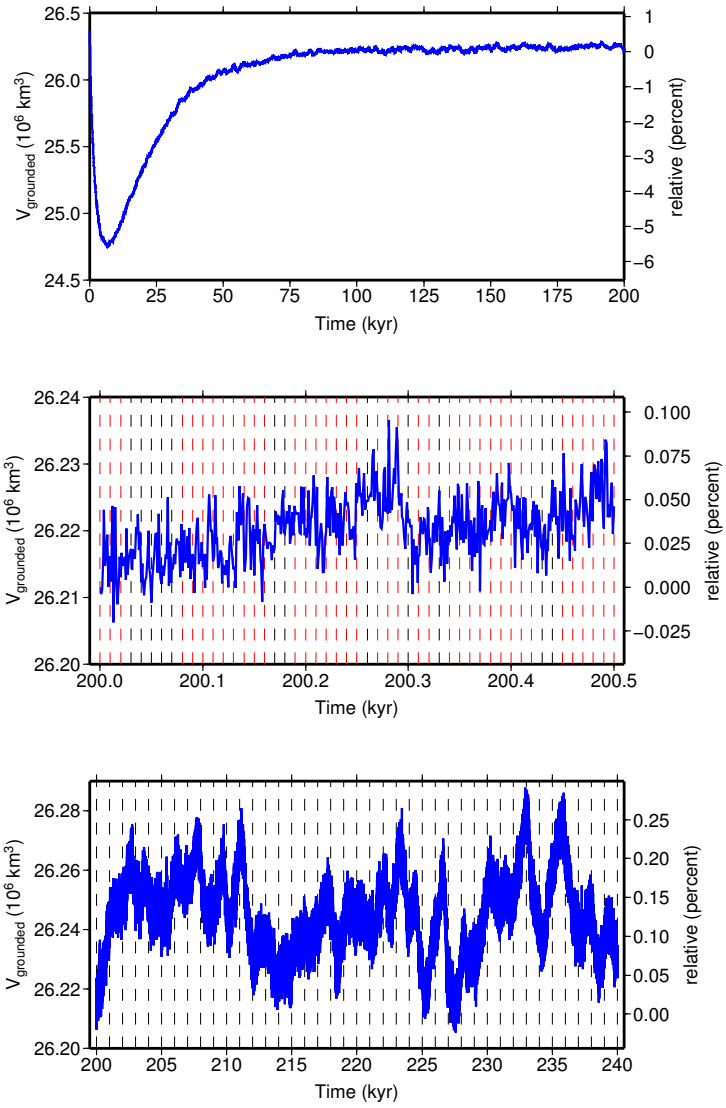

Figure D.3
Top: time series of grounded ice during the model initialization of the AIS (200 kyr). Center: The initialization run from 200 kyr to 200.5 kyr. The vertical dashed lines give the times which are considered as initial states for studying the capability of timing the collapse as discussed in Appendix D.4 (red $\hat{=}$ early collapse branch; black $\hat{=}$ late collapse branch. Bottom: The initialization run from 200 kyr to 240 kyr. The vertical lines give the times which are considered as initial times for the ensemble in the medium and strong forcing of the AIS as shown in Figures 4.7 and D.6 and discussed in Section 4.3.1. Only the first six of these samples are used for the strongly forced simulations. Note that no solid-Earth deformation and sea-level changes are considered in the initialization run.

D.3 Global glacier ice distribution

No.	Region	V_{reg} (km^3)	z_{reg} (m)	H_0 (m)	Grid nodes
1	Svalbard	10260	-65	99.78	349
2	Scandinavia	224	1280	76.78	4
3	Central Europe	194	2280	91.78	2
4	Franz Josef Land	2248	-65	107.43	85
5	Novaya Zemlya	9410	-70	125.17	190
6	Severnaya Zemlya	6046	20	80.84	243
7	Caucasus	88	2700	71.25	1
8	North and East Asia	170	2750	84.86	2
9	High Mountain Asia	12483	5250	78.75	124
10	Alaska	27436	1100	93.11	423
11	Western Canada and U.S.	1892	2650	79.20	21
12	Arctic Canada	80160	200	84.56	2036
13	Iceland	4889	300	71.11	108
14	South America I	344	4780	81.71	3
15	South America II	8116	1500	82.27	79
16	New Zealand	83	1320	75.23	1
17	Sub-Antarctic Islands	363	285	99.54	4

Table D.1
Glacier inventory applied in Section 4.3.2. V_{reg} gives the volume of ice stored in the glaciers of the respective region according to Radić and Hock (2010). The altitude z_{reg} gives the threshold above which the ice is assumed to be located. Note that these values are arbitrarily chosen to constrain the regionally constant ice thickness to values around 100 m. The last column gives the number of grid nodes that the respective region covers on the 512×1024 Gauss-Legendre grid of the SLE solver (cf. Section 2.3.3).

The glacier regions, their ice volumes and the respective coordinates including the regions are taken from Radić and Hock (2010). For each region, a topographical threshold z_{reg} is defined. All ice is distributed uniformly with ice thickness H_0 on all grid nodes of the SLE solver's Gauss-Legendre grid (Section 2.3.3)

1. that are located in the respective region, and
2. where $\zeta \geq z_{\text{reg}}$ with ζ being the present-day bathymetry as described in Section 4.2.1.

The values for z_{reg} are chosen such that the values of H_0 are around 100 m in all regions and (in the case of $z_{\text{reg}} < 0$) floatation is avoided. The resulting areas that are covered with ice as well as the respective ice thicknesses H_0 are shown in Figure D.4. Table D.1 also summarizes the results of this procedure.

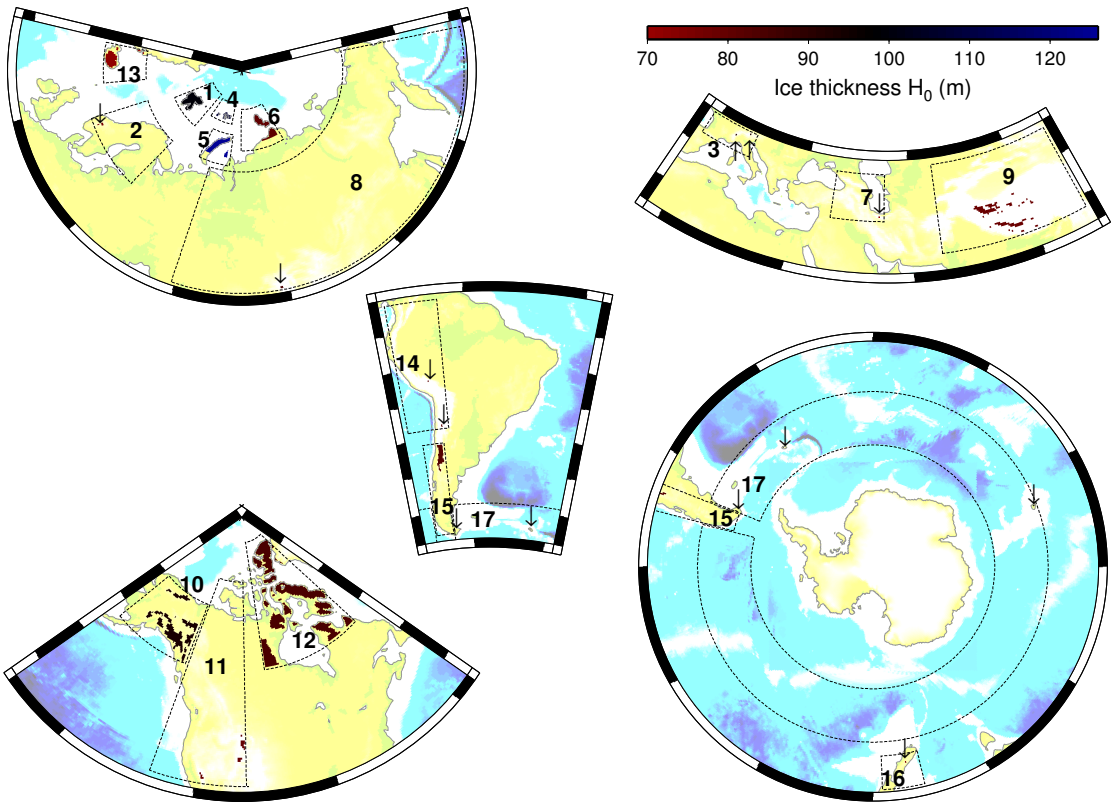

Figure D.4
Global glacier inventory in terms of mean regional ice thickness based on the data by Radić and Hock (2010) transferred to the Gauss-Legendre grid of the SLE solver (Section 2.3.3). See main text in Appendix D.3 for details. The numbers of the regions are given in Table D.1. The present-day topography as also shown in Figure 4.3 is illustrated in very light colors for better orientation. Note that the ice in some regions is located at only few grid points (Table D.1) which hinders their visual identification. These are indicated by black arrows.

D.4 On the timing of the collapse

After 200 kyr of initialization, the ice-sheet geometry and by that also the ice volume and the dynamics are still subject to small variations (less than 0.3 percent of grounded ice volume, cf. Figure D.3 in Appendix D). In order to assess the effect of these variations, a test ensemble was created from 51 different initial states by increasing the ocean temperature by $\Delta T_{\mathrm{oc}} = 1.2°\mathrm{C}$ and the air temperature by $\Delta T_{\mathrm{at}} = 2.4°\mathrm{C}$. In contrast to the experiments discussed in the main text of Chapter 4, the oceanic temperature forcing is applied not only in the Amundsen Sea Sector but all around Antarctica.
The k-th initial state is obtained as the final state of the above mentioned initialization run over 200 kyr + 0.01 $(k-1)$ kyr so that two 'neighbouring' initial states are separated by 10 yr in the unperturbed long-term simulation for initialization. There is no solid-Earth deformation, sea-level feedback or sea-level rise considered in these simulations.

The forcing is strong enough to have the WAIS collapsed after 6 kyr at the latest (corresponding to the state indicated in Figure 4.1B). The respective evolution of grounded ice volume in time in the 51 test runs is shown in Figure D.5A. The most prominent feature of these results is the strong scattering of the timing of the collapse: All simulations yield a similar behaviour for the first ∼2 kyr. Then, a stronger ice loss occurs in most simulations (associated to the WAIS collapse). A smaller number of the test runs reaches this status of accelerated collapse at ∼4 kyr. By that, the simulations form two branches which are separated by more then 1 kyr during the collapse on average (Figure D.5B). This gives rise to the conclusion that single simulations cannot provide a reasonable timing of the WAIS collapse (if it occurs). Instead, the nonlinearities in ice dynamics in general and probably in grounding line migration in particalur yield this quasi-chaotic behaviour, where slight changes in the initial state shift the collapse by more than 1 kyr.

Comparable simulations with a higher spatial resolution of 20 km yield a similar behaviour. Note that the evident clustering as discussed here and shown in Figure D.5 is not as prominent when solid-Earth deformation and sea-level feedbacks are included. Then, the respective ensembles scatter rather uniformly (Appendix D.5). This might be due to the restriction of oceanic warming to the Amundsen Sea Sector, or to the feedbacks with the solid-Earth, or to both, but is not further investigated here.

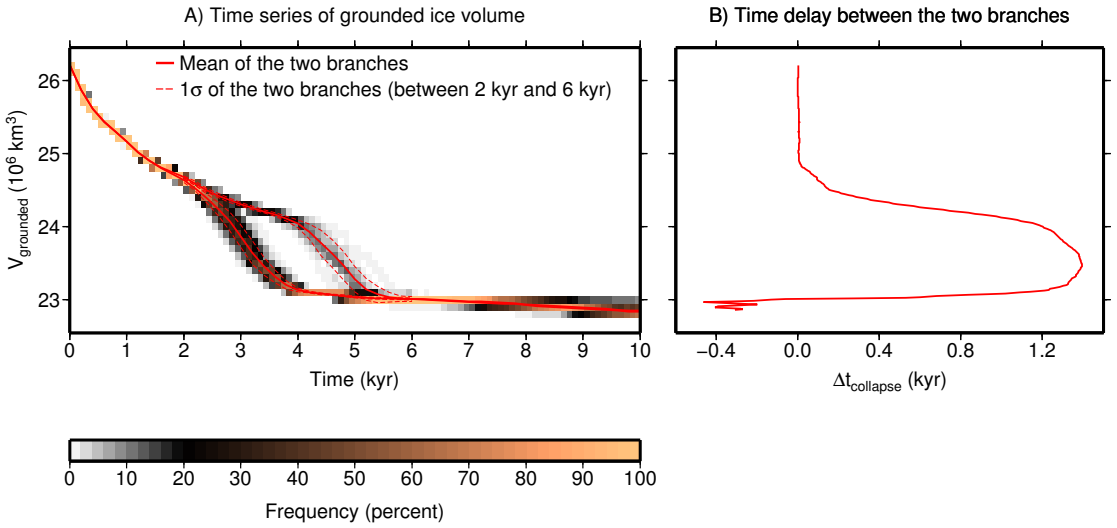

Figure D.5
A: Distribution of grounded ice volume in the temporal evolution in the 51 test runs (see main text in Appendix D.4). The background colouring illustrates the relative frequency, by which the time series of grounded ice volume in the test runs pass through the respective segments of the frame. Note the formation of two branches. The red lines represent mean and 1σ variability of the two branches. B: Time delay between the two branches (mean curves in A) as a function of the grounded ice volume (considered representative for the ice sheet's status).

D.5 Complete ensemble of WAIS collapse simulations

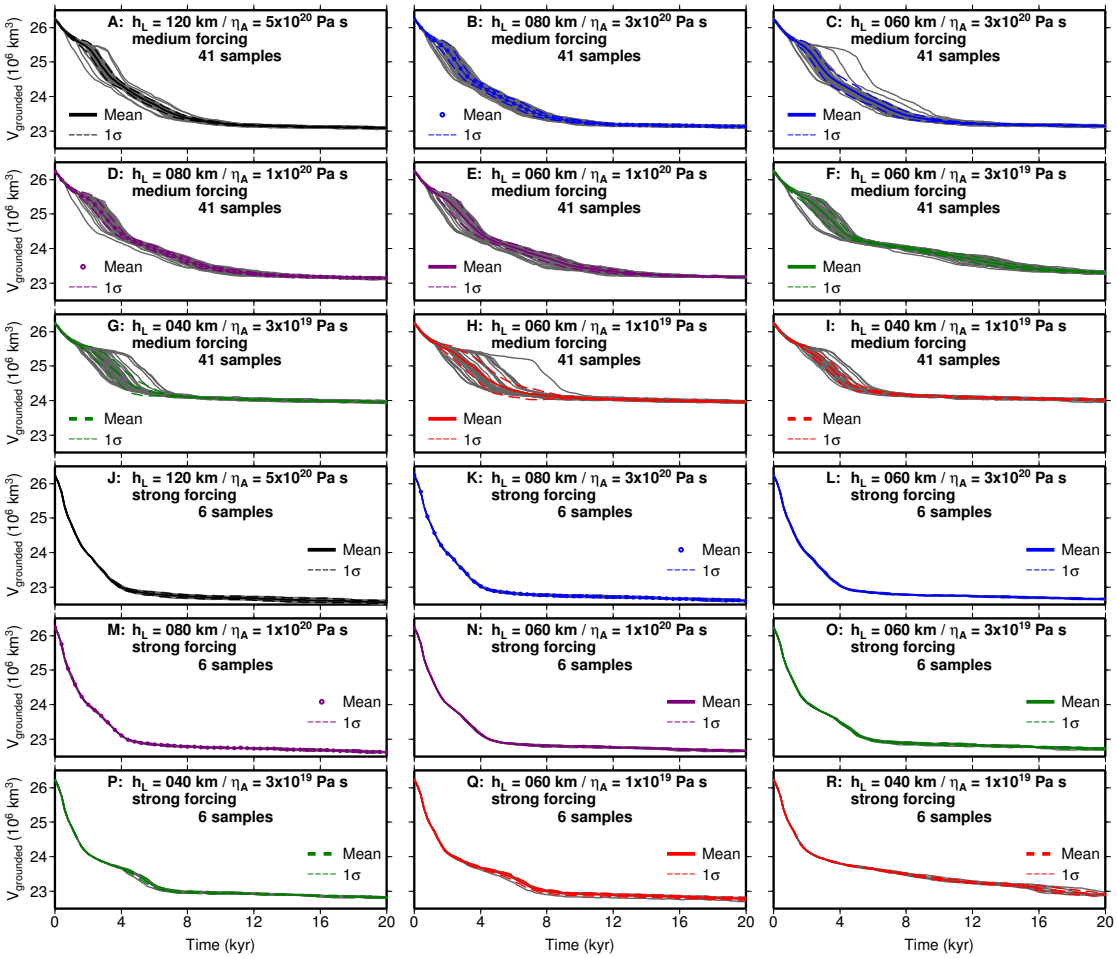

Figure D.6
Time series of all samples for the medium and strong forcing of the WAIS collapse as described in Section 4. The grey lines indicate the samples. The colored lines represent the respective mean and the 1σ uncertainty.

D.6 Temporal delay between the Earth structures

Figure D.7 summarizes the temporal delay ($\Delta t_{\mathrm{delay}}$) between each two Earth structures i and j for the named two values of grounded ice volume on the basis of the data in Figure 4.8. The convention for the temporal differences is:

$$\begin{aligned} \Delta t_{\mathrm{delay},ijk} &= t_i(V_{\mathrm{grounded,k}}) - t_j(V_{\mathrm{grounded},k}) \text{ with} \\ & \quad h_{\mathrm{L},i} < h_{\mathrm{L},j} \text{ and } \eta_{\mathrm{A},i} \leq \eta_{\mathrm{A},j} \text{ , or} \\ & \quad h_{\mathrm{L},i} \leq h_{\mathrm{L},j} \text{ and } \eta_{\mathrm{A},i} < \eta_{\mathrm{A},j} \text{ .} \end{aligned} \tag{D.1}$$

The underlines in Figure D.7 indicate that the respective values for $\Delta t_{\mathrm{delay}}$ exceed the respective uncertainties:

$$\Delta t_{\mathrm{delay},ijk} > \sqrt{\left(\Delta t_{\mathrm{std},i}(V_{\mathrm{grounded,k}})\right)^2 + \left(\Delta t_{\mathrm{std},j}(V_{\mathrm{grounded,k}})\right)^2} \tag{D.2}$$

with Δt_{std} defined in Eq. 4.5. The convention in Eq. D.1 implies that positive values of $\Delta t_{\mathrm{delay}}$ are expected because a thinner lithosphere and a softer asthenosphere are expected to provide more stability to the WAIS and thus to delay the ice loss. Naturally, this should also manifest in a monotonous increase in the timing of $V_{\mathrm{grounded},k}$ in Figure 4.8 when proceeding along the abscissa to softer Earth structures. Some of the results yield the reverse order for the timing and by that negative values for $\Delta t_{\mathrm{delay},ijk}$ in contrast to the expectations. These are, however, not significant in terms of relation D.2.

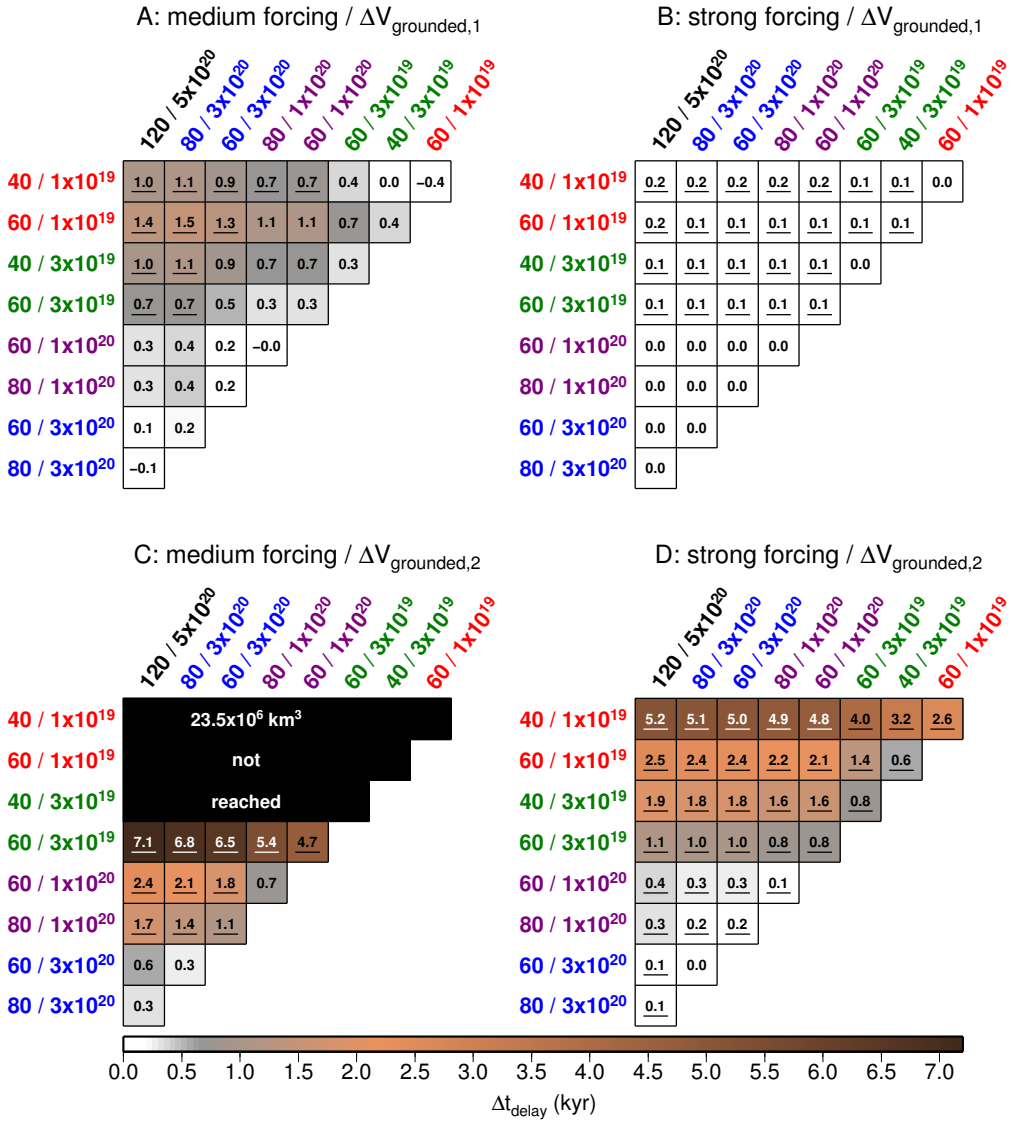

Figure D.7
Temporal delay Δt_{delay} for given values of grounded ice volume (A and B: $V_{\text{grounded},1} = 24.5{\times}10^6$ km^3; C and D: $V_{\text{grounded},2} = 23.5{\times}10^6$ km^3) between each two Earth structures (indicated as h_{L} / η_{A}); see Eq. D.1 for the convention for Δt_{delay}. The left frames (A and C) are for the mediumly forced simulations; the right ones (B and D) for the strongly forced ones. The number and the colorcoding in each cell both give Δt_{delay} (in kyr). The underlined numbers indicate a delay which is greater than the respective temporal uncertainties – cf. relation D.2. Note that $V_{\text{grounded},2}$ is not reached with every Earth structure (no WAIS collapse – black cells). The temporal delay is computed from the data illustrated in Figure 4.8.

D.7 Convergence of the present-day bathymetry in the glacial cycle simulations

As stated in Section 5.3, the paleo bathymetry after two iteration steps is considered to have converged sufficiently so that the results from iteration step 3 can be used for the analysis. When considering the area-weighted average of differences between the final and the observed present-day bathymetry, this seems feasible: Outside Antarctica (here: latitudes above $-60°$), the mean differences are 0 m $\pm$ 0 m for all Earth structures. Within Antarctica (latitudes below $-60°$), there is only a small mean deviation of -1 m in the case of the very soft Earth structure (Table D.2).

The maximum deviations, however, are still substantial for some Earth structures. Outside Antarctica, these are below 7 m, which indicates a reasonable convergence due to prescribed ice thickness fields which are not dynamically modeled and therefore independent from the iteration.[ix] Within Antarctica, these deviations exceed 200 m in the case of the very soft Earth structure and 50 m in the case of the soft Earth structure. The two stiffer Earth structures yield a tighter convergence. The differences within Antarctica can partially be attributed to deviations in the ice dynamical evolution close to the end of the experiment.

The largest deviations, however, stem from the initialization procedure: A large positive correction of the paleo bathymetry in the case of the softer Earth structures yields ice advance into the collapsed areas in Marie Byrd Land during the stationary forcing period (Figure 5.1) without coupling to the solid Earth. This readvance reduces the effective loading towards the LGM in the next iteration step, which leads to less subsidence at the LGM, and by that to a negative correction of the paleo bathymetry in the next iteration step. This eventually manifests in an alternation of the paleo bathymetry in this area. This effect is visualized and quantified in Table D.2 and Figure D.8 (in terms of the deviations of the present-day bathymetry to respective observations (ETOPO1/BEDMAP2; Figure 4.3), also for iteration steps beyond the third one. The local alternation could potentially be forced to a convergence by omitting the stationary forcing to reach a steady state. However, this would lead to an additional transient response of the ice sheet following the sudden change of the paleo bathymetry at the start of the simulation.

The discussion on the influence of the viscosity structure on the glacial cycle in

[ix] The deviations stem from the differences in the surface load σ, which does not only depend on the prescribed ΔH-fields, but also on the initial bathymetry and the sea-level evolution (cf. Section 2.3.2).

Section 5.4.3 focusses on the Ross Ice Shelf area (less than 4 m in total; less than 2 m in the case of the focussed stiff Earth structure; see Table D.2), which is hardly affected by this alternation, opposed to Marie Byrd Land, where the maximum values mentioned above (200 m in the case of the very soft Earth structure; 50 m in the case of the soft Earth structure) are reached. The further discussion of this issue is left open in the scope of this thesis.

Earth	Step	Lat. $\geq -60°$ Mean	Lat. $\geq -60°$ Max.	Lat. $\leq -60°$ Mean	Lat. $\leq -60°$ Max.	Ross Mean	Ross Max.
very soft	1	-3 ± 3	242	-5 ± 4	145	-19 ± 11	24
	2	0 ± 0	32	-1 ± 1	61	-3 ± 2	3
	3	0 ± 0	9	1 ± 0	207	0 ± 0	1
	4	0 ± 0	3	-1 ± 1	254	2 ± 1	2
	5	0 ± 0	1	0 ± 0	122	0 ± 0	1
	6	0 ± 0	1	0 ± 0	119	0 ± 0	1
soft	1	-3 ± 3	271	-5 ± 4	147	-28 ± 16	38
	2	-1 ± 0	57	-1 ± 1	59	-3 ± 2	5
	3	0 ± 0	14	0 ± 0	57	-2 ± 1	4
	4	0 ± 0	3	0 ± 0	65	0 ± 0	1
	5	0 ± 0	1	0 ± 0	61	1 ± 0	1
	6	0 ± 0	0	0 ± 0	48	0 ± 0	0
stiff	1	-3 ± 3	284	-3 ± 3	129	-28 ± 16	44
	2	-1 ± 0	40	-2 ± 1	30	-4 ± 2	6
	3	0 ± 0	7	0 ± 0	26	0 ± 0	2
	4	0 ± 0	1	0 ± 0	16	-1 ± 0	2
very stiff	1	-4 ± 3	393	-4 ± 3	135	-41 ± 22	68
	2	-1 ± 1	41	-2 ± 1	33	-9 ± 5	13
	3	0 ± 0	3	0 ± 0	8	-2 ± 1	2
	4	0 ± 0	0	0 ± 0	14	-1 ± 0	1

Table D.2
Convergence of the present-day bathymetry outside Antarctica (latitude $\geq -60°$), within Antarctica (latitude $\leq -60°$), and particularly in the Ross Ice Shelf (red in Figure D.8) in terms of the mean deviation from the Etopo1/BEDMAP2 data set (Figure 4.3) and the respective standard deviation as well as the maximum absolute deviation in meters. 'Step' refers to the respective iteration step according to Section 5.3. Note that the maximum deviations are taken from the absolute differences. The means and standard deviations are area-weighted.

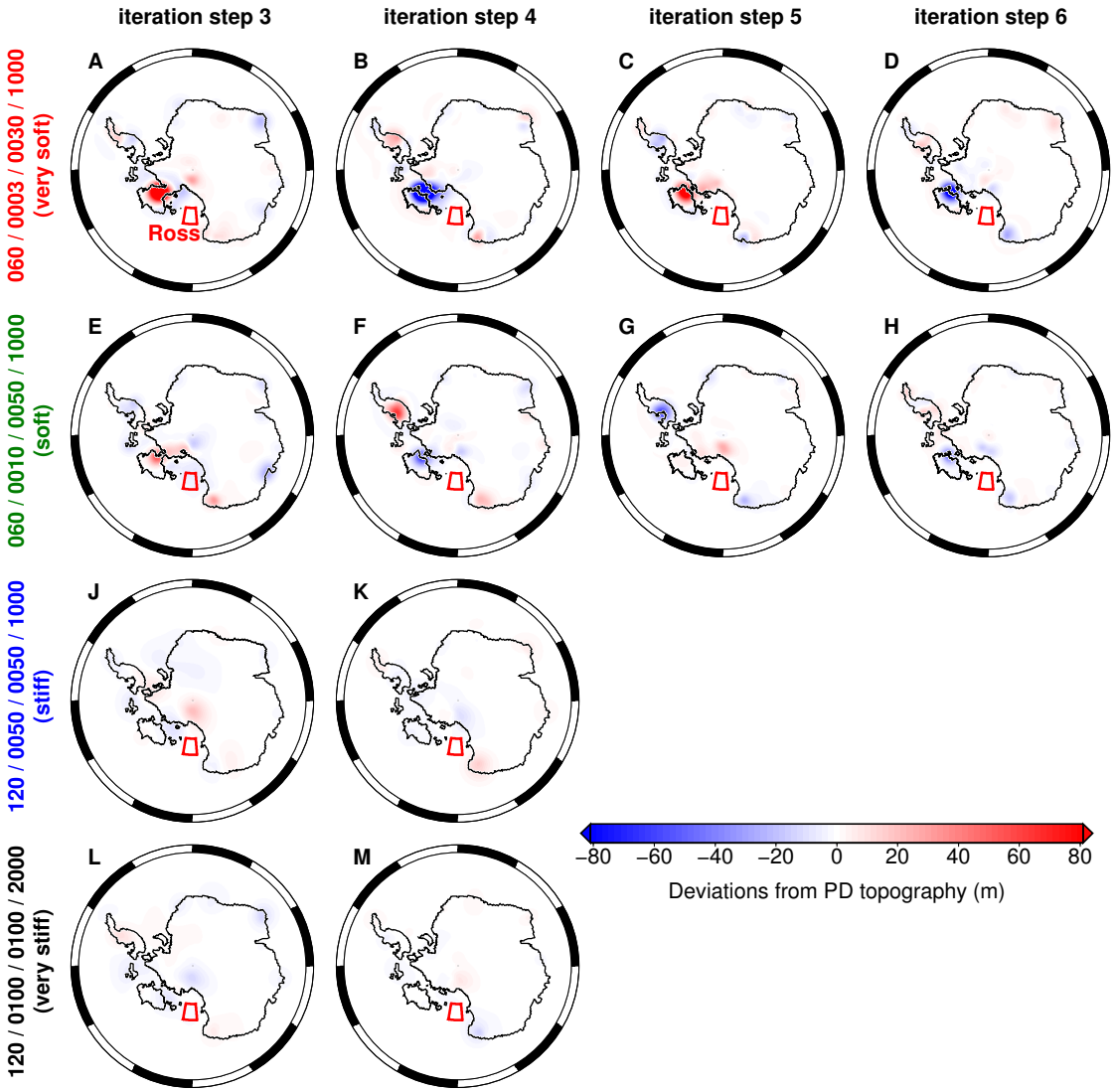

Figure D.8
Differences between the modeled present-day bathymetry and the present-day reference bathymetry (Figure 5.1) within Antarctica for various iteration steps starting at three (columns) and for the four Earth structures (rows). The black lines indicate the initial (Eemian) GL. The red outline shows the area which is considered for the values in Table D.2 labeled with 'Ross'. Note that the four points C, D, E, and F in Figures 5.8 and D.10 are included in this area.

D.8 Single results of the glacial cycle simulations

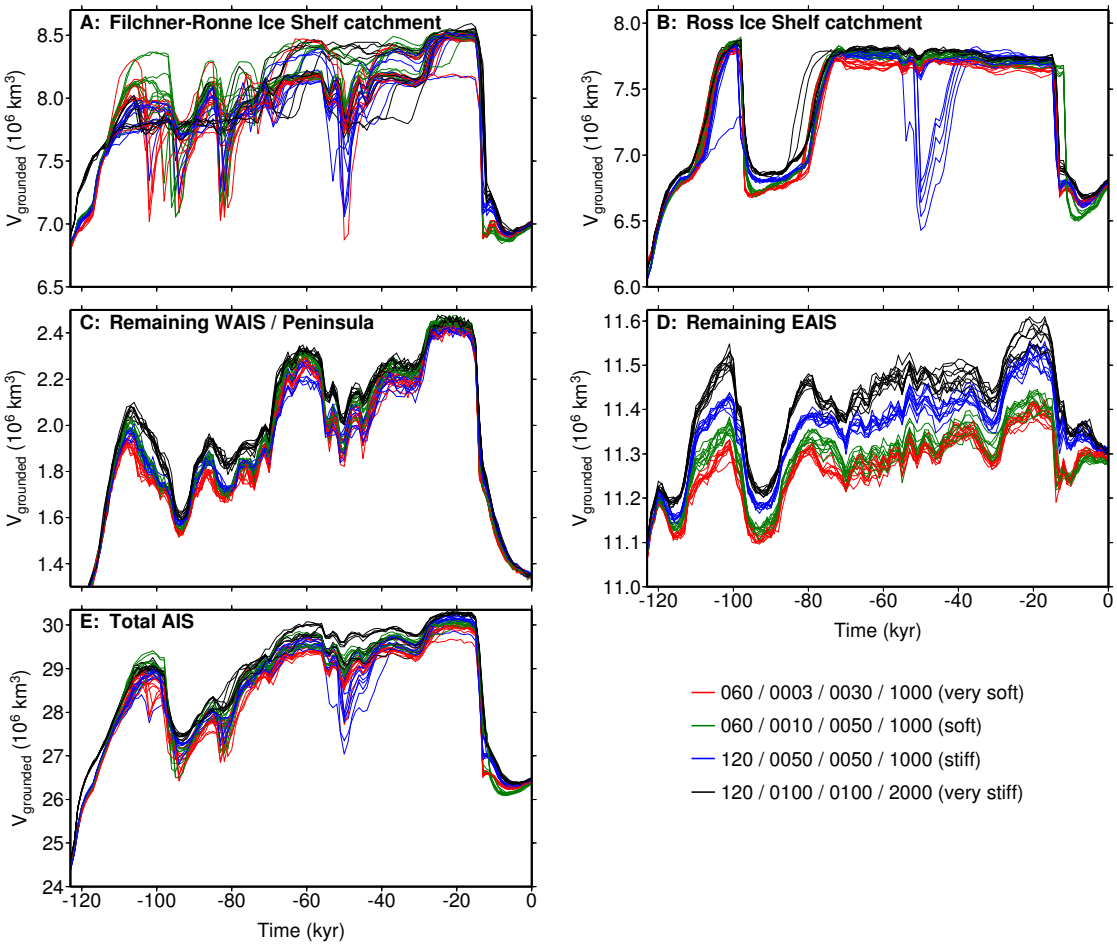

Figure D.9
Complete ensemble of ten runs per viscosity structure for iteration step 3 as summarized in Figures 5.4 and 5.7 for the four catchment areas (A–D) and the total AIS (E).

D.9 Northern hemispheric sea-level fingerprint in the Ross Ice Shelf catchment

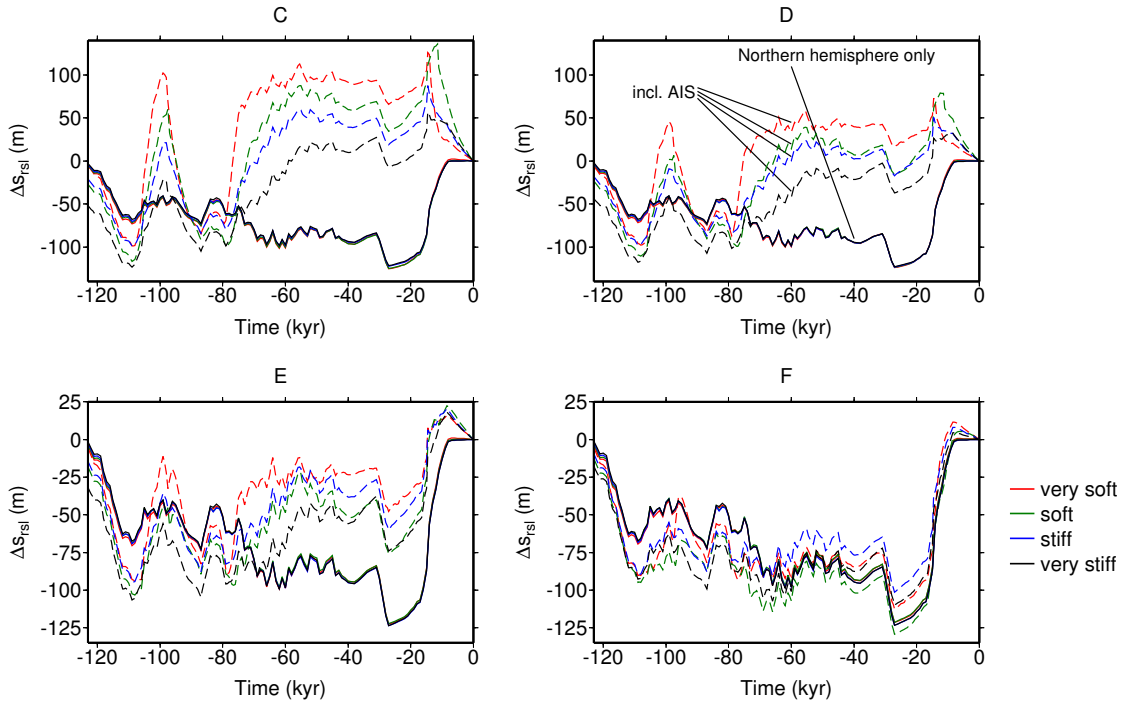

Figure D.10
Time series of Δs_{rsl} in the Ross Ice Shelf if only the northern hemispheric contributions from ICE-5G are considered (solid lines) and for the complete simulation including the AIS (dashed lines). Note that Δs_{rsl} is referenced to present-day ($t = 0$) here, because the s_{rsl} time series converge at one value in the complete simulations for all Earth structures due to the bathymetry iteration (Figure 5.8). The locations C–F are the same as in Figure 5.8. Frame labels 'A' and 'B' are missing for consistency with Figure 5.8. The solid lines are bundled (mean difference: 0.9 m ± 0.9 m; maximum difference: 5.4 m) as they roughly represent the eustatic response, whereas the dashed lines scatter broadly (mean difference: 16 m ± 20 m; maximum difference: 127 m). Consequently, the fingerprint from northern hemispheric ice mass variations is not responsible for the variations seen in the RSL as discussed in Chapter 5.

List of acronyms and abbreviations

AIS	–	Antarctic Ice Sheet
ALBMAPv1	–	Compilation of input data for ice-dynamical modeling at Antarctica (Le Brocq et al., 2010)
BDR	–	Bedrock deformation rates
BEDMAP2	–	Data set for Antarctic bedrock topography (Fretwell et al., 2013)
EAIS	–	East Antarctic Ice Sheet
EISMINT	–	European Ice Sheet Modeling Initiative (Payne et al., 2000)
ELRA	–	Elastic Lithosphere / Relaxing Asthenosphere (e.g. Le Meur and Huybrechts, 1996)
ESL	–	Equivalent sea level
ETOPO1	–	Global bathymetry data set (Amante and Eakins, 2009)
ICESat	–	Ice, Cloud and Land Elevation Satellite (Laser altimeter) (`http://www.nasa.gov/mission_pages/icesat/index.html`)
IPCC AR5	–	Fifth Assessment Report of the Intergovernmental Panel on Climate Change (Stocker et al., 2013)
IS1	–	Iteration step 1 of the paleo bathymetry adjustment in Chapter 5
IS3	–	Iteration step 3 of the paleo bathymetry adjustment in Chapter 5
GIA	–	Glacial-isostatic adjustment
GL	–	Grounding line
GRACE	–	Gravity Recovery And Climate Experiment
GrIS	–	Greenland Ice Sheet
ICE-5G	–	Global ice history for the last glacial cycle (Peltier, 2004)
LGM	–	Last Glacial Maximum
MISI	–	Marine Ice Sheet Instability
PDD	–	Positive Degree Day
PennState3d	–	Ice-sheet model (Pollard and DeConto, 2012b)
PREM	–	Preliminary Earth Reference Model (Dziewonski and Anderson, 1981)
RIMBAY	–	Revised Ice Model Based on frAnk PattYn (Thoma et al., 2014)
RSL	–	Relative sea level
S12	–	Viscosity distribution optimal for fitting GIA signatures over the northern Hemisphere (Sasgen et al., 2012)
SeaRISE	–	Sea-level Response to Ice Sheet Evolution (Bindschadler et al., 2013)
SGVEM	–	Self-gravitating viscoelastic Earth model
SIA	–	Shallow Ice Approximation
SLE	–	Sea-level equation
SMB	–	Surface mass balance

SSA	–	Shallow Shelf Approximation
VILMA	–	VIscoelastic Lithosphere and MAntle model (Martinec, 2000)
VM2	–	Commonly applied viscosity distribution (Peltier, 2004)
WAIS	–	West Antarctic Ice Sheet
WE	–	Water equivalent

List of figures

List of tables